# Bose-Einstein Condensation in the Quantum Spin-System $TlCuCl_3$: Any Sign of "Magnetic Superfluidity" ?

Dissertation

zur

Erlangung der naturwissenschaftlichen Doktorwürde
(Dr. sc. nat.)

vorgelegt der

Mathematisch-naturwissenschaftlichen Fakultät

der

Universität Zürich

von

Raffaele Dell'Amore
aus Italien

Promotionskomitee

Prof. Dr. Andreas Schilling (Vorsitz)
Prof. Dr. Hugo Keller (Direktor des Physik-Instituts)
Dr. Jorge Gavilano (PSI, externer Experte)

Zürich, 2008

a chi, se non a voi...
Antonio, Teresa, Michele ed Anina

Die vorliegende Arbeit wurde von der Mathematisch-naturwissenschaftlichen Fakultät der Universität Zürich auf Antrag des Promotionskomitees des Physik-Instituts unter der Leitung von Prof. Dr. Andreas Schilling als Dissertation angenommen.

# Abstract

1908 was an important year for experimental physics. Kamerlingh Onnes succeeded in liquefying Helium gas. This achievement opened the door to an experimentally accessible low-temperature range in which fascinating physical phenomena were found. Two of the most important discoveries occurring at low temperatures are undoubtely *superconductivity* and *Bose-Einstein condensation*. Both phenomena are still subject of modern research studies. *Superconductivity* describes the loss-less transport of current in solids. The Bose-Einstein condensation manifests the occupation of a single quantum state by a macroscopic number of physically indistinguishable particles.
The physics of superconductivity mainly concerns the solid state physics, while the phenomenon of Bose-Einstein condensation is an important concept in atomic physics. In modern research, Bose-Einstein condensation is starting to gain much interest in the field of quantum magnetism, as well. There are clear experimental indications that the manifestation of this phenomenon is also possible involving magnetic quasiparticles, spin-excitations with no physical extension, in contrast to hard-sphere atoms.
This thesis is concerned with the occurrence of Bose-Einstein condensation in magnetic materials. We will start with a discussion of pioneering theoretical concepts and follow it with a description of the main physical concepts of this phenomenon in low-dimensional spin-systems. From the analysis of experimental magnetization-data we conclude that the application of a BEC-like scenario in $\mathrm{TlCuCl_3}$ is valid under certain circumstances. In order to preserve the validity of a field-direction independent chemical potential we had to consider the contribution of a spin $S = 1$ Brillouin-like term in the condensed phase which is a priori not predicted by theory. Moreover, using a simple, general theoretical concept we predict the occurrence of system-anisotropies upon condensation which may considerably alter the correctness of the BEC-scenario in $\mathrm{TlCuCl_3}$ at lowest excitation energies. The experimental detection of a possible "magnetic-superfluid" component is, therefore, particularly complicated. A possible detection-method and the corresponding experimental set-up are presented in the last part of this thesis.

# Zusammenfassung

1908 war ein sehr wichtiges Jahr für die experimentelle Physik. Kamerlingh Onnes schaffte es, flüssiges Helium zu gewinnen. Dieses Gelingen öffnete die Tür zum Erreichen einer neuen Temperaturskala in der physikalischen Forschung. Neue und faszinierende Phänomene wurden entdeckt. Zwei der wichtigsten Naturerscheinungen bei tiefen Temperaturen sind zweifellos die *Supraleitung* und die *Bose-Einstein Kondensation*. Sie sind heute noch Inhalt aktueller Forschung. Die *Supraleitung* beschreibt die Eigenheit bestimmter Materialen, den Strom verlustfrei transportieren zu können. Die *Bose-Einstein Kondensation* äussert sich in der makroskopischen Besetzung eines Ein-Teilchen Zustands durch eine Vielzahl ununterscheidbarer Teilchen.
Die Supraleitung ist hauptsächlich Gegenstand der Festkörperphysik, während das Phenomonen der Bose-Einstein Kondensation hauptsächlich Inhalt atomarer Physik war. Heutzutage ist das Interesse in der Festkörperphysik gegenber dieser einzigartigen Naturerscheinung gestiegen. Aus Experimenten wurde deutlich, dass die Bose-Einstein Kondensation auch auf magnetischer Ebene geschehen kann. Die involvierten Teilchen sind magnetische Spin-Anregungen, die aufgrund ihrer eindeutig definierten Energie-Impuls Relation als Quasi-Teilchen beschrieben werden können.
Diese Doktorarbeit befasst sich mit dem Vorkommen der Bose-Einstein Kondensation in magnetischen Substanzen. Grundlegende theoretische Konzepte werden zu Beginn erläutert. Der Leser wird nachfolgend durch die theoretischen Grundsätze der Bose-Einstein Kondensation in magnetischen Materialien geführt. Anhand von experimentell gemessenen Magnetisierungs-Daten und entsprechenden Berechnungen wird ein mögliches Vorkommen der Bose-Einstein Kondensation in $\mathrm{TlCuCl_3}$ bestätigt, falls das Beisein eines Spin S=1 Brillouin-term in der kondensierten Phase berücksichtigt wird. Die Präsenz eines solchen Beitrags ist in der Theorie der Bose-Einstein Kondensation in magnetischen Substanzen jedoch "a priori" nicht vorausgesagt. Resultate weiterer Rechnungen weisen darauf hin, dass in $\mathrm{TlCuCl_3}$ beim Phasenübergang System-anisotropien auftreten können, deren Präsenz das Beschreiben des Phasenüberganges als Bose-Einstein Kondensation bei niedrigen Anregungsenergien in Frage stellen. Eine experimentelle Detektion der "magnetischen Supra-fluidität" ist ebenfalls aus diesem Grund erschwert. In dieser Hinsicht wird am Schluss dieser Arbeit ein Experiment und dessen Aufbau vorgestellt, welches zur Detektion "magnetischer Suprafluidität" in solchen Substanzen führen könnte.

# Sommario

Il 1908 é stato un anno fondamentale per la fisica. Kamerlingh Onnes riuscì nella liquefazione di gas elio. Quest' avvenimento fu la chiave per raggiungere basse temperature nella fisica esperimentale. Nuovi e affascinanti fenomeni fisici furono scoperti. Due di questi piu importanti apparizioni sono di sicuro la superconduttività e la condensazione di Bose-Einstein. La superconduttività si occupa della particolarità di certe sostanze di riuscire a trasportare corrente elettrica senza nessuna resistenza. La condensazione di Bose-Einstein dal canto suo si manifesta nella occupazione macroscopica di uno stato singolo da parte di indistinguibili particelle. La superconduttività é in maggior parte sostanza di ricerca nella fisica dello stato solido. La condensazione di Bose-Einstein dal canto é primariamente stata studiata nella fisica atomica. L'interesse nel fenomeno della condensazioen di Bose-Einstein é pero sostanzialmente aumentato negli ultimi anni anche nella ricerca di fisica dello stato solido. Oggi si é convinti che quest' ultimo evento si manifesti anche sul campo magnetico. Le particelle involte sono delle eccitazioni di spin, che a causa della loro evidente relazione tra energia ed impulso fisicalmente soddisfano le caratteristiche di una quasi-particella.
Questa tesi tratta dell'evento della condensazione di Bose-Einstein in materiali magnetici. All'inizio basilari concetti teorici sono introdotti per poi passare ad fondamentali concetti valevoli solo per i materiali magnetici. Analizzando i data di magnetizzazione dell'isolante $TlCuCl_3$ l'occorrere della condensazione die Bose-Einstein é confermata assumendo certi condizioni. Inoltre, facendo uso di un concetto teorico di validità generale suggeriamo una instabilità generale del systema all'avvenire della condensazione che complica la misurazione sperimentale di una componente "magneto-superfluida" che dovrebbe essere presente in certi casi. Negli ultimi capitoli della tesi un possible metodo di misurazione e respettiva disposizione sperimentale a questo scopo sono proposti e discussi.

# Contents

**Abstract** **i**

**1 Preface** **1**

**2 Bose-Einstein Condensation** **7**
2.1 The Bose-Einstein statistics . . . . . 7
2.2 The thermodynamical aspects of the ideal Bose-Einstein gas . . . . . 8
2.3 The interacting Bose-Einstein gas . . . . . 12
2.3.1 The quantum-field theoretical approach . . . . . 12
2.3.2 The microscopical approach . . . . . 15

**3 From Bose-Einstein condensation to superfluidity** **17**
3.1 The off-diagonal long range order . . . . . 17
3.2 The macroscopic wave function and the order parameter . . . . . 18
3.3 The $U(1)$-symmetry breaking and the Goldstone Mode . . . . . 20

**4 Superfluidity** **23**
4.1 The two-fluid model I . . . . . 23
4.2 The two-fluid model II . . . . . 26
4.3 The microscopic approach by Bogoliubov . . . . . 28
4.4 The sound propagation in a Bose-Einstein condensate . . . . . 29
4.4.1 First sound . . . . . 31
4.4.2 Second sound . . . . . 31
4.4.3 First and second sound in an interacting Bose gas at finite temperatures 33

**5 Low-dimensional magnetism and Bose-Einstein condensation** **35**
5.1 The quantum spin-dimer . . . . . 35
5.1.1 The influence of an external magnetic field . . . . . 36
5.2 The quantum spin systems . . . . . 37
5.3 The spin-dimer representation . . . . . 42
5.4 The Bose-Einstein condensation of $S$=1-triplons . . . . . 45
5.5 The candidates for Bose-Einsten condensation of triplons . . . . . 48

**6 The quantum spin system $TlCuCl_3$** **53**
6.1 The crystal structure and the magnetic exchange interactions . . . . . 53
6.2 The magnetic susceptibility . . . . . 57
6.3 The total magnetization . . . . . 59
6.3.1 The magnetization $M(T)$ for $1\mathrm{T} \leq \mu_0 H \leq \mu_0 H_{c1}$ . . . . . 59
6.3.2 The magnetization $M(T)$ for $6\ \mathrm{T} \leq \mu_0\mathrm{H} \leq 9\ \mathrm{T}$ . . . . . 64
6.3.3 The exponent $\alpha$ . . . . . 72
6.4 The Bose-Einstein condensation of triplons within the Hartree-Fock (HF) approximation . . . . . 73
6.4.1 The Bose-Einstein condensation of a dilute Bose gas . . . . . 77
6.5 $U(1)$-Symmetry breaking and violation of axial symmetry . . . . . 78

6.5.1 Comparison with results from Hartree-Fock calculations . . . 79
6.5.2 Instability of the condensate towards violation of axial symmetry . . 89
6.5.3 Uniaxial pressure effects ? . . . 92

**7 Search for "magnetic superfluidity" 93**
7.1 The model . . . 93
7.1.1 The density-density function for magnetic insulator studied within the BEC-scenario of magnetic quasiparticles . . . 95
7.1.2 The sound-mode in the condensate phase of $TlCuCl_3$ . . . 95
7.1.3 The characteristic resonance frequencies for the used $TlCuCl_3$-specimen 97
7.2 The detection of collective modes . . . 99
7.2.1 The ac-susceptometer . . . 102
7.2.2 The mathematical principles of the designed ac-susceptibility experiment 104
7.2.3 The measuring procedure and first results . . . 107

**8 Conclusions and outlook 113**

**9 Acknowledgements 115**

**Bibliography 117**

**A The coherent states 131**

**B The two-fluid picture and the momentum carried by excitations 132**

**C The two sound modes in a condensate 133**

**D The Hartree-Fock (Popov) approximation 135**

**E The LabView software 136**

**F The absolute values of the Bessel functions 137**

# List of Acronyms

| | |
|---|---|
| BEC | Bose-Einstein condensation |
| QMC | Quantum Monte-Carlo |
| ODLRO | off-diagonal long range order |
| He II | The superfluid phase of $^4\mathrm{He}$ |
| LRO | long-range order |
| VBS | valence bond solid |
| QCP | quantum critical point |
| QPT | quantum phase transition |
| HFP | Hartree-Fock Popov (approximation) |
| MFT | mean field theory |

# 1 Preface

It all started more than 100 years ago.
In December of 1900, Max Planck unveiled his derivation of the black-body radiation law to the Physikalischen Gesellschaft in Berlin [1]. Starting from purely mathematical foundations, he showed that light must be emitted and absorbed in discrete amounts of energy, called quanta (lat. *quantum* = how much?, a quantitiy of one unit). Up to this point, light had only been considered as a continuous electromagnetic wave. Consequently, this discrete behavior was totally unexpected. As a result of Planck's work Quantum Physics was born. In the years following, this led to revolutionary interpretations of understanding light and matter interactions.
Experiments first performed by Heinrich Hertz [2] and then by Wilhelm Hallwachs [3], showed that electrons escape out of metals when stimulated by light radiation (photoelectric effect). Explaining these results, Albert Einstein showed in 1905 [4] that the energy of such a light-quantum is determined by its frequency $\nu$, with $E = h\nu$ and $h$ is the Planck constant. Such a light-quantum is called *photon*, which is interpreted as a light-particle. For this discovery, Albert Einstein was awarded the Nobel Prize of Physics in 1921.
Meanwhile Louis-Victor de Broglie assumed that because light had both particle and wave properties, this might also be true for matter [5]. He assessed the respective relationship between the moment $p$ and the corresponding wavelength $\lambda$ with $p = \frac{h}{\lambda}$. Thus, the position of a particle with a thermal Energy $E = \pi k_{\mathrm{B}} T$ is spread out over a distance given by the thermal de Broglie wavelength

$$\lambda_{\mathrm{dB}} = \sqrt{\frac{2\pi\hbar^2}{m k_{\mathrm{B}} T}}.$$

In the early 1920s, the Indian physicist Satyendra Nath Bose was studying the behavior of a set of photons. Treating them as a gas of identical particles he succeeded in deriving Planck's law for the black-body radiation. Bose, however, had difficulties convincing the scientific establishments to publish his findings, so he sent them to Einstein. Einstein agreed with with Bose's theory and generalized it to an ideal (non-interacting) gas of atoms or molecules in which the number of particles is conserved [6]. Subsequently, Einstein predicted that at sufficiently low temperatures, exceeding a critical density, a macroscopic part of the particles (and at zero temperature all of them) would start to populate a single one-particle (energetically the most favorable) quantum state of the system.
Today, we know that this phenomenon, called Bose-Einstein condensation (hereafter abbreviated as BEC), only occurs for bosons - particles with a total spin being an integer multiple of Planck's constant $h$.
Descriptively speaking, lowering the temperature of a gas causes an increase of the thermal de Broglie wavelength $\lambda_{\mathrm{dB}}$ of each particle. They become correlated with each other, as soon as

Figure 1: Satyendra Nath Bose (1894-1974)

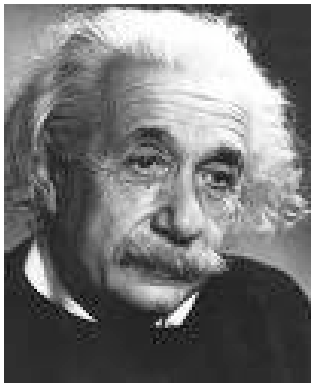

Figure 2: Albert Einstein (1879-1955)

their related wave functions start to overlap. The particles lose their identity, and their behavior is now governed by quantum statistics. They now act collectively as a coherent, classical wave. This requires the wavelength $\lambda_{\mathrm{dB}}$ to be larger than the mean interparticle distance $l$, $\lambda_{\mathrm{dB}} > l$. The average particle density $\rho = \frac{N}{\Omega}$ for $N$ particles in a volume $\Omega$ is related to the mean distance $l$ through the equality $\rho l^3 = 1$. Hence, the condition $\lambda_{\mathrm{dB}} > l$ may be rewritten as $\rho\lambda_{\mathrm{dB}}^3 > 1$. This yields the inequality

$$T < \frac{2\pi\hbar^2\rho^{\frac{2}{3}}}{mk_{\mathrm{B}}},$$

which tells us that the coherence state may develop if the temperature is sufficiently low or the density of particles is sufficiently high.

Experimenters had attempted to produce such a condensate in the laboratory for many years, achieving it only in 1995, in the atomic gases of rubidium[8] and sodium[9]. Two years later BEC was also discovered in a diluted vapor of lithium atoms[10, 11]. During these years enormous progresses in cooling techniques [12–15] had to be made in order to cool an atomic gas below the required microkelvin-range reaching densities of $10^{14}\mathrm{cm}^{-3}$, while preventing the atoms from condensing into a liquid or a solid.

Nonetheless, the idea of BEC was already used in 1938 by F. London and L. Tisza [16, 17] quite successfully explaining the transition of "normal" to "superfluid" $^4\mathrm{He}$ (liquid $^4\mathrm{He}$ flows without a viscous damping below a transition temperature of 2.17 K), although the strong interactions that exist in $^4\mathrm{He}$ [1] may alter the nature of the transition. This is underlined by the fact that while 90-95% of the particles in an atomic ensemble are condensed below the transition temperature, just a small percent ($\sim 9\%$) of the Helium-atoms are in the "superfluid" phase, even at very low temperatures. The notion that superfluidity was a manifestation of Bose-Einstein condensation was seen as highly controversial. L. Landau rejected the idea in favor

[1] it's still a liquid

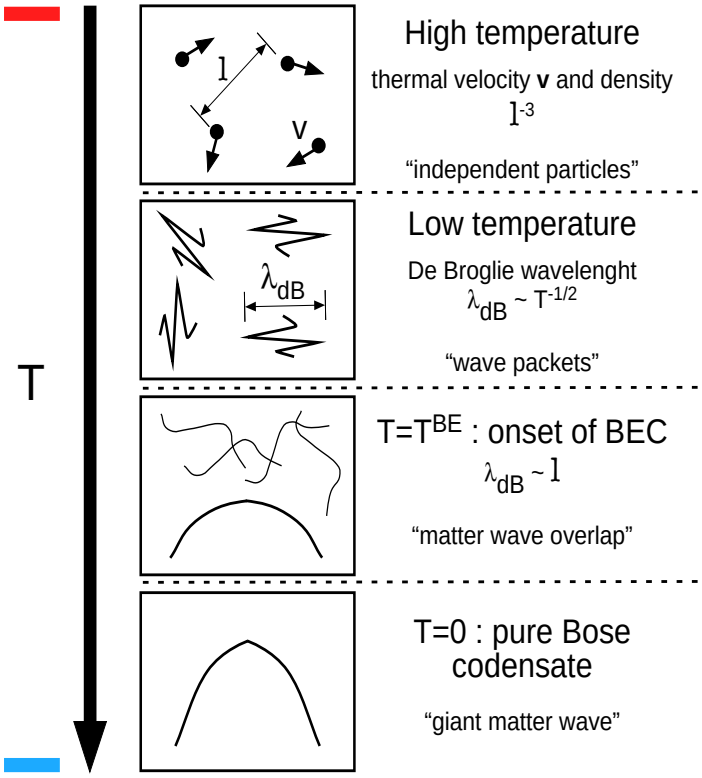


Figure 3: At high temperatures a weakly-interacting Bose gas can be treated as a system of independent particles. In a simplified quantum description, the particles can be regarded as wave packets with an extension $\lambda_{\mathrm{dB}}$. At the BEC transition temperature $T^{BE}$, $\lambda_{\mathrm{dB}}$ becomes comparable to the inter-particle distance and a Bose condensate starts to form. A pure condensate state is reached upon approaching zero temperature [7].

of a quantum hydrodynamical explanation setting up the theory for a ”two-fluid-model”[18]. This model explains ”superfluidity” in a conceptual and intuitive way, rather than explicitly demonstrating that it is a consequence of the Bose-statistics obeyed by the atoms. The convergence of these two approaches was suggested by the Bogoliubov theory of weakly-interacting Bose gases [19]. The theory proved that Bose-Einstein condensation could produce features of the excitation spectrum that Landaus' hydrodynamic theory postulated.

Experiment (neutron scattering experiments [20]) and theory (path-integral Monte Carlo simulations [21]) nowadays support the idea that the microscopic physics underlying superfluidity is a zero-momentum BEC.

A substantial amount of theoretical and experimental work in this regard has been done in the last decade. A matter of great interest, especially for experimenters, is the study of the coherence phenomena [22, 23] and superfluid effects [24, 25] in such (atomic) condensates. Spontaneous coherence in such novel systems is direct evidence for the existence of a Bose-

Einstein condensate. In more recent works, first theoretically [26, 27] and then experimentally [28–30], the concept of BEC has been extended to various types of quasiparticles, discrete (magnetic, electronic, lattice) excitations (in solids), that can be treated as real particles. The appeal of such quasiparticles in solids as systems to observe condensation is, in part, their light mass (roughly equal to the mass of an electron). The smaller the mass, the higher the critical temperature at which condensation might occur [2].

The discovery, however, of a BEC-like scenario of different types of quasiparticles in different materials raised various questions [31]. In one case [29], the lifetime of the quasiparticles is very short (a few picoseconds). In other cases, the number of quasiparticles is not conserved [30], or symmetry aspects are not entirely fulfilled [32]. To what extent these unfavorable conditions affect the coherence phenomena of the Bose-Einstein condensate on a laboratory time scale is still an issue of debate.

To prove that there is, in fact, a true condensate one has to show that the particles form a single coherent state, similar to the superfluid phase as observed in liquid $^4\mathrm{He}$. In analogy to $^4\mathrm{He}$ [33], a second-sound mode in such a phase should be present. Such a mode manifests itself as an oscillation of the local density of the quasiparticles (superfluid and normalfluid component flow relative to one another) and accordingly of the entropy in the system. The detection of second-sound modes consists therefore in measuring slight oscillations of the density of the condensed quasiparticles yielding standing entropy waves in the rf-range depending on the sample geometry. Experimental evidence of the presence of such a mode would be a convincing method to demonstrate the existence of a superfluid component in the system and a clear sign of the occurrence of a BEC.

We therefore built a new AC susceptometer to perform high-frequency magnetic-susceptibility measurements from 100 kHz up to 2 MHz. The design is a standard 3-coil configuration with a primary drive-coil and two secondary pick-up coils. Sweeping the frequency of the drive-signal and measuring the voltage difference $\Delta U$ between the two pick-up coils, we can detect how the signal output changes due to the sample. These changes are allocated to the excitation of some (magnetic) modes. A step motor enables us to move the sample in and out of the pick-up coils, or to move it from one secondary coil to the other one. Thus, an immediate background subtraction is implemented. Higher sensitivity is reached by modulating the drive-signal and implementing a corresponding phase-locked detection method.

The magnetic insulator $\mathrm{TlCuCl_3}$ is a quantum- spin- $\frac{1}{2}$ system, which for low magnetic fields $\mu_0 H_c \lessapprox 5.5\mathrm{T}$ and at low temperatures shows a gap between the ground state and the first excited states. The spin-spin correlation function decays exponentially defining a finite correlation length. Such systems are described as a spin-liquid, by analogy with standard liquids in contrast to solids. At higher magnetic fields a phase transition to a magnetic phase with

[2] there is no reason why the condensation of such quasiparticles cannot occur at room temperature

an antiferromagnetic order of the transversal spin components occurs. Theoretical and experimental work indicate that this transition can be interpreted as the Bose-Einstein condensation of the magnetic excitations carrying total spin $S = 1$ [27, 28]. In this respect, $\mathrm{TlCuCl_3}$ is an ideal candidate for us to study under this aspect. Limitations of our cryo-system (such as the lowest reachable temperature and the highest applicable magnetic field) do not impede us from investigating this phenomenon in this compound, as it is the case for other solids [34, 35].
Our latest theoretical findings, however, predict the presence of an anisotropy gap $\tilde{\Delta}$ in the excitation spectrum of $\mathrm{TlCuCl_3}$ in the ordered phase. $\tilde{\Delta}$ opens at the phase boundary and increases with increasing number of condensed particles (i.e., with increasing magnetic field). This gap covers an excitation-frequency range that is still crucial for experiments that rely on the existence of a long-lived condensate such as the detection of a second-sound like oscillation. In fact, the detection of such a mode in $\mathrm{TlCuCl_3}$ turned out to be a very tricky undertaking. Nonetheless, we believe that the here presented experimental set-up can be used in the future as a standard measurement method to perform such or similar measurements.

# 2 Bose-Einstein Condensation

We know that there are two kinds of quantum-particles, bosons and fermions, obeying either the Bose-Einstein or the Fermi-Dirac statistics, respectively. The method of counting quantum states introduced by Bose and Einstein applies to bosons, particles with an integral value of spin. Fermions are particles with a half-integer spin.

## 2.1 The Bose-Einstein statistics

Bosonic particles are quantum-mechanically indistinguishable, i.e., a single quantum state can be occupied by a free number of bosons.
Let us assume to have $N_s$ identical Bose particles in $M_s$ available quantum states. It then follows that there are

$$W_s = \frac{(N_s + M_s - 1)!}{N_s!(M_s - 1)!} \tag{2.1}$$

ways the particles can be distributed. We apply this combinatorial rule to the thermodynamics of an ideal gas of $N$ bosons.
The principles of statistical mechanics state that the total entropy of a gas is $S = k_{\mathrm{B}} \ln(W)$, where $k_{\mathrm{B}}$ is the Boltzmann's constant and $W$ is the total number of available states at a given energy $E$. In order to determine $W$, one must consider how a set of $N$ particles are distributed among the $\mathbf{k}$-space shells. The total number of available states for the whole gas is, therefore, simply the product of the number of the states in each $\mathbf{k}$-space shell. Using Eq. (2.1) we get

$$W = \prod_s W_s = \prod_s \frac{(N_s + M_s - 1)!}{N_s!(M_s - 1)!}. \tag{2.2}$$

With Stirling's approximation, $\ln(X!) \approx X \ln(X) - X$ and assuming that $N_s, M_s \gg 1$, we obtain

$$\frac{S}{k_{\mathrm{B}}} = \ln(W) = \sum_s \left[(N_s + M_s)\ln(N_s + M_s) - N_s \ln(N_s) - M_s \ln(M_s)\right] \tag{2.3}$$

In thermal equilibrium, the particles will distribute among the available states in such a way to maximize the total entropy $S$. Using the Lagrangian multiplier method, keeping the number of particles

$$N = \sum_s N_s \tag{2.4}$$

and the internal energy of the gas

$$U = \sum_s \varepsilon_s N_s \tag{2.5}$$

constant, it results that

$$\frac{\partial S}{\partial N_s} - k_{\mathrm{B}}\beta \frac{\partial U}{\partial N_s} + k_{\mathrm{B}}\beta\mu \frac{\partial N}{\partial N_s} = 0, \tag{2.6}$$

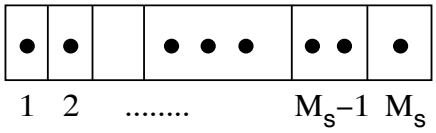


Figure 4: A descriptive illustration of the the Bose-Einstein statistics. One can count the number of possible configurations by considering that $N_s$ identical particles and $M_s - 1$ walls between the boxes can be arranged within an array in any order.

with $k_{\mathrm{B}}\beta$ and - $k_{\mathrm{B}}\beta\mu$ as Lagrangian multiplier constants.
The first law of thermodynamics for a gas of $N$ particles, where $T$ is the temperature, $p$ is the pressure and $\mu$ is the chemical potential yields

$$dS = \frac{1}{T}\left(dU + pd\Omega - \mu dN\right). \tag{2.7}$$

In our case we have

$$dS = \sum_s \frac{\partial S}{\partial N_s} dN_s \overset{\text{Eq. (2.6)}}{=} k_{\mathrm{B}}\beta \sum_s \left(\frac{\partial U}{\partial N_s} - \mu \frac{\partial N}{\partial N_s}\right) dN_s = k_{\mathrm{B}}\beta\left(dU - \mu dN\right). \tag{2.8}$$

Comparing Eq. (2.7) with Eq. (2.8), it results that $\beta = \frac{1}{k_{\mathrm{B}}T}$ and $\mu$ is the chemical potential, as expected.
Computing the differentiations in Eq. (2.6) and rearranging the equation to find $N_s$, one reproduces the result obtained by Bose [36] first and resumed by Einstein after,

$$N_s = \frac{1}{e^{\beta(\varepsilon_s - \mu)} - 1} M_s. \tag{2.9}$$

The average number of particles occupying any single quantum state is $\frac{N_s}{M_s}$, known as the **Bose-Einstein distribution**

$$\boxed{f_{\mathrm{BE}}(\varepsilon) = \frac{1}{e^{\beta(\varepsilon - \mu)} - 1}}. \tag{2.10}$$

## 2.2 The thermodynamical aspects of the ideal Bose-Einstein gas

The ideal Bose-Einstein gas is defined as a set of non-interacting bosons. It is, therefore, a unique occurrence that this gas undergoes a thermodynamic phase transition, the **Bose-Einstein condensation** . This phase transition is exclusively driven by the particles' statistics. The condensed particles all occupy a single quantum state of zero momentum, while the non-condensed particles all have finite momentum. Starting from the Bose-Einstein distribution, see Eq. (2.10), the total number of particles in the gas is expressed as

$$N = \sum_{\mathbf{k}} \frac{1}{e^{\beta(\varepsilon_{\mathbf{k}} - \mu)} - 1}. \tag{2.11}$$

Assuming $N$ bosons to occupy a volume $\Omega = L_x L_y L_z$ and using periodic boundary conditions, every individual particle will be in a quantum state

$$\psi_{\mathbf{k}}(\mathbf{r}) = \frac{1}{\sqrt{\Omega}} e^{i\mathbf{kr}}, \tag{2.12}$$

where the allowed wavevectors are

$$\mathbf{k} = \left( \frac{2\pi n_x}{L_x}, \frac{2\pi n_x}{L_x}, \frac{2\pi n_x}{L_x} \right). \tag{2.13}$$

The infinitesimal volume $d^3k = dk_x dk_y dk_z$ in $\mathbf{k}$-space thus contains $\frac{\Omega}{(2\pi)^3} d^3k$ quantum states. Each of these single quantum states has energy $\varepsilon_{\mathbf{k}} = \frac{\hbar^2 k^2}{2m^\star}$, where $m^\star$ is the mass of a particle. Dividing up the $\mathbf{k}$-space into thin spherical shells of radius $k_s$ and thickness $\delta k_s$, we get

$$M_s = 4\pi k_s \delta k_s \frac{\Omega}{(2\pi)^3} \tag{2.14}$$

available states per shell. The number of available states between energy $\varepsilon_s$ and $\varepsilon_s + \delta\varepsilon_s$ is, therefore,

$$M_s = \Omega g(\varepsilon_s) \delta\varepsilon_s, \tag{2.15}$$

where

$$g(\varepsilon) = \frac{m^{\frac{3}{2}}}{\sqrt{2}\pi^2\hbar^3} \varepsilon^{\frac{1}{2}} \tag{2.16}$$

is the density of states per unit volume.
In the thermodynamic limit ($N$ and $\Omega \to \infty$ with $N/\Omega$=const.), the possible momentum states become a continuum and one has to replace the summation of the discrete states in Eq. (2.11) with an integration

$$\sum_{\mathbf{k}} \to \int \frac{\Omega}{(2\pi)^3} d^3k. \tag{2.17}$$

For the particle density $n = \frac{N}{\Omega}$ we get

$$n = \frac{1}{(2\pi)^3} \int \frac{1}{e^{\beta(\varepsilon_{\mathbf{k}} - \mu)} - 1} d^3k, \tag{2.18}$$

which in terms of the density of states per unit volume $g(\varepsilon)$, see Eq. (2.16), corresponds to

$$n = \int_0^\infty \frac{1}{e^{\beta(\varepsilon - \mu)} - 1} g(\varepsilon) d\varepsilon. \tag{2.19}$$

From Eq. (2.19) we can determine the chemical potential $\mu(T, n)$ as a function of temperature $T$ and particle density $n$. Defining the dimensionless variables $z = e^{\beta\mu}$ and $x = \beta\varepsilon$, one can rewrite Eq. (2.19) as

$$n = \frac{(mk_{\mathrm{B}}T)^{\frac{3}{2}}}{\sqrt{2}\pi^2\hbar^3} \int_0^\infty \frac{ze^{-x}}{1 - ze^x} x^{\frac{1}{2}} dx. \tag{2.20}$$

Expanding

$$\frac{ze^{-x}}{1-ze^{x}} = \sum_{l=1}^{\infty} z^{l} e^{-lx} \tag{2.21}$$

and using the definition of the gamma function

$$\Gamma(t) = \int_{0}^{\infty} y^{t-1} e^{-y} dy, \tag{2.22}$$

with $\Gamma(t=\frac{3}{2}) = \frac{\sqrt{\pi}}{2}$, we obtain a simplified expression for the particle density

$$n = \left(\frac{mk_{\mathrm{B}}T}{2\pi\hbar^{2}}\right)^{\frac{3}{2}} g_{3/2}(z), \tag{2.23}$$

where

$$g_{3/2}(z) = \sum_{l=1}^{\infty} \frac{z^{l}}{l^{\frac{3}{2}}}. \tag{2.24}$$

In order to evaluate Eq. (2.23) a few considerations about $g_{3/2}(z)$ need to be presented. This series converges when $|z|$ <1, but diverges for $|z|$ >1. At $|z|$=1, however, the series is just convergent,

$$g_{3/2}(1) = \sum_{l=1}^{\infty} \frac{1}{l^{\frac{3}{2}}} = 2.612. \tag{2.25}$$

Rearranging Eq. (2.23), we can conclude that the value of the chemical potential $\mu$ is determined by

$$g_{3/2}(e^{\beta\mu}) = \left(\frac{2\pi\hbar^{2}}{mk_{\mathrm{B}}T}\right)^{\frac{3}{2}} n. \tag{2.26}$$

If we are at high temperatures or at low densities, the right-hand side of Eq. (2.26) is small and we can use the expansion series for $g_{3/2}(z = e^{\beta\mu}) \approx z$, neglecting all non-linear terms and obtain

$$\mu = -\frac{3}{2} k_{\mathrm{B}}T \ln\left(\frac{mk_{\mathrm{B}}T}{2\pi\hbar^{2}n^{\frac{2}{3}}}\right). \tag{2.27}$$

Fixing the density $n$ and cooling the gas to lower temperatures $|z|$ gradually increases until it reaches $|z| = 1$ with $g(z = 1) = 2.612$ and $\mu = 0$. The chemical potential becomes zero at this point . The corresponding temperature is defined as the critical temperature $T^{BE}$, also called **the BEC-temperature**

$$T^{BE} = \frac{2\pi\hbar^{2}}{mk_{\mathrm{B}}} \left(\frac{n}{2.612}\right)^{\frac{2}{3}}. \tag{2.28}$$

A macroscopic number $N_c$ of particles occupies the ground state $\varepsilon_{\mathbf{k}=0}$. For $T < T^{BE}$ we, therefore, must consider the $\mathbf{k} = 0$-state separately. Starting from

$$N = N_c + \sum_{\mathbf{k}\neq 0} \frac{1}{e^{\beta\varepsilon_{\mathbf{k}}} - 1} \tag{2.29}$$

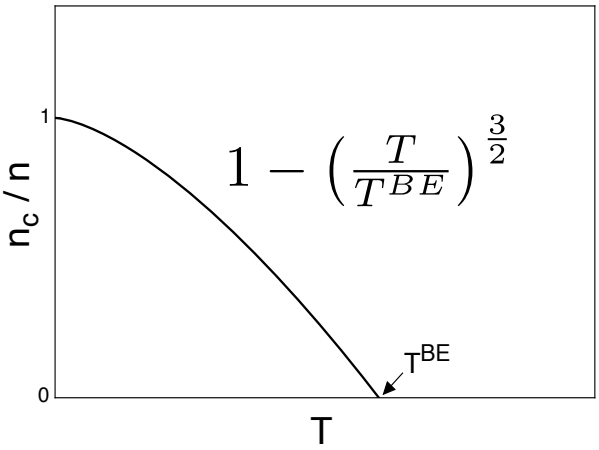


Figure 5: Sketch of the temperature-dependence of the condensate density $n_c$

and again replacing the summation with an integration (excluding $\mathbf{k} = 0$), we get

$$n = n_c + 2.612 \left(\frac{mk_{\mathrm{B}}T}{2\pi\hbar^2}\right)^{\frac{3}{2}}. \tag{2.30}$$

With $\lambda_{\mathrm{dB}} = \sqrt{\frac{2\pi\hbar^2}{mk_{\mathrm{B}}T}}$ we obtain from Eq. (2.30)

$$n_c = n - \frac{2.612}{\lambda_{\mathrm{dB}}^3}, \tag{2.31}$$

which defines a critical density at a fixed temperature

$$n_{crit}(T) = \frac{2.612}{\lambda(T)_{\mathrm{dB}}^3}, \tag{2.32}$$

above which condensation begins. This definition enables us to capture the phenomenon of the Bose-Einstein condensation in a descriptive way. More than 2.6 particles localized within the De Broglie-volume $\lambda_{\mathrm{dB}}^3$ leads to strong quantum effects governing the condensation.
The particle density $n$ can, therefore, be divided into a condensate density $n_c$ and a normal density $\tilde{n}$, where

$$n = n_c + \tilde{n}. \tag{2.33}$$

Combining Eq. (2.28) and Eq. (2.30) finally yields

$$\frac{n_c}{n} = 1 - \left(\frac{T}{T^{BE}}\right)^{\frac{3}{2}} \tag{2.34}$$

for the fraction of condensed particles. It is evident that at $T$=0 all particles populate the ground state.

## 2.3 The interacting Bose-Einstein gas

The original arguments of Einstein assumed the absence of interactions among the considered particles. In this section, I would like to present the generalization of the BEC-concept for an interacting system of bosons.
We again consider a large (fixed) number $N$ of bosons at position vector $\mathbf{r}_i$ with momenta $\mathbf{p}_i$ ($i$= 1, 2, ..., $N$). The interaction between the particles is described by the potential $V(\mathbf{r}_i - \mathbf{r}_j)$. The many-body Hamilton operator is, therefore, written as

$$\hat{H} = \sum_{i=1}^{N} -\frac{\hbar^2}{2m}{\nabla_i}^2 + \frac{1}{2}\sum_{i,j=1,N} V(\mathbf{r}_i - \mathbf{r}_j). \tag{2.35}$$

This operator acts on an $N$-particle wave function $\Psi(\mathbf{r}_1, \mathbf{r}_2, \ldots, \mathbf{r}_N)$. Such a function is per definition[3] symmetric under the permutation of two or more particles

$$\Psi(\ldots, \mathbf{r}_i, \ldots, \mathbf{r}_j, \ldots) = \Psi(\ldots, \mathbf{r}_j, \ldots, \mathbf{r}_i, \ldots) \qquad \forall i, j. \tag{2.36}$$

The possible quantum states of the system are the Eigenstates of the Hamiltonian $\hat{H}$, with

$$\hat{H}\Psi_n(\mathbf{r}_1, \ldots, \mathbf{r}_N) = E_n^{(N)}\Psi_n(\mathbf{r}_1, \ldots, \mathbf{r}_N), \tag{2.37}$$

where $E_n^{(N)}$ for $n$=0,1,2, ... are the energy levels. If the system is at zero temperature, one finds the $N$-particle ground state $\Psi_0(\mathbf{r}_1, \ldots, \mathbf{r}_N)$. Using the standard rules of statistical physics in the **grand canonical ensemble** using Quantum Monte Carlo (QMC) methods, theoreticians are able to calculate the observable quantities of an interacting many-boson system for large number of particles [21]. By systematically comparing the results of the calculations with increasing numbers of particles, they can successfully make accurate predictions concerning the thermodynamic limit $N \to \infty$.
In contrast to the non-interacting system, where at zero temperature all the particles are found to be in the ground state, corresponding results demonstrate that the zero momentum state of an interacting system of bosons is populated by "a macroscopic number of particles ", even at $T = 0$. This fact is known as *the depletion of the ground state*.

### 2.3.1 The quantum-field theoretical approach

Let us consider a single-particle state as a plane-wave state

$$\psi_{\mathbf{k}}(\mathbf{r}) = \frac{1}{\sqrt{\Omega}}e^{i\mathbf{kr}}. \tag{2.38}$$

This state can be multiply occupied by bosonic particles. A general quantum many-body state of the system will be a coherent superposition of different $N$-body plane wave states, see

[3] bosons are quantum-mechanically indistinguishable

App. A. The complete basis of all possible states can be represented by the set of all possible occupation numbers of each plane wave state

$$|n_{\mathbf{1}}, n_{\mathbf{2}}, \ldots, n_{\mathbf{k}}, \ldots\rangle, \tag{2.39}$$

where $n_{\mathbf{k}}$ denotes the number of times the state $\psi_{\mathbf{k}}$ is occupied, which corresponds to the number of particles residing in the state $\psi_{\mathbf{k}}$. Therefore, one can write

$$\sum_{k}^{\infty} n_{\mathbf{k}} = N. \tag{2.40}$$

The vector space generated by this basis is called the *Fock-space*. It is the direct sum of all the sub-spaces with a fixed number of particles: without particles (called the ground state or more generally the vacuum state $|0\rangle$), with one particle, two particles, etc.
One defines creation and annihilation operators $a^{\dagger}_{\mathbf{k}}$ and $a_{\mathbf{k}}$, which increase or decrease the occupation numbers $n_{\mathbf{k}}$ by

$$a^{\dagger}_{\mathbf{k}}|\ldots, n_{\mathbf{k}}, \ldots\rangle = \sqrt{n_{\mathbf{k}}+1}|\ldots, n_{\mathbf{k}}+1, \ldots\rangle \tag{2.41}$$

and

$$\langle\ldots, n'_{\mathbf{k}}, \ldots|a_{\mathbf{k}} = \sqrt{n'_{\mathbf{k}+1}}\langle\ldots, n'_{\mathbf{k}+1}, \ldots|. \tag{2.42}$$

The orthogonality condition

$$\langle\ldots, n'_{\mathbf{k}}, \ldots|a_{\mathbf{k}}|\ldots, n_{\mathbf{k}}, \ldots\rangle = \sqrt{n_{\mathbf{k}}}\delta_{n'_{\mathbf{k}+1}, n_{\mathbf{k}}} \tag{2.43}$$

leads to

$$a_{\mathbf{k}}|\ldots, n_{\mathbf{k}}, \ldots\rangle = \begin{cases} \sqrt{n_{\mathbf{k}}}|\ldots, n_{\mathbf{k}}-1, \ldots\rangle & n_{\mathbf{k}} \geqslant 1 \\ 0 & n_{\mathbf{k}} = 0. \end{cases} \tag{2.44}$$

In order to satisfy the Bose symmetry condition, see Eq. (2.36), it is necessary that

$$[a_{\mathbf{k}}, a^{\dagger}_{\mathbf{k}}] = a_{\mathbf{k}}a^{\dagger}_{\mathbf{k}} - a^{\dagger}_{\mathbf{k}}a_{\mathbf{k}} = 1. \tag{2.45}$$

Since the occupation numbers of two different plane wave states are independent of each other, the creation and annihilation operators must commute. The complete set of commutation relations is, therefore, given by

$$[a_{\mathbf{k}}, a^{\dagger}_{\acute{\mathbf{k}}}] = \delta_{\mathbf{k},\acute{\mathbf{k}}} \tag{2.46}$$

$$[a_{\mathbf{k}}, a_{\acute{\mathbf{k}}}] = 0 \tag{2.47}$$

$$[a^{\dagger}_{\mathbf{k}}, a^{\dagger}_{\acute{\mathbf{k}}}] = 0. \tag{2.48}$$

The momentum distribution of the particles is then obtained by taking the mean value of the occupation number

$$n_{\mathbf{k}} = \langle\hat{n}_{\mathbf{k}}\rangle = \langle a^{\dagger}_{\mathbf{k}}a_{\mathbf{k}}\rangle = f_{\mathrm{BE}}(\varepsilon_{\mathbf{k}}), \tag{2.49}$$

see Eq. (2.10).
Similarly, one can define *quantum field operators* $\hat{\psi}^\dagger(\mathbf{r})$ and $\hat{\psi}(\mathbf{r})$ which create and annihilate particles at position vector $\mathbf{r}$. These operators can be defined as a Fourier transform of the $\mathbf{k}$-space operators,

$$\hat{\psi}(\mathbf{r}) = \frac{1}{\sqrt{\Omega}} \sum_{\mathbf{k}} e^{i\mathbf{kr}} a_{\mathbf{k}} \tag{2.50}$$

$$\hat{\psi}^\dagger(\mathbf{r}) = \frac{1}{\sqrt{\Omega}} \sum_{\mathbf{k}} e^{-i\mathbf{kr}} a^\dagger_{\mathbf{k}}. \tag{2.51}$$

The inverse Fourier transforms are then

$$a_{\mathbf{k}} = \frac{1}{\sqrt{\Omega}} \int e^{-i\mathbf{kr}} \hat{\psi}(\mathbf{r}) d^3r \tag{2.52}$$

$$a^\dagger_{\mathbf{k}} = \frac{1}{\sqrt{\Omega}} \int e^{i\mathbf{kr}} \hat{\psi}^\dagger(\mathbf{r}) d^3r. \tag{2.53}$$

Using these definitions and the Bose commutation laws for the $\mathbf{k}$-space field operators, see Eq. (2.46)-Eq. (2.48), we get the following commutation restrictions for the real-space field operators,

$$[\hat{\psi}(\mathbf{r}), \hat{\psi}^\dagger(\acute{\mathbf{r}})] = \delta(\mathbf{r} - \acute{\mathbf{r}}) \tag{2.54}$$

$$[\hat{\psi}(\mathbf{r}), \hat{\psi}(\acute{\mathbf{r}})] = 0 \tag{2.55}$$

$$[\hat{\psi}^\dagger(\mathbf{r}), \hat{\psi}^\dagger(\acute{\mathbf{r}})] = 0. \tag{2.56}$$

Any operator acting on quantum states defined in real-space can be expressed in terms of these creation and annihilation operators. In particular, the Hamiltonian 2.35 becomes

$$\begin{aligned} \hat{H} = &\int \left( \hat{\psi}^\dagger(\mathbf{r}) \left[ -\frac{\hbar^2}{2m} \nabla^2 \right] \hat{\psi}(\mathbf{r}) \right) d^3r \\ &+ \frac{1}{2} \int V(\mathbf{r} - \acute{\mathbf{r}}) \hat{\psi}^\dagger(\mathbf{r}) \hat{\psi}(\mathbf{r}) \hat{\psi}^\dagger(\acute{\mathbf{r}}) \hat{\psi}(\acute{\mathbf{r}}) d^3r d^3\acute{r}, \end{aligned} \tag{2.57}$$

where the combination $\hat{\psi}^\dagger(\mathbf{r})\hat{\psi}(\mathbf{r})$ is the density operator of particles at position vector $\mathbf{r}$.
One can go back to the $\mathbf{k}$-space formalism using the Fourier transformations Eq. (2.52) and Eq. (2.53). For the kinetic-energy term we get

$$\begin{aligned} \hat{T} &= -\int \left( \hat{\psi}^\dagger(\mathbf{r}) \frac{\hbar^2}{2m} \nabla^2 \hat{\psi}(\mathbf{r}) \right) d^3r \\ &= \frac{1}{\Omega} \sum_{\mathbf{k}\acute{\mathbf{k}}} \int \left( a^\dagger_{\acute{\mathbf{k}}} e^{-i\acute{\mathbf{k}}\mathbf{r}} \frac{\hbar^2 k^2}{2m} a_{\mathbf{k}} e^{i\mathbf{kr}} \right) d^3r \\ &= \sum_{\mathbf{k}} \frac{\hbar^2 k^2}{2m} a^\dagger_{\mathbf{k}} a_{\mathbf{k}}. \end{aligned} \tag{2.58}$$

The potential energy term is then

$$\begin{aligned}\hat{U} =&\frac{1}{2}\int V(\mathbf{r}-\acute{\mathbf{r}})\hat{\psi}^\dagger(\mathbf{r})\hat{\psi}^\dagger(\acute{\mathbf{r}})\hat{\psi}(\mathbf{r})\hat{\psi}(\acute{\mathbf{r}})d^3r d^3\acute{r}\\ =&\frac{1}{2\Omega^2}\sum_{\mathbf{k_1k_2k_3k_4}}\int V(\mathbf{r}-\acute{\mathbf{r}})a^\dagger_{\mathbf{k_1}}a^\dagger_{\mathbf{k_2}}a_{\mathbf{k_3}}a_{\mathbf{k_4}}\\ &\times e^{i(-\mathbf{k_1}\mathbf{r}-\mathbf{k_2}\acute{\mathbf{r}}+\mathbf{k_3}\acute{\mathbf{r}}+\mathbf{k_4}\mathbf{r})}d^3r d^3\acute{r}\\ =&\frac{1}{2\Omega}\sum_{\mathbf{k_1k_2k_3k_4}}a^\dagger_{\mathbf{k_1}}a^\dagger_{\mathbf{k_2}}a_{\mathbf{k_3}}a_{\mathbf{k_4}}\delta_{\mathbf{k_3}+\mathbf{k_4},\mathbf{k_1}+\mathbf{k_2}}\int V(\mathbf{r})e^{i(\mathbf{k_4}-\mathbf{k_1})\mathbf{r}}d^3r.\end{aligned} \tag{2.59}$$

Introducing

$$V_{\mathbf{q}} = \frac{1}{\Omega}\int V(r)e^{i\mathbf{q}\mathbf{r}}d^3r \tag{2.60}$$

as the Fourier transform of the interaction potential $V(r)$ and replacing $\mathbf{k_1} \rightarrow \mathbf{k}+\mathbf{q}$, $\mathbf{k_2} \rightarrow \acute{\mathbf{k}}-\mathbf{q}$, $\mathbf{k_3} \rightarrow \acute{\mathbf{k}}$ and $\mathbf{k_4} \rightarrow \mathbf{k}$, one can express the whole Hamiltonian 2.57 as

$$\begin{aligned}\hat{H} =&\hat{T}+\hat{U}\\ =&\sum_{\mathbf{k}}\frac{\hbar^2k^2}{2m}a^\dagger_{\mathbf{k}}a_{\mathbf{k}}+\frac{1}{2}\sum_{\mathbf{k}\acute{\mathbf{k}}\mathbf{q}}V_{\mathbf{q}}a^\dagger_{\mathbf{k}+\mathbf{q}}a^\dagger_{\acute{\mathbf{k}}-\mathbf{q}}a_{\acute{\mathbf{k}}}a_{\mathbf{k}}.\end{aligned} \tag{2.61}$$

In this case, the interaction term can be interpreted as a process in which a pair of particles with initial states $\mathbf{k}$ and $\acute{\mathbf{k}}$ are scattered to the final states $\mathbf{k}+\mathbf{q}$ and $\acute{\mathbf{k}}-\mathbf{q}$. The momentum transferred between the particles is $\mathbf{q}$ and the matrix element is $V_{\mathbf{q}}$, whereby the total momentum is conserved.

### 2.3.2 The microscopical approach

The definition of the ground state $|0\rangle$, see Eq. (2.39), serves as the starting point in this microscopic theory. It implies that the application of all annihilation operators $a_{\mathbf{k}}$ gives zero, $a_{\mathbf{k}}|0\rangle = 0$. For the interacting Bose gas, however, this description is not exact, since the ground state is occupied by a macroscopically large number of particles $N_c \sim N$ at $T = 0$.
Using a Lagrangian multiplier technique, N.M. Hugenholtz and D. Pines solved this problem by eliminating the consideration of the zero momentum state at the outset [37], as well as proposing to replace corresponding operators with an expression depending on the condensate density, $a_{\mathbf{0}}\Omega^{-1} = a^\dagger_{\mathbf{0}}\Omega^{-1} = \sqrt{n_c}$. The new Hamiltonian describing the interacting Bose gas is then

$$\hat{H}(n = n_c) = \hat{T} + \hat{U}(n = n_c), \tag{2.62}$$

whereby it is assumed that the physics in the system is not altered, since $N_c \sim N$. However, strictly observing the number of particles is now no longer conserved, since $\hat{U}(n = n_c)$ (and with it $\hat{H}(n = n_c)$) does not commute with the new number operator $\tilde{N} = \sum_{k'} a^\dagger_{\mathbf{k}}a_{\mathbf{k}}$, where

the ˜ denotes the sum of all $\mathbf{k} \neq 0$.
One, therefore, has to impose the condition

$$\langle \tilde{N} \rangle = N - n_c \Omega, \tag{2.63}$$

where $N$ is the total number of particles in the system.
From these definitions, it immediately follows that the ground state of the Hamiltonian (2.62) is also the ground state of

$$\tilde{H} = \hat{H}(n_c) - \mu \tilde{N}. \tag{2.64}$$

The ground state wave function $|0\rangle = \psi_0(n_c, \mu)$ and with it the corresponding expectation values of $\tilde{H}$ and $\tilde{N}$, respectively, depend on the parameter $\mu$, which itself is determined by the particle conservation restriction

$$\tilde{n}(n_c, \mu) = n - n_c. \tag{2.65}$$

The condensate density $n_c$ is determined in such a way that the ground state energy $E_{\mathbf{k}=0}$ is minimal, i.e.,

$$\frac{1}{\Omega} \frac{dE_0}{dn}_{|n=n_c} = 0. \tag{2.66}$$

Keeping the total particle density $n$ fixed, the expression 2.65 determines the parameter $\mu(n_c)$ in terms of $n_c$. Finally, the parameter $\mu$ represents the chemical potential of the system and is determined by the condition

$$\mu = \frac{1}{\Omega} \frac{dE_0}{dn}. \tag{2.67}$$

The replacement of $\hat{H}$ by $\tilde{H}$ is then equivalent to substitute the particle kinetic energy $\frac{k^2}{2m}$ with the value $\frac{k^2}{2m} - \mu$, which means measuring the particle energies from the chemical potential $\mu$. Eq. (2.61) becomes

$$\hat{H} = \sum_{\mathbf{k}} \left( \frac{\hbar^2 k^2}{2m} - \mu \right) a^\dagger_{\mathbf{k}} a_{\mathbf{k}} + \frac{1}{2} \sum_{\mathbf{k}\acute{\mathbf{k}}\mathbf{q}} V_{\mathbf{q}} a^\dagger_{\mathbf{k}+\mathbf{q}} a^\dagger_{\acute{\mathbf{k}}-\mathbf{q}} a_{\acute{\mathbf{k}}} a_{\mathbf{k}}. \tag{2.68}$$

# 3 From Bose-Einstein condensation to superfluidity

The understanding of a few theoretical concepts is needed to provide an in depth mathematical, as well as an accurate physical description of the relation between the phenomenon of BEC and the consequent onset of superfluidity. Some concepts are described in the appendix, whereas more detailed information is found in [38], [39], [40] and[41].

## 3.1 The off-diagonal long range order

In a Bose-Einstein condensate all condensed particles have *spontaneously* entered the same single-particle quantum state. They now act collectively representing one coherent state. This phenomenon is also known as the **quantum-mechanical phase coherence** or just **phase coherence**.

Using the field operators introduced above, see Chapter 2.3.1, we can define a correlation function

$$\rho(\mathbf{r}-\acute{\mathbf{r}}) = \langle\hat{\psi}^{\dagger}(\mathbf{r})\hat{\psi}(\acute{\mathbf{r}})\rangle, \tag{3.1}$$

known as the *single-particle density matrix*. $\rho$ represents the probability amplitude to find a particular particle at $\mathbf{r}$ times the amplitude to find it at $\acute{\mathbf{r}}$ averaged over the behavior of all other $N-1$ particles in the system.

Using the Fourier transformations defined in Eq. (2.50) and Eq. (2.51), one finds

$$\rho(\mathbf{r}-\acute{\mathbf{r}}) = \frac{1}{\Omega}\sum_{\mathbf{k}} e^{-i\mathbf{k}(\mathbf{r}-\acute{\mathbf{r}})}\langle a_{\mathbf{k}}^{\dagger}a_{\mathbf{k}}\rangle, \tag{3.2}$$

being just the Fourier transform of the momentum distribution $n_{\mathbf{k}} \equiv \langle a_{\mathbf{k}}^{\dagger}a_{\mathbf{k}}\rangle$.

We already know that in a Bose-Einstein condensate the energetic most-favorable momentum state $\mathbf{k}_0$ (typically $\mathbf{k}_0$=0) is occupied by a macroscopically number $N_c$. One can, therefore, replace

$$n_{\mathbf{k}} = N_c\delta_{\mathbf{k},\mathbf{k_0}} + f(\mathbf{k}), \tag{3.3}$$

where $f(\mathbf{k})$ is a smooth function over $\mathbf{k}$. Thus, substituting the summation in Eq. (3.2) with an integration, we obtain for the single-particle density matrix

$$\rho(\mathbf{r}-\acute{\mathbf{r}}) = n_c + \frac{2}{(2\pi)^3}\int d^3k e^{-i\mathbf{k}(\mathbf{r}-\acute{\mathbf{r}})} f(\mathbf{k}), \tag{3.4}$$

with $n_c = N_c/\Omega$. The second term in Eq. (3.4) will vanish for large $|\mathbf{r}-\acute{\mathbf{r}}|$, if the function $f(\mathbf{k})$ is sufficiently smooth. Hence, the $\rho$ remains finite

$$\langle\hat{\psi}^{\dagger}(\mathbf{r})\hat{\psi}(\acute{\mathbf{r}})\rangle \to n_c \qquad \text{for} \quad |\mathbf{r}-\acute{\mathbf{r}}| \to \infty \tag{3.5}$$

and of the order of the particle density, regardless of how large $|\mathbf{r}-\acute{\mathbf{r}}|$ is. This occurrence is called the *off-diagonal long range order* (ODLRO), first introduced by O. Penrose [42].

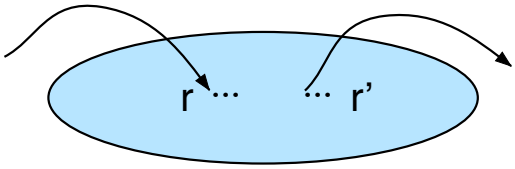


Figure 6: A descriptive illustration of the ODLRO in a Bose-Einstein condensate. A particle is inserted into the condensate at $\mathbf{r}$ while 'coherently' another particle is removed from it at $\acute{\mathbf{r}}$.

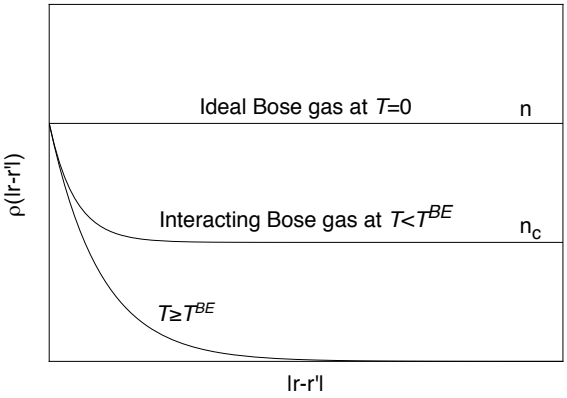


Figure 7: The single-particle density matrix $\rho(|\mathbf{r}-\acute{\mathbf{r}}|)$ for different Bose gases at different temperatures .

In Fig. 7 the physical interpretation of ODLRO is illustrated. The single-particle density matrix can be interpreted as the overlap in the wave function, when a particle is removed from the condensate at $\acute{\mathbf{r}}$ and another particle is, thereby, absorbed into the condensate at position $\mathbf{r}$. This overlap persists to infinite separations [4]. It follows that, there is a finite possibility of removing a particle from the condensate and placing it back into the same quantum state, however great the distance between $\mathbf{r}$ and $\acute{\mathbf{r}}$ is. In any non-condensed phase of a quantum liquid this process would be incoherent, except when $\mathbf{r}$ and $\acute{\mathbf{r}}$ are very close together [5] .

## 3.2 The macroscopic wave function and the order parameter

The dependence of $\rho(\mathbf{r}-\acute{\mathbf{r}})$ on $\mathbf{r}$ and $\acute{\mathbf{r}}$ is given independently of the condensate wave function $\psi$, which allows us to treat these two points statistically independent of each other. We can, therefore, replace

$$\langle\hat{\psi}^{\dagger}(\mathbf{r})\hat{\psi}(\acute{\mathbf{r}})\rangle \rightarrow \langle\hat{\psi}^{\dagger}(\mathbf{r})\rangle\langle\hat{\psi}(\acute{\mathbf{r}})\rangle \tag{3.6}$$

for $|\mathbf{r}-\acute{\mathbf{r}}| \rightarrow \infty$.
Consequently, we can define a complex *macroscopic wave function* as

$$\psi_0(\mathbf{r}) = \langle\hat{\psi}(\mathbf{r})\rangle. \tag{3.7}$$

[4] in a classical system this overlap would die away quickly over a distance $\lambda_{\mathrm{dB}}$
[5] smaller than $\lambda_{\mathrm{dB}}$

Using Eq. (3.6) we can now express the single-particle density matrix $\rho$ in terms of the macroscopic wave function $\psi_0(\mathbf{r})$, resulting in

$$\rho(\mathbf{r}-\acute{\mathbf{r}}) = \langle\hat{\psi}^\dagger(\mathbf{r})\rangle\langle\hat{\psi}(\acute{\mathbf{r}})\rangle = \psi_0^\star(\mathbf{r})\psi_0(\acute{\mathbf{r}}). \tag{3.8}$$

Considering the occurrence of ODLRO in a BE-condensate, see Eq. (3.5), the macroscopic wave function can be expressed as

$$\psi_0(\mathbf{r}) = \psi_0 = \sqrt{n_c}e^{i\phi}, \tag{3.9}$$

where $\phi$ is an arbitrary constant phase angle.

The following Gedankenexperiment [43] may facilitate the understanding of the physical meaning of the order parameter and of the ODLRO .

Imagine a condensate divided into $K$ boxes. For each box, we can define the operators $a_{\mathbf{0}}^{(i)}$ and $a_{\mathbf{0}}^{\dagger(i)}$ $i = 1, \ldots, K$. The annihilation operator of the total system is consequently defined as

$$a_{\mathbf{0}} = \frac{1}{\sqrt{K}}\sum_i^K a_{\mathbf{0}}^{(i)} \tag{3.10}$$

Assuming $n_c$ to be the total condensed particle density, we can write

$$\begin{aligned} n_c = \langle a_{\mathbf{0}}^\dagger a_{\mathbf{0}}\rangle &= \langle\frac{1}{K}\sum_i \underbrace{a_{\mathbf{0}}^{\dagger(i)}a_{\mathbf{0}}^{(i)}}_{n_c^{(i)}}\rangle + \langle\frac{1}{K}\sum_{i\neq j} a_{\mathbf{0}}^{\dagger(i)}a_{\mathbf{0}}^{(j)}\rangle \\ &= \frac{n_c}{K} + \frac{1}{K}\sum_{i\neq j}\langle a_{\mathbf{0}}^{\dagger(i)}a_{\mathbf{0}}^{(j)}\rangle. \end{aligned} \tag{3.11}$$

It results that the condensates in the $K$ boxes must be phase-correlated, otherwise $\langle a_{\mathbf{0}}^{\dagger(i)}a_{\mathbf{0}}^{(j)}\rangle = 0$ leading to the incorrectness of Eq. (3.11).

The presence of the macroscopic wave function $\psi_0$ allows defining the order parameter of the phase transition as

$$\psi_0^\dagger\psi_0 = |\psi_0|^2 = n_c. \tag{3.12}$$

The order parameter is a quantity which characterizes the onset of order at the phase transition. It is zero in the normal phase and non-zero in the ordered phase. The definition (3.12) of the order parameter reveals even more to us. From Eq. (2.50), one easily recognizes that the field operator $\hat{\psi}(\mathbf{r})$ acts on states of the Fock-space. The relation Eq. (3.9) proves, therefore, that the macroscopic wave function $\psi_0(\mathbf{r})$ of the condensate consists of several coherent parts of multiple $N$-single particle sub-spaces of the Fock-space.

$$\langle\psi_0(\mathbf{r})\rangle \sim \sum_N \ldots\langle\Phi_{N-1}|\psi|\Phi_N\rangle. \tag{3.13}$$

In other words, the condensation state is a coherent state, see App. A. In such a state the phase is fixed, but the number of particles fluctuates. The observables $N$ and $\phi$ are said to be complex conjugate variables.

## 3.3 The $U(1)$-symmetry breaking and the Goldstone Mode

Expressing the Hamiltonian Eq. (2.68) in real space,

$$\begin{aligned}\hat{H} = &\int \left(\hat{\psi}^\dagger(\mathbf{r})\left[-\frac{\hbar^2}{2m}\nabla^2 - \mu\right]\hat{\psi}(\mathbf{r})\right) d^3r \\ &+ \frac{1}{2}\int V(\mathbf{r}-\acute{\mathbf{r}})\hat{\psi}^\dagger(\mathbf{r})\hat{\psi}(\mathbf{r})\hat{\psi}^\dagger(\acute{\mathbf{r}})\hat{\psi}(\acute{\mathbf{r}})d^3r d^3\acute{r}\end{aligned} \tag{3.14}$$

one recognizes that this expression is invariant under the transformation

$$\begin{aligned}\hat{\psi}(\mathbf{r}) &\rightarrow \hat{\psi}(\mathbf{r})e^{i\phi} \\ \hat{\psi}^\dagger(\mathbf{r}) &\rightarrow \hat{\psi}^\dagger(\mathbf{r})e^{-i\phi}\end{aligned} \tag{3.15}$$

of the field operators, since in expression 3.14 an equal number of annihilation and creation operators is present. The set of all these possible transformations is called the $\mathbf{U(1)}$ **symmetry** group. The Hamiltonian 3.14 is said to be invariant under the global $U(1)$ gauge transformation. In this case, any expectation value $\langle\hat{\psi}(\mathbf{r})\rangle$ is expected to be zero. Generally, a non-zero value of the order parameter $\langle\hat{\psi}(\mathbf{r})\rangle$ signals a spontaneously broken symmetry. The spontaneous breakdown of the global $U(1)$ gauge symmetry of the Hamiltonian 3.14 leads to BEC. In terms of quantum-mechanics, a symmetry is said to be spontaneously broken, if the ground state of the system is not an eigenstate of the symmetry's generator.
The $U(1)$ symmetry group is generated by the the number operator $\hat{N} = \int \hat{\psi}^\dagger(\mathbf{r})\hat{\psi}(\mathbf{r})d^3r$ [44], which by definition is expressed as

$$[\hat{N}, \hat{\psi}(\mathbf{r})] = \hat{\psi}(\mathbf{r}). \tag{3.16}$$

This can easily be proved by using the commutation relation defined in Eq. (2.54)-Eq. (2.56). We have to show that the ground state $\psi_0(\mathbf{r})$ is, indeed, not an eigenstate of the number operator $\hat{N}$. This is accomplished by realizing that $\psi_0(\mathbf{r})$ is a coherent state with a fixed phase and fluctuating number of particles, see Eq. (3.13).
Goldstone's theorem states that for every physical system, of which a continuous symmetry has spontaneously been broken, there exists a massless low-frequency excitation (mode) called the "Goldstone mode" [45].
The $U(1)$ symmetry group is a continuous symmetry, since the phase $\phi$ can be continuously varied in the range of $[0, 2\pi]$. By minimizing the potential energy $\hat{U}$, the Bose gas spontaneously enters one of the energetically most favorable ground states $\langle\hat{\psi}(\mathbf{r})\rangle = \psi_0 = |\psi_0|e^{-i\phi}$ arbitrarily fixing its phase to $\phi \in [0, 2\pi]$. The interaction potential $V(|\mathbf{r}-\acute{\mathbf{r}}|) = v_0\delta(|\mathbf{r}-\acute{\mathbf{r}}|)$ can be expressed by a delta-function interaction, which is a good approximation in the low-density limit. The ground state of the system is, therefore, given by solving the condition $\frac{\partial u}{\partial\psi}_{|_{\psi=\psi_0}} = 0$, where $u = \frac{\hat{U}}{\Omega} = -\mu\hat{\psi}^\dagger(\mathbf{r})\hat{\psi}(\mathbf{r}) + \frac{v_0}{2}\left(\hat{\psi}^\dagger(\mathbf{r})\hat{\psi}(\mathbf{r})\right)^2$ is the corresponding energy density.

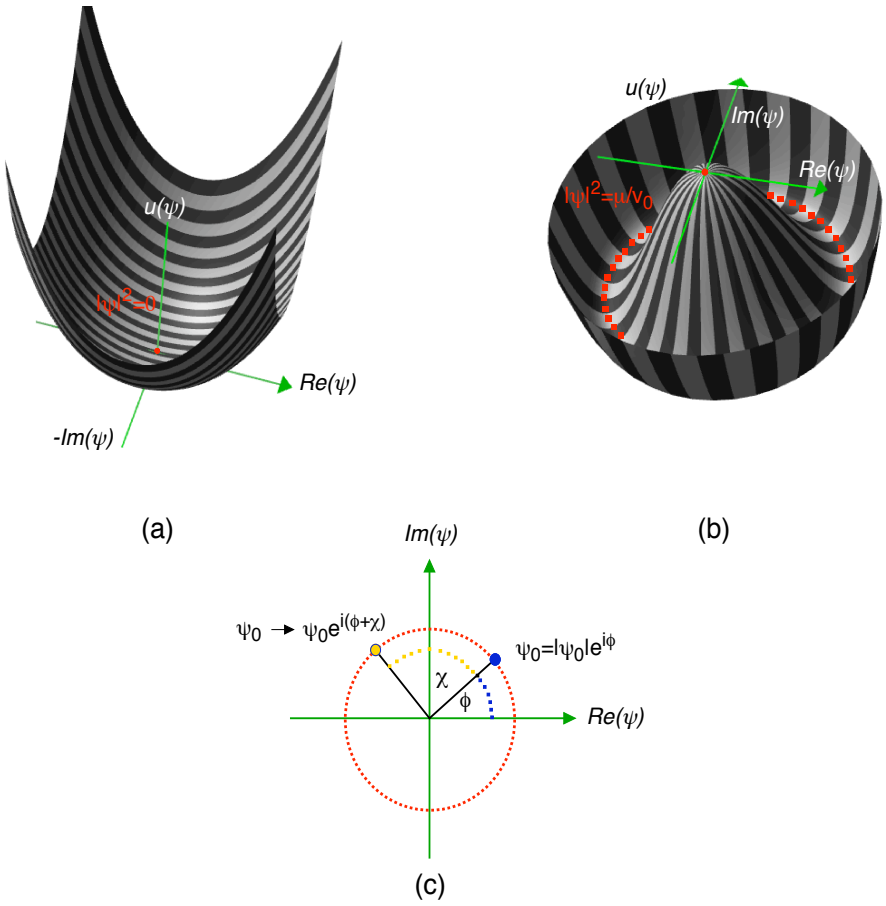


Figure 8: Sketch of the potential energy density $u(\psi)$ in the case of $\mu \leq 0$ (a) and $\mu > 0$ (b). For $\mu = 0$, the potential minimum $u_{min}$ is reached at $|\psi| = 0$ (red dots). In the case of $\mu \neq 0$, $u_{min}$ is reached at $|\psi|^2 = \mu/v_0$ (red contour). (c) The $U(1)$ symmetry breaking leads to an arbitrary choice of the phase angle $\phi$ for the macroscopic wave function $\psi_0$. See text for further explanations.

This minimum depends on two parameters; the interaction potential $V$ and the chemical potential $\mu$, respectively. If $\mu \leq 0$, then the minimum potential energy value is $u_{min} = 0$ with $\langle\hat{\psi}(\mathbf{r})\rangle = 0$, see Fig. 8a. This trivial solution corresponds to a stable ground state, since $\frac{\partial^2 u}{\partial\hat{\psi}\partial\hat{\psi}^\dagger} > 0$. In this case, there is no $U(1)$-symmetry breakdown. Once the chemical potential is $\mu > 0$, the minimum value for the potential energy density is given by $u_{min} = -\frac{\mu^2}{2v_0}$ at $\langle\hat{\psi}(\mathbf{r})\rangle = \psi_0$ with $|\psi_0| = \sqrt{\frac{\mu}{v_0}}$. The trivial solution has become unstable, see Fig. 8b. Therefore, we can conclude that the spontaneous breaking of the $U(1)$-symmetry in an interacting Bose system occurs only if the chemical potential $\mu$ becomes positive[6]. The minimum value $u_{min}$ is attained on a full "circle of minima" (red dotted contour in Fig. 8b). A non-zero value of the order parameter $|\psi_0|^2 \neq 0$ implies that the Bose system resides in a ground state with

[6]Note, there is no spontaneous symmetry breaking in an ideal Bose gas, since the chemical potential $\mu \leq 0$, even at T=0.

a corresponding phase $\phi \in [0, 2\pi]$, although all other possible ground states were energetic equally favorable. This arbitrary choice leads to an inertia of the system which strives to maintain this phase. This circumstance defines the phase stiffness $\rho^s = \frac{\hbar^2}{2m^\star}|\psi_0|^2$, i.e., an energy cost related to the phase changing from $\phi$ to $\phi+\chi$. Consequently, infinitesimal changes expend just very little energy, and there is virtually no use for a uniform transformation $\phi \to \phi + 2\pi$. It is, therefore, possible to create a new mode in the condensed phase with a long-wavelength modulation of the phase $\phi \to \phi + \mathbf{k}\cdot\mathbf{r}$, with $|\mathbf{k}| = \frac{2\pi}{\lambda}$, i.e., an oscillation of the order parameter along the direction where the potential remains at its minimum, along the circle of minima. This mode encounters no resistance; one says, it has no mass. This mode is called the *Goldstone mode*. It always has bosonic character and its energy spectrum $\omega_G = c_0 \cdot |\mathbf{k}|$ is linear, with $c_0$ being phase velocity of the excitations in the long-wavelength limit.

# 4 Superfluidity

Generally, superfluidity describes the property of a fluid (liquid or gas) to circulate around an extended body without dragging it. Any massive particle can move through the (super-)fluid without being slowed down. However, the term superfluidity is mainly associated with the phase of liquid $^4\mathrm{He}$ emerging below the characateristic temperature $T_\lambda \sim 2.17$ (denoted He II). The nomenclature of this temperature stems from the characteristic shape of the heat-capacity curve at low temperatures, reminiscent of the greek $\lambda$-letter, manifesting a phase transition occurring at this temperature [46].
In He II, the thermal conductivity is anomalously large [47–49]. Stimulated by these results, J.F. Allen, as well as A.D. Misener [50] in collaboration with P. Kapitza [51] measured in the same time period the viscosity of liquid helium independently from one another. Both experiments showed that for temperatures $T < T_\lambda$ liquid $^4\mathrm{He}$ has the ability to flow without apparent friction, as if it has no viscosity. It was this anomalous behavior that brought P. Kapitza to introduce the term "superfluid", in an obvious analogy to the term "superconductivity". Today we know that superfluids and superconductors are, indeed, analogous states of matter.
F. London [16], recalling that $^4\mathrm{He}$ -atoms were Bose particles obeying the Bose-statistics, then proposed the occurrence of BEC to be the cause for the phase transition. This idea was later confirmed by neutron scattering experiments [52].
Even today, however, the general relation between BEC and superfluidity is not completely understood. Although one believes that superfluidity and BEC are closely related to each other [19], it is also true, that the occurrence of one of these phenomenon is not necessary or dependent on the other.
Theoretically, one can show that in 2-D, strong phase fluctuations destroy the phase coherence [53], which by definition implicates the absence of BEC [54, 55]. However, J.M. Kosterlitz and D.J. Thouless [56] proved that in a two-dimensional Bose system, superfluidity can exist even without BEC. In fact, superfluidity was actually observed in $^4\mathrm{He}$ films [57].
The following chapters should clarify the relation of Bose-Einstein condensation and superfluidity for three-dimensional interacting Bose fluids.

## 4.1 The two-fluid model I

Contradictory to previous measurements [50, 51], other experiments on liquid helium seemed to imply a finite viscosity for He II [58, 59]. These observations were successfully explained by the phenomenological two-fluid model first introduced by L. Tisza [17]. This model is based on the idea that the system consists of a superfluid component, which behaves completely frictionless and a viscous (ordinary) part called normalfluid component. Note, the two components do not correspond to physically distinguishable species.

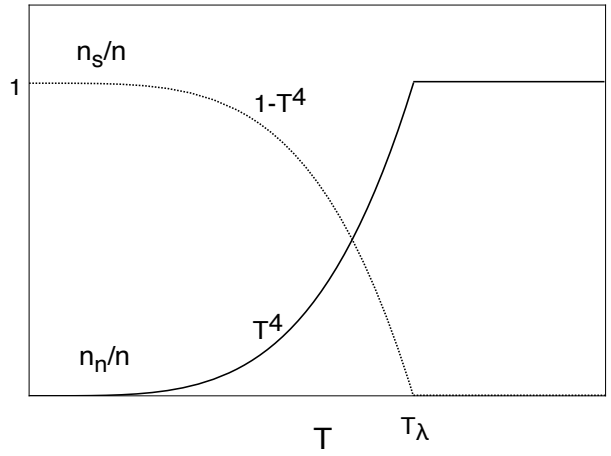


Figure 9: Sketch of the temperature dependence of the normal- (solid line) and the superfluid (dotted line) component in He II, analyzed within the two-fluid model.

Nevertheless, one can describe the whole particle density of the fluid as a sum of the two components

$$n = n_n + n_s, \tag{4.1}$$

where the subscripts {n, s} denote the superfluid and the normalfluid parts, respectively. Consequently, the total mass density $\rho = m \cdot n$ is also a sum of two density parts

$$\rho = \rho_n + \rho_s. \tag{4.2}$$

The key assumptions of the two-fluid model are given in Table 1. The amount of the normal-

Table 1: The key assumptions of the two-fluid model

| | density | viscosity | entropy |
|---|---|---|---|
| normalfluid component | $\rho_n$ | $\eta_n = \eta$ | $S_n = S$ |
| superfluid component | $\rho_s$ | $\eta_s = 0$ | $S_s = 0$ |

and superfluid component in the fluid varies with temperature. Experiments of torsional oscillation disk stack in He II [59] tracked a $T^4$- dependence for the normal component, $n_n(T) = AT^4$ and correspondingly a $n_s(T) = n - AT^4$ for the superfluid component, where A is a constant, see Fig. 9. The theoretical derivation of these results is given in App. B.
From these temperature dependencies it immediately follows that at $T = 0$, all particles will participate to the superflow ($n \approx n_s$ and $n_n \approx 0$), whereas close to the critical temperature $T_\lambda$, all of the fluid is in the normal state ($n \approx n_n$ and $n_s \approx 0$).
Furthermore, this model successfully described the superflow in terms of the phase $\phi$ of the

condensate's macroscopic wave function $\psi_0(\mathbf{r}) = \sqrt{n_c}e^{i\phi}$.
Superflow arises whenever the phase of the macroscopic wave function varies over space $\phi = \phi(\mathbf{r})$. Such a motion involves the condensed particles as a whole. Superfluid flow, thus, appears as a *collective phenomenon*, in which the particles move together to preserve the occupation of a single state. A Gedankenexperiment illustrates this fact [60].
Imagine two different BE-condensates (denoted 1 and 2) enclosed in two different reservoirs but connected through a superleak (a channel, which can be switched over). At the beginning, the superleak is closed. In this case, the condensates are described by two different macroscopic wave functions with two different phases $\phi_1$ and $\phi_2$, respectively. As soon as the superleak is opened, the new system (now consisting of both condensates) tends to establish one phase (of the new macroscopic wavefunction). This means that the potential energy of the merged system $U = U(\Delta\phi)$ depends on the phase difference $\Delta\phi = \phi_1 - \phi_2$. Since the number of condensed particles $N_j$ $(j = 1, 2)$ is complex conjugated to the phase $\phi_j$, the Hamilton equation

$$i\hbar\frac{\partial N_j}{\partial t} = -\frac{\partial H}{\partial \phi_j} \tag{4.3}$$

yields the existence of a current of condensed particles

$$I = \frac{\partial N_1}{\partial t} = |-\frac{\partial N_2}{\partial t}| = \frac{1}{\hbar}\frac{\partial U(\Delta\phi)}{\partial \Delta\phi}. \tag{4.4}$$

In the following, we compare two different expressions for the superfluid current density $j_s$ in order to get an expression for the superfluid velocity $v_s$. For the first equation we obtain

$$\begin{aligned} j_s = \frac{I}{A} =& \frac{1}{A\hbar}\frac{\partial U(\Delta\phi)}{\partial \Delta\phi} \\ =& \frac{1}{\Omega\hbar}\frac{\partial U(\Delta\phi)}{\partial \nabla\phi} \\ =& \frac{1}{\hbar}\frac{\partial u(\Delta\phi)}{\partial \nabla\phi}, \end{aligned} \tag{4.5}$$

and $u = \frac{U}{\Omega}$ is the energy density. Defining $n_s$ as the density of particles participating to the superflow, we can write $\frac{\partial u}{\partial(\frac{1}{2}m{v_s}^2)} = n_s$.
By definition, expression 4.5 is the same as

$$\begin{aligned} j_s =& n_s \cdot v_s \\ =& \frac{\partial u}{\partial(\frac{1}{2}m{v_s}^2)} \cdot v_s \\ =& \frac{1}{m}\frac{\partial u}{\partial v_s}. \end{aligned} \tag{4.6}$$

Finally, this leads to

$$\mathbf{v}_s = \frac{\hbar}{m}\nabla\phi. \tag{4.7}$$

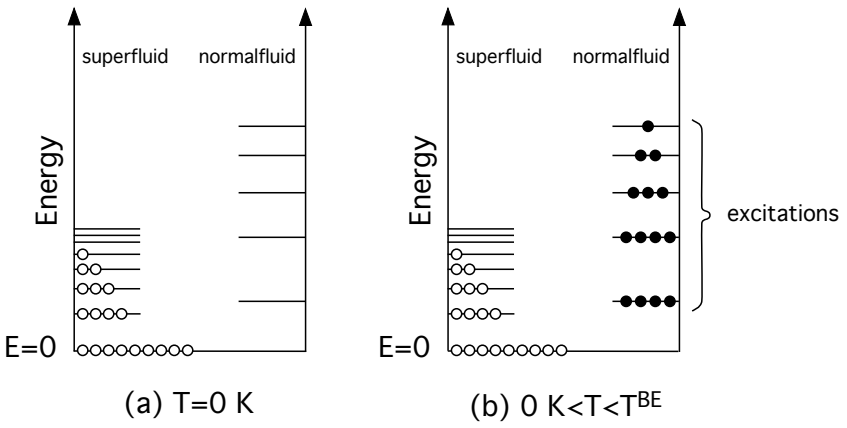


Figure 10: A descriptive representation of the energy level occupation of the super- and normalfluid components in an interacting Bose gas. (a) At $T = 0$ all the particles are superfluid, although the interaction scatters some particles into levels $E > 0$. The number of particles in the ground state is, therefore, reduced. This is called "the depletion of the ground state". (b) For $0 < T < T^{BE}$ some energy states $E > 0$ are occupied by thermal excitations, which form the normalfluid part.

Therefore, the wave function $\psi_0$ describes the ground state as viewed from a frame of reference moving at velocity $-\mathbf{v}_s$. Such a transformation is equivalent to adding the same amount $\mathbf{q} = \hbar \nabla\phi$ to the momentum of all particles. However, a macroscopic part of the particles still occupies the energetically most favorable single quantum state. It is in this sense that BEC and superfluidity are related.
One should be careful not to confuse the condensate density $n_c$, number of particles per unit volume populating the ground state, and the superfluid density $n_s$. In fact, in He II $n_s = n$ at $T$=0 K [61], but $n_c \approx 0.1\ n$, even at the lowest temperatures.

## 4.2 The two-fluid model II

This qualitative model did not reveal why the superfluid component flowed without friction. A more quantitative approach was presented by L. Landau [18].
Generally, in a (normal-)fluid, friction and viscosity arise whenever the particles are scattered from the walls of the vessel. This leads to an energy and momentum transfer from the fluid to the walls causing energy dissipation. However, such a scenario does not apply for a superfluid (component). Hence, L. Landau introduced the concept of a "quasiparticle"; an excitation of the system from the ground state, which is characterized by a definite momentum and discrete energy. He consequently postulated that He II consisted of a superfluid part, associated with the part of the liquid that remained in its ground state, and a normal component, which corresponded to the set of quasiparticles. Thus, in such a fluid the superflow decays whenever a

quasiparticle can be excited by interaction with the surfaces of the vessel.
Let us imagine a superfluid moving with a velocity $\mathbf{v}_s$. An elementary excitation (quasiparticle) in the co-moving frame has momentum $\hbar\mathbf{k} = \mathbf{p}$ and energy $\varepsilon_{\mathbf{p}}^{mov}$. A Galilean-transformation to the rest-frame of the wall leads to

$$\varepsilon_{\mathbf{p}}^{rest} = \varepsilon_{\mathbf{p}}^{mov} + \mathbf{p} \cdot \mathbf{v}_s. \tag{4.8}$$

The energy of the superfluid expressed in coordinates of the rest-frame is then

$$E = \varepsilon_{\mathbf{p}}^{rest} + \frac{1}{2} M \mathbf{v}_s^2, \tag{4.9}$$

where $M$ is the sum of the masses of superfluid particles and $\frac{1}{2}M\mathbf{v}_s^2$ is the kinetic energy of the superfluid system. Therefore, no quasiparticles can be created as long as $\varepsilon_{\mathbf{p}}^{rest} > 0$. An excitation can only be realized, if

$$\varepsilon_{\mathbf{p}}^{rest} < 0, \tag{4.10}$$

since only then, dissipative processes cause viscous damping of the superfluid. Ideally we get

$$\varepsilon_{\mathbf{p}}^{mov} - |\mathbf{p}| \cdot |\mathbf{v}_s| < 0, \tag{4.11}$$

which leads to

$$v_s > \frac{\varepsilon_p^{mov}}{p}. \tag{4.12}$$

Thus at a velocity

$$v = \frac{\varepsilon_p^{mov}}{p}, \tag{4.13}$$

that is, when the phase velocity of the excitation is equal to the velocity of the fluid, it becomes kinematically possible to create excitations parallel to $\mathbf{v}_s$. At higher velocities, excitations whose momenta are not parallel to the motion of the fluid are possible. The critical velocity (also called *Landau critical velocity*) is, therefore, defined as

$$v_c = min\left(\frac{\varepsilon_p^{mov}}{p}\right). \tag{4.14}$$

For velocities $v < v_c$ it is impossible to create excitations and, consequently, there is no mechanism for degrading the motion of the condensate, which will become manifested in the occurrence of superfluidity. Analyzing the ideal Bose gas within this framework, one obtains a critical velocity $v_c^{id.BG} = 0$, since an excitation of free particles has energy $E = \frac{p^2}{2m}$. This means that an ideal non-interacting Bose gas is not a superfluid.

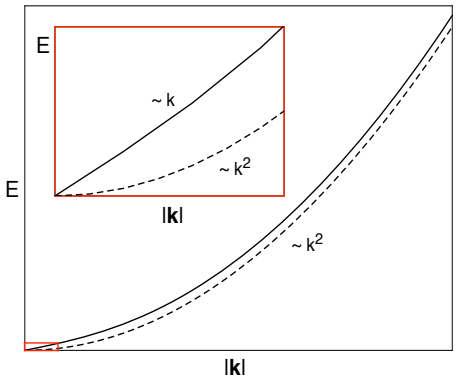


Figure 11: Sketch of the energy spectrum of a weakly-interacting Bose gas derived by Bogoliubov. The spectrum is linear at small $|\mathbf{k}|$ (see inset) and approaches the free particle energy $\frac{\hbar^2 k^2}{2m}$ (dashed line) for large $|\mathbf{k}|$.

## 4.3 The microscopic approach by Bogoliubov

It was N.N. Bogoliubov [19] who then showed that interactions between the particles are crucial for obtaining a non-zero critical velocity. He considered a dilute, weakly interacting gas of atoms, obeying Bose statistics, with a repulsive interatomic potental $V(\mathbf{r}_i - \mathbf{r}_j) = v_0\ \delta(\mathbf{r}_i - \mathbf{r}_j)$. Starting from Eq. (2.35) and assuming the system to undergo BEC, he was able to derive the following excitation spectrum (for detailed derivation consult Ref.[38] or Ref.[62]):

$$E(\mathbf{k}) = \left(\frac{\hbar^2 k^2}{2m^\star}\right)^{\frac{1}{2}} \left(\frac{\hbar^2 k^2}{2m^\star} + 2n_c v_0\right)^{\frac{1}{2}}, \tag{4.15}$$

sketched in Fig. 11. For (small) $|\mathbf{k}| < \mathbf{q}_0 = \frac{1}{\xi}$, where $\xi = \frac{\hbar}{(2m^\star n_c v_0)^{\frac{1}{2}}}$ is the coherence length [7], the spectrum

$$E(k) \approx \hbar c_0 \cdot |\mathbf{k}| \tag{4.16}$$

is linear, where

$$c_0 = \left(\frac{n_c v_0}{m^\star}\right)^{\frac{1}{2}} \tag{4.17}$$

is the sound velocity.

In this range, the kinetic energy-term $\epsilon_k = \frac{\hbar^2 k^2}{2m^\star}$ is smaller compared to the potential energy-term of a particle, $n_c v_0$. For large $|\mathbf{k}|$ the excitations spectrum joins smoothly onto the free particle energy. We can, therefore, conclude that the presence of an (even very small) interaction in a Bose gas drives the energy spectrum $E(\mathbf{k})$ at small wavevectors $|\mathbf{k}|$ from a quadratic dependence for free particles to a linear one (in agreement with what is observed experimentally for $^4$He [63, 64]).

[7] It is basically the distance over which the macroscopic wave function tends to its bulk value. It is sometimes also referred as *healing length*, when subjected to localized perturbations.

Consequently, on length scales longer than the coherence length $\frac{1}{|\mathbf{k}|} > \xi$, the particles move collectively. In this case, single particle-like excitations with energy $\epsilon_k = \frac{\hbar^2 k^2}{2m^\star}$ are absorbed into a collective mode (sound wave or density wave, see below) with a linear spectrum $E(\mathbf{k}) = c_0 \cdot \mathbf{k}$ corresponding to the Glodstone mode. On shorter length scales $\frac{1}{|\mathbf{k}|} < \xi$ the particles act independently of each other. Any interacting Bose gas is a superfluid!

## 4.4 The sound propagation in a Bose-Einstein condensate

By gradually considering different length scales (or correspondingly different time scales), we divide the sound propagation in a condensed system into two different regimes, "collisionless regime" and "hydrodynamic regime", see Table 2. We differentiate between pulse propagation (ballistic) at short wavelengths and collective modes at longer wavelengths.
Sound propagation in a condensate depends mainly on the hierarchy of three length (time) scales:

- The wavelength of the excitation $\lambda_{ex}$ (the excitation frequency $\omega$).
- The coherence length $\xi$. Modifications of the macroscopic wave function on this length scale imply by definition a kinetic energy, which is of the order of the chemical potential $\mu$ (the relaxation time $\tau_r$ required for achieving local equilibrium).
- The mean-free path $l_{mfp}$ for collisions between the quasiparticles (the life time a quasiparticle excitation $\tau$) .

Table 2: The nature of sound excitations in various regimes

| regime | length scale | condensate fraction | thermal excitations |
|---|---|---|---|
| collisionless | $\lambda_{ex} < \xi, l_{mfp}$ | ballistic | ballistic |
| collisionless | $\xi < \lambda_{ex} < l_{mfp}$ | Bogoliubov (zero) sound | ballistic |
| hydrodynamic | $\xi < l_{mfp} < \lambda_{ex}$ | second sound | first sound |

Sound propagation is ballistic, when the excitation wavelength $\lambda_{ex}$ is shorter than the coherence length $\xi$ and the mean free path of the quasiparticles $l_{mfp}$.
The condition $\lambda_{ex} < l_{mfp}$ defines the collisionless regime. In this regime the spectrum of elementary excitations is the Bogoliubov spectrum, see Eq. (4.15). At long wavelengths ($\lambda_{ex} \gg \xi$), the excitation energy depends linearly on the wavevector, implying phonon-like excitations with velocity $c_0$, see Eq. (4.17). At short wavelengths ($\lambda_{ex} \ll \xi$) the excitations are free-particle-like.
In the hydrodynamic regime the circumstances are a little bit more complex. Much of todays

understanding of the nature of sound in this regime in quantum fluids comes from the context of superfluid helium [61]. The propagation of sound in He II is described by the set of hydrodynamic equations established by Landau [18, 65]. These equations are rather complicated. To solve them is a fairly laborious and difficult job. Using some assumptions, which define the hydrodynamic regime, these expressions may be linearized to two conservation laws and two dynamic equations.

Let us, therefore, assume that the thermal excitations collide frequently enough that they are locally in thermodynamical equilibrium (temporal variations are slow compared to the relaxation time needed to establish such an equilibrium). Furthermore, the spatial variations are assumed to be minimal compared to the mean free path of the excitations. This implicates that the temperature $T$ and the velocities $\mathbf{v}_n$ and $\mathbf{v}_s$ of the normal- and superfluid component, respectively, are slowly varying in space and time. Moreover, we want to focus our attention on the reversible fluid motion, neglecting viscous (dissipative) processes. Under such conditions, the state of the system can be locally specified in terms of the total density of particles $n$, the velocities $\mathbf{v}_n$ and $\mathbf{v}_s$ and the temperature $T$. The first conservation law is the continuity equation for the mass density $\rho = m \cdot n$ and the total mass current density $\mathbf{j} = \rho_n \mathbf{v}_n + \rho_s \mathbf{v}_s$.

$$\frac{\partial \rho}{\partial t} + \nabla \cdot \mathbf{j} = 0. \tag{4.18}$$

In the absence of energy dissipation, the entropy of the system is conserved. Defining $\tilde{s} = \frac{S}{Nm}$ as the entropy fraction per unit mass, we can write

$$\frac{\partial(\rho\tilde{s})}{\partial t} + \nabla \cdot (\rho \tilde{s} \mathbf{v}_n) = 0,$$

which linearized becomes

$$\tilde{s}\frac{\partial \rho}{\partial t} + \rho \frac{\partial \tilde{s}}{\partial t} + \tilde{s}\rho \nabla \cdot \mathbf{v}_n = 0. \tag{4.19}$$

In the absence of an external potential and neglecting non-linear effects, the acceleration of the superfluid can be expressed as

$$m\frac{\partial \mathbf{v}_s}{\partial t} = -\nabla \mu, \tag{4.20}$$

where $\mu$ is the chemical potential defined by the Gibbs-Duhem relation

$$N d\mu = \Omega dp - S dT. \tag{4.21}$$

The second dynamic equation describes the motion of the entire liquid as

$$\frac{\partial \mathbf{j}}{\partial t} = -\nabla p, \tag{4.22}$$

where $p$ is the local pressure acting on the liquid.

The key concept in determining the two sound modes of a condensate in the hydrodynamic

regime is to properly combine the two conservation laws, Eq. (4.18) and Eq. (4.19), with the two dynamic equations, Eq. (4.20) and Eq. (4.22), in order to obtain a system of coupled partial differential equations, which can finally be solved with a simple ansatz [61], see App. C. After making use of the appropriate thermodynamic identities, we find

$$\left[\frac{\omega^2}{v_1^2 q^2} - 1\right]\left[\frac{\omega^2}{v_2^2 q^2} - 1\right] = \left[1 - \frac{c_v}{c_p}\right], \tag{4.23}$$

where

$$v_1^2 = \left(\frac{\partial p}{\partial \rho}\right)_{\tilde{s}} \tag{4.24}$$

and

$$v_2^2 = \frac{\rho_s}{\rho_n}\tilde{s}^2\left(\frac{\partial T}{\partial \tilde{s}}\right)_{\rho} = \frac{\rho_s}{\rho_n}\left(\frac{\tilde{s}^2 T}{C_v}\right). \tag{4.25}$$

The two expressions within the brackets on the left-hand side of Eq. (4.23) each describe an oscillation mode with corresponding dispersion relation. These modes are weakly coupled by the expression on the right-hand side of Eq. (4.23). In fact, this value is very small, almost zero at low temperatures. It vanishes completely at $T = 0$ K. One can, therefore, assume that the two modes of wave propagation in a superfluid are effectively uncoupled and their velocities are accurately specified by Eq. (4.24) and Eq. (4.25). For a more detailed analysis the reader is referred to Ref.[65].

### 4.4.1 First sound

First sound waves [8] are the analogue to ordinary sound waves in a normal fluid. These are oscillations of the total density $\rho$, giving rise to pressure variations. There are no temperature or entropy oscillations. The normal- and the superfluid component move in phase with one another with $\mathbf{v}_n = \mathbf{v}_s$, see Eq. (C.1) and Eq. (C.2).
The dispersion relation is defined by Eq. (4.23) and Eq. (4.24) to:

$$\boxed{\textit{Density Waves (First sound)} \quad \omega^2 = v_1^2 q^2 \quad \text{and} \quad v_1^2 = \left(\frac{\partial p}{\partial \rho}\right)_{\tilde{s}}} \tag{4.26}$$

### 4.4.2 Second sound

In a second sound wave the temperature $T$ and the entropy $S$ oscillate, whereas the pressure $p$ and the density $\rho$ do not vary. From Eq. (4.22), we see that the total momentum density $\mathbf{j} = \rho_n \mathbf{v}_n + \rho_s \mathbf{v}_s$ is constant or equal to zero. The former option is not possible due to geometrical limitations. We, therefore, get $\rho_n \mathbf{v}_n + \rho_s \mathbf{v}_s = 0$. Hence, in this mode the normal- and the

[8] These are called so for the aim of clarity. There is a second sound mode!

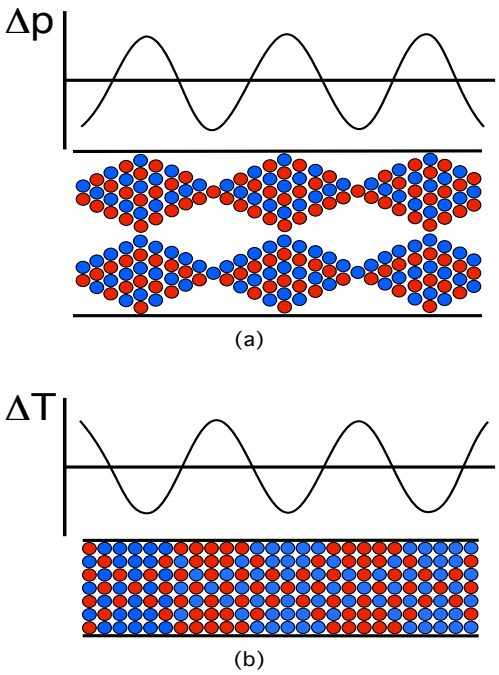


Figure 12: Sketch representations of the first sound mode (a) and second sound mode (b). Blue dots represent superfluid particles and red dots particles of the normalfluid component. The proportions of the red and blue dots on any vertical line represent the proportions of the normal- and superfluid component at that place, respectively. The total number of symbols in a vertical line represents the total density of the liquid. The waves are travelling horizontally. See text for further explanations.

superfluid part move out of phase in opposite directions, see also App. C for further explanations. This leads to a variation over space of a relative concentration of the two components. At "hot spots" the superfluid part is converted into normal fluid at a rate sufficient to absorb the heating energy. Thus, an excess of the normal fluid part and a deficiency of the superfluid part exist in such "hot regions". In this sense, low $\rho_s$ corresponds to a "hot region" and low $\rho_n$ to a "cold region" in the condensed Bose system, respectively. That means that an increase in the concentration of the superfluid component at a point, lowers the temperature there, whereas half a wavelength away, an increase in the concentration of the normal part leads to a temperature rise. Recalling the fact that just the normal fluid component carries entropy, this mode can also be interpreted as an entropy wave. The dispersion relation for a second sound mode is defined by Eq. (4.23) and Eq. (4.25) and we obtain:

$$\boxed{\textit{Temperature (Entropy) Waves (Second sound)} \quad \omega^2 = v_2^2 q^2 \quad \text{and} \quad v_2^2 = \frac{\rho_s}{\rho_n}\left(\frac{\tilde{s}^2 T}{C_v}\right)} \tag{4.27}$$

The possibility of sustaining an undamped temperature wave is a specific property of a superfluid. In normal substances temperature waves are damped by the thermal conduction in

distances of the order of a wavelength $l \approx \frac{\kappa c_0^2}{\omega^2 C}$, where $\kappa$ is the thermal conductivity, $c_0$ the sound velocity and $C$ the heat capacity.

### 4.4.3 First and second sound in an interacting Bose gas at finite temperatures

Finally, we will consider an interacting Bose gas at finite temperatures. In Chapter 4.2 we argued that the critical velocity for creating excitations in an ideal Bose gas is zero. Consequently, when inter-particle interactions are neglected, the second sound mode is absent. Here, we want to calculate the leading correction of the second sound velocity due to the interactions.
For temperatures $T \gg \tilde{T} = \frac{nv_0}{k_\mathrm{B}}$, the Hartree-Fock (HF) approximation applies, see App. D. The total mass density is then given by

$$\rho = mn_c + m\tilde{n}, \tag{4.28}$$

where $n_c$ is the condensate particle density and $\tilde{n}$ is the density of excited particles not being part of the condensate. The momentum density is then defined as

$$\mathbf{j} = mn_c\mathbf{v}_s + m\tilde{n}\mathbf{v}_n. \tag{4.29}$$

Assuming the normal component is not moving, the continuity equation, see Eq. (4.18), becomes

$$\frac{\partial n_c}{\partial t} + \nabla \cdot (n_c\mathbf{v}_s) = 0. \tag{4.30}$$

The chemical potential $\mu$ within the HF- approximation is given by

$$\mu = (n_c + 2\tilde{n})v_0, \tag{4.31}$$

and we therefore get $\delta\mu = v_0\delta n_c$ for the change in the chemical potential. From the expression of the acceleration of the condensate, see Eq. (4.20), it results

$$m\frac{\partial \mathbf{v}_s}{\partial t} = -v_0\nabla\delta n_c. \tag{4.32}$$

Combining Eq. (4.30) with Eq. (4.32) and linearizing the result we obtain

$$\frac{\partial^2\delta n_c}{\partial t^2} = \frac{n_c v_0}{m}\nabla^2\delta n_c. \tag{4.33}$$

The velocity of this second sound mode [9] is then given by

$$v_2 = \left(\frac{n_c v_0}{m}\right)^{\frac{1}{2}}. \tag{4.34}$$

[9] normal and superfliud component move in opposite directions

To conclude, the motion of the condensate and the thermal excitations are primarily independent of each other. As we have noted, second sound involves an oscillation of the condensed particles (superfluid density) and is a soft mode that vanishes in the normal phase. In a weakly interacting Bose-condensed gas, the second sound mode is the long-wavelength continuation of the short-wavelength Bogoliubov mode. A more extensive discussion about these two sound modes in Bose gases is given in Ref.[66].

# 5 Low-dimensional magnetism and Bose-Einstein condensation

The field of low-dimensional magnetism is one of the research topics that gained much interest in the last 10 years. Recently, the focus has been on systems where quantum effects are essential (hence, the nomenclature). Quantum fluctuations become increasingly important the more the dimensionality is reduced. For a detailed overview, please consult Ref.[67, and references therein]. Intensive investigations focused on magnetic insulators, in which the magnetic properties are due to unpaired shell electrons of metallic ions, such as $\mathrm{Cu}^{2+}$ $(3\mathrm{d}^9)$, which realizes a total spin $S = \frac{1}{2}$. In the last five years new materials have been synthesized, where an even number of $\mathrm{Cu}^{2+}$ ions per unit cell are arranged pairwise to form crystalline network of dimers. In our specific case, dimers correspond to a pair of interacting spins, in which the two spins are antiferromagnetically (AFM) coupled with the exchange energy $J < 0$ deriving from the overlap of the electronic wavefunctions.

## 5.1 The quantum spin-dimer

The corresponding quantum-mechanical description for such a single spin-dimer is well described by the Heisenberg exchange Hamiltonian as

$$\hat{H}_{dimer} = -J\boldsymbol{S}_1 \cdot \boldsymbol{S}_2, \tag{5.1}$$

where $\boldsymbol{S}_i$ corresponds to the spin operator representing the spin on site $i$.
Applying some rules of elementary quantum mechanics, the spin-spin interaction $\boldsymbol{S}_1 \cdot \boldsymbol{S}_2$ can be expressed as a function of the total spin $\boldsymbol{S}_{tot} = \boldsymbol{S}_1 + \boldsymbol{S}_2$, with

$$\boldsymbol{S}_1 \cdot \boldsymbol{S}_2 = \frac{1}{2}[(\boldsymbol{S}_1 + \boldsymbol{S}_2)^2 - \boldsymbol{S}_1^2 - \boldsymbol{S}_2^2] = \frac{1}{2}\boldsymbol{S}_{tot}^2 - S(S+1) \tag{5.2}$$

with $S = \frac{1}{2}$. Thus, the Hamiltonian in Eq. (5.1) becomes

$$\hat{H}_{dimer} = JS(S+1) - \frac{J}{2}\boldsymbol{S}_{tot}^2. \tag{5.3}$$

The Eigenstates can be classified according to the value of $S_{tot}$ and $S_{tot}^z$ with

$$\hat{H}_{dimer}|S_{tot}, S_{tot}^z\rangle = \left(JS(S+1) - \frac{J}{2}S_{tot}(S_{tot}+1)\right)|S_{tot}, S_{tot}^z\rangle. \tag{5.4}$$

In this expression, $S_{tot}$ can vary from 0 to $2S$, while $S_{tot}^z$ can assume all values from $-S_{tot}$ to $S_{tot}$. The ground state of such a dimer is a spin singlet, denoted $|0,0\rangle$, with a total spin $S_{tot} = 0$. This ground state is separated by an energy gap $\Delta = J$ from the excited (three-fold

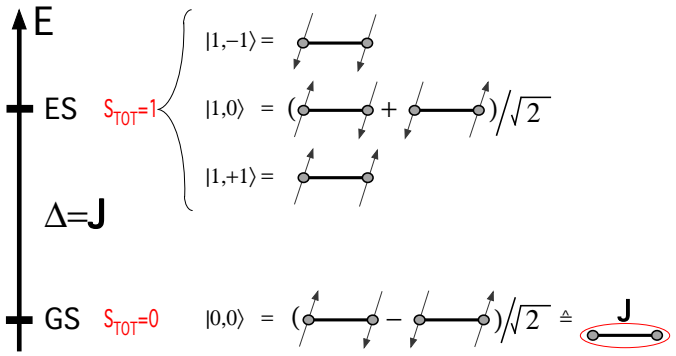


Figure 13: An illustration of the energy scheme of a single spin-dimer. The ground state (GS) of a dimer is a $S = 0$ singlet (represented by the red ellipsis). The first exited state (ES) is a 3-fold degenerated $S = 1$ triplet which is separated by an energy gap $\Delta$ from the ground state.

degenerated) triplet states with total spin $S = 1$ and $S^z_{tot} = -1, 0, 1$ labeled as $|1, \pm 1\rangle$ and $|1, 0\rangle$, respectively. The Eigenenergies of a single dimer are

$$\begin{aligned} \varepsilon_{|0,0\rangle} &= \frac{3}{4}J \\ \varepsilon_{|1,\sigma\rangle} &= -\frac{1}{4}J \quad (\sigma = +1, 0, -1) \quad J < 0. \end{aligned} \tag{5.5}$$

### 5.1.1 The influence of an external magnetic field

The application of a magnetic field $H$ (along the quantization axis) does not alter the singlet ground state, but leads to a Zeeman splitting of the excited triplet states causing a linear reduction of the singlet-triplet gap $\Delta$, according to the Zeeman energy $g\mu_B H_z S_z$. For $g\mu_B H > \Delta$ the applied magnetic field is sufficiently strong to completely suppress the gap at a critical field $H_{c1}$[10].

Including the application of the magnetic field $H$ into Eq. (5.3), the Hamiltonian can be rewritten to

$$\hat{H}_{dimer\ in\ field} = JS(S+1) - \frac{J}{2}\boldsymbol{S}^2_{tot} - g\mu_B H S^z_{tot}. \tag{5.6}$$

Assuming axial symmetry along the $z$-direction, the Eigenstates of the Hamiltonian 5.6 are still $|S_{tot}, S^z_{tot}\rangle$, which yield the Eigenvalue equation

$$\hat{H}_{dimer\ in\ field}|S_{tot}, S^z_{tot}\rangle = \left(JS(S+1) - \frac{J}{2}S_{tot}(S_{tot}+1) - g\mu_B H S^z_{tot}\right)|S_{tot}, S^z_{tot}\rangle, \tag{5.7}$$

[10]There is a second critical magnetic-field amplitude $H_{c2}$.

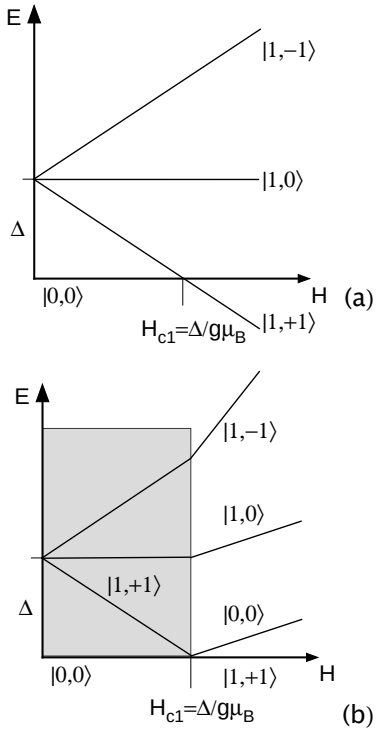


Figure 14: (a) Sketch of the magnetic-field dependence of the excited triplet states of an antiferromagnetically coupled single dimer. As long as $H < \Delta/g\mu_B$, the ground state is a non-magnetic singlet $|0,0\rangle$. The Zeeman splitting leads to an intersection of the lowest triplet excitation at $H = H_{c1} = \Delta/g\mu_B$. (b) Above this critical field the new ground state is of pure triplet nature and the energetical lowest excitation is now a singlet.

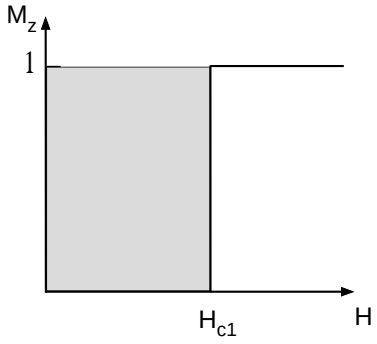


Figure 15: Sketch of the magnetization per dimer along the field-direction. The $S_{tot} = 1$ branch $|1,+1\rangle$ intersects the singlet ground state at $H_{c1} = \Delta/g\mu_B$, which leads to a finite magnetization value for $H > H_{c1}$, even at $T$=0.

with $S = \frac{1}{2}$.
The Eigenvalues change, accordingly, to

$$\begin{aligned} \varepsilon_{|0,0\rangle}(H) &= \frac{3}{4}J \\ \varepsilon_{|1,1\rangle}(H) &= -\frac{1}{4}J - \sigma g\mu_B H \quad (\sigma = +1, 0, -1). \end{aligned} \tag{5.8}$$

## 5.2 The quantum spin systems

In real magnetic systems, such dimers form a crystalline network, see Fig. 16b. Additional interdimer interactions, denoted as $J_\perp$, $J_\parallel$ and $J'$ must be considered. Whenever these dimers

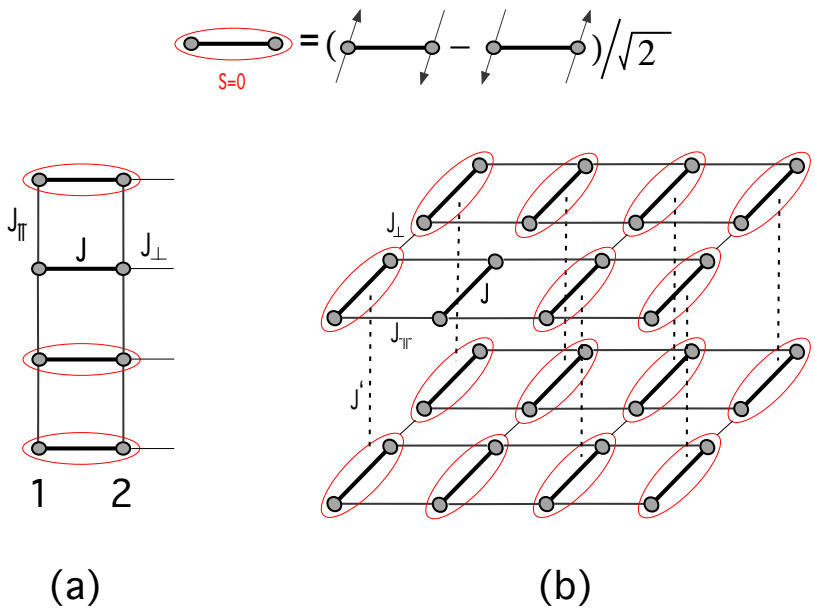


Figure 16: (a) A descriptive representation of a ladder-like dimer network and (b) a 3D dimer network with coupling constants $J_\perp$ (thin and shorter solid line), $J_\parallel$ (thin and longer solid line) and $J'$ (dashed line). The ovals represent the $S = 0$ singlet ground state of a single dimer.

are uncoupled ($J_\perp$=$J_\parallel$=$J'$ = 0), the exact ground state of the system is a direct product of the singlet states $\otimes_{i,dimers}|0,0\rangle_i$. This corresponds to a paramagnetic state, which preserves spin rotation invariance and any existing lattice symmetry [68].

The corresponding Hamiltonian for such a 3D dimer network is described by the so called Heisenberg spin-exchange model

$$H_{3D} = -\sum_i J\boldsymbol{S}_{i,1}\cdot\boldsymbol{S}_{i,2} - \sum_{\langle\alpha,\beta\rangle}\sum_{ij} J^{inter}_{i\alpha,j\beta}\boldsymbol{S}_{i,\alpha}\cdot\boldsymbol{S}_{j,\beta} - g\mu_B H\sum_{i\alpha} S^z_{i\alpha}, \tag{5.9}$$

where $i$ is the index of the dimer with $\boldsymbol{S}_{i,1}$ and $\boldsymbol{S}_{i,2}$ representing the two spins forming the dimer and $\langle\alpha,\beta\rangle$ label pairs of nearest-neighbor ladders in the respective directions, see Fig. 16a. The interdimer interactions are represented by $J^{inter}_{i\alpha,j\beta}$, respectively.

The dimer-states are localized, as long as the interdimer interactions are much lower than the singlet bond $J^{inter} \ll J$ (strong coupling limit). Whenever the exchange energies between dimers are comparable to the the intradimer interaction $J^{inter} \sim J$, the triplet excitations can hop from site to site and propagate dispersively through the (now magnetically 3D-like) dimer network. The hopping of the triplet states is described as a magnetic quasiparticle excitation with $S = 1$ that is defined as a spin boson obeying the Bose statistics and called triplon [68–70], see Fig. 17 [11]. Hence, theoretical aspects about the possible occurrence of BEC in such

[11] Note, that this quasiparticle is not a spin-wave (magnon), since the magnetic system is not necessarily ordered. Unfortunately, these excitations are sometimes confusingly called so!

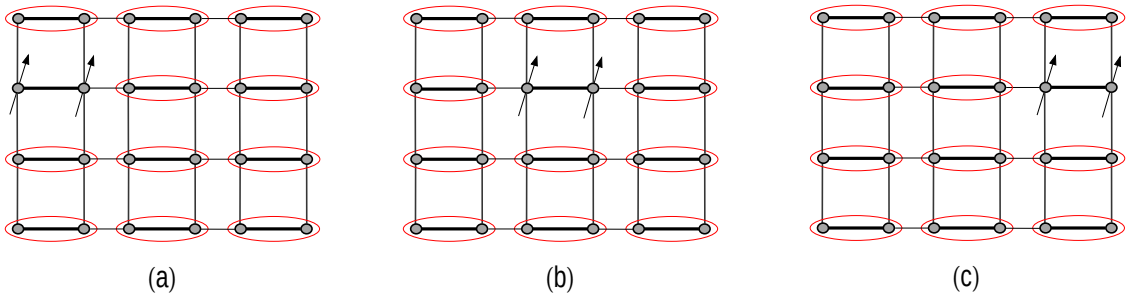


Figure 17: (a)-(c) A descriptive representation of a bosonic $S = 1$ excitation in a paramagnet dispersing along the rung of a planar dimer network. This magnetic quasiparticle is called a *triplon*.

magnetic systems has been put forward [71–73]. The relation $\frac{J}{J^{inter}}$ between the intradimer exchange coupling $J$ and the interdimer exchange interaction $J^{inter}$=$J_\perp$, $J_\parallel$ and $J'$, respectively, is a measure for the excitation bandwidth in the corresponding direction. For large values, a relatively strong localization of the excited states is expected with corresponding small dispersion bandwidths and vice versa [74].
The dispersing triplet states gain in kinetic energy reducing the gap $\Delta$ to (second order in perturbation theory) to $\Delta \approx J - J^{inter} + \frac{J^{inter\,2}}{2J}$ [75], see Fig. 18. The triplons are treated as hardcore bosons with a repulsive interaction amplitude $v_0$, see Chapter 5.3. In this case, the ground state of the system is determined by the balance between the kinetic energy and the repulsive interactions [76]. If the repulsive interaction is the dominant term, *magnetization plateaux* in the magnetization curve $M$ vs. $H$ can be expected at a rational fraction of the saturation magnetization, reflecting the finite energy cost necessary to create an additional polarized boson [77–80]. Is the kinetic term dominant, a continuous rise of the magnetization $M(H)$ starting from the critical (threshold) value $H_{c1}$ is observable, see Fig. 19. $H_{c1}$ is considered to be a quantum critical point (QCP) at which a quantum phase transition (QPT) occurs separating a gapped spin liquid phase ($H < H_{c1}$) with a zero uniform magnetization to an incommensurate phase ($H > H_{c1}$) with nonzero magnetization.
When the magnetic field $H$ is further increased, the system may stay in this critical phase up to a saturation value $H_{c2}$, above which the system is in a saturated ferromagnetic state. $H_{c2}$ is reached when the energetically lowest dispersive triplet-excitation branch crosses the ground state energy, see Fig. 18. Each dimer site is then occupied by a triplon leading to a saturation value of the magnetization $\frac{M_z^{tot}}{N_d}$, where $N_d$ is the total number of dimers in the system.

The QPT at $H_{c1}$ separates the spin liquid state from a three-dimensional ordered state. The residual exchange interactions $J^{inter}$ drive this phase transition to finite temperatures [71, 72]. The evolution of the critical transition temperature as a function of the applied magnetic field

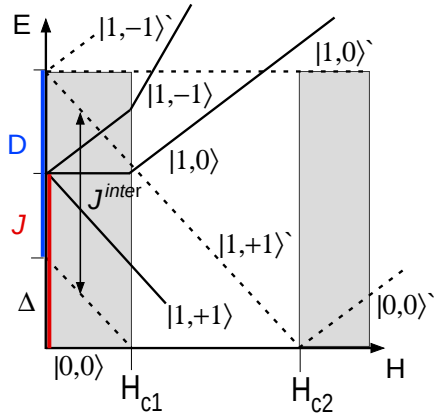


Figure 18: Sketch of the Zeeman splitting of excited triplet modes with gap $\Delta$ and bandwidth $D$. $J^{inter}$ represents the different interdimer interaction constants responsible for dispersion in corresponding directions. As long as $H < \Delta/g\mu_B$, the ground state corresponds to a non-magnetic singlet $|0,0\rangle$. For $H_{c1} < H < H_{c2}$ the ground state is a coherent linear superposition of the singlet state $|0,0\rangle$ and triplet state $|1,+1\rangle$. For $H > H_{c2}$, the ground state is the $S = 1$ spin-triplet $|1,+1\rangle$. In this case, the spins are fully polarized along the direction of the applied magnetic field defining a saturation value of the total magnetization.

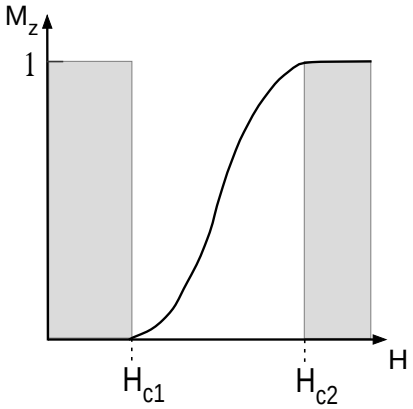


Figure 19: Sketch of the magnetization per dimer along the field-direction of antiferromagnetically coupled spin-dimers. The triplet-branch $|1,+1\rangle$ intersects the singlet ground state $|0,0\rangle$ at $H = H_{c1}$. A finite magnetization will appear for $H > H_{c1}$, increasing with rising magnetic field and saturating for $H \geq H_{c2}$.

is depicted in Fig. 20. A quantum-mechanical description of this phase is given below. At $H_{c2}$, the QPT separates the three-dimensional ordered phase from the fully-polarized phase.

The characteristic length-scale $\xi_{ss}$ in a gapped quantum antiferromagnet is defined as the typical distance, over which the spin-spin correlations decay. It can be expressed as $\xi_{ss} \simeq \frac{D}{\Delta}a$, where $a$ is the lattice constant of the analyzed material, and $D \sim J^{inter}$ is the triplet excitations bandwidth of the same order of magnitude as the interdimer interaction couplings $J^{inter}$. At low fields ($H < H_{c1}$) and zero temperature this length can be approximated as $\xi_{ss} \sim \frac{H_{c1}}{H_{c1}-H}a$. At finite temperatures thermal excitations (spin flips) have to be taken into account, and an additional (thermal) length scale $\xi_T$ must be considered at which the quantum spin-correlations are cut off due to such thermal effects. Depending on the relative values of these two length scales, the $T - H$ phase diagram of gapped antiferromagnetic spin system is divided into different regimes [81], see Fig. 20.

If $k_{\mathrm{B}}T < \Delta$, the density of the thermal excitations is low and $\xi_T > \xi_{ss}$. In this case, thermal

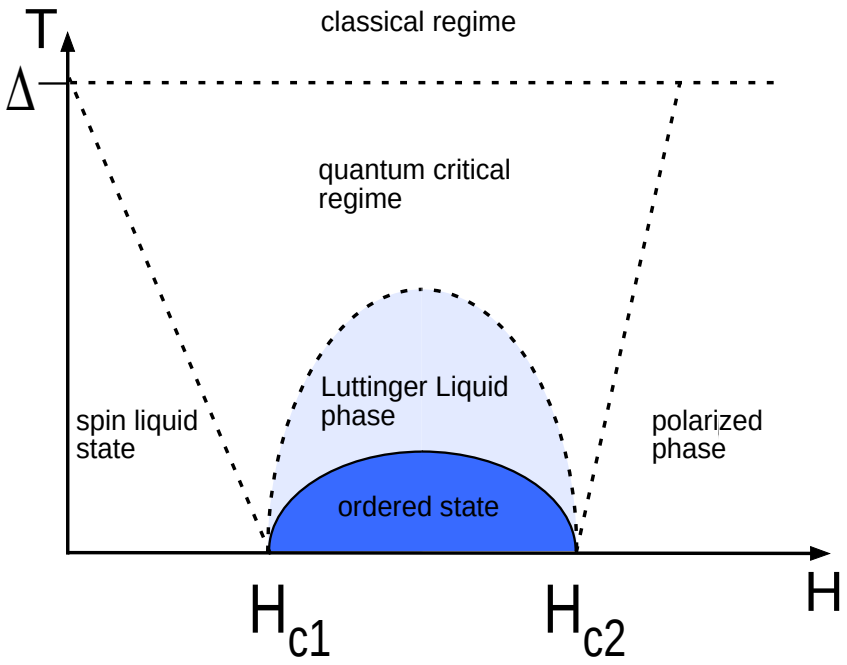


Figure 20: Schematic representation of a full phase diagram of a quantum antiferromagnet in a magnetic field. Below $H_{c1}$ the ground state of the spin system has a non-magnetic singlet ground state and an energy gap $\Delta$. Above $H_{c1}$, the phase is magnetic and gapless, and it belongs to the same universality class as the Heisenberg XXZ model. The dashed lines represent the crossover lines where $\xi_l \sim \xi_T$ separates two quantum regimes from the quantum critical regime dominated by $T$. The dark blue area between the critical fields is a 3D ordered phase, in which BEC presists. In the same field range ($H_{c1} < H < H_{c2}$) at higher temperatures a Tomanaga-Luttinger liquid regime is present. Above $H_{c2}$ a field-polarized ferromagnetic phase results. The dashed lines signalize crossover phenomena and the continuous line represents a border at which a phase transition occurs. See text for further explanations.

excitations do not influence the spin-correlations considerably. When $\Delta \ll k_{\mathrm{B}}T$ and $D$, then $\xi_{ss} > \xi_T$ and the density of excitations is solely governed by $k_{\mathrm{B}}T$. This regime is called the quantum critical regime. Properties of the system are now determined by the length scale $\xi_T$. The dotted lines in Fig. 20 represent the crossover lines at which $\xi_{ss} \sim \xi_T$.
The $T_c(H)$-curve encloses a half-elliptical dome for $H_{c1} < H < H_{c2}$, where the antiferromagnetically ordered phase persists [26, 71, 82]. At low temperatures ($k_{\mathrm{B}}T \lesssim J - J^{inter}$) and low magnetic fields $H < H_{c1}$ the system is in a spin liquid phase. In the same temperature range but at higher fields ($H_{c1} < H < H_{c2}$) the 3D ordered phase persists. In the same field regime, but at higher temperatures, a "Tomanga-Luttinger spin liquid phase" emerges [83–86], characterized by a algebraic decay (powerlaw) of the spin-spin correlations [87, 88] and a $k$-linearized spectrum of excitations. For $H > H_{c2} \sim \frac{J+2J^{inter}}{g\mu_B}$ a ferromagnetic phase is present, in which all spins are polarized along the magnetic field. In the spin liquid and the fully polarized phase $\xi_{ss}$ is the relevant quantum correlation length.
Since such a quantum antiferromagnet with magnetic $S = 1$ triplet excitations can be mapped onto an interacting Bose gas of hardcore triplons, see section 5.4 for more detailed information, the (quantum) phase transition to the three-dimensional, magnetic field-ordered phase with a macroscopic occupation of the ground state by $S = 1$ triplet state has been interpreted as a Bose-Einstein condensation of dilute triplons [26, 27, 71, 73, 89]. .

## 5.3 The spin-dimer representation

Close to $H_{c1}$, the energetically higher triplet states can be neglected, and one can define the lowest $S^z = 1$-triplet state $|1, +1\rangle$ and the $S = 0$ singlet state $|0, 0\rangle$ as the new "up" and "down" states of an effective spin $s = \frac{1}{2}$ spin [90]

$$|\tilde{\downarrow}\rangle = \frac{1}{\sqrt{2}}\left(|\uparrow\downarrow\rangle - |\downarrow\uparrow\rangle\right) \quad \text{and} \quad |\tilde{\uparrow}\rangle = |\uparrow\uparrow\rangle, \tag{5.10}$$

respectively. The effective spin operators are defined as

$$\begin{aligned} \sigma^z|\tilde{\downarrow}\rangle &= -\frac{1}{2}|\tilde{\downarrow}\rangle \quad & \sigma^z|\tilde{\uparrow}\rangle &= +\frac{1}{2}|\tilde{\uparrow}\rangle \\ \sigma^+|\tilde{\downarrow}\rangle &= |\tilde{\uparrow}\rangle & \sigma^+|\tilde{\downarrow}\rangle &= 0 \\ \sigma^-|\tilde{\downarrow}\rangle &= 0 & \sigma^-|\tilde{\uparrow}\rangle &= |\tilde{\downarrow}\rangle. \end{aligned} \tag{5.11}$$

The original spin $S = \frac{1}{2}$ operators can be expressed in terms of the new effective operators by the following transformation

$$\boldsymbol{S}^+_{1,2} = \mp\frac{1}{\sqrt{2}}\sigma^+ \quad \boldsymbol{S}^-_{1,2} = \mp\frac{1}{\sqrt{2}}\sigma^- \quad \boldsymbol{S}^z_{1,2} = \frac{1}{2}[\sigma^z + \frac{1}{2}]. \tag{5.12}$$

The macroscopic occupation of the single-particle ground state is described as the coherent superposition of the non-magnetic singlet $|\psi_s\rangle = |\tilde{\downarrow}\rangle$ and the lowest triplet state $|\psi_t\rangle = |\tilde{\uparrow}\rangle$.

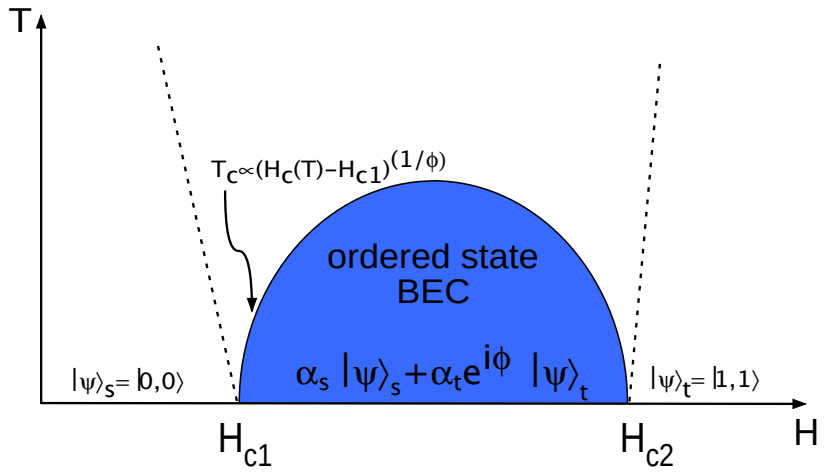


Figure 21: Sketch of the phase diagram of a gapped antiferromagnet at low temperatures. For $H < H_{c1}$ the ground state is a spin singlet, and the system can be described by the wavefunction $|\psi_s\rangle$. A coherent superposition of the singlet and triplet states persists in the ordered regime. The system is described by $|\psi\rangle = \alpha_s|\psi_s\rangle + \alpha_t e^{i\phi}|\psi_t\rangle$. For $H > H_{c2}$, the system is in a fully polarized state where the ground state is magnetic and can be described by a triplet wavefunction $|\psi_t\rangle$.

The condensate wavefunction $|\psi\rangle$ can, therefore, be expressed as

$$\begin{aligned} |\psi\rangle &= \alpha_s(H)|\psi_s\rangle + \alpha_t(H)e^{i\phi}|\psi_t\rangle \\ &= \alpha_s(H)|\tilde{\downarrow}\rangle + \alpha_t(H)e^{i\phi}|\tilde{\uparrow}\rangle, \end{aligned} \tag{5.13}$$

where $\alpha_s(H)$ and $\alpha_t(H)$ are the amplitudes for singlet and triplet state, respectively, which satisfy $\alpha_s^2 + \alpha_t^2 = 1$. The phase factor $\phi$ corresponds to the angle between the reference direction (supposingly $x$) and the transverse component of the total spin $\langle \boldsymbol{S}_1^x + \boldsymbol{S}_1^y \rangle$ in the XY plane [91–93]. These observables are determined calculating the respective spin excitation values on a single dimer. One obtains

$$\begin{aligned} \langle\psi|\boldsymbol{S}_1^x|\psi\rangle = \langle\psi|\boldsymbol{S}_1^+ + \boldsymbol{S}_1^-|\psi\rangle &\propto -\langle\psi|\sigma^+ + \sigma^-|\psi\rangle \\ &\propto \left( \alpha_s \cdot \alpha_t \cdot e^{-i\phi} \underbrace{\langle\tilde{\uparrow}|\sigma^+|\tilde{\downarrow}\rangle}_{1} + \alpha_s \cdot \alpha_t \cdot e^{i\phi} \underbrace{\langle\tilde{\downarrow}|\sigma^-|\tilde{\uparrow}\rangle}_{1} \right) \\ &\propto = \alpha_s \cdot \alpha_t \cos(\phi) \\ &= -\langle\psi|\boldsymbol{S}_2^x|\psi\rangle \end{aligned} \tag{5.14}$$

$$\begin{aligned}\langle\psi|\boldsymbol{S}_1^y|\psi\rangle = -i\langle\psi|\boldsymbol{S}_1^+ - \boldsymbol{S}_1^-|\psi\rangle &\propto -i\langle\psi|\sigma^+ - \sigma^-|\psi\rangle \\ &\propto -i\left(\alpha_s\cdot\alpha_t\cdot e^{-i\phi}\underbrace{\langle\tilde{\uparrow}|\sigma^+|\tilde{\downarrow}\rangle}_{1} - \alpha_s\cdot\alpha_t\cdot e^{i\phi}\underbrace{\langle\tilde{\downarrow}|\sigma^-|\tilde{\uparrow}\rangle}_{1}\right) \\ &\propto= \alpha_s\cdot\alpha_t\sin(\phi) \\ &= -\langle\psi|\boldsymbol{S}_2^y|\psi\rangle\end{aligned} \tag{5.15}$$

$$\begin{aligned}\langle\psi|\boldsymbol{S}_1^z|\psi\rangle &= \langle\psi|\boldsymbol{S}_2^z|\psi\rangle \\ &= \frac{1}{2}\langle\psi|\sigma^z + \frac{1}{2}|\psi\rangle \\ &= \frac{1}{4}\langle\psi|Id|\psi\rangle + \frac{1}{2}\langle\psi|\sigma^z|\psi\rangle \\ &= \frac{\alpha_t^2}{4}\underbrace{\langle\tilde{\uparrow}|Id|\tilde{\uparrow}\rangle}_{1} + \frac{\alpha_s^2}{4}\underbrace{\langle\tilde{\downarrow}|Id|\tilde{\downarrow}\rangle}_{1} + \frac{\alpha_t^2}{4}\underbrace{\langle\tilde{\uparrow}|\sigma^z|\tilde{\uparrow}\rangle}_{1} + \frac{\alpha_s^2}{4}\underbrace{\langle\tilde{\downarrow}|\sigma^z|\tilde{\downarrow}\rangle}_{-1} \\ &= \frac{\alpha_t^2}{2}.\end{aligned} \tag{5.16}$$

We note that the magnetic moment of a single dimer has a non-zero small uniform component parallel to the magnetic field, which per definition of the condensate wavefunction $|\psi\rangle$, see Eq. (5.13), is proportional to the number of condensed particles,

$$N_c \propto \alpha_t^2. \tag{5.17}$$

Moreover, the transverse spin components $\langle\boldsymbol{S}_i^x\rangle$ and $\langle\boldsymbol{S}_i^y\rangle$ order antiferromagneically in the XY-plane. This spontaneous magnetic ordering perpedicular to the field direction corresponds to the spontaneous symmetry breaking of the $U(1)$ rotational symmetry of the triplon system. A non-vanishing staggered magnetization $M_{xy}$ evolves, which corresponds to the order parameter of the phase transition. It is important to note that the $z$-component of the total spin $S_{tot}^z$ commutes with the Hamiltonian Eq. (5.6), as long as axial symmetry along the field-direction persists. The total magnetization and consequently the total number of triplons is conserved [94].

In conclusion, a gapped, dimerized spin system undergoes a QPT at $H = H_{c1}$ passing from a paramagnetic phase into a 3D canted antiferromagnetic ordered phase. This phase transition can be interpreted as the BEC of triplons. The characteristic off-diagonal long ranged order of BEC in an interacting Bose gas, see Eq. (3.4), manifests itself as antiferromagnetic long-range order perpendicular to the magnetic field. The Goldstone mode of the condensate corresponds to a rotation of the staggered magnetic moment $m_\perp = g\mu_B\langle S_x + S_y\rangle$ around the axis of broken symmetry.

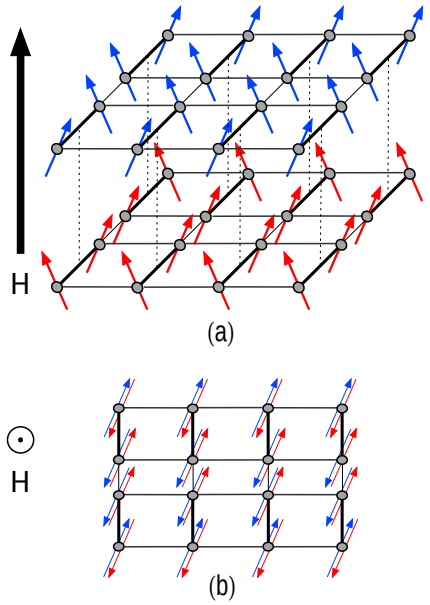


Figure 22: (a) A descriptive representation of a quantum magnet in the antiferromagnetically ordered phase for $H_{c1} < H < H_{c2}$. (b) The ordered phase viewed from along the quantization axis. The magnetic spin moments of different dimer-layers are slightly shifted sidewise for reasons of clarity.

## 5.4 The Bose-Einstein condensation of $S$=1-triplons

As already mentioned, a quantum spin-dimer system with magnetic $S$=1 triplet excitations can be mapped onto an interacting Bose gas of hardcore bosons [89] with a short-range repulsion $v_0$ by replacing each dimer with an effective site that can either be occupied by a singlet state with $S^z = 0$ or by a $S^z = +1$ triplet state. No two bosons are allowed to occupy one dimer, and exactly one boson (one singlet or the triplet) must be present at each dimer.
It follows that the corresponding Hamiltonian can be expressed as

$$\hat{H}_{mapped} = \sum_i (J - g\mu_B H) a_{\mathbf{i}}^\dagger a_{\mathbf{i}} + \sum_{ij} t_{ij} a_{\mathbf{i}}^\dagger a_{\mathbf{j}} + \frac{1}{2} \sum_{i,j} v_0 a_{\mathbf{i}}^\dagger a_{\mathbf{j}}^\dagger a_{\mathbf{j}} a_{\mathbf{i}}, \tag{5.18}$$

where $a_{\mathbf{i}}^\dagger(a_{\mathbf{i}})$ creates (annihilates) a boson on dimer $i$, $t_{ij}$ is the hopping term from dimer $i$ to dimer $j$ deriving from the transverse spin components $S_i^x S_j^x + S_i^y S_j^y$ and $v_0$ describes the repulsive interaction arising from the Ising component $S_i^z S_j^z$ of the spin moment when two triplons occupy neighboring dimers [94], see Fig. 23. The resemblence of the Hamiltonian 5.18 with the Hamiltonian 2.68 describing an interacting Bose gas confirms the picture described above.
Close to the critical field $H_{c1}$ the total density of triplons $n$ is small, which results in a "collision-poor" regime, simplifying the theoretical interpretation to a dilute (weakly interacting) gas of bosons [94]. This description is valid [27, 95] when the average distance between the triplons $l_{mfp} \sim n^{-\frac{1}{3}}$ is much larger than the s-wave scattering length $a_s$, which is the characteristic length scale representing the influence of the repulsive potential $v_0$. This implicates $\frac{a_s}{l_{mfp}} \sim n^{\frac{1}{3}} a_s \ll 1$, which represents the diluteness of the triplons [95].

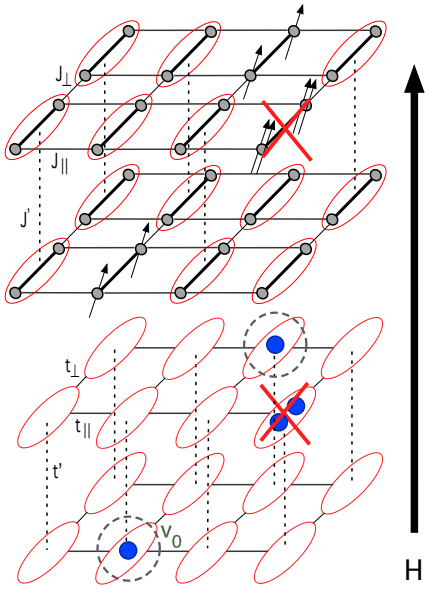


Figure 23: (top) A descriptive representation of a dimer network with 3D coupling constants $J_\perp, J_\parallel, J'$ and excited triplet states (arrows) mapped onto a 3D interacting Bose gas (bottom) of triplons (blue spheres) with corresponding hopping terms $t_i$ ($i = \perp$ , $\parallel$ and $\prime$) and a contact interaction repulsion of amplitude $v_0$. This impedes the occupation of a dimer by more than one triplon.

The spin system undergoes BEC when the gap $\Delta$ is closed by the applied magnetic field $H$. The lowest triplet mode intersects the singlet ground state at $H_{c1}$, and the gas of triplons starts to condensate occupying the single-particle ground state. The density of condensed triplons can, therefore, be tuned by increasing the magnetic field $H$ which assumes the role of the chemical potential $\mu = g\mu_B H - \Delta$[94].
In the HF approximation the phase-boundary is expressed by a power-law

$$(H_c(T) - H_{c1}) \propto T_c^{\phi}, \tag{5.19}$$

with a universal exponent $\phi = \frac{d}{\zeta}$ depending on the dimensionality $d$ of the phase transition and the dynamical critical exponent $\zeta$ given by the dispersion relation of the studied quasiparticles $\varepsilon \sim k^{\zeta}$ [71, 94, 95]. For a spin system with 3D coupling and a quadratic triplon energy dispersion band the expected exponent is $\phi = \frac{3}{2}$. Using the same theoretical framework the critical density of the triplons is expected to vary as

$$n_c(T) \propto T^{\phi} \tag{5.20}$$

and the staggered magnetic moment $m_\perp = g\mu_B \langle S_x + S_y \rangle$ as

$$m_\perp \propto (T_c(H) - T)^{\beta}, \tag{5.21}$$

with $\beta \sim 0.35$ for $H$ fixed [27]. Experimental data measured by various techniques (magnetization, neutron scattering or specific heat) enable to examine such predictions [93].
A short overview of the correspondences between the BEC in an atomic gas and in a spin-dimer quantum antiferromagnet is given in Table 3 [94].

Table 3: The correspondences between BEC in a Bose gas and in a quantum antiferromagnet

| Bose gas | antiferromagnet |
|---|---|
| massive particles | spin $S = 1$ excitations (triplons) |
| boson number $N_c$ | spin component $S^z$ |
| $U(1)$ gauge symmetry | rotational $U(1)$ (or $O(2)$) |
| condensate wavefunction $\langle\psi(\mathbf{r})\rangle$ | transverse magnetic order $\langle S_i^x + S_i^y\rangle$ |
| off-diagonal long-range order | long-range magnetic order |
| chemical potential $\mu$ | magnetic field $H$ |
| superfluid density $\rho_s$ | transverse spin stiffness $\rho_s^{\perp}$ |

The spin stiffness $\rho^s$ measures the increase of energy required to slowly rotate the order parameter of a magnetically long-range ordered system by a small angle $\theta$.

$$\Delta E(\theta) = \frac{1}{2}\rho^s\theta^2 + O(\theta^4), \tag{5.22}$$

The transverse spin stiffness $\rho_s^{\perp}$, therefore, represents the inertia of the transverse magnetic moment $m_{\perp,i}$ on every dimer site $i$ to rotate around the direction of the external magnetic field. The rotation of $m_{\perp,i}$ occurs maintaining small angle-differences between neighboring dimer sites.

The idea to describe the field-induced 3D ordering as Bose-Einstein condensation of triplons has gained much attention in the last ten years. A number of spin-dimer compounds, $\mathrm{TlCuCl_3}$, $\mathrm{KCuCl_3}$, $\mathrm{NH_4CuCl_3}$, $\mathrm{Cu_2(C_5H_{12}N_2)_2Cl_4}$, $\mathrm{(C_5H_{12}N_2)_2CuBr_4}$ and $\mathrm{BaCuSi_2O_6}$ [96–100] were found to have an experimentally accessible gap $\Delta$. Various theoretical approaches based on the scenario of Bose-Einstein condensation were used to investigate this phenomenon and explain peculiar experimental data [27, 71, 73, 91, 101–104].

In this regard, $\mathrm{TlCuCl_3}$ is one of the most accurately studied compounds. *Matsumoto et al.* [91, 105] interpreted theoretically neutron scattering data [28, 106, and references therein], as well as high-field magnetization measurements. *Nikuni et al.* [27] used the Hartree-Fock approximation to explain temperature-dependent magnetization data $M(T)$ obtaining a good qualititative agreement with the experiment. *Sirker et al.* [95, 107] improved this approach considering spin-phonon and spin-orbit coupling. *Sherman et al.* [108] showed that the use of a relativistic dispersion relation $\varepsilon_{\mathbf{k}} = \sqrt{\Delta^2 + \hbar^2k^2/2m^\star}$, where $m^\star$ is the effective mass of a triplon, led to a good quantitative agreement with experimental data. *Misguich et al.* [103] resumed this idea and used the realistic dispersion relation determined from former neutron scattering measurements [106] in order to obtain a good quantitative agreement with experimental data within the HF framework. Last year, *F. Yamada et al.* used the same approach to analyze magnetization data measured at very low temperatures ($< 0.1$ K) for different magnetic-field directions accurately determining the amplitude of the repulsion potential $v_0$.

The presence of anisotropies (anisotropic exchange energies, cristalline anisotropies, spin-orbit coupling or spin-phonon coupling, etc.) may alter the physics of BEC in such spin systems considerably, especially in the vicinity of the QCP. The breakdown of the rotational symmetry $U(1)$ may no longer occur spontaneously but explicitly [94, 95]. The presence of a gapless Goldstone mode down to lowest energy ranges is, therefore, compromised [32, 69, 101]. Depending on the type of the anisotropy and its influence on the preexisiting symmetry, the phase transition changes its dimensionality, is smeared out to a crossover or even completely vanishes [95]. Striking results in this regard for $\mathrm{TlCuCl_3}$ are presented below.

## 5.5 The candidates for Bose-Einsten condensation of triplons

A similar quantum-mechanical description is used for a second and third class of low-dimensional spin systems.
Quasi one-dimensional $S = \frac{1}{2}$ antiferromagnetic chain-like compounds are described by alternating exchange interaction constants $J_1$ and $J_2$, whereby $|J_1| > |J_2|$. Non-magnetic singlet states are therefore localized on these bonds, see Fig. 24. The corresponding Heisenberg Hamiltonian is

$$\widehat{H} = -\sum_i J_1 \boldsymbol{S}_{i-1} \cdot \boldsymbol{S}_i + J_2 \boldsymbol{S}_i \cdot \boldsymbol{S}_{i+1}. \tag{5.23}$$

In case of 3D coupling between these chain-like structures an additional interaction constant $J_3$ has to be considered. $\mathrm{Cu(NO_3)_2 \cdot 2.5H_2O}$ is one of the most accurately studied compound within this model [109].
One dimensional chain-like systems with antiferromagnetic coupling between the integer-spins (often $S = 1$) form the third class of compounds, which are studied within the BEC-scenario. Such systems are well known for the existence of the Haldane energy gap [110, 111] between the non-magnetic ($S = 0$) spin singlet ground state and the lowest excited $S = 1$ triplet state. In this case, it is not really intuitive to understand the existence of a non-magnetic ground state. An explanation for that is given by the *valence bond solid* (VBS) model [112, 113].
The key idea for obtaining such a ground state is to avoid the total spin of two neighboring spins to be equal to two. Such a configuration can be accomplished by regarding every spin-$S = 1$ moment as a composite object consisting of two symmetrized $S = \frac{1}{2}$ spins and linking each of them to its nearest neighbor with a singlet bond, see Fig. 24. Experimentally, such systems are mostly realized in one dimensional system, in which the spin $S = 1$ arises from a $\mathrm{Ni^{2+}ion}$. The most general Hamiltonian describing such a system is given by

$$\widehat{H} = -\sum_{i,\alpha} J_\alpha \boldsymbol{S}_i \cdot \boldsymbol{S}_{i,i+1_\alpha} - D \sum_i \left(S_i^z\right)^2, \tag{5.24}$$

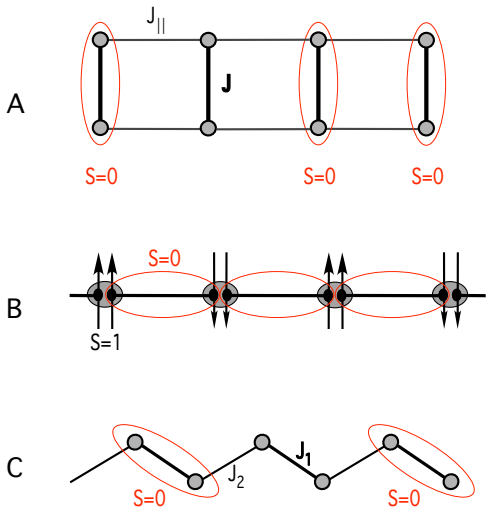


Figure 24: The three classes of gapped antiferromagnets. (A) Spin ladder, which can be coupled to a 2D or 3D network. In the strong coupling limit ($J > J_{\|}$), singlets are localized on the rungs of the ladder. (B) Integer spin chain featuring a Haldane gap with valence bond solid ground state, see text. (C) Dimerized spin-$S = \frac{1}{2}$ chain, which are characterized by two alternating bonds $J_i$ (i=1,2) and $J_1 > J_2$. Singlets are localized on the stronger bond.

with $\alpha = \{x, y, z\}$. The constant $D$ takes the single-ion anisotropy into account (assumed to be along the z-axis in this case) caused by enhanced spin-orbit effects mostly present in such compounds [34, 83–86]. Generally, in all these three classes of low-dimensional spin systems the magnetic interaction between the 1D ladder- or chain-like elements is usually small compared to the singlet bond exchange constant, i.e., $J^{inter} < \{J, J_1, J_{x,y}\}$, respectively. Therefore, such compounds have quasi-1D properties at high temperatures ($k_B T \gg J^{inter}$), while at low temperatures a 1D to 3D ordering transition can occur, if the excitation gap $\Delta$ can be suppressed.

In the last couple of years, a handfull of new low-dimensional spin-compounds were synthesized which emerged as possible candidates to observe BEC in. Even experimental data of older compounds [114] were reconsidered and analyzed within the BEC-framework.

In this section we want to give a brief overview of the most important characteristics of these materials. Each compound can be assigned to one the three different structural classes introduced above, see Fig. 24.

- ***A*** Coupled spin-$S = \frac{1}{2}$ dimer (ladder) system
- ***B*** Haldane gap spin-$S = 1$ quasi one-dimensional chain system
- ***C*** Dimerized spin-$S = \frac{1}{2}$ chain, with two alternating bonds $J_i$ (i=1,2) and $J_1 > J_2$.

Table 4: The low-dimensional spin-system compounds in which an antiferromagnetic field-induced ordered phase (BEC of triplons) has been detected. Ideal axial-symmetrical aspects and experimental confirmations of theoretical calculations are denoted in bold.

| material | symmetry | class | magnetic ion | spin $S$ | $H_{c1}/H_{c2}$ | $T_c^{max}$ | $\phi$ | $\beta$ | $\Delta(H)$ |
|---|---|---|---|---|---|---|---|---|---|
| $TlCuCl_3$ | monoclinic | A (3D) | $Cu^{2+}$ | $1/2$ | 5.6T/>80T [91] | 6 K | 1.67-2.2 [27, 95, 103, 115, 116] | [96] | [28] |
| $KCuCl_3$ | monoclinic | A (3D) | $Cu^{2+}$ | $1/2$ | >20T/>80T[105] | 5K | 2.3 [117] | [28] | [118] |
| $(CH_3)_2HNH_3CuCl_3$ | triclinic | A | $Cu^{2+}$ | $1/2$ | 9T/∼12T | 2K | [119, 120] | [119, 120] | [121] |
| $(C_5H_14N_2)_2CuBr_4$ | monoclinic | A | $Cu^{2+}$ | $1/2$ | 6.6T/∼14.6T | < 4.5K [99] | ... | ... | ... |
| $Cu_2(C_5H_{12}N_2)_2Cl_4$ | monoclinic | A | $Cu^{2+}$ | $1/2$ | 7T/∼13T | 2K | [98, 122] | [98, 122, 123] | ... |
| $Cu_2(C_5H_{12}N_2)_2Br_4$ | monoclinic | A | $Cu^{2+}$ | $1/2$ | 15T/∼23.4T[124] | 2K | ... | ... | ... |
| $BaCuSi_2O_6$ | **tetragonal** | A | $Cu^{2+}$ | $1/2$ | 23T/∼49T | 5K | 1-**1.5**[100, 125] | [100] | [100] |
| $Cu_2Cl_4H_8C_4SO_2$ | ... | A | $Cu^{2+}$ | $1/2$ | 4T/ ... | ∼ 2K | 1.98-2.38[126] | ... | ... |
| $PbV_3O_9$ | triclinic | A | $Va^{4+}$ | 1/2 | 4T/ 38T [127] | ∼ 6K | [127, 128] | ... | ... |
| $(C_4H_{14}N_2)Cu_2Cl_6$ | ... | A (2D) | $Cu^{2+}$ | 1/2 | 8T/ 36T [129] | 6K | [129, 130] | 0.34 [129, 130] | ... |
| $Cs_2CuCl_4$ | ... | A (2D) | $Cu^{2+}$ | 1/2 | 8.5T/ 60T [35] | 0.5K | **1.5** [35, 131] | ... | ... |
| $Cs_3Cr_3Br_9$ | **hexagonal** | A (2D) | $Cr^{3+}$ | 3/2 | 1.5T/ ... [132] | <0.5K | **1.5** [132, 133] | ... | [132, 133] |
| $CsFeCl_3$ | **hexagonal** | B | $Fe^{2+}$ | 2 | 6T/ 10T | 2.8K | [134] | 0.22-0.33 | [134] |
| $NiCl_2 - 4SC(NH_2)_2$ | **tetragonal** | B | $Ni^{2+}$ | 1 | 3.5T/ 12T | 1K | **1.5** [34, 135] | ... | ... |
| $Ni(C_5H_14N_2)_2N_3PF_6$ | **orthorhombic** | B | $Ni^{2+}$ | 1 | 3.5T/ >10T | 2K | 0.34-0.57 [83, 84, 86] | [83] | [85] |
| $Ni(C_5H_14N_2)_2N_3ClO_4$ | **orthorhombic** | B | $Ni^{2+}$ | 1 | 2.6T/ 7.1T | 0.8K [136] | [137] | ... | ... |
| $PbNi_2V_2O_8$ | **tetragonal** | B | $Ni^{2+}$ | 1 | 14T-19T/ ... [138] | 2K | [100, 138] | ... | ... |
| $Cu(NO_3)_2 \cdot 2.5H_2O$ | monoclinic [139] | C | $Cu^{2+}$ | $1/2$ | 1.67T/ 4.4T[109, 114, 140] | < 0.2K[109, 114] | ... | ... | ... |
| $Cu(NO_3)_2 \cdot 2.5D_2O$ | monoclinic [139] | C | $Cu^{2+}$ | $1/2$ | 2.2T/ 4.2T[109, 114] | < 0.175K[141] | ... | ... | [119, 142, 143] |

In Table 4, the crystal structure, the value of critical exponent $\phi$, the value of critical exponent $\beta$ and the value of the two critical magnetic fields $H_{c1}, H_{c2}$ are listed to the best of our knowledge for every candidate. Important publications concerning experimental data on the Zeeman splitting of the triplet excitations $\Delta(H)$ and the phase boundary $T_c(H)$ are also cited.

# 6 The quantum spin system $TlCuCl_3$

We focused our experimental work on the spin-dimer compound $TlCuCl_3$. This material was one of the first solids, in which experimental work indicated that the triplons form a Bose-Einstein condensate above the critical field $\mu_0 H_{c1} \approx 5.5\mathrm{T}$ at low temperatures [27, 28]. It is certainly one of the most studied compounds and, therefore, the literature offers vast access to various important data concerning the phase diagram, magnetic exchange interactions and dispersion relation of triplons [91, 106].
The small critical field $H_{c1}$ provides a great applicability for experiments.

## 6.1 The crystal structure and the magnetic exchange interactions

$TlCuCl_3$ has a monoclinic structure (space group $P2_1/c$) with lattice constants $a$ = 3.9815 Å, $b$ = 14.144 Å, $c$ = 8.89 Å and $\beta$ = 96.32 ° at room temperature with $b$ being the twofold axis [144, 145]. The structure consists of nearly planar $(Cu_2Cl_6)^{2-}$ dimer-clusters, which are stacked on top of one another to infinite double chains along the short $a$-axis. These dimer-chains occupy the edges and the center of the $b-c$-plane, and are separated from each other by $Tl^+$ cations, see Fig. 25.

Well-localized spins reside at the Cu site in a $3d_{x^2-y^2}$ configuration, whereas these orbitals spread in to a nearly planar $Cl^-$ environment in the $(10\bar{2})$ plane. Magnetic interactions between the $Cu^{2+}$ are provided in a first approximation by the superexchange pathways through the 3p and 3s orbitals of the $Cl^-$ anions [146].

The magnetic properties of $TlCuCl_3$ are determined by the exchange interactions between the $Cu^{2+}$ ions which are arranged in dimer pairs within $Cu_2Cl_6$-clusters.
The magnetic ground state of $TlCuCl_3$ is a non-magnetic spin singlet that is separated from the first excited triplet state by an excitation gap $\Delta \approx 0.7$ meV in zero magnetic field. The origin of the spin gap is the strong antiferromagnetic coupling $J$ = -5.26 meV between the two $Cu^{2+}$ ions within the $(Cu_2Cl_6)^{-2}$ cluster forming a spin-dimer [106].
Inelastic neutron-scattering experiments revealed three-dimensional dispersion of the triplet quasiparticles [106, 147]. The neighboring dimers couple magnetically along the chain direction (crystallographic $a$-axis) and mostly in the $(10\bar{2})$ plane, favored by the nearly planar dimer arrangement, see Fig. 26. Neutron-scattering measurements [106] evidenced that the magnetic structure of $TlCuCl_3$ must be considered as a strongly coupled spin-dimer system with relative small spin gap and a large triplon dispersion bandwidth caused by the strong 3D inter-dimer interactions. The best theoretical description of corresponding data is achieved with a Heisenberg-type Hamiltonian of a spin-dimer model considering strong interdimer interactions [106],

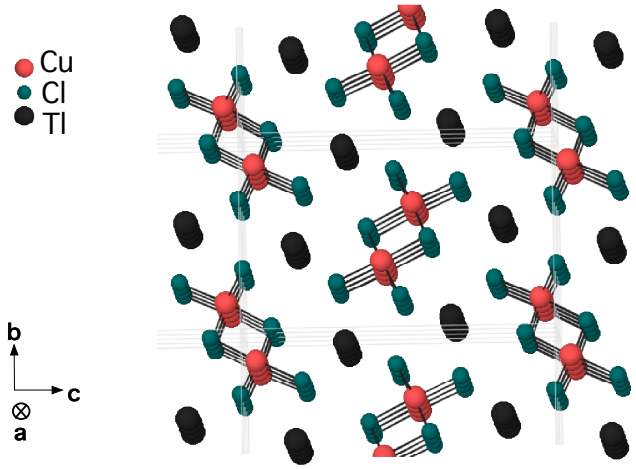


Figure 25: The crystal structure of $TlCuCl_3$ . $(Cu_2Cl_6)^{-2}$ octahedral-like clusters are located in the center and at the edges of the unit cell in the $b-c$-plane. The two Cu ions within these clusters are antiferromagnetically coupled forming a dimer. Such dimers are stacked in ladder-like manner along the $a$- direction.

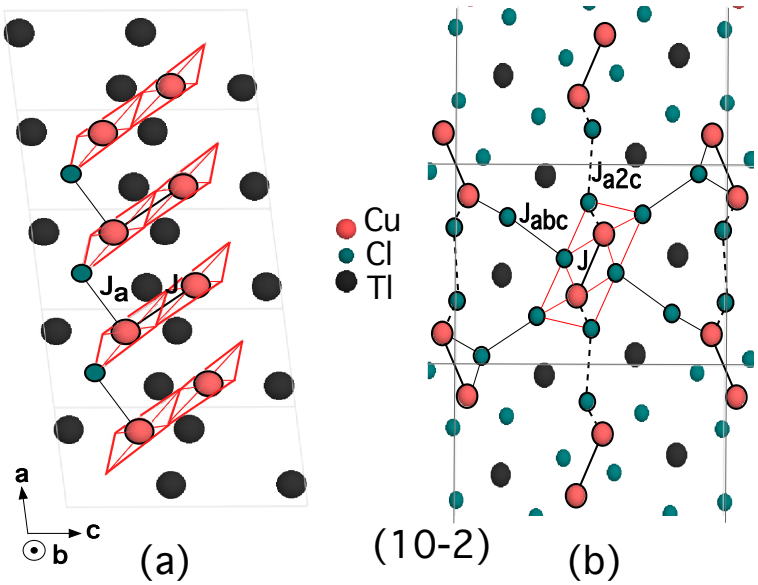


Figure 26: A schematic view of the magnetic structure of $TlCuCl_3$. (a) The antiferromagnetic dimers are located in the basal planes of distorted octahedra (highlighted in red). Cl-atoms are partly omitted for clarity. The dimers are stacked one on another along the $a$-axis. The magnetic intradimer interaction is labeled as $J$, the interdimer interaction (out of plane) along $a$ as $J_a$. (b) The magnetic interactions in the (10-2) plane are accordingly highlighted. See text for detailed information.

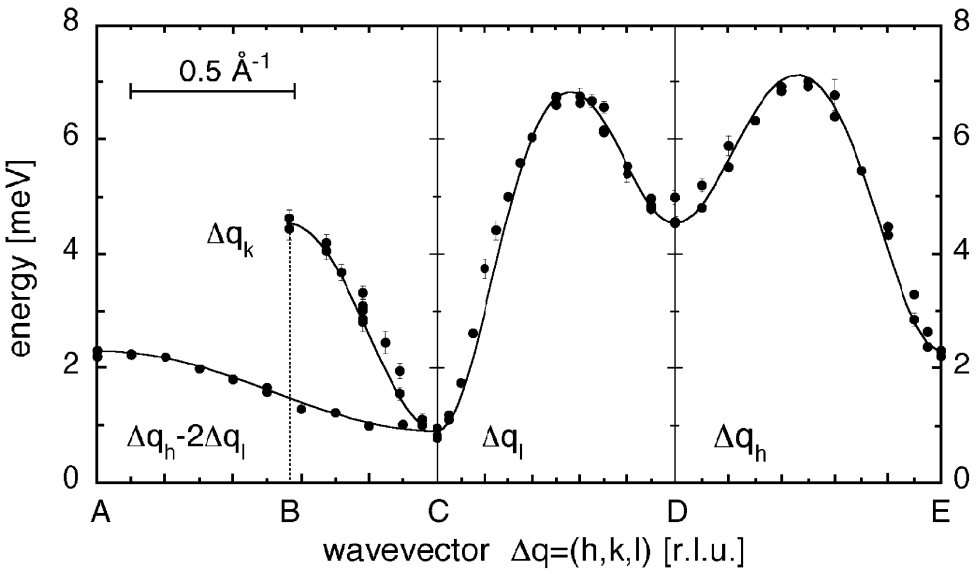


Figure 27: Energy dispersion of the magnetic modes in $TlCuCl_3$ at $T$=1.5 K. Figure is taken from [106]. The data are plotted versus the relevant directions in the reciprocal space $(\mathbf{a}^\star, \mathbf{b}^\star, \mathbf{c}^\star)$ and arranged in a reduced scheme representation with $A = E$ =(0.5,0,0), $B$ =(0,1,0),$D$ =(0,0,0) [ r.l.u. ]. The zone centers corresponds to $C$= (0,0,1) for $\Delta q = (h, 0, l)$ and $C$= (0,0,0) for $\Delta q = (0, k, 0)$. The solid lines represent a least-square fit based on Eq. (6.1).

$$
\begin{aligned}
H_{TlCuCl_3} =& H_{dimer} + H_{inter} \\
H_{TlCuCl_3} =& - J \sum_i \boldsymbol{S}_{i,1}\boldsymbol{S}_{i,2} - \frac{1}{2} \sum_{i,j;\mu,\nu} J_{i,j;\mu,\nu}\boldsymbol{S}_{i,\mu}\boldsymbol{S}_{i,\nu},
\end{aligned}
\tag{6.1}
$$

where $H_{dimer}$ represents the isolated dimer limit with intradimer interaction $J$ $(J < 0)$ and $H_{inter}$ considers the interactions between neighboring dimer $\langle i, j\rangle$ with $\mu = \{1, 2\}$ and $\nu = \{1, 2\}$ denoting the individual ion on dimer $i$ and $j$, respectively. The dispersion of the excited triplets originate from the coupling constants $J_{i,j;\mu,\nu}$ leading to a characteristic dispersion bandwidth $D$ of about 6 meV, see Fig. 27.

The minimum excitation energy $\Delta \sim 0.75$ meV has been reported at $Q_0 = (0, 0, 1)$ in zero magnetic field [106]. From fits to the inelastic neutron scattering data the effective magnetic interactions $J_{i,j}$, the weighted average of all competing exchange interactions between two neighboring dimers [146] have been determined. Corresponding results are presented in Table 5, whereby slightly different values were obtained using different fitting approaches. *Cavadini et al.* [106] used a least-squares fit based on Eq. (6.1), whereas *Matsumoto et al.* started from the same Hamiltonian using the bond-boson approach and the Holstein-Primakov transformation [91].

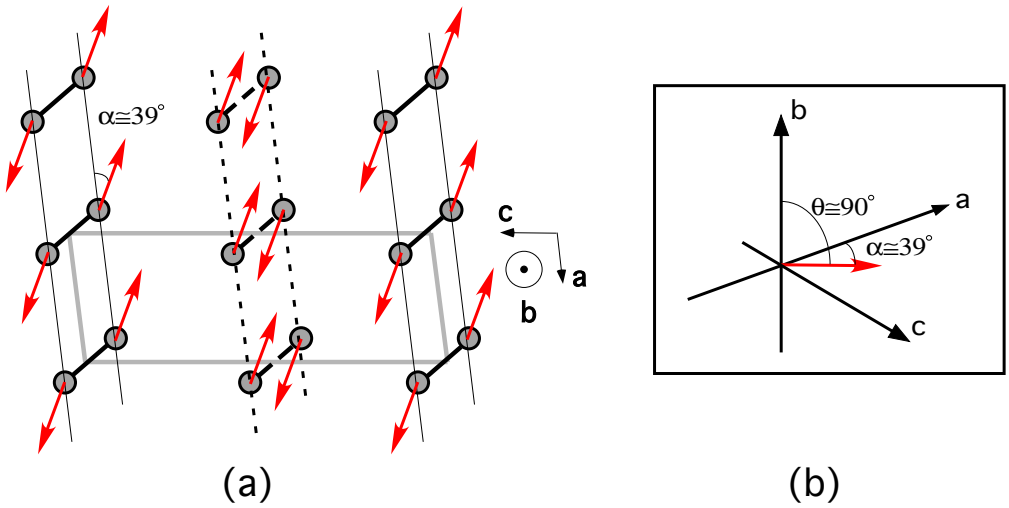


Figure 28: A schematic view of the spin structure observed in the field-induced magnetic ordered phase of $TlCuCl_3$ for $H \parallel b$. The double chains located at the corner and the center of the chemical unit cell in the $b-c$ plane are represented by solid and dashed lines, respectively. The $Cu^{2+}$-ions are the gray spheres. The in gray framed area is the chemical unit cell and the red arrows indicate the spins. (b) The inclination of the ordered magnetic moment versus the $b$-axis has been detected to be 90° within the measurement resolution .

Table 5: The effective coupling interactions in $TlCuCl_3$

| $J_{i,j}$ [ meV ] | $R_{i,j}$ [ l.u ] | from Ref.[106] | from Ref.[91] |
|---|---|---|---|
| $J$ | ± (0 0 0) | -5.424 | - 5.501 |
| $J_a$ | ± (1 0 0) | 0.427 | 0.215 |
| $J_{a2c}$ | ± (2 0 1) | 1.430 | 1.581 |
| $J_{abc}$ | ± (1 +$\frac{1}{2}$ $\frac{1}{2}$) | -0.619 | -0.455 |
| | ±(1 -$\frac{1}{2}$ $\frac{1}{2}$) | -0.619 | -0.455 |

As soon as the external magnetic field $H$ is larger than a critical field $H_c$ with

$$g\mu_B H_c(T = 0) = g\mu_B H_{c1} = \Delta, \tag{6.2}$$

where $\mu_B$ is the Bohr magneton and $g$ is the Landé g-factor, the excitation gap closes due to the Zeeman splitting, and the triplet states $S^z = +1$ are populated, eventually forming the BE-condensate. The 3D interdimer interactions drive this quantum phase transition to finite temperatures leading to a temperature dependent critical field $H_c(T)$.
Antiferromagnetic ordering of the spin system in the plane perpendicular to the applied magnetic field has been observed by elastic neutron scattering at $Q_0$ for magnetic fields $H > H_c(T)$ as predicted by theory [27, 115]. The spin structure was determined at $T$= 1.9 K and $\mu_0 H \parallel b$ = 12 T. The transverse spin components on the same dimer are aligned antiparallel, whereas spin components on the same leg along the double-chains are parallel, enclosing an angle of 39° with the a-axis, see Fig. 28.

## 6.2 The magnetic susceptibility

Magnetic-susceptibility measurements were performed in a commercial PPMS (Physical Property Measurements System, Quantum Design) on a $TlCuCl_3$ single crystal with mass m = 12.36 mg, for 1.8 K $\leq T \leq$ 300 K at $\mu_0 H$ = 1 T for $\mathbf{H} \parallel b$ and $\mathbf{H} \parallel$ [201]. The sample was provided by Dr. Karl Krämer, from the Department of Chemistry and Biochemistry at the University of Bern.
The susceptibility $\chi(T)$ of $TlCuCl_3$ is typical for a low-dimensional spin gap system, showing a well pronounced maximum at $T_{\chi_{max}} \sim$ 36 K and an exponential decrease at low temperatures indicating the existence of a gap $\Delta$ between the ground state and the first excited triplet state, see Fig. 29.
For Heisenberg spin systems with identical spin subsystems that are weakly coupled to each other, a good fit to the data in the paramagnetic regime is provided by the molecular mean-field theory (MFT) and its extensions [148]. We, therefore, used this approach within the model of dimers coupled by an effective interdimer coupling $\widetilde{J}$, representing the sum of all exchange coupling constants $J_{kl}$ for a given dimer $k$ interacting with neighboring dimers $l$ [148]. An additional temperature-independent diamagnetic term $\chi_0$ which contains the orbital diamagnetic core contribution $\chi^{core}$ (including the background contribution of the sample holder) and a paramagnetic Van Vleck contribution $\chi^{VV}$ are considered.
We, therefore, fitted the magnetic susceptibility $\chi(T)$ for temperatures $T > 20$ K according to

$$\chi(T) = \chi_0 + \chi_{MF}(T), \tag{6.3a}$$

with

$$\chi_0 = \chi^{core} + \chi^{VV}, \tag{6.3b}$$

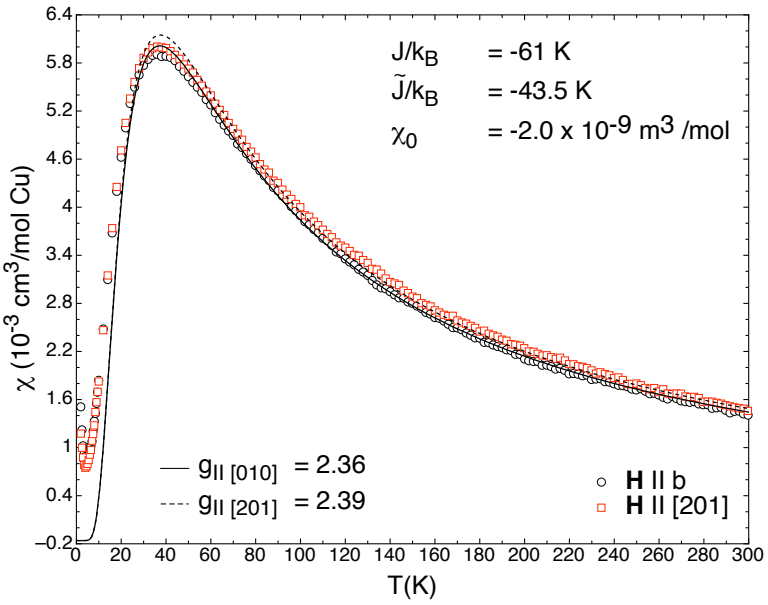


Figure 29: The magnetic susceptibility $\chi(T)$ of $TlCuCl_3$ with $\mu_0 H$ = 1 T applied along the crystallographic $b$-axis and along [201]. The corresponding fits to the data are discussed in the text.

and

$$\chi_{MF}(T) = \frac{\chi^{dimer}(T)}{1 + \chi^{dimer}(T)\frac{\widetilde{J}}{N_A g^2 \mu_B^2 \mu_0}}. \tag{6.3c}$$

Here,

$$\chi^{dimer}(T) = \frac{N_A g^2 \mu_B^2 \mu_0}{3 k_B T} \frac{2(S+1)exp(-\frac{J}{k_B T})}{1 + 2(S+1)exp(-\frac{J}{k_B T})} \tag{6.3d}$$

is the susceptibility of a non-interacting spin-dimer system with single spins $S = \frac{1}{2}$ and the intradimer coupling $J$. $\chi_{MF}$ accounts for the mean-field correction [148].

For a given measured data set of $\chi(T)$-data we therefore used four fitting parameters: $\chi_0$, $g$, $J$ and $\widetilde{J}$. We forced the values for $\chi_0$, $J$ and $\widetilde{J}$ to be identical for both magnetic-field directions. This restriction is physically reasonable, since these three fitting parameters are independent of the magnetic-field orientation. A small anisotropy of the $g$-factor was considered, however, although it is not predicted by ESR measurements [145]. In fact, the obtained g-values for the two investigated crystallographic directions are the same within the error margin, see Table 6. The best obtained fits are shown in Fig. 29. They yield a good description of the experimental data for $T \geq 20$ K. However, the distinct upturn in $\chi(T)$ at lower temperatures is not at all reproduced by the fits. We believe that this term is intrinsic for $TlCuCl_3$ [145] and we shall discuss it in more detail in Chapter 6.3. Note that the inclusion of a Curie-like term for fitting the data at $T > 20$ K does not significantly change the results presented in Table 6.

The value of the intradimer coupling $J$ is close to the result obtained by neutron scattering

Table 6: The extracted fitting parameters from $\chi(T)$ data of $TlCuCl_3$ ($T \geq 20$ K). $\chi_0$, $J$ and $\widetilde{J}$ were forced to be identical for the two field directions.

| | $H \parallel b$ | $H \parallel [201]$ | |
|---|---|---|---|
| $J/k_B$ (K) | -61 | | $\pm 1$ |
| $\widetilde{J}/k_B$ (K) | -43.5 | | $\pm 0.5$ |
| $\chi_0$ ($m^3$ /mol) | $-2.0 \times 10^{-9}$ | | $\pm 10^{-10}$ |
| $g$ | 2.36 | 2.39 | $\pm 0.05$ |

measurements ($J/k_B \sim -64$ K [106]) . For $TlCuCl_3$ the interdimer exchange interaction $\widetilde{J}$ is a sum of three exchange constants $J_a$, $J_{a2c}$ and $J_{abc}$ which are defined in Ref. [106].
Unfortunately, the fit does not allow us to distinguish between these interaction constants, but the fact that $\widetilde{J} \approx J$ clearly shows the strong 3D coupling between the dimers. From Eq. (6.3a), we find that the peak value $\chi_{max} = \chi(T \approx 36$ K) increases with either increasing the $g$-factor or the intradimer coupling constant $J$, or by decreasing the interdimer coupling constant $\widetilde{J}$. Since our value of $J$ is consistent with published data from neutron scattering measurements [106], the slight overshoot of the fitting curve with respect to the measured data around $\chi_{max}$ implicates an underestimate of $\widetilde{J}$ and/or an overestimate of the Landé g-values, respectively. The latter scenario is supported by comparing our results to high precision ESR- measurements [145] which obtain a value of $g$ = 2.06 for both magnetic-field directions.

## 6.3 The total magnetization

In the theory of BEC of magnetic quasiparticles in insulating spin-dimer materials, the total magnetic moment $M = g\mu_B N$ is proportional to the excited triplons $N$, which depends on both the temperature $T$ and magnetic field $H$ [27]. We, therefore, decided to analyze in detail the low-temperature region of the magnetization for both low magnetic fields (1 T $\leq \mu_0 H \lesssim \mu_0 H_c$) and high magnetic fields ($\mu_0 H_c \lesssim \mu_0 H \leq 9$ T) using a consistent approach including adequate contributions for the respective magnetic field regions. We note here that all the magnetization data presented in this section are expressed as magnetic moment $M$ per single $Cu^{2+}$ ion . The later used quantity $m(T) = M(T)/N_d = g\mu_B n(T)$ (where $N_d$ is the number of dimers and $n(T) = N(T)/N_d$ is the total triplon fraction) differs from that by a factor 2. All values extracted from fits and calculations are presented in the latter units.

### 6.3.1 The magnetization $M(T)$ for $1\text{T} \leq \mu_0 H \leq \mu_0 H_{c1}$

Fig. 30 shows the variation of $M$ of $TlCuCl_3$ at low temperatures along the crystallographic $b$- axis and the [201]- direction, respectively, for magnetic fields up to $\mu_0 H = 5$ T. The magnetization decreases exponentially to almost zero with decreasing temperature for both crystal-

lographic directions, but showing an upturn at low temperatures for low magnetic fields. With an increasing magnetic field, the anisotropic behavior of the magnetization in the two different field orientations becomes apparent. Because in both field directions the upturn in $M$ at low temperatures is gradually suppressed with an increasing $H$, the magnetization curves for $\mathbf{H} \parallel [201]$ cross at $T_{cross} \sim 3.2$ K . For $\mathbf{H} \parallel b$ a similar crossing of $M(T)$ data cannot be seen in the analyzed temperature range, but by extrapolating the respective magnetization curves to lower temperatures a $T_{cross}$ below 2 K seems to be plausible.

This crossing of $M(T)$-data is caused by the fact that the upturn in $M(T)$ at low temperatures does not grow linearly with $H$. Moreover, this upturn is quantitatively different in the two considered field directions. If this low-temperature contribution was due to an extrinsic paramagnetic impurity phase it could be expected to be isotropic. We therefore consider this behavior to be intrinsic to $TlCuCl_3$. This upturn in $M(T)$ can be expressed as a temperature and field-dependent Curie-Weiss-like term, assumed to be proportional to the Brillouin function $B_S(x)$ with $x = g\mu_B\mu_0 HS/k_BT$ and a constant $C_S$. Because we assume this term to be intrinsic to the here studied dimer-system, it is reasonable to assign it to magnetic moments associated with the triplet states with $S = 1$. A similar observation confirming this fact was reported in Refs. [145, 149]. The magnetic-field dependence of our low-temperature data showing an almost saturated behavior in $M(H)$ for $H < H_c$, see Fig. 31, can indeed be qualitatively well reproduced by assuming a magnetization term that is proportional to a Brillouin function $B_S(x)$. The additional $H$-dependence for $H < H_c$ can be explained by taking again a diamagnetic term $m_{dia} = \chi_0 \cdot H$ and an additional paramagnetic term $m_{HL}(H)$ (to be discussed below) into account. However, the quality of corresponding fits to our low-temperature $M(H)$-data does not allow us to clearly distinguish between $S$=1 and $S = \frac{1}{2}$, see Fig. 31. Therefore, we will consider in the following both scenarios for the Curie-Weiss-like term $\tilde{C}_S \cdot B_S(x)$, and we will later argue that only the $S = 1$ case fits to our data in a physically meaningful way.

From the expression for the free energy per unit length of a Heisenberg ladder [75]

$$f = -\frac{k_BT}{2}\left[1 + 2cosh\left(\frac{g\mu_B\mu_0 HS}{k_BT}\right)\right] z(T) \tag{6.4a}$$

with

$$z(T) = \frac{1}{2\pi}\int_{-\pi}^{\pi} e^{-\frac{\varepsilon_{\mathbf{k}}}{k_BT}}\, dk, \tag{6.4b}$$

we can estimate the magnetization per dimer by multiplying $f$ from Eq. (6.4a) with the mean dimer-dimer distance $\bar{a} = (a \cdot b \cdot c \cdot sin\beta)^{(1/3)} = 0.79$ nm, where $a$, $b$ and $c$ and $\beta = 96.32°$ are taken from crystallographic data of $TlCuCl_3$ [93]. Using a simple quadratic approximation for the triplon dispersion relation, $\varepsilon_{\mathbf{k}} \propto \Delta + \hbar^2k^2/2m^\star$ (where $m^\star$ corresponds to the effective

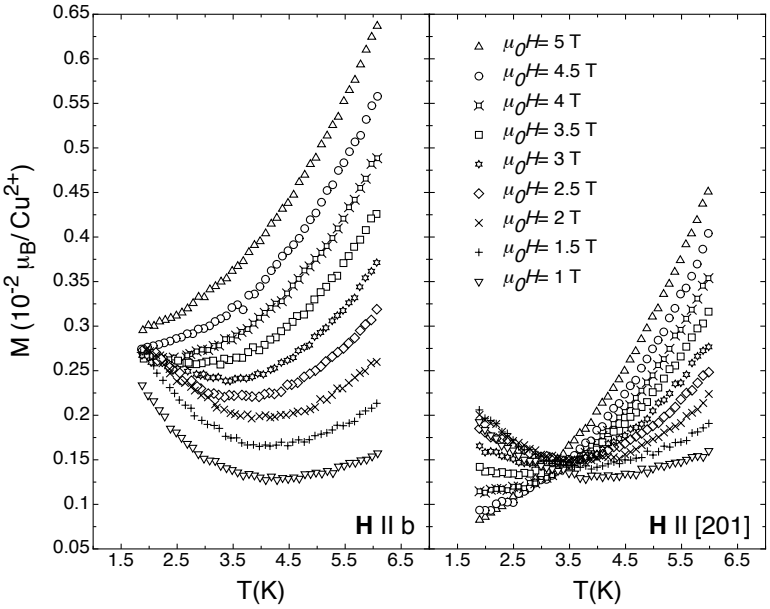


Figure 30: The magnetization $M(T)$ of $TlCuCl_3$ for 1T $\leq \mu_0 H \leq$ 5 T applied along the crystallographic $b$-axis (left) and along [201] (right). .

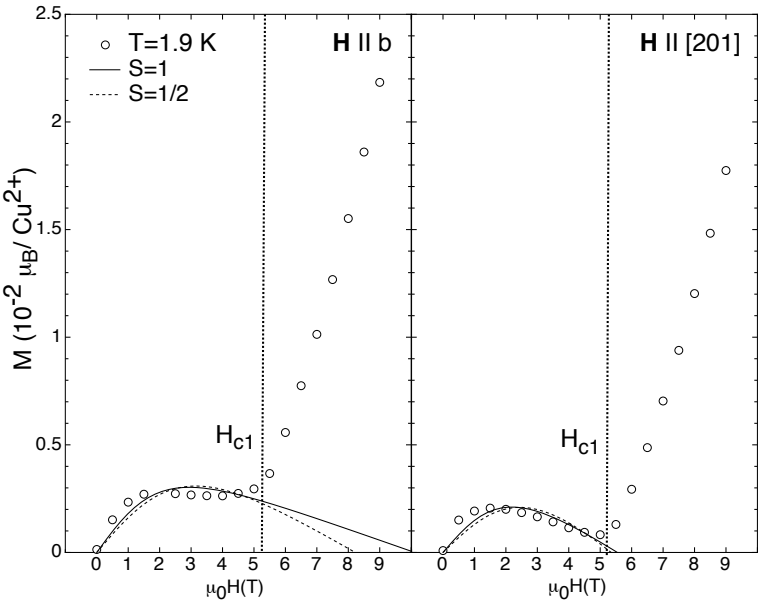


Figure 31: The magnetization $M(H)$ of $TlCuCl_3$ for $T$ = 1.9 K with $H$ applied along the crystallographic $b$-axis (left) and along [201] (right). The fits to the data were calculated using $M(H) = \chi^{dia} H + \tilde{C}_S B_S(x)$ for $S = 1$ and $S = \frac{1}{2}$, respectively.

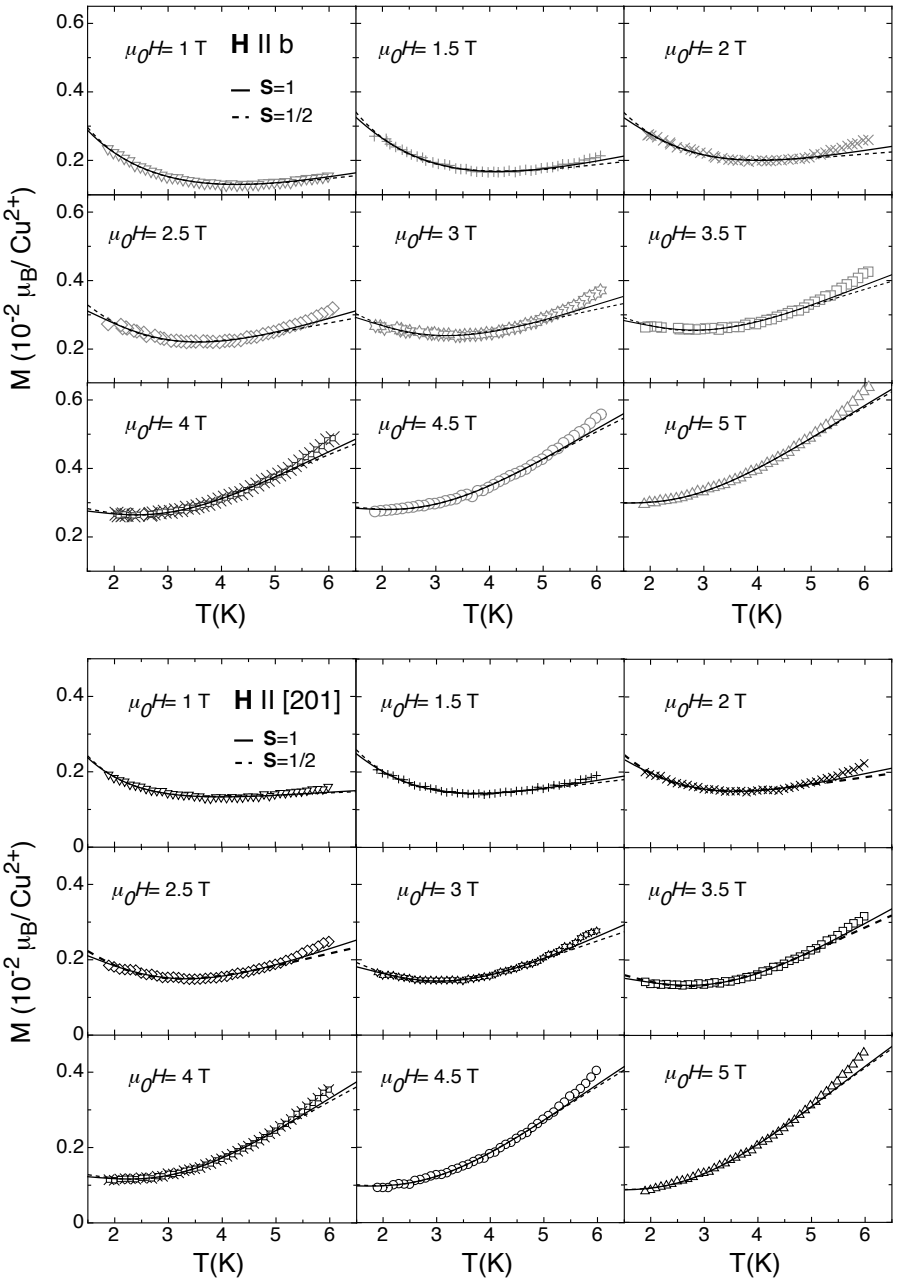


Figure 32: The magnetization $M(T)$ of $\mathrm{TlCuCl_3}$ for 1T $\leq \mu_0 H \leq$ 5 T applied along the crystallographic $b$-axis (upper frames) and along [201] (lower frames) . The continuous and the dashed lines denote fits for $S = 1$ and $S = \frac{1}{2}$, respectively (see text).

mass of the triplons), one obtains [75]

$$z(T) \approx \frac{1}{2\sqrt{\pi}} \left( \frac{\hbar^2}{2m^\star k_B T} \right)^{-\frac{1}{2}} e^{-\frac{\Delta}{k_B T}}. \tag{6.5}$$

For the magnetization per dimer we, therefore, have

$$\begin{aligned} m_{HL}(T) &= -\bar{a} \frac{\partial f}{\partial H} \\ &= d \cdot \sqrt{T} e^{-\frac{\Delta}{k_B T}} sinh \left( \frac{g \mu_B \mu_0 H}{k_B T} \right), \end{aligned} \tag{6.6a}$$

with

$$d = g \mu_B \bar{a} \sqrt{\frac{k_B m^\star}{2\pi\hbar^2}}. \tag{6.6b}$$

In order to analyze the upturn in $M(T)$ at low $T$, we include the above mentioned magnetization term

$$m_{up}(T) = g \mu_B S \cdot \beta \cdot C_S \cdot B_S \left( \frac{g \mu_B \mu_0 H}{k_B T} S \right) \begin{cases} \beta = 1 & (S = 1) \\ \beta = 2 & (S = \frac{1}{2}) \end{cases} \tag{6.7}$$

for a fixed magnetic field $H$. We distinguish between $S = \frac{1}{2}$ (non-intrinsic paramagnetic impurities, $\beta = 1/2$) and the scenario $S = 1$ (intrinsic term related to triplet states, $\beta = 1$). The constant $\beta$ is introduced here in order to count the magnetic contribution $m_{up}$ per dimer for both scenarios. We fitted the magnetization data at low enough temperatures ($T \leq 5$ K) and 1 T$\leq \mu_0 H \leq$5 T for both field directions according to

$$\begin{aligned} m(T) &= \frac{M(T)}{N_d} \\ &= m_{HL}(T) + m_{up}(T) + m_{dia} \\ &= g \mu_B \bar{a} \sqrt{\frac{k_B m^\star}{2\pi\hbar^2}} \cdot \sqrt{T} e^{-\frac{\Delta}{k_B T}} sinh \left( \frac{g \mu_B \mu_0 H}{k_B T} \right) \\ &\quad + g \mu_B S \cdot \beta \cdot C_S \cdot B_S \left( \frac{g \mu_B \mu_0 H}{k_B T} S \right) + m_{dia} \end{aligned} \tag{6.8}$$

with $g = 2.06$.

Because we were using the $T$-independent diamagnetic contribution $m_{dia} = \chi_0 H$ extracted from the high-temperature susceptibility fits presented above; it follows that only the gap $\Delta$, the constant $C_S$ (for $S$=1 or $\frac{1}{2}$) and the effective mass of a triplon $m^\star$ were fitting parameters. The corresponding fits to the magnetization data are shown in Fig. 32, while the corresponding results for the fitting parameters are presented in Fig. 33. The values for the gap $\Delta$ slightly vary with the magnetic field for both field directions around $\Delta/k_B \approx 13$ K, which is somewhat larger than $\Delta \approx 0.7$ meV = 8.3 K [106] determined by neutron scattering. The triplon mass $m^\star \approx 0.2 \cdot 10^{-29}$ kg is an order of magnitude smaller than the results obtained from

calculations and a corresponding analysis of high-field magnetization data within the Hartree-Fock approximation [150]. This discrepancy might be explained by our choice of a simplified quadratic energy-dispersion relation for this temperature region. The range of validity of a quadratic approximation is, indeed, restricted to lower temperatures ($T$ <1 K) [75, 95, 103] that are not accessible in our experiment.
The Curie-like contribution $C_S$ decreases for both cases $S$=1 and $S = \frac{1}{2}$ with increasing magnetic field $H$. For both field directions $C_S(H)$ shows a similar trend, although the variation with $H$ is much less pronounced for $S$=1. Since $C_S$ is expected to be a constant for a given magnetic-field direction, this fact already here strongly supports an $S = 1$ scenario for a correct description of the paramagnetic background. We may speculate that this Curie-like term with $S$= 1 comes from a contribution of defects in the crystal or from dimers that are situated near the crystal boundaries.

### 6.3.2 The magnetization $M(T)$ for $6\ \mathrm{T} \leq \mu_0 \mathrm{H} \leq 9\ \mathrm{T}$

The temperature dependence of the magnetization $M(T)$ along the applied magnetic field **H** shows a cusp-like minimum at a critical temperature $T_c(H)$ for fixed magnetic field $H \geq H_{c1}$, see Fig. 34 and Fig. 35. The increase of $M$ for $T < T_c$ is a consequence of the condensation of the magnetic quasiparticles and the increasing number of particles $N_c$ in the ground state forming the condensate. Theoretical arguments suggest within a simplified model a $T$-dependence of $M \propto \left(1 - \frac{T}{T_c}\right)^{\frac{3}{2}}$ for $T < T_c$ [27] which is not observed in the experimental data, however. At high magnetic fields we have, therefore, fitted the low-temperature magnetization per dimer $m(T)$ according to a more general power-law, including the diamagnetic contribution that we extracted from high-temperature magnetic-susceptibility measurements and again a net paramagnetic moment $m_{up}(T, H)$ assumed to be proportional to the Brillouin function $B_S(x)$ for $S = 1$ and $S = \frac{1}{2}$, respectively. For 6 T$\leq \mu_0 H \leq$9 T we use

$$\begin{aligned} m(T) &= \frac{M(T)}{N_d} \\ &= g\mu_B \frac{N(T)}{N_d} + m_{up}(T) + m_{dia} \\ &= g\mu_B (n_{crit} + n_0 \left(1 - \left(\frac{T}{T_c}\right)^{\alpha}\right)) \\ &\quad + g\mu_B S \cdot \beta \cdot C_S(H) \cdot B_S \left(\frac{g\mu_B \mu_0 H}{k_B T} S\right) + m_{dia} \end{aligned} \tag{6.9}$$

where $n_{crit} = N(T = T_c)/N_d$ is the critical fraction at which condensation occurs corresponding to the normalized magnetization $m(T = T_c) = g\mu_B n_{crit}$. The physical meaning of the exponent $\alpha$, see Fig. 38(b), is not discussed here, but a possible interpretation is presented below. At zero temperature we have for fixed magnetic field $H$

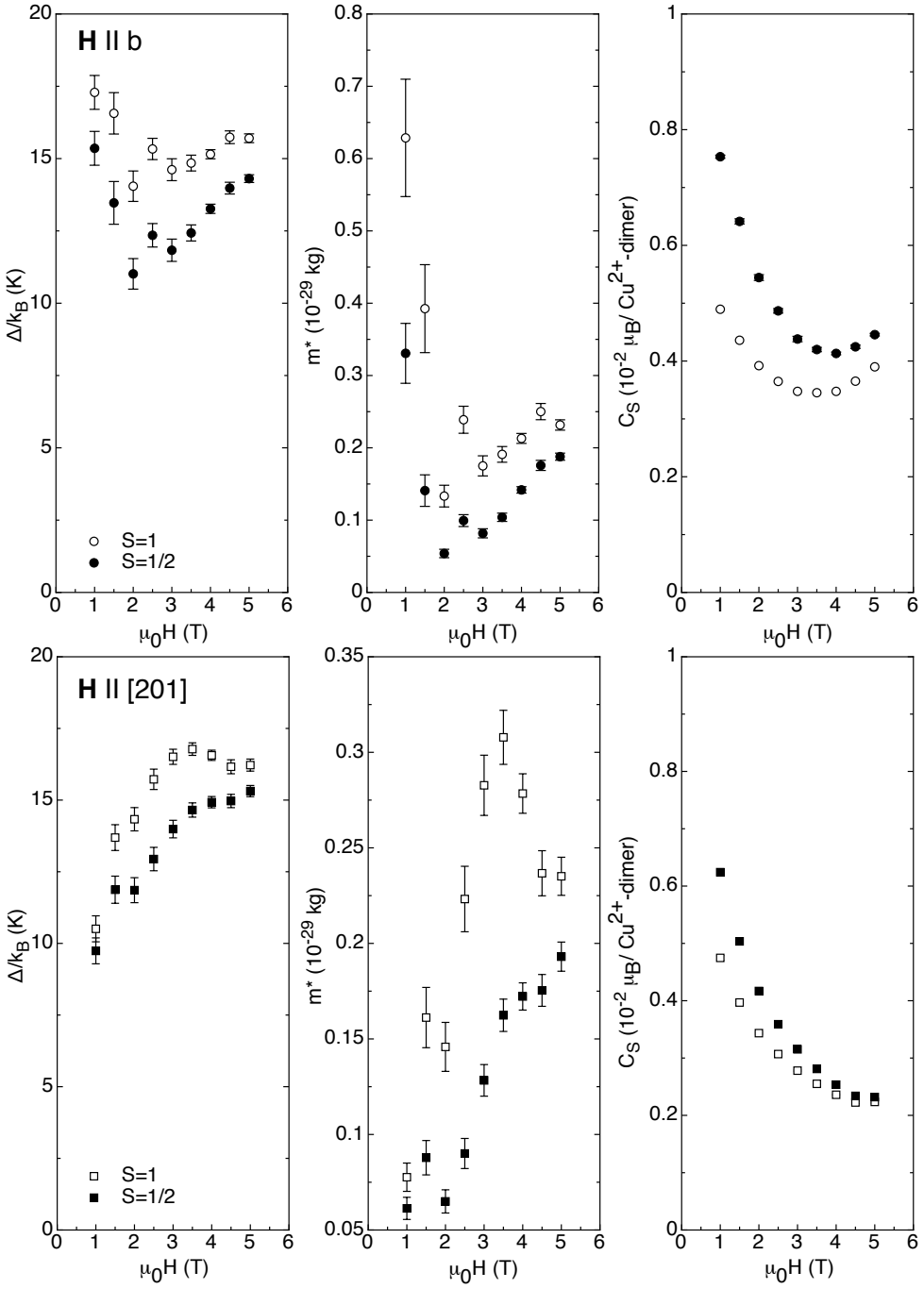


Figure 33: The parameters $\Delta$, $m^\star$ and $C_S$ extracted from fits to the low-temperature magnetization data for $H \parallel b$-axis (upper frames) and for $H \parallel$ [201] (lower frames). Different scenarios for $m_{up}$ are indicated with open marks ($S$=1) and filled marks ($S = \frac{1}{2}$), respectively. The error bars of $C_S$ are of the order of the dot size.

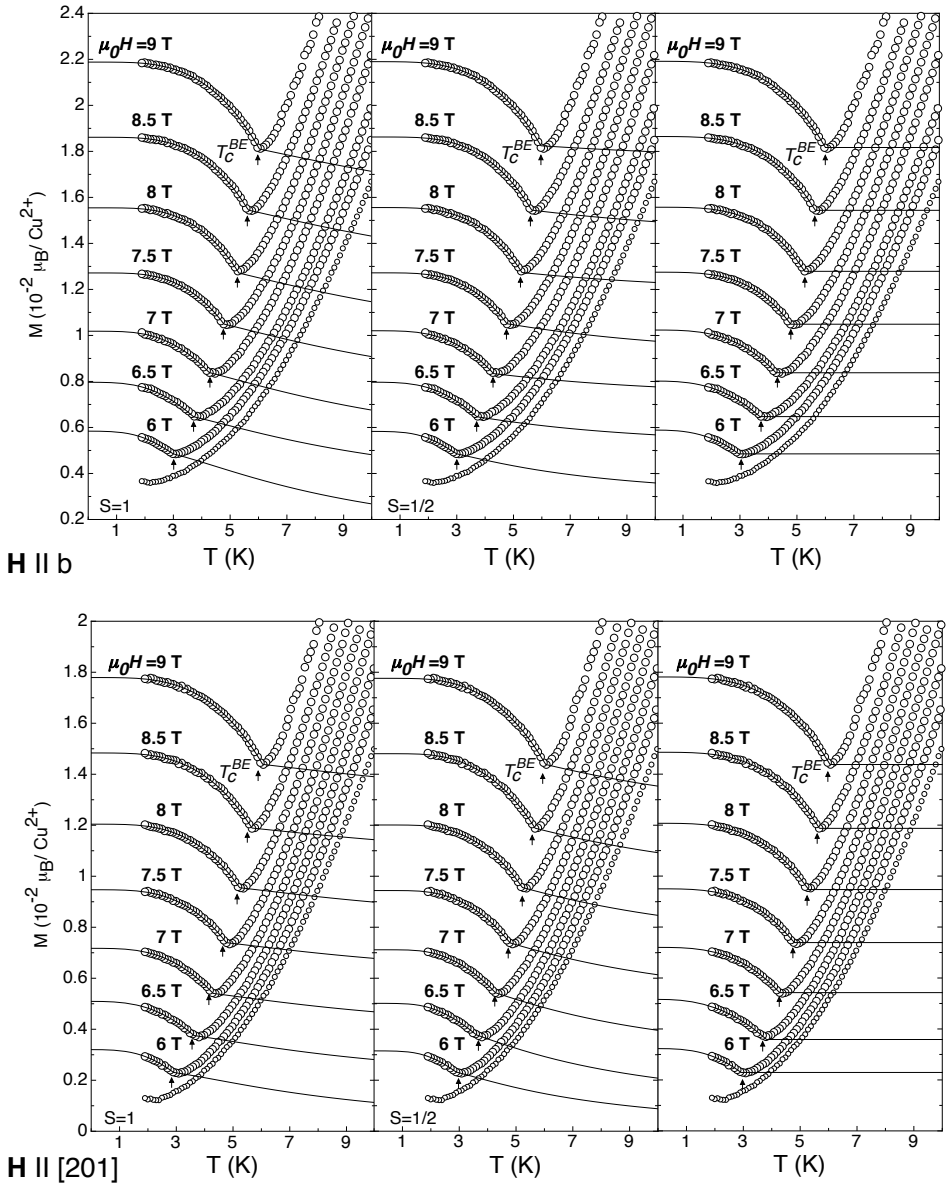


Figure 34: The magnetization $M(T)$ of $TlCuCl_3$ for 5.5 T $\leq \mu_0 H \leq$ 9 T applied along the $b$-axis (upper frames) and along [201] (lower frames). The graphs on the left and in the center show the fits for $S = 1$ and $S = \frac{1}{2}$, respectively. For the fits presented in the graphs on the right hand side no additional moment contribution ($C_S$=0) was considered. The critical temperature $T_c^{BE}$ is marked by arrows. Data taken at $\mu_0 H = 5.5$T are plotted in smaller dots.

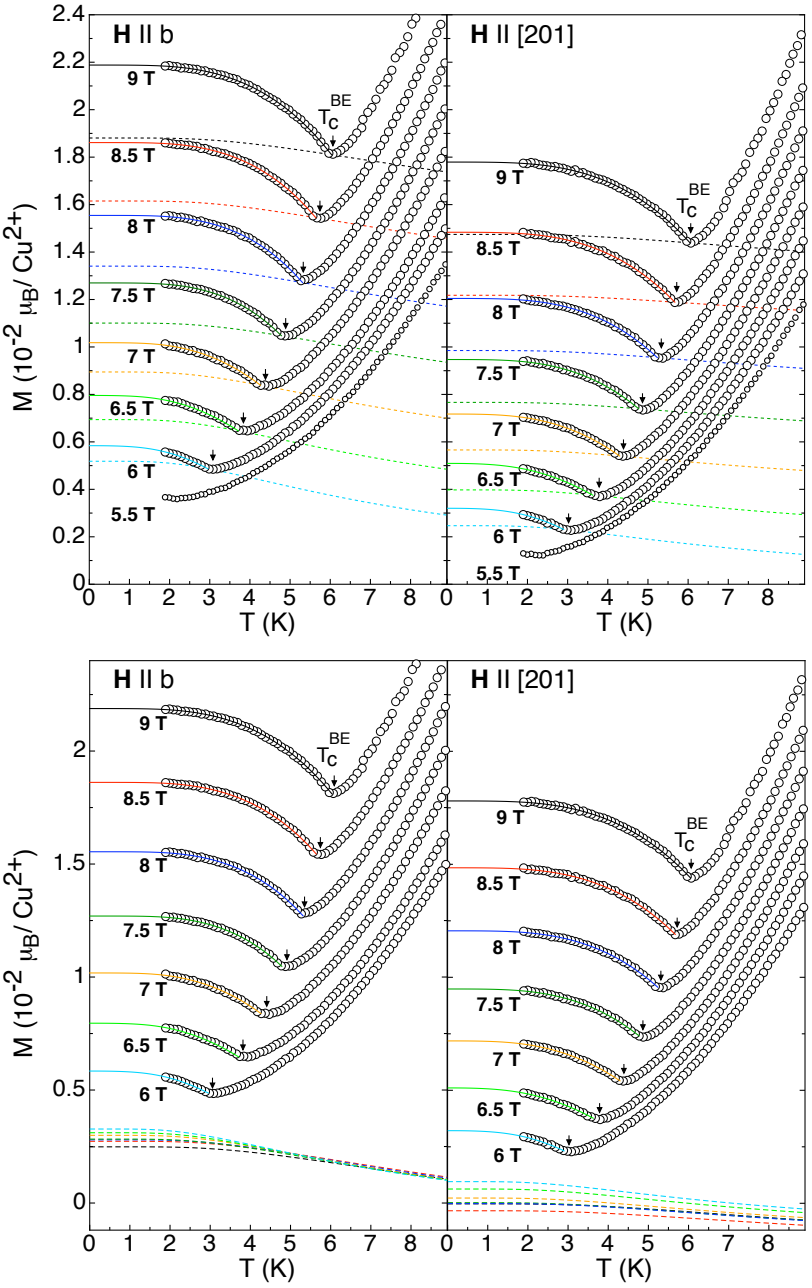


Figure 35: The magnetization $M(T)$ of $TlCuCl_3$ for 5.5 T $\leq \mu_0 H \leq$ 9 T applied along the $b$-axis (frames on the left) and along [201] (frames on the right), respectively. The solid lines in the graphs on the top and in the center represent the fits to the data using the function $m(T < T_c^{BE})$ for $S = 1$ at fixed magnetic field. The dashed lines represent the same function $m(T)$ with $n_0 = 0$ (top) and $n_0 = n_{crit} = 0$ (bottom), respectively. For this latter case the dashed curves correspond to the background contribution $m_{up}(T) + m_{dia}$.

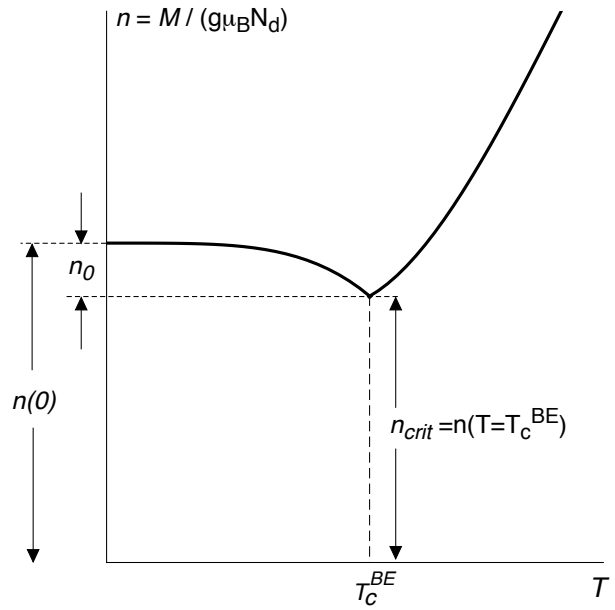


Figure 36: A sketch of the magnetization $M(T)$ of $\mathrm{TlCuCl_3}$ expressed in terms of the triplon density $n$ (see text).

$$\begin{aligned} m(T=0) &= g\mu_B(n_{crit}+n_0) + m_{up}(T=0) + m_{dia} \\ &= g\mu_B n(0) + m_{up}(T=0) + m_{dia} \end{aligned} \tag{6.10}$$

with the total triplon fraction at $T = 0$, $n(0) = n_{crit} + n_0$. In Fig. 36, the corresponding quantities are represented in an illustrative sketch.

For an ideal Bose gas, $n(0)$ corresponds to the total condensate particle density at T=0. As soon as interactions between the particles are considered, the depletion of the condensate has to be taken into account. The quantity

$$n(0) = n_c(0) + \tilde{n}(0) \tag{6.11}$$

is then a sum of the condensate fraction $n_c(0)$ and the density of noncondensed fraction $\tilde{n}(0)$. The latter term represents the number of triplons per $Cu^{2+}$ dimer scattered out of the ground state due to the interactions between the particles. It depends on the number of condensed particles and can be expressed as [27]

$$\tilde{n}(0) = \frac{1}{3\pi^2}\left(\frac{m^\star \bar{a}^2 V_0 n_c(0)}{\hbar^2}\right)^{\frac{3}{2}}, \tag{6.12}$$

where $m^\star \approx 2.8 \times 10^{-29}$ kg is the mass of a triplon and $V_0/k_B \approx 315$ K [150] is the two-particle interaction potential. Replacing $\tilde{n}(0)$ in Eq. (6.11) with the expression in Eq. (6.12), we obtain

$$n(0) = n_c(0) + \frac{1}{3\pi^2}\left(\frac{m^\star \bar{a}^2 V_0 n_c(0)}{\hbar^2}\right)^{\frac{3}{2}}. \tag{6.13}$$

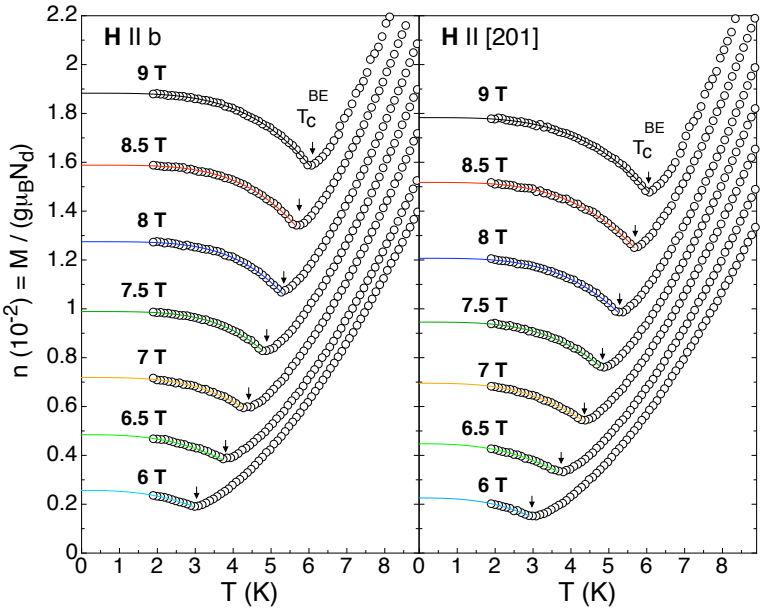


Figure 37: The triplon density $n(T)$ of $TlCuCl_3$ for 5.5 T $\leq \mu_0 H \leq$ 9 T applied along the $b$-axis (left) and along [201] (right), respectively. The triplon fraction $n$ corresponds to the corrected magnetization data with subtracted background. Fits correspond to the function $m(T < T_c^{BE})/g\mu_B N_d$ setting $m_{up} = m_{dia} = 0$. The critical temperature $T_c^{BE}$ is marked by arrows.

From our fits, see Fig. 37, according to Eq. (6.9) and with $n(0) = n_{crit} + n_0$ we can now calculate the condensate fraction at zero temperature $n_c(0)$ for various magnetic fields using Eq. (6.13), see Fig. 38(a).

As one would expect from simple arguments [27, 150], $n_c(0)$ increases with increasing magnetic field. It is essential to note that the number of triplons $N_c(0) = n_c(0) \cdot N_d$ forming the condensate at $T = 0$ is the same for both field directions only in the $S = 1$ scenario for $m_{up}(T)$, see Fig. 39, and only in this scenario $n_c(0)$ extrapolates to zero at the correct critical field $\mu_0 H_{c1} \approx$ 5.5 T. These facts again strongly support our hypothesis that $m_{up}(T)$ is intrinsic with $S = 1$, and it confirms the interpretation of the magnetic field **H** acting as the chemical potential [94]. Right above the critical field $H_{c1}$ the percentage of the condensed particles $n_c(0)$ with respect to the total density of triplons $n(0)$ is approximately 98% and slightly decreases with increasing magnetic field, see Fig. 40. This result is consistent with a similarly low, noncondensed magnon density as calculated in Ref. [95], where $\tilde{n}(0)$ increases from zero for $H = H_{c1}$ to approximately 7% of the total triplon density at $T$ = 0 in $\mu_0 H = 7$ T. From the high percentage of condensed particles we can confirm that the triplons in $TlCuCl_3$ form a *weakly-interacting Bose gas* [95] right above $H_{c1}$, and that the interaction increases with increasing particle density, i.e. with increasing the magnetic field $H$.

Finally, we want to mention that the Curie-like contribution $C_S$ is small and essentially con-

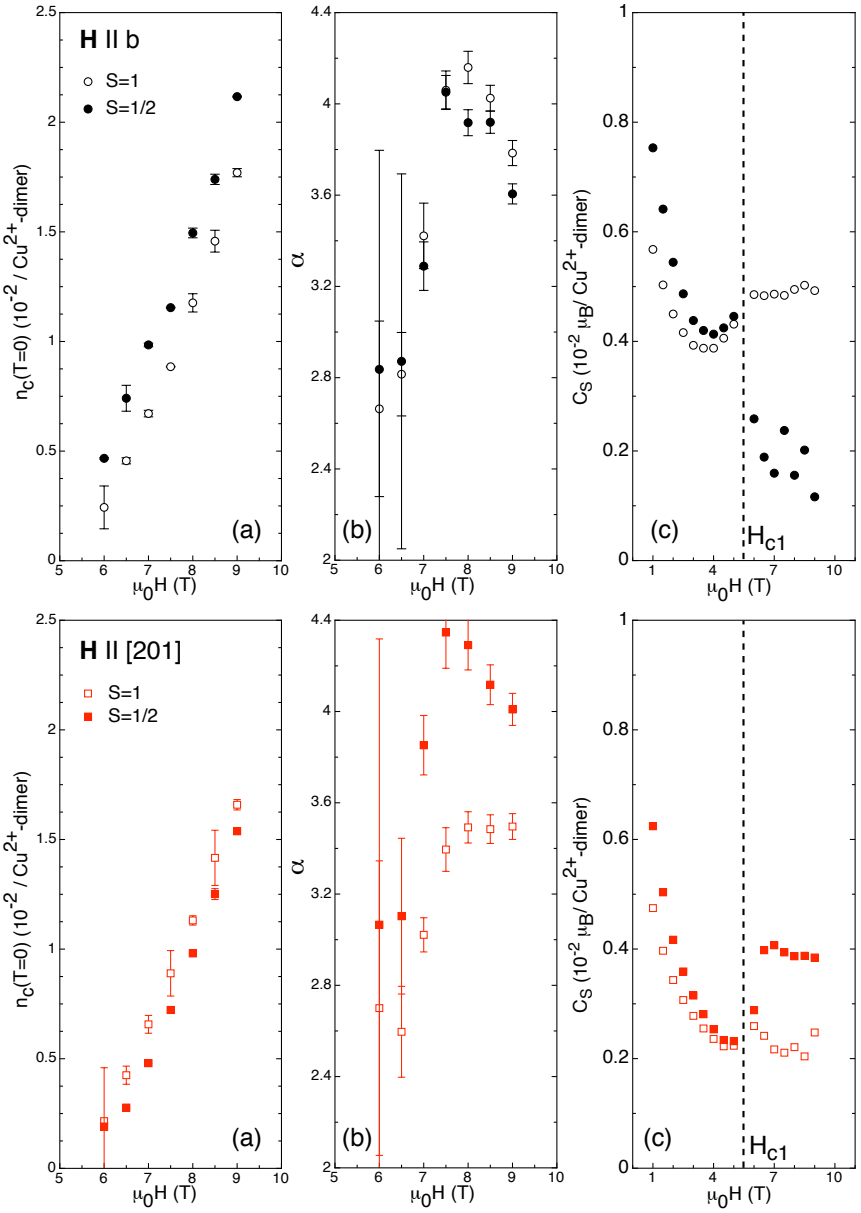


Figure 38: The condensate fraction $n_c(T=0)$ (a), the exponent $\alpha$ (b) and the Curie- like contribution $C_S$ (c) for $H \parallel b$ (upper frames) and for $H \parallel$ [201] (lower frames). Different scenarios for $m_{up}$ are indicated with open marks ($S$=1) and filled marks ($S = \frac{1}{2}$), respectively. The error bars of $C_S$ are of the order of the dot size.

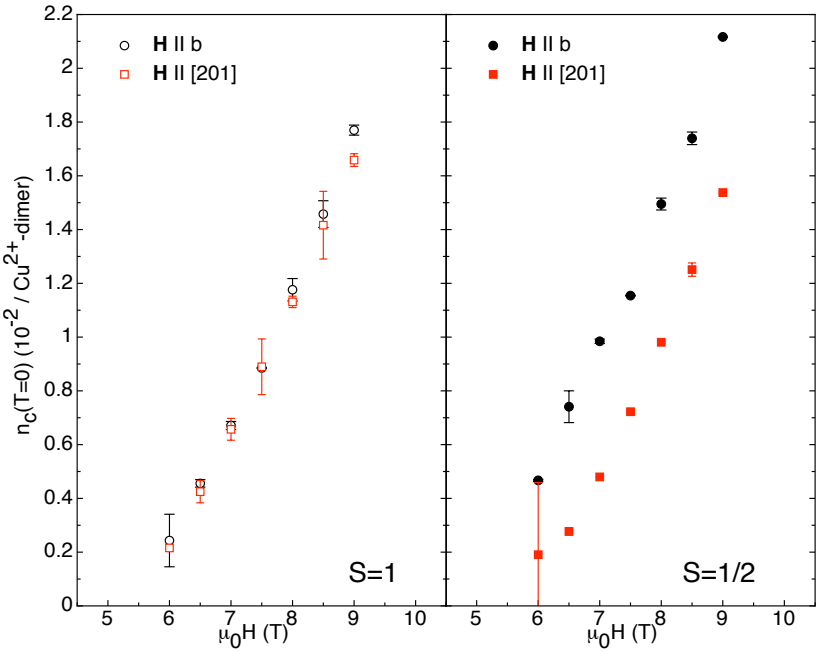


Figure 39: The condensate fraction $n_c(T = 0)$ with different scenarios for $m_{up}$ (left: $S = 1$, right: $S = \frac{1}{2}$).

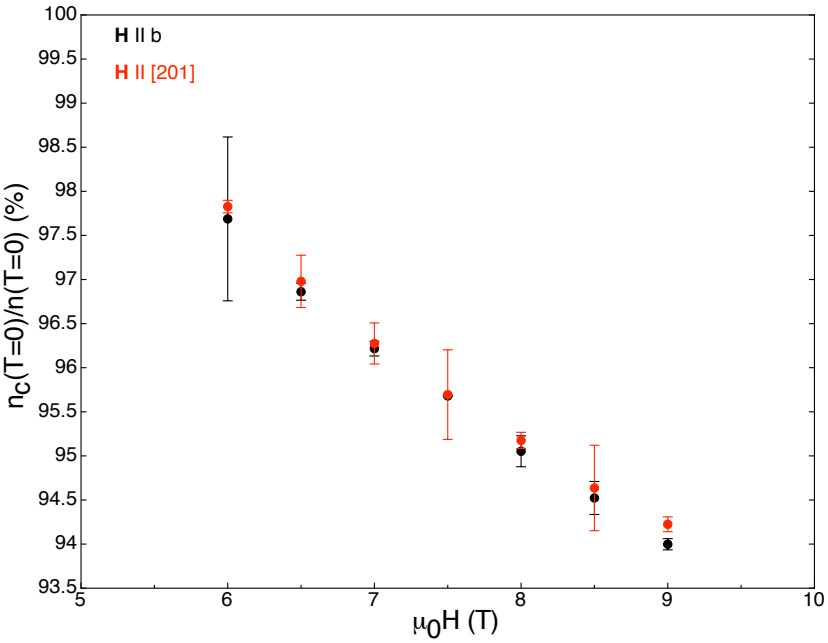


Figure 40: The triplon ratio $n_c(0)/n(0)$ forming the condensate in the $S = 1$ scenario for $m_{up}$.

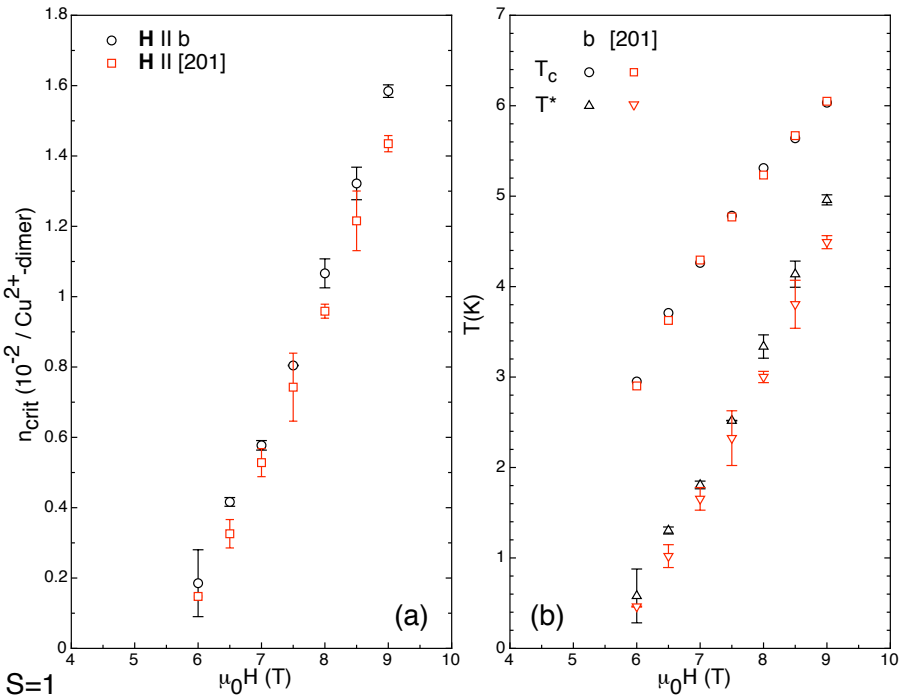


Figure 41: The critical triplon fraction $n_{crit}$ (a) and the corresponding typical temperatures $T^* \approx n_{crit}V_0/k_{\rm B} < T_c$ (b) in the $S = 1$ scenario for $m_{up}$ as functions of the applied magnetic field for $\mathbf{H} \parallel b$ (circles and upward triangles) and $\mathbf{H} \parallel [201]$ (squares and downward triangles), respectively.

stant for $H > H_{c1}$ in both the $S = \frac{1}{2}$ and the $S = 1$ scenarios, see Fig. 38(c). However, the corresponding data for $S = 1$ are more or less smooth continuations of the respective data for $H < H_{c1}$, in very contrast to the $C_S$ data for $S = \frac{1}{2}$ that show a discontinuity around $H = H_{c1}$, see Fig. 38(c). The comparably moderate variation of $C_S$ with $H$ over the whole considered range of magnetic fields for the $S = 1$ scenario (covering both the normal phase and the BEC obeying an entirely different physics) may indicate that $C_S$ is indeed a constant for each magnetic-field direction, and that our interpretation of a $S = 1$ paramagnetic background is correct.

We can conclude that the percentage of $n_c(0)$ with respect to the total fraction of triplons $n(0)$ is approximately 98% right above the critical field $H_{c1}$ and slightly decreases with an increasing magnetic field. We demonstrated that this fraction is the same for both $\mathbf{H} \parallel b$ and $\mathbf{H} \parallel [201]$ if we assume the presence of a small number of intrinsic $S = 1$ magnetic moments that are not part of the Bose-Einstein condensate of triplons even at the lowest temperatures.

### 6.3.3 The exponent $\alpha$

We want to emphasize that we do not interpret the exponent $\alpha$ in the power-law approach (Eq. (6.9)) used for fitting the low-temperature magnetization data at high magnetic fields as a

universal critical exponent. In this sense its physical meaning is not clear.
In general, the normalfluid density in a dilute Bose gas in the condensed phase is proportional to $T^4$ at low enough temperatures ($T \ll T^* \approx nV_0/k_\mathrm{B}$), where $n$ is the total particle fraction and $V_0$ the interaction energy.
In the case of $\mathrm{TlCuCl_3}$ we can estimate $T^*$ by replacing $n \cong n_{crit}$ and $V_0/k_B \approx 313$ K [103], see Fig. 41. The values for $\alpha$ extracted from the fits, see Fig. 38(b), vary around $\alpha \sim 4$ with a decreasing tendency and increasing fitting error as $H \to H_{c1}$. This can be explained by the fact that for high magnetic fields $T^*$ is fairly close to $T_c$, whereas for low magnetic fields the difference between the two characteristic temperatures increases, thereby restricting the validity of the $T^4$- power law to very low temperatures that are not accessible in our experiment. Nevertheless, it is clear that the increasing magnetization for $T \to 0$ is related to the increasing fraction of the condensed particles $n_c(T)$. The evaluation of $n(0)$ from our phenomenological power law, see Eq. (6.9), and the calculation of $n_c(0)$ using Eq. (6.13) gives, in any case, a reliable estimate of the intercept of $n_c(T)$ at $T = 0$, irrespective of the correct functional form of $n_c(T)$.

## 6.4 The Bose-Einstein condensation of triplons within the Hartree-Fock (HF) approximation

Within the HF approximation the low-density triplon gas is described by the Hamiltonian

$$\hat{H} = \sum_{\mathbf{k}} (\varepsilon_{\mathbf{k}} - \mu) a^\dagger_{\mathbf{k}} a_{\mathbf{k}} + \frac{v_0}{2} \sum_{\mathbf{k}\acute{\mathbf{k}}\mathbf{q}} a^\dagger_{\mathbf{k}+\mathbf{q}} a^\dagger_{\acute{\mathbf{k}}-\mathbf{q}} a_{\acute{\mathbf{k}}} a_{\mathbf{k}}, \tag{6.14}$$

see Eq. (2.61), where $\varepsilon_{\mathbf{k}}$ is the kinetic energy determined at lowest excitation point $\mathbf{Q_0}$ [rlu], $\mu = g\mu_B(H - H_{c1})$ is the chemical potential and $v_0 = V_0 \cdot \Omega$ is the amplitude [103, 150] of the interaction (contact) potential $V(\mathbf{r}) = v_0\delta(\mathbf{r})$. This is a good approximation in the low-density limit, since only single-triplon scattering processes can be considered. It follows then that this expression is then independent of the moment and the amplitude of the interaction potential $v_0 = \frac{4\pi\hbar^2 a_s}{m}$ is proportional to the $s$-wave scattering length $a_s$ [12].
The momentum distribution of the triplons, see App. D and [27], is given by

$$\begin{aligned} n_k = \langle a^\dagger_{\mathbf{k}} a_{\mathbf{k}} \rangle &= \frac{1}{exp(\frac{\varepsilon_{\mathbf{k}} - \mu_{eff}}{k_\mathrm{B}T}) - 1}, \quad \text{with} \\ \varepsilon_{\mathbf{k}} &= \frac{\hbar^2 k^2}{2m} \quad \text{and} \\ \mu_{eff} &= \mu - 2v_0 n, \end{aligned} \tag{6.15}$$

whereby $n' = \frac{N}{N_d \Omega}$ is the total triplon-fraction density, normed on the total number of dimer $N_d$ with $N$ being the absolute total number of triplons and $\Omega$ defined as the particle volume.

[12] For hard-sphere-bosons, $a_s$ corresponds to the diameter of the particles.

Note that for a a triplon gas the absolute number of excited particles is normed on the absolute number dimers $N_d$ present in the system. By definition $n'$ corresponds to

$$\begin{aligned} n' &= \frac{1}{(2\pi)^3}\int n_k d^3k \\ &= \left(\frac{m^\star k_\mathrm{B} T}{2\pi\hbar^2}\right)^{\frac{3}{2}} g_{3/2}(z), \quad \text{with} \\ z &:= e^{\frac{\mu_{eff}}{k_\mathrm{B}T}} \end{aligned} \tag{6.16}$$

and $m^\star$ being the effective triplon mass, see Eq. (2.18) and Eq. (2.23). BEC occurs when $\mu_{eff}$ vanishes, which implicates $\mu = 2v_0 n'$ and $z = 1$. Setting

$$\mu = g\mu_B[H(T) - H_{c1}] = 2v_0 n', \tag{6.17}$$

it results

$$\mu_c = g\mu_B[H_c(T) - H_{c1}] = 2v_0 n'(z = 1, T_c^{BE}) = 2v_0 n'_{crit} =: 2V_0 n_{crit}, \tag{6.18a}$$

where $n_{crit}(T)$ corresponds to the triplon fraction at the transition temperature $T = T_c^{BE}$ defined by the minimum of the magnetization $m_{crit} := \frac{M(T_c^{BE})}{N_d} = g\mu_B n_{crit}$. Using Eq. (6.16), we obtain

$$\mu_c = 2v_0 \left(\frac{m^\star k_\mathrm{B} T}{2\pi\hbar^2}\right)^{\frac{3}{2}} \underbrace{g_{3/2}(1)}_{2.616}. \tag{6.18b}$$

Within the HF-approximation [27] the phase boundary is, therefore, described by

$$\begin{aligned} \frac{g}{2}[H_c(T) - H_{c1}] &= AT^\phi, \quad \text{with} \\ H_{c1} &= H_c(T = 0\ \mathrm{K}), \\ A &= \frac{2.616 v_0}{\mu_B}\left(\frac{m^\star k_B}{2\pi\hbar^2}\right)^{\frac{3}{2}} \quad \text{and} \\ \phi &= \frac{3}{2}. \end{aligned} \tag{6.19}$$

A linear relation between $H_c(T)$ and $n_{crit}(T)$ is expected, see Eq. (6.18a). This is indeed confirmed up to experimental data taken at low triplon-densities [95], i.e. at low magnetic fields, see Fig. 42. At larger triplon fractions this dependence starts to deviate from linearity. This discrepancy might be explained by the fact that at higher triplon fractions the scenario of a weakly-interacting Bose gas is no longer justified [95]. The values obtained for the critical fields $H_{c1}$ are in good agreement with previous results [27, 103, 106]. From the linearity constant $A$, see Eq. (6.19), we can estimate the absolute value of the interaction potential $V_0 = \frac{v_0}{\Omega}$. We will, thereby, use the approximation introduced by *Yamada et al.* [150], where $\Omega = \bar{a}^3$, with $\bar{a} = [a \cdot b \cdot c \cdot sin(\beta)]^{\frac{1}{3}}$ the average lattice constant and $a$, $b$, $c$ and $\beta$ the corresponding

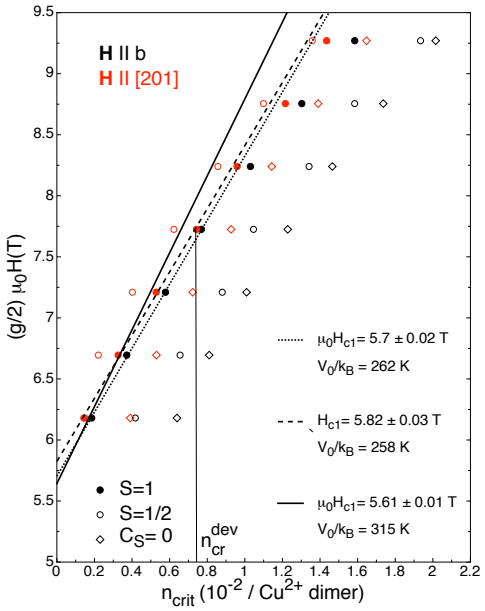


Figure 42: The dependence of critical field $H_c(T)$ (normalized on the respective g-factors of the two magnetic-field directions) on the critical fraction $n_{crit}$. Different background contributions were considered (see text). Divers fits were calculated using Eq. (6.18a). For $n > n_{cr}^{dev}$ the critical field $H_{c1}$ no longer increases linearly with $n_{crit}$.

lattice parameters for $TlCuCl_3$ [13].

We present three different fits corresponding to three different values of the constant $A$. Within the $S = 1$-background scenario and using a parabolic dispersion relation [27] we obtain a value of $\frac{V_0}{k_B} \approx 262$ K, see Fig. 42. Using a realistic dispersion relation in Eq. (6.15) [103], *Yamada et al.* obtained the slightly larger value $\frac{V_0}{k_B} = 315$ K [150].

As predicted by the HF- approximation, see Eq. (6.19), the phase transition is independent of the magnetic field direction, see Fig. 43. Using Eq. (6.19) to fit the data in the temperature range up to $T_{max} \sim 6$ K, we analyze the phase boundary for $\mathbf{H} \parallel b$ and $\mathbf{H} \parallel [201]$, respectively. Keeping the value for the interaction potential $V_0$ fixed, we can determine the effective mass of triplon $m^\star$. The best fits were obtained for $\mu_0 H_{c1}$= 5.3 T, $\phi = 2.2$ with $m^\star = 1.27 \cdot 10^{-29}$ kg and $\mu_0 H_{c1}$= 4.6 T , $\phi = 1.6$ with $m^\star = 2.81 \cdot 10^{-29}$ kg, respectively.

The value of the critical exponent $\phi$ predicted by the HF-approximation, considering a parabolic energy dispersion relation of the triplons [27], is $\phi = 1.5$. We get a slightly larger value $\phi = 1.6$ but with a corresponding rather unreasonable critical field $\mu_0 H_{c1} = 4.6$ T. However, the value obtained for the mass $m^\star = 2.81 \cdot 10^{-29}$ kg is in good agreement with former results derived from the curvature of the energy dispersion $m^\star = 3.4 \cdot 10^{-29}$ kg [103]. Considering a slightly lighter triplon mass $m^\star = 1.27 \cdot 10^{-29}$ kg, we obtain a larger value of the critical

[13] However, this approximation is a little bit controversial, since for $TlCuCl_3$ there are two dimers per unit cell

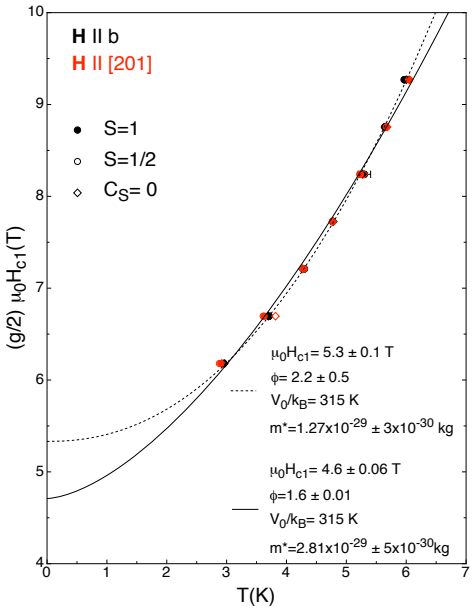


Figure 43: The temperature-dependence of the critical magnetic field $H_{c1}$ in $TlCuCl_3$ for two different field directions normalized on the $g$-factors, respectively. Different background scenarios were considered. The solid black and dashed curves corresponds to fits to the data for $g_{[010]}$=$g_{[201]}$=2.06 [145]) using Eq. (6.19), respectively. The error bars are in the order of magnitude of the dot sizes.

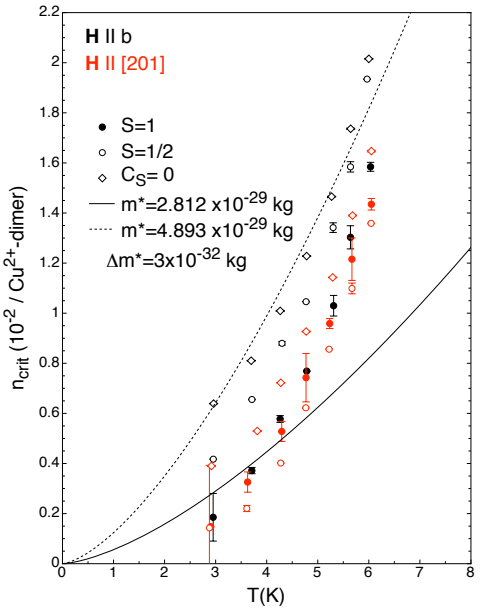


Figure 44: The temperature-dependence of the critical triplon-fraction density $n_{cr}$ for two magnetic-field directions. Different background scenarios were considered. The solid and dashed curves represent fits to the data obtained within the $S = 1$- and $S = \frac{1}{2}$-background scenario, respectively. For the $S = 1$ case only data points for $T < 5$ K were included. The effective mass of a triplon results to be in the order of $m^\star \approx 10^{-29}$ kg.

exponent $\phi = 2.2$ and a corresponding critical field $\mu_0 H_{c1} = 5.3$ T, which is consistent with the value extracted from neutron scattering experiments [106, 145].

Nevertheless, our overestimation of the critical exponent $\phi$ is consistent with other (magnetization) measurements [27, 95, 103, 115, 116], see Table 4. The reason for this discrepancy is not quite clear yet, but it is assumed to be manifold. *Sherman et al.* [108] argued that a more realistic dispersion relation for the triplons has to be considered. They assumed a "relativistic" dispersion $\varepsilon_{\mathbf{k}} = \sqrt{\Delta^2 + c\mathbf{k}^2}$, which is usually significant in case $T_c^{BE}$ is of the same order of magnitude as the excitation gap $\Delta$, as it is indeed the case for $TlCuCl_3$ . In fact, the deviation of the dispersion curve from the parabolic form gives rise to the experimental, smaller critical exponent [103]. *Nohadani et al.* [151] argued that $\phi$ decreases with decreasing fitting temperature range due to temperature-driven renormalization of the effective mass of the triplons.

The value of the triplon mass $m^\star$ can also be derived from the temperature-dependence of critical triplon-fraction density $n'_{crit}(T) = \left(\frac{m^\star k_B T}{2\pi\hbar^2}\right)^{\frac{3}{2}} 2.616$, see Eq. (6.18b) and Fig. 44. From

corresponding fits, we cannot exactly determine the absolute value of $m^\star$. We can, however, restrict its value to $2.8\times10^{-29}$ kg to $4.9\times10^{-29}$ kg, depending on the fitting range, and considered $S=1$- or $S=\frac{1}{2}$ background-contribution scenario, respectively. The smaller value of the effective mass $m^\star$ is obtained by fitting the data at lower temperatures ($T<5$ K) considering only the $S=1$-background contribution. In this temperature range the parabolic dispersion relation is assumed to be more accurate [151]. The larger value of $m^\star$ has been obtained by taking the $S=\frac{1}{2}$ background-contribution into account.
To summarize, the calculated triplon mass $m^\star$ is roughly $\frac{1}{60}$ of a proton mass. Qualitatively speaking, the relative light mass of these magnetic quasiparticles compensates the relatively low critical particle fractions $n_{crit}\sim10^{-2}$ making the occurrence of BEC in such low-dimensional spin systems with $T_c^{BE}\sim\frac{n}{m^\star}$, see Eq. (2.28), at helium temperatures possible.

### 6.4.1 The Bose-Einstein condensation of a dilute Bose gas

Generally, the concept of BEC in a dilute, weakly-interacting Bose gas becomes valid only if the particle number per unit volume $n'=\frac{N}{N_d\Omega}$ is small. More precisely, the average distance between two interacting particles $l\sim n'^{-\frac{1}{3}}$ should be much larger than the s-wave scattering length $a_s$, which is the characteristic length scale representing the wideness of the influence of the repulsive potential $V_0$. This implicates that

$$\frac{a_s}{l}\sim n'^{\frac{1}{3}}a_s\ll 1. \tag{6.20}$$

In the case of $\mathrm{TlCuCl_3}$ there are two dimers per unit cell volume $\Omega_{uc}$, see Fig. 26. This defines the unit volume $\Omega$ accordingly to

$$\frac{2}{\Omega_{uc}}=\frac{1}{\Omega} \tag{6.21a}$$

and, therefore,

$$\Omega=\frac{\Omega_{uc}}{2}. \tag{6.21b}$$

The interaction amplitude $v_0$ can be expressed as

$$\begin{aligned} v_0 &= V_0\cdot\Omega \\ &= \frac{V_0\Omega_{uc}}{2} := \frac{4\pi\hbar^2 a_s}{m^\star}. \end{aligned} \tag{6.22}$$

This defines the s-wave scattering length for the triplon gas in $\mathrm{TlCuCl_3}$ to

$$\begin{aligned} a_s &= \frac{V_0\Omega_{uc}m^\star}{8\pi\hbar^2} \\ &\approx 6.1\text{Å}. \end{aligned} \tag{6.23}$$

Using Eq. (6.20) and Eq. (6.21b), we find

$$\begin{aligned} n' &= \frac{N}{N_d \Omega} = \frac{2N}{\Omega_{uc} N_d} \\ &= \frac{2n}{\Omega_{uc}} \end{aligned} \tag{6.24}$$

which included in the condition for diluteness, see Eq. (6.20), leads to

$$\left(\frac{2n}{\Omega_{uc}}\right)^{\frac{1}{3}} \cdot a_s \ll 1 \quad \text{or} \tag{6.25a}$$

$$n^{\frac{1}{3}} \ll 0.97 \tag{6.25b}$$

$$\text{whereby we used} \quad \Omega_{uc} = a \cdot b \cdot c \cdot sin(\beta) = 500.3 \mathring{A}^3. \tag{6.25c}$$

Therefore, Eq. (6.25) represents the condition for which the consideration of a triplon gas as a weakly interacting Bose gas is still valid. From Fig. 42 we extract $n_{cr}^{dev}(\mu_0 H \approx 7.7$ T) $\approx 7.3 \cdot 10^{-3}$ as the critical value where the dependence of the critical field $H_{c1}$ on the critical triplon fraction $n_{crit}$ starts to deviate from linearity. As expected, $n_{cr}^{dev}$ satisfies Eq. (6.25b). In this sense the triplon gas in $\mathrm{TlCuCl_3}$ can be studied analytically within the scenario of BEC in a weakly-interacting Bose gas up to $\mu_0 H \approx 7.7$ T.

## 6.5 $U(1)$-Symmetry breaking and violation of axial symmetry

In recent years various scenarios for the consequences of anisotropy on the properties of a magnetic BEC have been discussed in detail [32, 95, 152, 153]. The presence of any kind of anisotropy will, in principle, explicitly break the rotational symmetry of the bosonic system [95]. The degree of spontaneous $U(1)$-symmetry breaking then depends on the order of magnitude of the anisotropic terms compared to the energy scale associated with the isotropic interactions of the Bose gas [153]. The relatively large triplon bandwidth in $\mathrm{TlCuCl_3}$ [106] exceeds the spin-nonconserving terms, such as an intradimer exchange (IE) anisotropy and a Dzyaloshinsky-Moriya (DM) anisotropy, by more than two orders of magnitude [32, 95, 152]. Nonetheless, the question to what extent the existing anisotropies in $\mathrm{TlCuCl_3}$ do affect the magnetic phase diagram, the Goldstone mode and other measurable quantities of $\mathrm{TlCuCl_3}$ are still issues under investigation [32, 95, 152, 154].

By taking a perturbative anisotropy term into account we will consider in the following the influence of an IE-like anisotropy that explicitly violates the axial symmetry, and we will study a few consequences on the condensate phase of $\mathrm{TlCuCl_3}$. Fatal consequences concerning the experimental observation of such a magnetic condensate can be drawn that may even be valid for other similar spin systems in general. The influence of a possible DM-like anisotropy

[95, 107] is not considered here [155]. Based on an energy consideration we will then argue that, as a consequence of an unavoidable magnetoelastic coupling, even an axially symmetric magnetic system is unstable towards a spontaneous violation of this symmetry as soon as the BEC-state is formed.

We describe the condensate at $T$ = 0 K with a macroscopic wave function, a complex scalar field $\hat{\psi}(\mathbf{r}, \mathbf{t})$ that determines the condensate fraction $n_c(0) = \psi^\dagger\psi$, where $\psi^\dagger$ is the complex conjugate of $\psi$. Standard functional methods used to describe a dilute Bose gas in the classical limit at $T$ = 0 yield an extremity condition [156] for the potential energy per dimer, namely

$$u(\psi) = -\mu\psi^\dagger\psi + \frac{v_0}{2}\left(\psi^\dagger\psi\right)^2_{|_{\psi=\psi_0}} = min., \tag{6.26}$$

where $\mu$ is the chemical potential and $v_0$ is a constant related to a repulsive short-range interaction, e.g. to a delta-function potential $V(\mathbf{r}) = v_0\delta(\mathbf{r})$ [157]. The minimum value $\psi_0$ then determines the condensate fraction $n_c(0) = \psi_0^\dagger\psi_0$, here defined as $n_c(0) = N_c/N_d$ with $N_c$ the number of condensed triplons and $N_d$ the number of dimers.

In the case of an explicitly violated axial symmetry we may include a perturbation term $|\tilde{\gamma}|\left(\psi\psi + \psi^\dagger\psi^\dagger\right)$ [26, 95] to the potential energy that can arise in a real magnetic system from various sources such as anisotropic intra- and interdimer interaction constants $J$ and $\tilde{J}$, respectively. For $TlCuCl_3$ we have, for example, $\mu_0 H_{c1} \approx$ 5.6 T [96], $v_0/k_B$ = 315 K [150], and an absolute value $|\tilde{\gamma}|$ of the order of 0.01 meV [95, 152], depending on the orientation of the magnetic field $\mathbf{H}$ with respect to the crystal lattice [152]. Such an anisotropy term may arise from a pre-existing violated axial symmetry of the system, or from a spontaneous distortion at the magnetic phase transition that we will discuss below. We, therefore, have to minimize

$$u(\psi) = -\mu\psi^\dagger\psi + |\tilde{\gamma}|\left(\psi\psi + \psi^\dagger\psi^\dagger\right) + \frac{v_0}{2}\left(\psi^\dagger\psi\right)^2, \tag{6.27}$$

where we assume that $H_{c1}$ itself is at first unchanged by the presence of the small perturbative anisotropy $|\tilde{\gamma}| \ll \Delta$.

### 6.5.1 Comparison with results from Hartree-Fock calculations

Without any explicit anisotropy ($i.e., |\tilde{\gamma}| = 0$) we obtain the well-known minimum value $\psi_0^\dagger\psi_0$ = $n_c(0)$ = $\mu/v_0$ [27]. The phase $\phi$ of $\psi_0 = |\psi_0|e^{i\phi}$ is not fixed in this case, leading to the $u(\psi)$ landscape sketched in Fig. 45 (left panel, "mexican-hat potential"). However, any nonzero value for $|\tilde{\gamma}|$ locks the phase of $\psi_0$ to the imaginary axis (i.e., $\phi = \pm\pi/2$ and therefore $\psi_0$=const), and leads to an optimum value $n_c(0) = (\mu + 2|\tilde{\gamma}|)/v_0$ in a "Napoleon's hat potential" (see Fig. 45, right panel). The minimum potential energy becomes $u_{min} = -(\mu + 2|\tilde{\gamma}|)^2/2v_0$ which is smaller than in the axially symmetric case. The saddle-point value for $u$ on the real axis for $\mu > 2|\tilde{\gamma}|$ is $-(\mu - 2|\tilde{\gamma}|)^2/2v_0$. Note that these energy densities are all

expressed per dimer. The corresponding energies per condensed triplon are $u/n_c(0)$.
We want to compare the results of these simple calculations with corresponding predictions from advanced (HF) calculations and with experimental data on $TlCuCl_3$. Despite the simple formalism used here we can still make specific predictions that would otherwise be more difficult to obtain.
A vanishing $n_c(0)$ is realized only when $(\mu + 2|\tilde{\gamma}|) = 0$. As a consequence, the gap field $H_{c1}$ that would be observed in an ideal system with axial symmetry is renormalized to a value $H_{c1}^{exp} = H_{c1} - \Delta H_{c1}$ (with $\Delta H_{c1} = 2|\tilde{\gamma}|/g\mu_0\mu_B$) above which condensation occurs, see Fig. 46a. Taking a reasonable value for $|\tilde{\gamma}| \approx 0.01$ meV for $TlCuCl_3$ [95, 152] and $\mathbf{H} \parallel b$ with $g$ =2.06 [152], we obtain a renormalization of the critical field due to $|\tilde{\gamma}|$ alone by $\mu_0\Delta H_{c1} \approx 0.2$ T for this particular magnetic-field direction.
The resulting condensate fraction, $n_c(0) = \mu^{exp}/v_0$ where $\mu^{exp} = g\mu_B\mu_0(H - H_{c1}^{exp})$, is in full agreement with HF calculations for spin dimer systems [27], see Fig. 46b. Focusing further on the effects of an explicit violation of axial symmetry, the condensate fraction at $T = 0$ is changed by $2|\tilde{\gamma}|/v_0$ in our calculation, see again Fig. 46b. If we use the fact that the total triplon fraction $n(0) \approx n_c(0)$ and take the result $n(T_c^{BE}) = n(0)/2$ from Ref. [27] assuming a quadratic triplon dispersion relation, we obtain a shift $|\tilde{\gamma}|/v_0$ in $n(T_c^{BE})$ that is again in full agreement with the corresponding HF calculations [95], see Fig. 46b.
In Fig. 47 we show the condensate triplon-fraction $n_c(0)$ as deduced from our magnetization $M(T, H)$-data of $TlCuCl_3$ [158], which we have already corrected for a small fraction $\tilde{n}$ of non-condensed triplons [27]. A linear fit to the data in the dilute limit ($\mu_0 H_{c1} < \mu_0 H \lesssim 7.5$ T [95]) yields $v_0/k_B = 311.4 \pm 0.5$ K which is in very good agreement with available literature values [95, 103, 150]. The deviation from the linear behavior at larger magnetic fields can be attributed to the contribution of higher triplet states [105].
Our simple formalism does not include the influence of such triplet states, nor does it allow for a determination of $\tilde{n}$ itself, but this latter correction is of the order of a few percents at most in our data [27, 158], as it is typical for a weakly interacting Bose gas, see inset of Fig. 47.
We may relate the minimum value $u_{min}$ at $T = 0$ to the transition temperature $T_c^{BE}$ if we assume that $|u_{min}|/n_c(0)$, the energy gain per triplon upon condensation, is proportional to $k_B T_c^{BE}$ with a field-dependent proportionality factor of the order of unity. Any nonzero $|\tilde{\gamma}|$ leads to an increase in $T_c^{BE}$ as compared to the axially symmetric case. This trend can be clearly seen in the calculated $M(T, H)$-curves from Ref. [95], where the minimum in $M$ that is usually taken as a criterion to define $T_c^{BE}$ is shifted towards higher temperatures as soon as $|\tilde{\gamma}| > 0$, see also Fig. 48a. If we again take $|\tilde{\gamma}| = 0.01$ meV we obtain a shift in $T_c^{BE}$ of the order of $\Delta T_c^{BE} \approx |\tilde{\gamma}|/k_B \approx +0.1$ K, which has to be compared to the result of the more precise HF calculations with $\Delta T_c^{BE} \approx +0.5$ K [95]. Considering the effects of violated axial symmetry, the condensate density at $T = 0$ is changed in our calculation by $2|\tilde{\gamma}|/v_0$, see Fig. 48a. Using the fact that the total triplon fraction $n(0) \approx n_c(0)$ and taking $n(0) = 2n(T_c^{BE})$ [27], we obtain

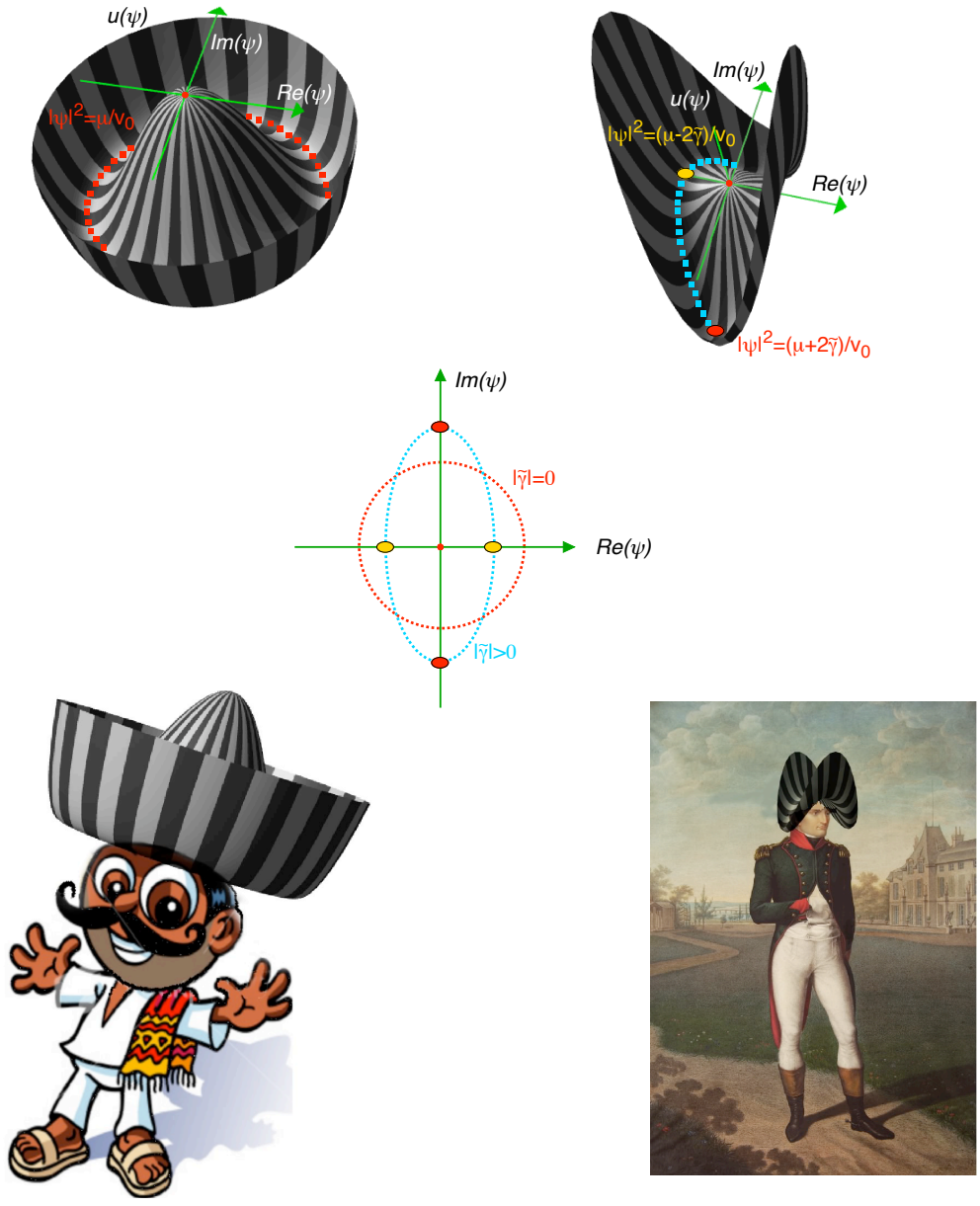


Figure 45: Potential-energy density $u$ as a function of $\psi$ for axial symmetry (left panels, "mexican-hat potential") and violated axial symmetry (right panels, "Napoleon's hat potential"), respectively. In the symmetric case the minimum value $u_{min} = -\mu^2/2v_0$ is realized along a circle (red, dashed line), while in the anisotropic case isolated minima $u_{min} = -(\mu + 2|\tilde{\gamma}|)^2/2v_0$ are on the imaginary axis (red, filled ellipsis). The saddle points are highlighted by yellow dots.

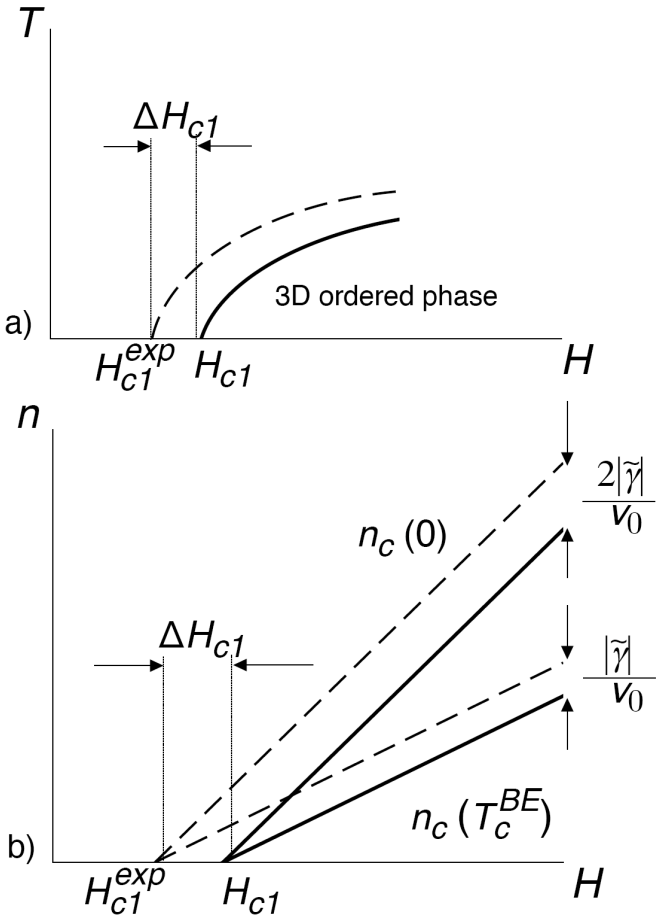


Figure 46: Effect of a violated axial symmetry on a) magnetic phase diagram, b) triplon fraction at $T = 0$ and $T = T_c^{BE}$. Solid lines: axially symmetric system. Dashed lines: system with axial anisotropy.

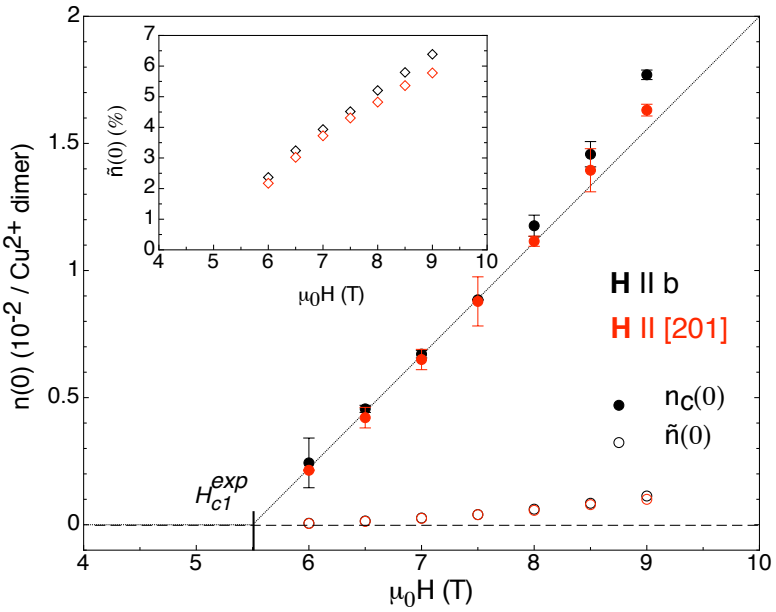


Figure 47: Triplon-fraction $n(0)$-data obtained from magnetization $M(T)$ data for $\mathbf{H} \parallel b$, see Chapter 6.3.2 or Ref. [158]. Condensate triplon-fraction $n_c(0)$, non-condensed triplon-fraction $\tilde{n}(0)$, and the percentage of non-condensed triplons (inset) [158]. A linear fit to the $n_c(0)$-data in the dilute limit [95] below 7.5 T (dotted line) gives $\mu_0 H_{c1}^{exp} = 5.501 \pm 0.003$ T and $v_0/k_B = 311.4 \pm 0.5 \mathrm{Km}^3$.

a shift $|\tilde{\gamma}|/v_0$ in $n(T_c^{BE})$ that is again in full agreement with the corresponding HF calculations [95], see Fig. 48a.

As a consequence of the anisotropy term $|\tilde{\gamma}|$ the original invariance of $u(\psi)$, with respect to a transformation $\psi \rightarrow \psi e^{i\phi}$, is lifted. The maximum variation in the potential-energy per dimer $u$ along the ellipsoid contour with local minima in the radial $|\psi|$-direction, see Fig. 45, is $4\mu|\tilde{\gamma}|/v_0$, or $\tilde{\Delta} \approx 4|\tilde{\gamma}|$ per ground-state triplon.This determines the order-of-magnitude of an anisotropy gap that can be calculated to $\tilde{\Delta} = \sqrt{8\tilde{\gamma} g \mu_B \mu_0 (H - H_{c1})}$, see Ref.[95]. This expression can also be qualitatively obtained within our formalism if we take $\Delta u = 4\mu\tilde{\gamma}/v_0$, the energy-density difference along the ellipsoid contour sketched in Fig. 45, to be approximately equal to $\tilde{\Delta}^2/v_0$. $1/v_0$ corresponds to the triplon-density per energy $\partial n_c(0)/\partial\mu$ at the ground state $\psi_0$, and $\tilde{\Delta}$ represents a gap energy per triplon that is needed to compensate for $\Delta u$. Excitations above the ground state $\psi_0$ with energies below $\tilde{\Delta}$ will clearly not show the typical gapless Goldstone-like behavior as expected for an axially symmetric system. For $\mathrm{TlCuCl_3}$ we calculate with $|\tilde{\gamma}| = 0.01$ meV [95, 152] a gap $\tilde{\Delta} \approx 0.3$ meV for $\mu_0 H = 14$ T along $b$, which is somewhat below what has been considered to be relevant in inelastic-neutron scattering measurements [28]. For excitation energies larger than $\tilde{\Delta}$, the presence of an anisotropy gap may remain unnoticed, see Fig. 48b.

In $\mathrm{TlCuCl_3}$ such a gap may arise from a pre-existing anisotropy that is already present in $H =$

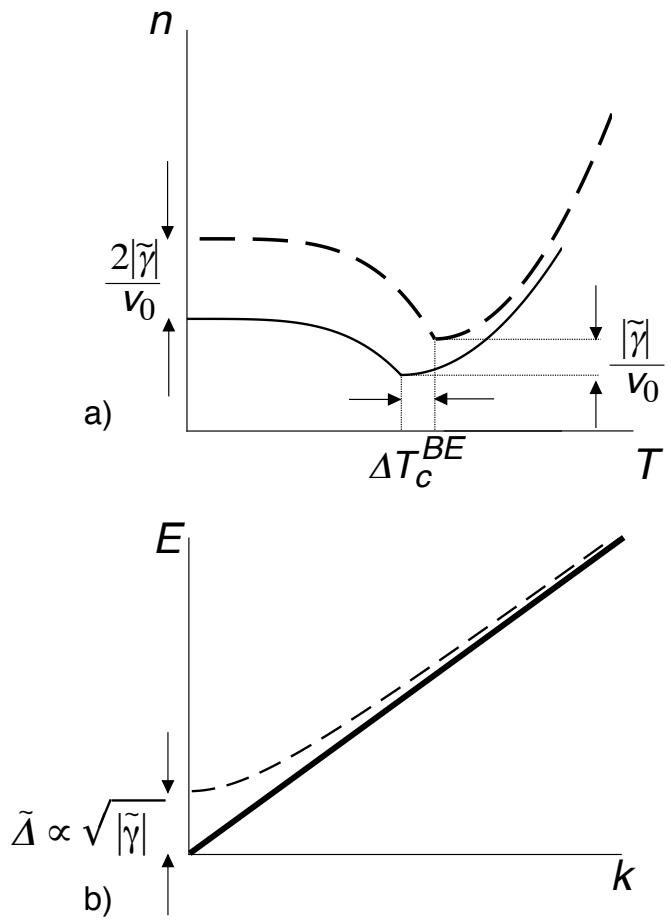


Figure 48: Effect of a violated axial symmetry on a) triplon fraction at a fixed magnetic field $H > H_{c1}$, b) Excitation spectrum $E(k)$ (sketch, axes are not to scale). Solid lines: axially symmetric system. Dashed lines: system with axial anisotropy.

0 [32]. In the following we argue, however, that even a perfectly axially symmetric magnetic system is unstable towards a spontaneous violation of this symmetry at $H_c$, which inevitably leads to the formation of a small anisotropy gap $\tilde{\Delta}$ above $H_{c1}$ of real materials.
It is interesting to note that electron-spin resonance (ESR) data taken on $\mathrm{TlCuCl_3}$ do indeed show a clearly gapped behavior [32, 152] at and above $H = H_{c1}^{exp}$ for **H** along $b$ and $[201]$ as well as perpendicular to $(10\bar{2})$, respectively. These data are fitted nicely by a linear regression of the lowest energy level according to the Zeeman model $h\nu = \Delta = g\mu_0\mu_B(H - H_{c1})$ in the range of $H \leq H_{c1}^{\star}$ and an evolving quasiparticle gap $h\nu = \tilde{\Delta}(H) = \sqrt{8\tilde{\gamma}g\mu_B\mu_0(H - H_{c1}^{exp})}$ for $H \geq H_{c1}^{\star}$ with a $\tilde{\gamma}$ and $H_{c1}$ as fitting parameters, see Fig. 49 and Table 7. Furthermore,

Table 7: The extracted fitting parameters from ESR-data $\nu(H)$ in $\mathrm{TlCuCl_3}$ taken at $T = 1.5$K [32, 152] assuming the presence of an anisotropic term $\tilde{\gamma}$

| | $H \parallel b$ | $H \parallel [201]$ | $H \perp (10\bar{2})$ |
|---|---|---|---|
| $H_{c1}(T)$ | 5.71± 0.01 | | 4.91 ± 0.02 |
| $\tilde{\gamma}$ (meV) | 1.64 $\cdot 10^{-2} \pm 3 \cdot 10^{-4}$ | 1.18 $\cdot 10^{-2} \pm 4 \cdot 10^{-4}$ | 3.4 $\cdot 10^{-3} \pm 2 \cdot 10^{-4}$ |

our theory is in full agreement with former field-dependent neutron-scattering data [28], which were analyzed within a commensurate Zeeman model, see Fig. 50. Corresponding to our model a possible reopening of the gap at higher magnetic fields $H > H_{c1}$ (yellow dot in the main frame) is supposed to show a peak-like feature around $\sim 0.35$ meV in the neutron-scattering spectrum for $\mu_0 H = 12$ T and $T = 50$ mK marked by yellow bar in the inset of Fig. 50). Unfortunately, the intensity increase at lowest energy is believed to be due to strong field-induced magnetic Bragg contamination, preventing further data analysis below a resolution limit of 0.75 meV [28], see inset of Fig. 50. The presence of a possible anisotropic behavior of the spin system remained, therefore, unnoticed. We may remark that in the main frame, data are presented up to a maximum field amplitude of $\mu_0 H$ = 14 T. The inset, however, shows an energy scan at $\mu_0 H$ = 12 T. At higher magnetic fields the reopening of the gap should be easier to detect, since the expected peak-like feature emerging in an energy scan is expected to be detected at higher transfer energies (light-blue bar in the inset of Fig. 50).

In this regard, neutron-scattering measurements cannot uniquely exclude nor determine the presence of a possible anisotropy gap $\tilde{\Delta}$.
*Garlea et al.* [119] and *Zheludev et al.* [121] presented neutron-scattering data performed on the spin-ladder system $(\mathrm{CH_3})_2\mathrm{CNH_3CuCl_3}$, see Fig. 51. The presence of a Goldstone mode with a linear energy spectrum down to lowest transfer energies is suggested, although, in this case, as well, a resolution limit of $\sim 0.3$ meV make the data-analysis below this limit impossible. Therefore, we believe that the opening of an anisotropic gap at lowest energies $E \leq 0.3$ meV can, even in this case, not entirely be excluded, see Fig. 51. In our opinion, high-field

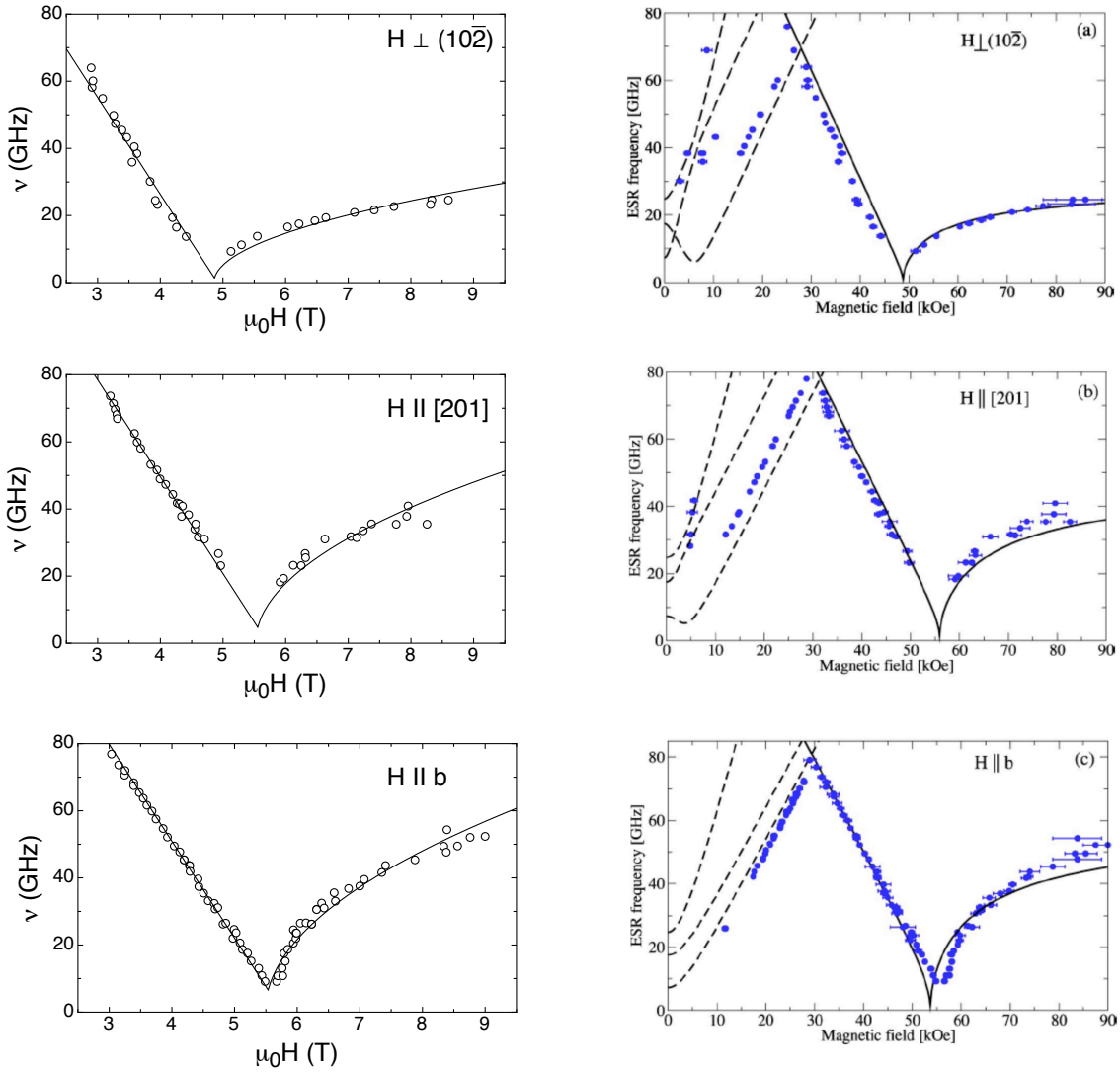


Figure 49: Dependencies of the ESR frequency on the magnetic field for different orientations at $T$=1.5 K. Data are taken from Ref. [152]. Two different theoretical approaches are presented. In the left panels, our fits are shown assuming a "violated axial symmetry" with a corresponding gapped behavior at the critical field region. Fits to the same data of *Kolezhuk et al.* [152] are shown in the right panels (original plots), for which no axial symmetry violation has been considered. Within this model the lowest triplon gap vanishes at the critical field and then reopens as a quasiparticle gap $E_g \propto C\sqrt{H^2 - H_{c1}^2}$ with a orientation-dependent constant $C$. For both approaches the solid lines correspond to the fits to the lowest triplon-gap data. The dashed lines correspond to fits of the thermally activated transitions between three branches of the $S = 1$-triplet at **q**=0, see Ref. [32].

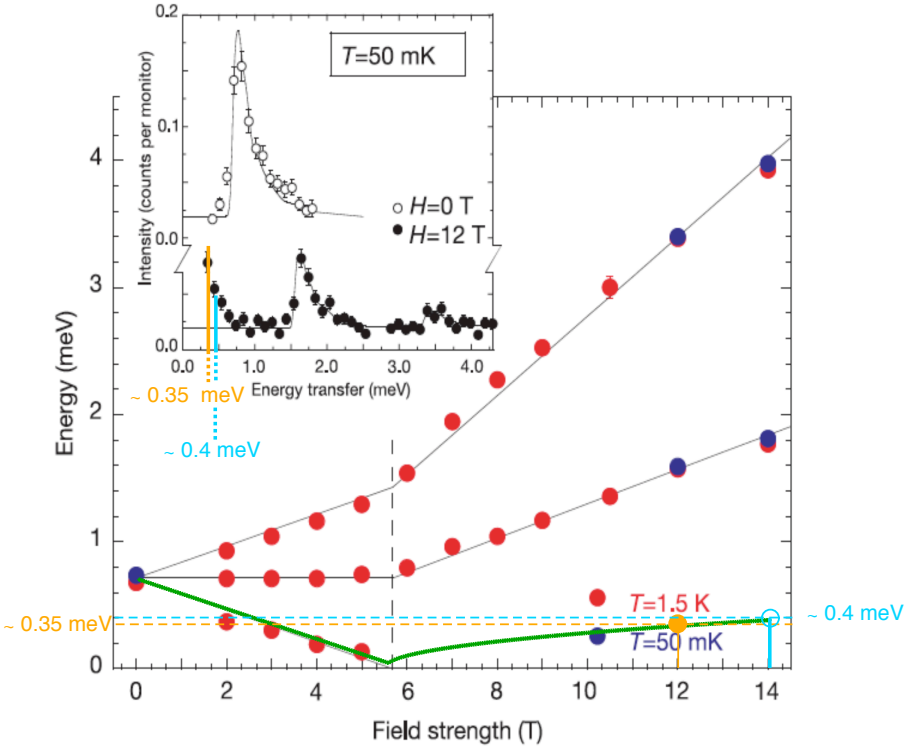


Figure 50: The dependence on the external magnetic field $\mathbf{H} \parallel b$ of the magnetic excitation energy measured in $TlCuCl_3$ at the Bragg point $\tau$= (0 4 0) [r.l.u.], for fixed temperature $T$= 1.5 K (red symbols) and $T$= 50 mK (blue symbols). Original plot taken from Ref.[28]. The thin black curves represent the Zeeman model. The green curve represents our fit extracted from the ESR-data, see Fig. 49. The yellow and light-blue data dots have been added as a posteriori by us. See text for comments and explanations.

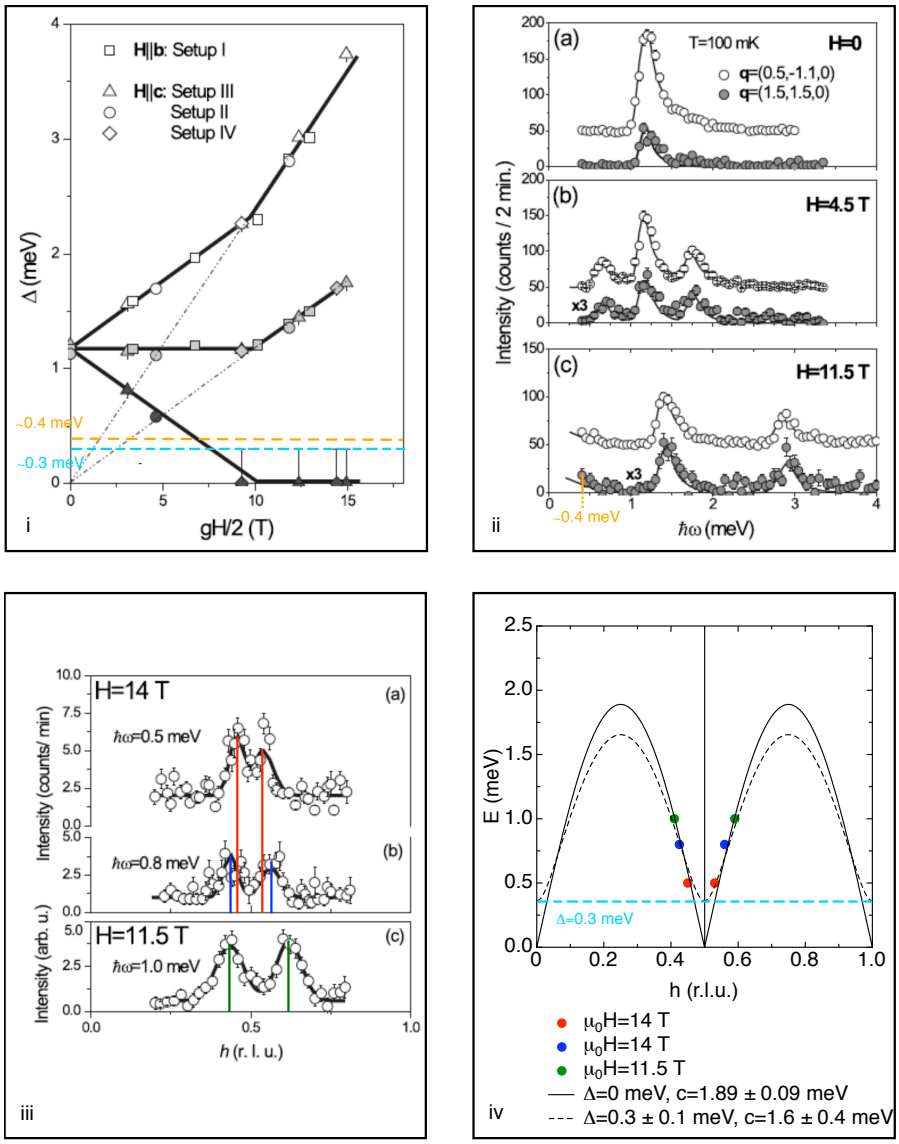


Figure 51: Neutron-scattering data of $(CH_3)_2CNH_3CuCl_3$. Panels (i)-(iii) correspond to original plots taken from Ref.[121]. (i) The dependence of the gap energies on the reduced magnetic field $(g/2)H$, where $g$ is the Landé g-factor, for fixed temperature $T < 100$ mK for different experimental geometries (different symbols). See Ref.[121] for further explanations. The black curves represent the Zeeman model. The blue and yellow dashed lines represent the resolution limits extracted from $\mathbf{q}-$scans and energy-scans, respectively. (ii) Energy-scans at different magnetic fields. Resolution limit is approximately $\sim 0.4$ meV. (iii) $\mathbf{q}$-scans at fixed transfer energy for different magnetic fields. Extracted values are plotted in (iv). Their analysis results in a resolution limit of $\sim 0.3$ meV (blue dashed line).

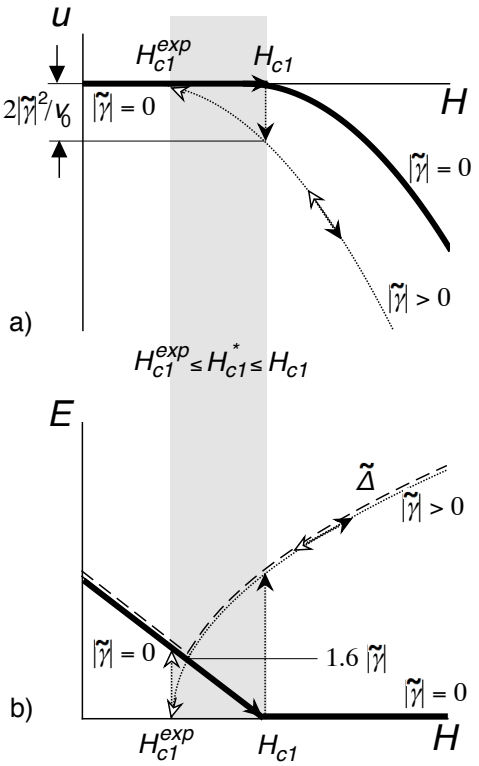


Figure 52: Effects of a violated axial symmetry on a) potential energy per dimer, and b) energy-level scheme of the lowest triplon branch of an axially symmetric system ($|\tilde{\gamma}| = 0$, thick solid lines). The corresponding changes of a system that shows a spontaneous axial distortion ($|\tilde{\gamma}| > 0$) above $H_c^\star$ are represented by thin lines and arrows (axes are not to scale), respectively. The transition may take place at $H_{c1}$ ($H$ increasing) or $H_{c1}^{exp}$ (H decreasing, see arrows). Without any hysteretic effects one may expect a $H_{c1}^\star$ with $H_{c1}^{exp} \leq H_{c1}^\star \leq H_{c1}$ indicated by the grey shaded area which corresponds to the maximum hysteresis width of a possible weakly first-order transition at $H_{c1}^\star$ with $H_{c1}^{exp} \leq H_{c1}^\star \leq H_{c1}$ (filled arrows: $H$ increasing; open arrows: $H$ decreasing). The dashed line in b) reproduces the trend in the ESR data from Refs. [152] and [32] for $\mathrm{TlCuCl_3}$ and $\mathbf{H} \parallel b$ (see text).

ESR measurements represent the most powerful tool to determine whether a quasiparticle gap $\tilde{\Delta}$ at and above the critical field $H_{c1}$ is present, see [32, 152, 153]. Such measurements are, therefore, desirable to avoid further ambiguities.

### 6.5.2 Instability of the condensate towards violation of axial symmetry

This means that a distortion of the original crystal symmetry may spontaneously occur at $H_c$ together with an increase of $|\tilde{\gamma}|$, provided that the total energy, including both magnetic and crystal-lattice contributions, is lowered along with this distortion. This argument is so general that it should be applicable to all insulating spin systems that are supposed to show a Bose-Einstein condensation of magnetic bosonic quasiparticles. As it does not make any specific assumptions on the microscopic arrangement of the spin-carrying atoms, any more precise,

universal statement about the details of the resulting lattice distortion cannot be made here.
The gain in potential energy per dimer upon condensation in combination with this simultaneous distortion is $2|\tilde{\gamma}|^2/v_0$, see Fig. 52a. If the critical field is approached from below with $H$ increasing, the parameter $|\tilde{\gamma}|$ may therefore jump discontinuously from zero to its optimum value either at $H_{c1}$ or at a transition field $H_{c1}^{\star}$ with $H_{c1}^{exp} \leq H_{c1}^{\star} \leq H_{c1}$, while with $H$ decreasing the transition can take place at a different field in the same magnetic-field interval, see grey shaded area in Figs. 52a and b. In an ideal situation with a perfect axial symmetry in $H = 0$, the critical field $H_{c1}$ corresponds to a "normal-state" value with $|\tilde{\gamma}| = 0$ that is determined only by the gap energy, while in the condensate phase the effective critical field is $H_{c1}^{exp} = H_{c1} - \Delta H_{c1} < H_{c1}$, lowered by $\Delta H_{c1} = 2|\tilde{\gamma}|/g\mu_B\mu_0$ with respect to $H_{c1}$ due to the increase in $|\tilde{\gamma}|$. If the transition occurs at a transition field $H_{c1}^{\star}$ that is strictly larger than $H_{c1}^{exp}$, one will observe at $T = 0$ corresponding small discontinuities in $u$ ($\Delta u \leq 2|\tilde{\gamma}|^2/v_0$, see Fig. 52a, $n_c$ ($\Delta n_c \leq 2|\tilde{\gamma}|/v_0$, see Fig. 46b and $M$ ($\Delta M = \Delta n_c g\mu_B N_d$), see Fig. 48a, which would qualify the transition as of weakly first order with a maximum observable hysteresis width $\Delta H_{c1}$. The occurrence of hysteretic effects in a real material may depend, however, on further conditions that are not considered here, such as material-quality issues or the relevance of possible quantum fluctuations at $T$ = 0 to the order of the phase transition.
Even if a non-zero $|\tilde{\gamma}|$ evolves continuously above the critical field as a function of $H$ along with a continuous structural distortion with no detectable hysteresis, one should still be able to distinguish between the normal-state $H_{c1}$ extracted from the experimental data taken below $H_{c1}^{exp}$, and a $H_{c1}^{exp} < H_{c1}$ from corresponding data taken well above $H_{c1}$, respectively, to obtain an estimate for $|\tilde{\gamma}|$ from the resulting difference $\Delta H_{c1}$. In any case, if $H_{c1}^{exp} < H_{c1}^{\star} < H_{c1}$, one expects a finite energy difference $\leq 1.6|\tilde{\gamma}|$ at the transition field $H_{c1}^{\star}$ between the lowest-triplon state and the singlet states, respectively, see Fig. 52b.
A possible pre-existing anisotropy that may already be present at $H$ = 0 (which is likely to be the case in $TlCuCl_3$) can be easily included in this formalism by identifying $H_{c1}$ with a renormalized "normal-state" value that already contains this pre-existing anisotropy. Any additional $|\tilde{\gamma}|$ that may develop together with the lattice distortion around this critical field will somewhat change the value of the anisotropy gap $\tilde{\Delta}$. The difference $\Delta H_{c1}$, however, and possible discontinuities in $u$, $n_c$ and $M$ are determined by the additional $|\tilde{\gamma}|$ alone.
It should be mentioned that ESR frequencies due to the lowest magnon gap measured on $TlCuCl_3$ in the "normal" phase for $\mathbf{H} \parallel b$ do, indeed, extrapolate to zero at a somewhat larger $H_{c1}$ (by $\mu_0\Delta H_{c1} \approx 0.2$ T) than the square-root like gap that we attribute to $\tilde{\Delta}$ in the condensate phase [32, 152], see Fig. 52.
The present picture may also account for the first-order like features like the $^{35}$Cl quadrupole shift [154] that has been interpreted as an indication of a weakly-first order lattice deformation or for the pronounced hysteretic behavior (with a $\mu_0\Delta H_{c1} \approx 0.2 - 0.3$ T) of the observed peaks in the sound-attenuation data of $TlCuCl_3$ at $H_c(T)$ [108] as well as for the observa-

tion of a lattice instability at the field-induced phase transition of the spin-gapped compound $Cu_2(C_5H_{12}N_2)_2Cl_4$ [159].

Such a spontaneous distortion arising from the interplay between the emerging magnetic Bose-Einstein condensate and its host crystal that lowers the total energy, with a tendency to increase or *even create* an anisotropy perpendicular to the external magnetic field above $H_{c1}$ even in a perfectly axially symmetric system, is rather unique and is reminiscent of the Spin-Peierls instability in one dimensional magnetic chains. It should be a universal feature of magnetic BEC systems at their magnetic phase transition, and it is not expected to occur in axially symmetric Bose gases composed of real particles such as in superfluid $^4$He or atomic condensates, where the condensate cannot create an axial-symmetry breaking term by itself. However, it can occur even in perfectly axially symmetric spin systems and may become larger with increasing ground-state triplon density $\psi_0^\dagger\psi_0$, i.e., with decreasing temperature. A further pertinent indication for a considerable coupling of the spin system to the lattice that may result in an apparent first-order phase transition is obtained from magnetocaloric-effect measurements on the axially symmetric $S = 1$ system $NiCl_2 - 4SC(NH_2)_2$ [34]. It is, therefore, not unreasonable to assume that the evolution of an observed-gap feature in ESR-data of this compound at $\mu_0 H$ = 8 T, with decreasing temperature and deeply into the supposed BEC-state [160] are related to such a distortion. Further experimental observation of lattice-distortion was done in a X-ray diffraction experiment on the spin-ladder compound $Cu_2(C_5H_{12}N_2)_2Cl_4$ [161–163]. Such an instability should be a universal feature of magnetic BEC systems at their magnetic phase transition, and it is not expected to occur in axially symmetric Bose gases composed of real particles such as superfluid $^4$He or atomic condensates, where the condensate cannot create an axial-symmetry breaking term by itself.

In a microscopic picture, the tendency of a magnetic condensate to spontaneously violate the axial symmetry can be interpreted as a natural consequence of the transverse magnetic ordering that develops in the condensate phase and that locks to the crystal lattice due to unavoidable magnetoelastic coupling [27, 115, 164]. As soon as the transverse magnetic moments point to a specific, energetically preferred crystal direction, the phase $\phi$ that is associated with the angle between these moments and the crystal axes [94] is indeed fixed (in $TlCuCl_3$ with an angle $\alpha \approx 39^\circ$ to the $a$-axis [115]), and the magnetic analogue to a supercurrent velocity $\mathbf{v}_s = \hbar/m^\star \nabla\phi$ (where $m^\star$ is the effective mass of a triplon) is naturally zero for excitation energies below the anisotropy gap $\tilde{\Delta}$. This gap covers an excitation-frequency range that is crucial for experiments that rely on the existence of a long-lived phase coherent condensate [31], such as the detection of a long-lived spin supercurrent as in $^3\mathrm{He} - \mathrm{B}$ [165, 166], of macroscopic second-sound like oscillations as observed in superfluid $^4$He [167] or of stable vortex-like structures as they have been observed both in superfluid $^4$He and in atomic condensates [168] in atomic condensates [168]. To achieve a lifetime of the order of seconds for a phase coherent condensate, a corresponding anisotropy gap may not exceed a few femto elec-

tron volts.
In the absence of a Goldstone mode (for which all values of the phase $\phi$ have to be energeticaly equivalent), the quantity $\psi_0^\dagger\psi_0$ in the zero-frequency limit does no longer represent a condensate fraction, but it is rather related to the order parameter characterizing the antiferromagnetic state [26].

### 6.5.3 Uniaxial pressure effects ?

We finally want to suggest a way of how an existing anisotropy gap $\tilde{\Delta}$ could be suppressed. It is known, that the application of hydrostatic pressure changes the magnetic phase diagram of $\mathrm{TlCuCl_3}$, leading to a complete suppression of $\Delta$ at a critical pressures $p_c \approx 0.1$-$0.2$ GPa [169, 170]. This pressure dependence can be attributed to a change of specific interdimer coupling-constants that influence the phase diagram with decreasing bond-lengths [105, 171]. In our case, $|\tilde{\gamma}|$ essentially represents the difference between the coupling-constant components belonging to the crystal directions perpendicular to the applied magnetic field, e.g., $|\tilde{\gamma}| \propto |J_x - J_y|$ for $\mathbf{H} \parallel z = b$ [95, 152]. An external *uniaxial* pressure that is applied perpendicular to the magnetic-field direction in the $ac$ plane, therefore, leads to strong variation of $|\tilde{\gamma}|$ and therefore of $\tilde{\Delta}$. A uniaxial pressure effect on $H_{c1}^{exp}$ (and along with it on $T_c^{BE}$ as well as $n_c(0)$ and $n(T_c^{BE})$) may be masked by even larger changes due to the variation in the magnon spectrum [105, 171]. The anisotropy gap $\tilde{\Delta}$ itself, however, can be shifted with $|\tilde{\gamma}|$ upwards or downwards, *and even be suppressed*, depending on the direction of the uniaxial pressure within the $ac$ plane and with $\mathbf{H} \parallel b$. In this case, a true gapless Goldstone mode can probably be restored by such a procedure.
To conclude, we have analyzed the spontaneous symmetry breaking in a Bose gas of triplet excitations in a low-dimensional spin system based on simple functional methods in the classical limit. Our results are in remarkable agreement with former theoretical predictions based on HF approximated computations [27, 95, 107]. Various experimental findings in $\mathrm{TlCuCl_3}$ such as the occurrence and the magnitude of an anisotropy gap [32, 152] and a weakly first-order like behavior at the magnetic phase transition [108, 154] can be easily explained. We expect that the magnetic BEC systems are intrinsically unstable towards a spontaneous anisotropic distortion perpendicular to the external magnetic field, and that an anisotropy gap can be suppressed applying a moderate uniaxial pressure perpendicular to the magnetic field direction. Further, new experiments should confirm or invalidate these statements.

# 7 Search for "magnetic superfluidity"

The current knowledge about the occurrence of macroscopic occupation of the ground state by magnetic $S = 1$ quasiparticles in low-dimensional spin systems still allows for, in many important aspects, ambiguous interpretations [31]. There is still a lack of experimental evidence for the presence of macroscopic coherence in such condensates. Furthermore, to what extent the presence of (structural) anisotropies influence on a possible preexisting macroscopic coherence and an eventual manifestation of a "magnetic superfluidity" is still an issue of debate . In our opinion to prove that there is, in fact, a true condensate one has to show that the particles form *spontaneously* a single long-living phase coherent state similar to the superfluid state as observed in liquid $^4$He. A convincing method would therefore be to demonstrate the existence of such a superfluid component in the system. In analogy to $^4$He, a second-sound mode in such a condensate phase would manifest itself as an oscillation of the density of the quasiparticles (superfluid and normalfluid component flow relative to one another) and accordingly in the entropy of the system. The detection of such a collective mode would, therefore, be a clear indication of the occurrence of BEC.

## 7.1 The model

The second sound mode in a BE-condensate is a soft mode that vanishes in the normal phase. It involves an oscillation of the superfluid and normalfluid density relative to one another. Normal- and the superfluid part move out of phase in opposite directions leading to a variation over space of a relative concentration of the two components with no variation in the total particle density, see Chapter 4.4. Since just the normalfluid component carries entropy, this mode can be interpreted as an undamped standing entropy wave in the condensate.
Using the hydrodynamic formulation given above we investigate the response of the condensate to a space- and time-dependent external potential $u(\mathbf{x}, t) = u_0 e^{i(\mathbf{q}\cdot\mathbf{x}-\omega t)}$ considering small deviations of the gas (of triplons) from its equilibrium state.
We express the condensate density as $n_c = n_c^{eq} + \delta n_c$, where $n_c^{eq}$ is the equilibrium density and $\delta n_c$ is the deviation from its equilibrium value. By treating the velocity $\mathbf{v}$ and $\delta n_c$ as small quantities and using the linearized versions of Eq. (4.18) and Eq. (4.20), respectively, we find

$$\frac{\partial n_c}{\partial t} + \nabla \cdot (n_c^{eq}\mathbf{v}) = 0 \tag{7.1}$$

and

$$\frac{\partial \mathbf{v}}{\partial t} + \nabla \cdot (\delta\mu) = 0, \tag{7.2}$$

where $\delta\mu$ is the change in the chemical potential $\mu$. Taking the time derivative of Eq. (7.1) and combining this result with Eq. (7.2) we obtain the expression for the equation of motion

$$m\frac{\partial^2 n_c}{\partial t^2} = \nabla \cdot (n_c^{eq}\nabla\delta\mu). \tag{7.3}$$

Note, this equation describes the excitations of a Bose gas in an arbitrary potential $u$. We are looking for solutions where the change in the chemical potential $\delta\mu$ and in the number of particle in the condensate $\delta n_c$, correspondingly, is proportional to $e^{i(\mathbf{q}\cdot\mathbf{x}-\omega t)}$. The change in the chemical potential $\delta\mu$ is then given by [62]

$$\delta\mu = \left(u_0 + V_0 + \frac{\hbar^2 q^2}{4mn_c^{eq}}\right)\delta n_c, \tag{7.4}$$

where $u_0$ is the amplitude of the applied oscillating external potential and $V_0$ is the interaction potential of the Bose gas. Eq. (7.3) then becomes

$$m\omega^2\delta n_c = \left(n_c^{eq}u_0q^2 + n_c^{eq}V_0q^2 + \frac{\hbar^2q^4}{4m}\right)\delta n_c. \tag{7.5}$$

For a constant external potential the first term on the right hand side of Eq. (7.5) vanishes. In this case the non-trivial solutions of Eq. (7.5) are given by

$$\omega^2 =: \omega_0^2 = \frac{\varepsilon_q^2}{\hbar^2}, \tag{7.6}$$

with

$$\varepsilon_q^2 = \frac{\hbar^2q^2}{2m}\cdot\left(2n_c^{eq}V_0 + \frac{\hbar^2q^2}{2m}\right). \tag{7.7}$$

Eq. (7.7) corresponds to the Bogoliubov spectrum, see Eq. (4.15).
Applying a space-and time dependent external potential $u(\mathbf{x},t) = u_0e^{i(\mathbf{q}\cdot\mathbf{x}-\omega t)}$ and using Eq. (7.5), we obtain

$$m\left(\omega^2-\omega_0^2\right)\delta n_c = n_c^{eq}q^2u_0 \tag{7.8a}$$

or

$$\delta n_c = \chi(q,\omega)u_0, \tag{7.8b}$$

where

$$\chi(q,\omega) = \frac{n_c^{eq}q^2}{m\left(\omega^2-\omega_0^2\right)} \tag{7.8c}$$

is defined as the density-density response function of the condensate [62]. The response diverges if the frequency of the external potential is equal to the frequency of the excited mode of the condensate.
In real systems a damping term $\Gamma$ has to be considered. In this case, Eq. (7.8c) passes over to

$$\chi(q,\omega) = \frac{n_c^{eq}q^2}{m\left(\omega^2-\omega_0^2+i\Gamma\omega\right)} \tag{7.9}$$

and the new resonance frequency $\omega_{res} = \sqrt{\left(\omega_0^2 - \frac{\Gamma^2}{4}\right)}$ varies with the damping term $\Gamma$, see Fig. 53.

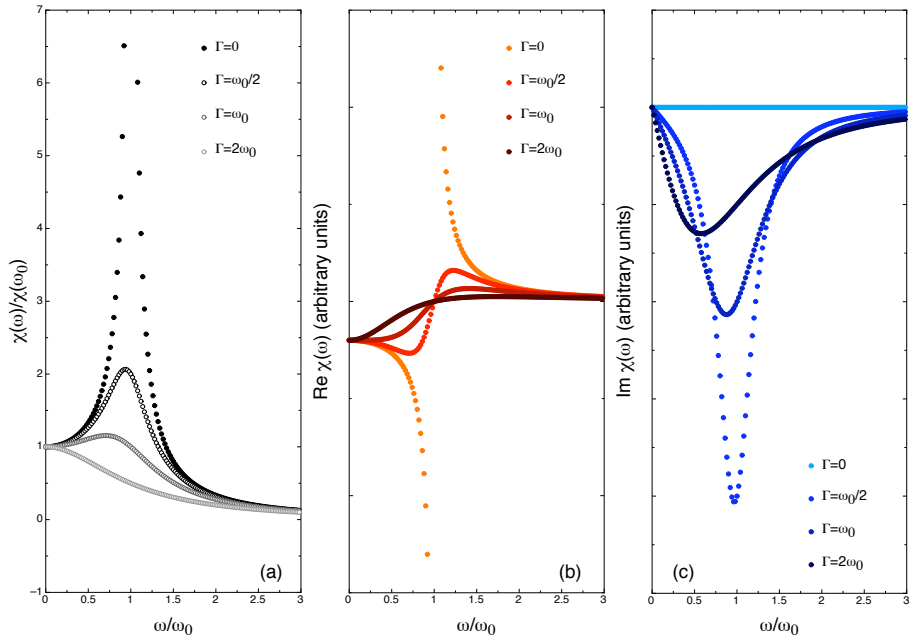


Figure 53: a) The amplitude of the density-density response function for different damping constants. Its real and imaginary part are shown in b) and c), respectively. $\Gamma = 2\omega_0$ defines the value for critical damping.

### 7.1.1 The density-density function for magnetic insulator studied within the BEC-scenario of magnetic quasiparticles

The total magnetization in magnetic insulators for $T < T_c^{BE}$ is defined as $M = g\mu_B N$ [27] and is, therefore, proportional to the total number of excited triplons $N$, see Chapter 6.3. At low temperatures and high magnetic fields one can assume $N \sim N_c$. From Eq. (7.8b), it immediately follows that

$$\chi(q,\omega) \propto \frac{\partial M}{\partial H_{ac}^0} = \chi_{ac}, \tag{7.10}$$

if an oscillating magnetic field $H_{ac}(\mathbf{x},t) = H_{ac}^0 e^{i(\mathbf{q}\cdot\mathbf{x}-\omega t)}$ takes the part of the external potential $u(\mathbf{x},t)$. We can conclude that in such compounds the density-density function defined in Eq. (7.8b) can be expressed as the magnetic ac-susceptibility $\chi_{ac}$.

### 7.1.2 The sound-mode in the condensate phase of $TlCuCl_3$

Rüegg et al. [28] showed by means of inelastic neutron-scattering experiments that the excitation spectrum of $TlCuCl_3$ becomes gapless and linear above a certain resolution limit ($\sim$ 3 meV) by applying a magnetic field $H$ larger than the critical field $H_{c1}$. This linear excitation spectrum has been interpreted as the gapless Goldstone mode predicted by theory [91, 105]. Within the scenario of Bogoliubov, the linear spectrum at long wavelengths pro-

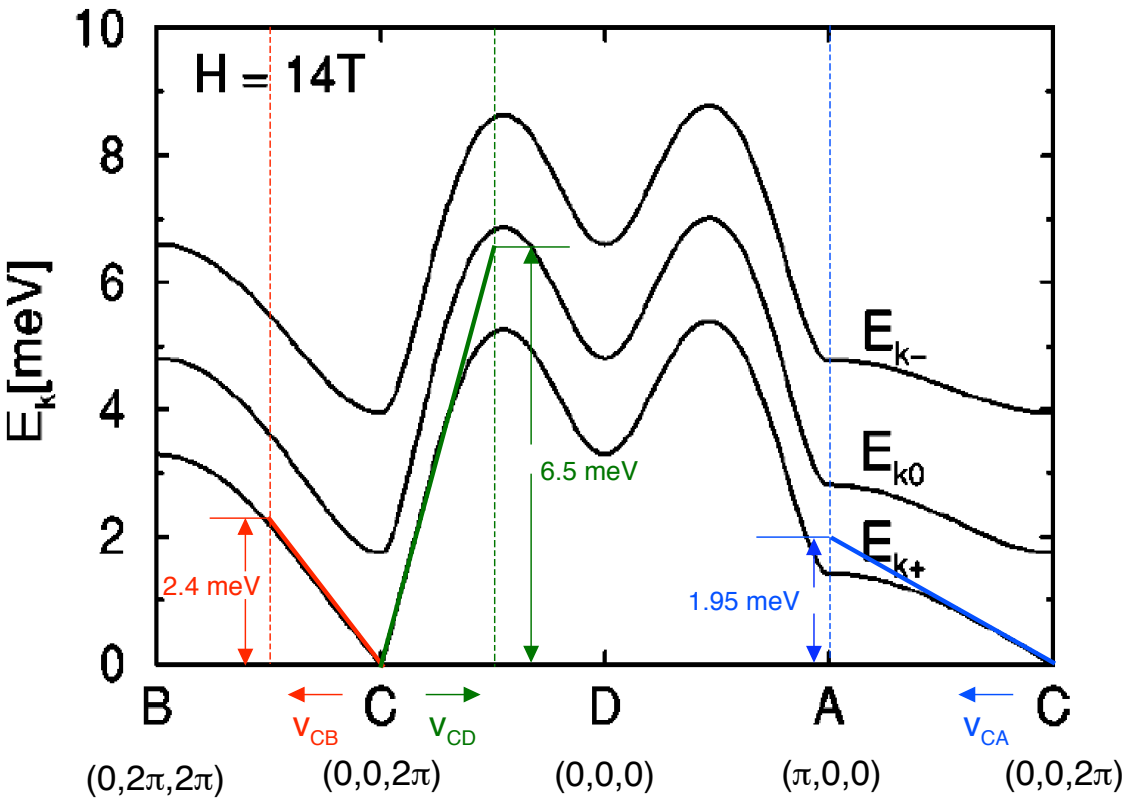


Figure 54: The dispersion relation $\varepsilon_{\mathbf{k}}$ in the condensate phase of $TlCuCl_3$ calculated by *Matsumoto et al.*. Original plot taken from Ref.[105]. The linear energy dependences at small wave vectors along different directions are highlighted in colors. Corresponding sound velocities are calculated using Eq. (7.11)

vides the existence of a superfluid component, see Chapter 4.3.
In the hydrodynamic description, the linearity of the excitation spectrum is expressed as sound-like mode

$$\varepsilon_{\mathbf{k}} \simeq v\hbar\mathbf{k}. \tag{7.11}$$

From the calculated dispersion relation $\varepsilon_{\mathbf{k}}$ in the condensate phase of $TlCuCl_3$ [91], we can derive the different sound velocities along the corresponding crystallographic directions approaching

$$v_i \simeq \frac{\Delta\omega}{\Delta k_i} \quad (i = CA, CD, CB). \tag{7.12}$$

For $\Delta k_i = \frac{\pi}{i}$ we evaluated the increase in energy $\Delta\varepsilon$=$\hbar\Delta\omega$, see Fig. 54. We finally get the following values for the three velocities along the respective crystallographic axis

$$\begin{aligned} v_{CA} &= 375.7 \pm 20\frac{m}{s} \\ v_{CB} &= 1660 \pm 120\frac{m}{s} \\ v_{CD} &= 2790 \pm 140\frac{m}{s}, \end{aligned} \tag{7.13}$$

whereby we assumed a 5% absolute error in determining $\Delta\varepsilon$ from the plot shown in Fig. 54. In the following we will approximate

$$\begin{aligned} v_{CA} &\simeq v_a \\ v_{CB} &\simeq v_b \\ v_{CD} &\simeq v_c. \end{aligned} \tag{7.14}$$

Using Eq. (4.34), which gives an expression of the second-sound velocity for $T \to 0$ K we can check the accuracy of the calculated value $v_b$ approximating $n_c^{eq}(\mu_0 H_{\|b} = 14\text{ T}) \approx n_c(T = 0)$ at $\mu_0 H \parallel b = 14$ T . From high-field magnetization measurements, see Ref. [105], we can estimate $n_c(T = 0) \sim 5.33 \cdot 10^{-2}$ for $\mu_0 H \parallel b = 14$ T and obtain $v_b = 1642\ \frac{m}{s}$ for $\frac{V_0}{k_B}$=315 K, reproducing the previously calculated value quite satisfactorily.

### 7.1.3 The characteristic resonance frequencies for the used $\mathrm{TlCuCl_3}$-specimen

In order to clarify at which frequencies such possibly emerging collective modes in the condensate phase of $\mathrm{TlCuCl_3}$ can be expected, we have to solve the following wave equation for anisotropic group velocities, which we estimated from the triplon-dispersion relation. Moreover, boundary conditions according to the geometry of the specimen must be fulfilled.

$$\frac{\partial^2}{\partial t^2}\tilde{u}(a,b,c,t) = v_a^2\frac{\partial^2\tilde{u}}{\partial a^2} + v_b^2\frac{\partial^2\tilde{u}}{\partial b^2} + v_c^2\frac{\partial^2\tilde{u}}{\partial c^2} \tag{7.15}$$

Unfortunately, for our particular sample the axes do not perfectly coincide with the crystallographic directions of the sample. We, therefore, have to consider the following coordinate transformation:

$$\begin{aligned} x &:= a \\ y &:= b \\ z &:= \frac{1}{cos(\phi)}c + tan(\phi)\cdot a. \end{aligned} \tag{7.16}$$

Let us set $u(x,y,z,t) := \tilde{u}(a = x, b = y, c = z\cdot cos(\phi) - x\cdot sin(\phi))$. We are now able to calculate the derivative in Eq. (7.15) as a function of the crystallographic directions using

$$\frac{\partial\tilde{u}}{\partial i} = \left(\frac{\partial}{\partial x}\frac{\partial x}{\partial i} + \frac{\partial}{\partial y}\frac{\partial y}{\partial i} + \frac{\partial}{\partial z}\frac{\partial z}{\partial i}\right)u \ \text{ for } \ i = a,b,c. \tag{7.17}$$

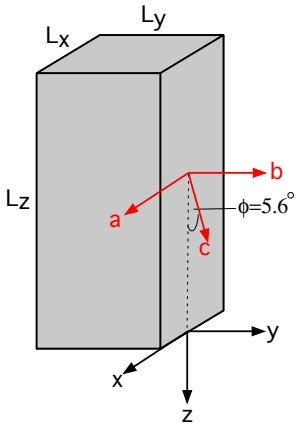


Figure 55: Sketch of the sample geometry ($L_x \approx L_y \approx 2$ mm, $L_z \approx 7$ mm) of the $TlCuCl_3$-specimen used for sound-mode experiments. The setting of the crystallographic directions is slightly distorted compared to the sample axis.

For the derivatives in Eq. (7.15) we finally get

$$\begin{aligned}
\frac{\partial^2 \tilde{u}}{\partial a^2} &= \left( \frac{\partial^2}{\partial x^2} + 2tan(\phi)\frac{\partial}{\partial x}\frac{\partial}{\partial z} + tan^2(\phi)\frac{\partial^2}{\partial z^2} \right) u, \\
\frac{\partial^2 \tilde{u}}{\partial b^2} &= \frac{\partial^2}{\partial y^2} u, \\
\frac{\partial^2 \tilde{u}}{\partial c^2} &= \frac{1}{cos^2(\phi)}\frac{\partial^2}{\partial z^2} u,
\end{aligned} \tag{7.18}$$

which inserted in Eq. (7.15) leads to the following boundary value problem

$$\begin{aligned}
\frac{\partial^2}{\partial t^2} u(x,y,z,t) &= \left( \frac{\partial^2}{\partial x^2} + 2tan(\phi)\frac{\partial}{\partial x}\frac{\partial}{\partial z} + tan^2(\phi)\frac{\partial^2}{\partial z^2} + \frac{\partial^2}{\partial y^2} + \frac{1}{cos^2(\phi)}\frac{\partial^2}{\partial z^2} \right) u(x,y,z,t), \\
u(\mathbf{x}=0) &= u(x=L_x, y=L_y, z=L_z, t).
\end{aligned} \tag{7.19}$$

We can solve Eq. (7.19) with a commonly used separation ansatz $u(x,y,z,t) = u_0 e^{i\mathbf{k}\cdot\mathbf{x}} e^{i2\pi\nu t}$. In order to satisfy the boundary condition, the components of the wave vectors are restricted to

$$k_j = n_j \frac{\pi}{L_j}, \quad n_j \in \mathbb{N} \text{ and } j = x,y,z. \tag{7.20}$$

After a few algebraic transformations, we find the following expression for the Eigenfrequencies

$$\nu_{res} = \nu_0 \sqrt{\alpha_a^2 \left( \frac{n_x}{\beta_x} + tan(\phi)\frac{n_z}{\beta_z} \right)^2 + \alpha_b^2 \left( \frac{n_y}{\beta_y} \right)^2 + \alpha_c^2 \left( \frac{n_z}{\beta_z cos(\phi)} \right)^2}, \quad n_x, n_y, n_z \in \mathbb{N} \tag{7.21}$$

with

$$\begin{aligned}\nu_0 &= \frac{1}{2}\left(\frac{v_a v_b v_c}{L_x L_y L_z}\right)^{\frac{1}{3}} = 198 \pm 130 \text{ kHz},\\ \alpha_i &= \frac{v_i}{(v_a v_b v_c)^{1/3}} \text{ for } i = a, b, c,\\ \beta_j &= \frac{L_j}{(L_x L_y L_z)^{1/3}} \text{ for } j = x, y, z\end{aligned} \tag{7.22}$$

and $\phi = 5.6°$, see Fig. 55.
The calculation shows that the relevant frequency range for the first collective modes in our specimen is of the order of 0.3-0.6 MHz, see Table 8.
The corresponding spectrum, including higher harmonics up to $\nu_{res} \leq 1$ MHz, is shown in Fig. 56.

Table 8: The calculated resonance frequencies for $\nu_{res} \leq 600$ kHz in a $TlCuCl_3$-specimen

| $n_x$ | $n_y$ | $n_z$ | $\nu_{res}(kHz)$ |
|---|---|---|---|
| 1 | 1 | 1 | 470 |
| 2 | 1 | 1 | 498 |
| 3 | 1 | 1 | 541 |
| 1 | 1 | 2 | 585 |
| 4 | 1 | 1 | 596 |

We suggest that these modes can be excited by an external ac magnetic field oscillating in this particular frequency range. Corresponding absorption phenomena might be detectable if the BE-condensate remains intact during the period of the magnetic cycle, i.e. on a time scale larger than $\tau \sim \frac{1}{\nu_{res}}$. The damping of these modes depends on the interaction of the spin system with the crystal lattice. Presently, we are not able to make any quantitative predictions in this regard.

## 7.2 The detection of collective modes

In order to excite and detect such collective modes, we built an ac-susceptometer operating in a RF-range and designed according to a standard coil configuration consisting of a primary coil and two secondary (pick-up) coils, see Fig. 57 and Fig. 58.
The principles of measuring magnetic ac-susceptibility are simple. The sample is subjected to a relatively small alternating magnetic field $H_{ac}$ which is generated inside the primary coil. The flux variation, due to the sample, is picked up by a sensing coil surrounding the specimen which is called secondary or pick-up coil. An identical pick-up coil is located away from the first-coil area but still inside the primary coil. These two (secondary) coils are placed coaxially

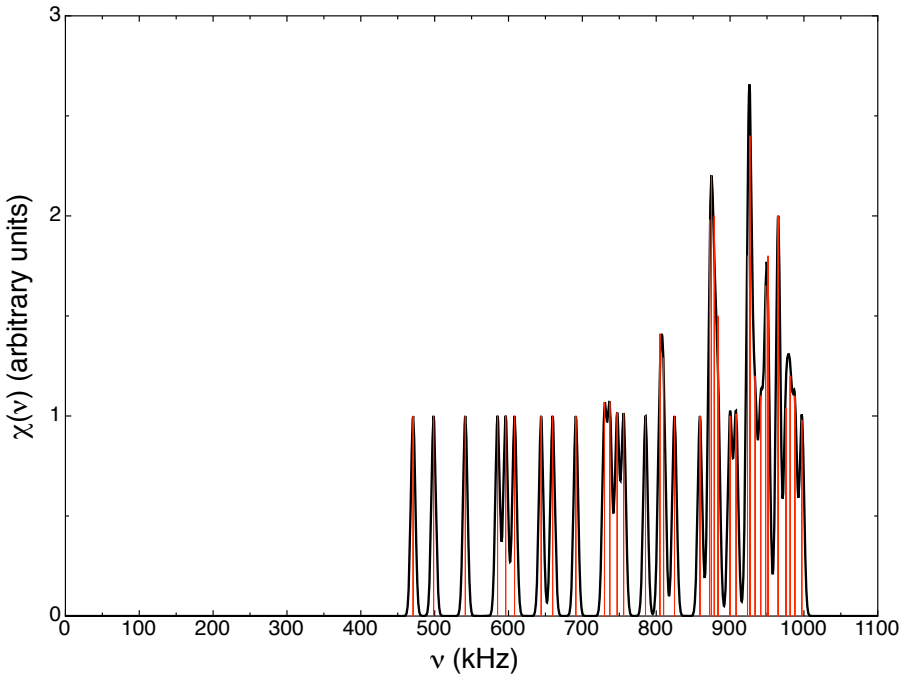


Figure 56: The calculated resonance-frequency spectrum for $\nu_{res} \leq 1$ MHz valid for the $TlCuCl_3$-specimen shown in Fig. 55. The absolute values of the frequencies at which resonance phenomena are expected depend on the geometry of the sample and are highlighted in red. A Gaussian-like resonance curve with an arbitrarily fixed resonance-width was thereby assumed for every resonance phenomenon.

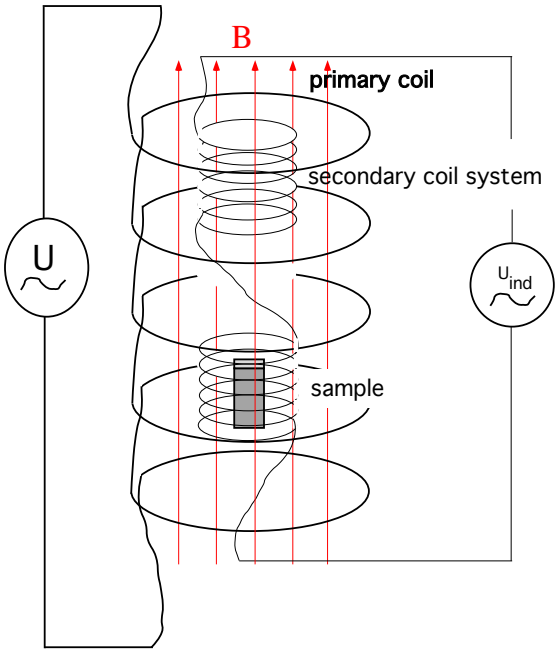


Figure 57: Sketch of a standard ac susceptometer coil set-up

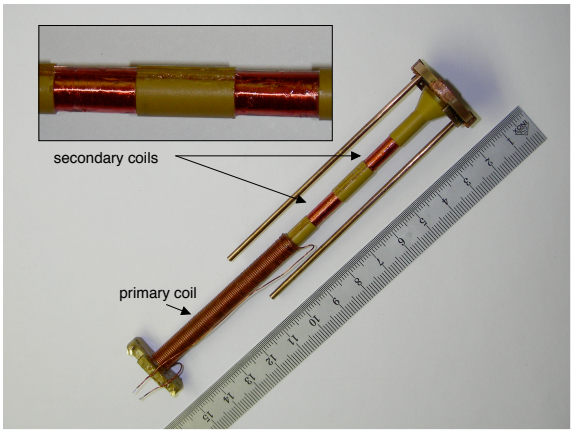


Figure 58: The disassembled RF coil system showing the primary coil and the secondary coils, see also inset.

to each other, as well as to the primary coil and connected in opposite directions in order to produce an induced voltage of equal magnitude, but opposite sign. Therefore, in the absence of a sample the total induced voltage across these two pick-up coils is ideally zero. When a sample is inserted into one of these (secondary) coils, the detected voltage is proportional to the time derivative of the sample's magnetization, as will be shown below.
Normally, such a standard 3-coil set-up is used for ac-susceptibility measurements in the few-kHz range [172], since the maximal reachable magnetic-field amplitude within the primary coil is the limited for a fixed driving voltage $U$.
Using the long-solenoid approximation for the magnetic inductance $B$ inside the primary coil, we obtain

$$B = \mu_0 H = \mu_0 N \frac{I}{l}, \tag{7.23}$$

where $N$ is the number of turns, $l$ is the length of the solenoid, $I$ the current passing through it and $\mu_0 = 4\pi \cdot 10^{-7}$ N/A$^2$ is the permeability constant of free space. Neglecting the capacity term of a solenoid the total impedance of the primary coil is expressed as

$$Z = \sqrt{R^2 + (\omega L)^2}, \tag{7.24}$$

where $R$ is the resistance arising from the wiring used to build the coil, $\omega = 2\pi\nu$ is the angular frequency at which the magnetic field oscillates and $L$ is the self-inductance. In the long-coil approximation the self-inductance is estimated to be

$$L = \mu_0 N^2 \frac{A}{l}, \tag{7.25}$$

where $A$ is the area of a single loop. From Eq. (7.23) -Eq. (7.25) one recognizes that the impedance increases with (angular) frequency limiting the current $I \sim \frac{U}{Z}$ and, consequently, also the amplitude of the generated magnetic (field) inductance.
We overcame this problem using a high-frequency power amplifier to the voltage source which was designed and built in collaboration with the electrical workshop of the Physik-Institut, University of Zurich. It should be noted that the number of turns of the primary coil also affects the amplitude of the oscillating magnetic field. Increasing $N$ also increases the value of the self-inductance $L$ by an even faster rate than the magnetic inductance $B$. Thus, the current passing through the primary coil is thereby reduced. At higher frequency, this fact must be considered [172].

### 7.2.1 The ac-susceptometer

We, therefore, carefully designed and built an ac-susceptometer that is suitable for measurements in the frequency range 0.2 - 2 MHz. The insert is designed to fit into a commercially available PPMS (Physical Property Measurement System) equipped with a $^4$He-cryostat and a $\mu_0 H$= 9 T superconducting dc-magnet.
As mentioned above, a highly symmetric arrangement of the primary and the pick-up coils, as well as a homogeneous ac magnetic field inside the primary coil is necessary to avoid any unbalance of the induced voltage signal, see Fig. 58. The center of the primary coil coincides with the center (of homogeneity) of the dc magnet. The two inner pick-up coils are located symmetrically about this center point. All coils share the same central axis. For construction materials, we used the nonmagnetic copper beryllium for the metallic parts. Its relatively high thermal conductivity ensures good thermal interexchange in the region close to the sample. The pick-up coils were wound from a manganin wire of 0.03 mm diameter on torlon forms and then fixed with Toluol-diluted GE varnish. Manganin is a copper alloy (Cu 86 % Mn 12% Ni 2%), with a constant resistance over a wide temperature range down to lowest temperatures. This should reduce any possible temperature-dependent background contributions to its minimum. Torlon is a high strength plastic with a very large stiffness and a relatively high thermal conductivity. The characteristic parameters of the coil-system are listed in Table 9. In order to reduce the capacitive coupling between the primary coil and the pick-up coils, we installed a grounded multi-wire Faraday shield between them, see Fig. 59.
The shield was made by winding a single layer on a large diameter teflon form and setting in

Table 9: The characteristic parameter of the coil-system forming the ac susceptometer

| | | *primary coil* | *secondary coils* |
|---|---|---|---|
| length | $l$ | 81 mm | 9 mm |
| diameter | $\phi$ | 6.5 mm | 4.9 mm |
| number of turns | $N$ | 119 | 242 |
| inductance | $L$ | 7.3 $\mu$H | 0.15 mH |
| maximal field amplitude | $H_{ac}^0$ | $\sim$ 392 A/m $\sim$ 4.4 Oe (at $\nu$ = 50 kHz) | |
| | | $\sim$ 89 A/m $\sim$ 1.1 Oe (at $\nu$ = 1 MHz) | |
| coil separation | | | 15 mm |

Toluol-diluted GE varnish. Before the glue fully cured, this coil was cut perpendicular to the windings and removed from the form. This produced a fairly flexible sheet of parallel wires, which were insulated from each other in order to reduce the presence of eddy currents. At the very bottom of the shield, the wires are all connected with each other and put on ground.
An additional compensation coil is mounted at the outermost border of the insert. It is counter-wound to the primary coil and connected in series with it, so that the same excitation signal is fed into them, see Fig. 60. This compensation coil generates the same magnetic field amplitude at the border of the sample chamber inside the cryostat as the drive coil does but in opposite direction. The excitation fields are, thereby, confined to the inner volume of the coil set. The influence of stray fields around the measuring region is should to be reduced. The presence of eddy currents is minimized. A step motor enables us to move the sample in and out of the pick-up coils or to move it from one secondary coil to the other. Thus an immediate background subtraction is implemented. The drive signal (Signal Generator, SMG Rhode-Schwarz) is (low) frequency-modulated by the output signal of a lock-in amplifier (EG & G Instruments 7260 DSP). This signal is fed into the primary coil after being amplified by the home-made power source. The voltage difference between the two pick-up coils is detected differentially by low-capacitance probes (Le Croy PP002A) and then amplified (Differential Amplifier AM 502 Textronix). The resulting signal is low-pass filtered and rectified. It now only varies with modulation frequency $\nu_m$, see Fig. 61, and is finally detected with a phase-sensitive lock-in amplifier.
It represents a measure for the derivative of the resonance curve with respect to the frequency whereas the peak-to-peak value scales with the peak frequency deviation $\Delta\nu$ (setting parameter of the signal generator) if this value is much smaller than the resonance linewidth, see following Chapter 7.2.2.

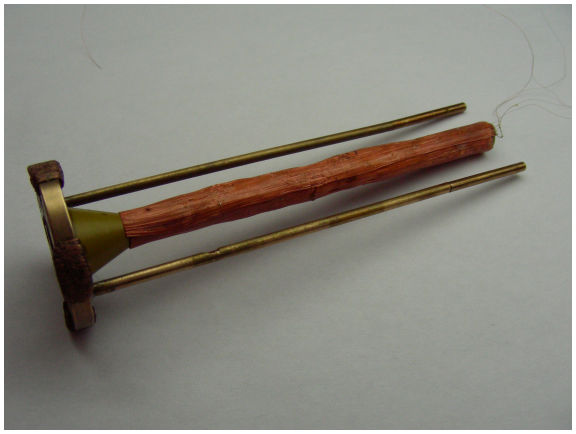

Figure 59: The home-made Faraday-shield wrapped around the pick-up coil system in order to reduce the capacitive coupling between the primary coil and secondary coils. It consists of identical thin insulated Cu-wires glued together with Toluol-diluted GE varnish in order to reduce the presence of eddy currents.

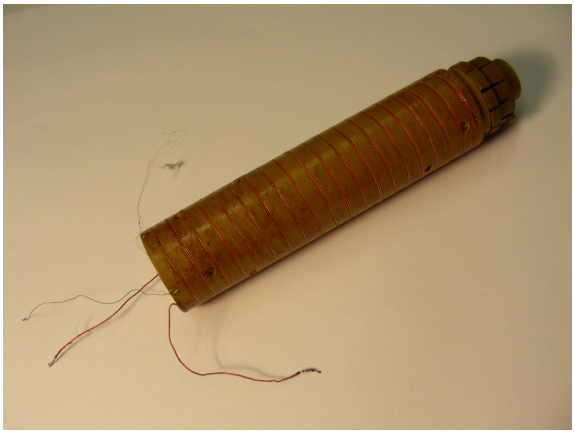

Figure 60: The compensation coil wound around the whole coil system.

### 7.2.2 The mathematical principles of the designed ac-susceptibility experiment

The generated oscillating magnetic field inductance $\mathbf{B} = \mu_0\mathbf{H}$ induces a voltage across a pick-up coil of

$$u(t) = -N\frac{\partial\phi}{\partial t}, \tag{7.26}$$

where $N$ is the number of turns of the coil and $\phi$ is the magnetic flux defined as

$$\phi(t) = \int \mathbf{B}\cdot d\mathbf{A}, \tag{7.27}$$

which simplifies to

$$\phi(t) = |\mathbf{B}|\cdot A \tag{7.28}$$

for a constant magnetic field within the cross section area $A$.
Let us now focus on the pick-up (secondary) coil system. We will refer to the coil in which the sample is placed with index 1 and to the other one with index 2. The additional magnetization $M$ inside the coil now contributes to the local magnetic field $B$, leading to a total field inductance inside the coil 1 of $B_1(t) = \mu_0\,(H(t) + M)$ and a corresponding magnetic flux $\phi(t) = \mu_0\,A_1\,(H(t) + M)$. Since the sample does not entirely fill the coil volume we have to express $M = V_f \cdot m$, with $m$ the magnetization of the sample and $V_f$ the volume-filling factor defined as the relation of the sample- and the coil-volume $V_f = \frac{V_{sample}}{V_{coi}}$. The magnetic

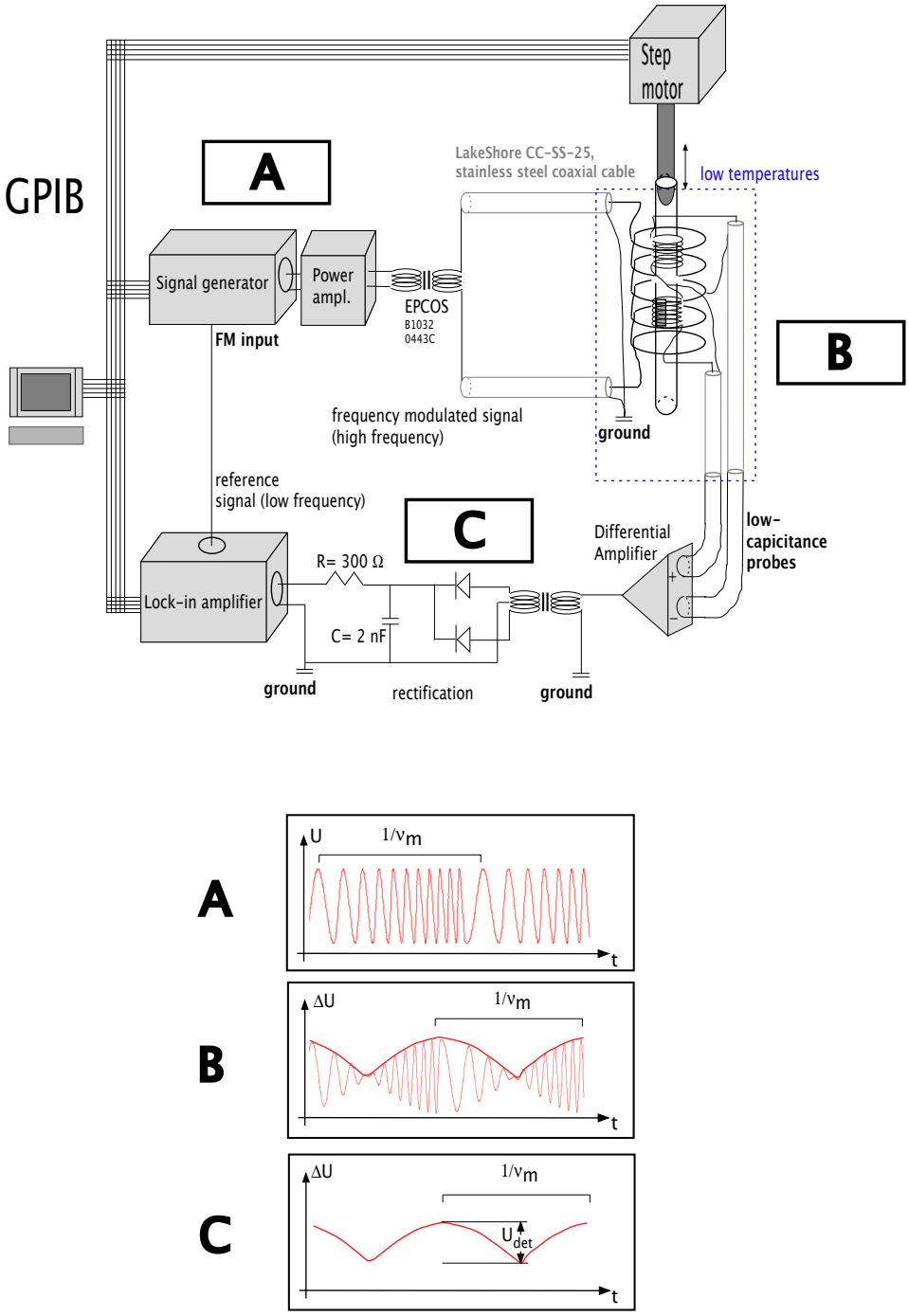


Figure 61: Schematic of the experimental arrangement used for FM ac-susceptibility measurements. For the connections from room temperature down to helium temperatures, stranded stainless-steel coaxial cables were utilized. The whole experiment was controlled by a LabView home-written software, see App. E. The driving signal is frequency-modulated (A). The detected signal (B) is amplified and rectified (C). See text for further explanations.

flux inside the pick-up coils is, therefore,

$$\begin{aligned}\phi_1(t) &= \mu_0 A_1(H(t) \ + \ m \cdot V_f),\\ \phi_2(t) &= \mu_0 A_2(H(t)),\end{aligned} \tag{7.29}$$

respectively. We finally obtain

$$\begin{aligned}u_1(t) &= -N_1\mu_0 A_1\left(\frac{\partial H}{\partial t} + \frac{\partial m}{\partial t}\cdot V_f\right) \quad \text{and}\\ u_2(t) &= N_1\mu_0 A_2\frac{\partial H}{\partial t}\end{aligned} \tag{7.30}$$

for the corresponding induced voltages. The different sign is due to the different winding-directions of the two secondary coils, respectively.
For the time-derivative of the sample-magnetization we can write

$$\frac{\partial m}{\partial t} = \frac{\partial m}{\partial H}\frac{\partial H}{\partial t} = \chi \cdot \frac{\partial H}{\partial t}, \tag{7.31}$$

where we used the definition of the magnetic ac-susceptibility $\chi = \frac{\partial m}{\partial H}$. Considering the magnetic field inside the primary coil $H(t) = H^0_{ac} sin(\omega t)$ to be harmonic, we finally obtain for the absolute voltage difference detected across the two secondary coils

$$\Delta U = \mu_0 A \omega H^0_{ac} N_1 V_f [\chi cos(\omega t) \ - \ \Delta N], \tag{7.32}$$

where $\Delta N = |N_1 - N_2|$ is the absolute difference between the number of turns of the two different coils. We assumed the cross section areas to be identical $A_1 = A_2$. The magnetic-field amplitude $H^0_{ac} = \frac{N^{prim} \cdot I^{prim}}{l^{prim}}$ can be expressed in terms of the current $I^{prim}$ passing through the primary coil, its number of turns $N^{prim}$ and its length $l^{prim}$. Knowing all these parameters, the magnetic susceptibility $\chi$ can now be calculated.
The frequency modulation of the driving signal leads to a modulated magnetic field $H_{\mathrm{FM}}$ inside the primary coil with the following time-dependence

$$H_{\mathrm{FM}}(t) = H^0_{ac} sin[\omega_c t + m_f \cdot sin(\omega_m t)], \tag{7.33}$$

where

$$m_f = \frac{\Delta\omega}{\omega_m} = \frac{2\pi\Delta\nu}{2\pi\nu_m} = \frac{\Delta\nu}{\nu_m} \tag{7.34}$$

is the modulation index defined as the fraction between the peak deviation $\Delta\nu$ and the modulation frequency $\nu_m$.
Without going through the detailed mathematics, Eq. (7.33) can be expressed as

$$H_{\mathrm{FM}}(t) = H^0_{ac} \sum_{n=0}^{\infty} J_n(m_f)[sin(\omega_c - n\omega_m)t + (-1)^n sin(\omega_c + n\omega_m)t], \tag{7.35}$$

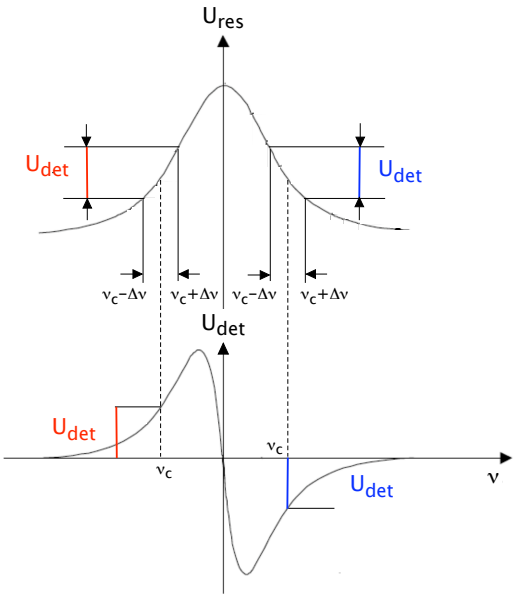


Figure 62: Sketch of a resonance curve and the corresponding measured signal when a frequency-modulation detection technique is used. In this case, the detected signal corresponds to the first derivative of the spectral feature.

with $J_n$ corresponding to the Bessel functions of order $n$ and $\omega_c = 2\pi\nu_c$ being the carrier (angular) frequency. For $m_f \lesssim 1$ one can assume $J_{n\geq 2}(m_f) \approx 0$, see App. F. In this case, the spectral output of an RF-frequency modulated signal consists of a carrier frequency $\omega_c$ and side band frequencies $\omega_c \pm \omega_m$. Consequently, the voltage difference $\Delta U$ across the two pick-up coils varies correspondingly, see Fig. 61. The rectified and low-pass filtered signal $U_{det}$ is now proportional to the intensity of $\Delta U$, which varies with modulation frequency $\omega_m$. The phase-locked (in phase component) is now proportional to the difference in loss experienced by the upper ($\omega = \omega_c + \omega_m$) and the lower ($\omega = \omega_c - \omega_m$) sideband, respectively. Assuming that $\omega_m$ is small compared to the width of the spectral feature of interest, the detected signal $U_{det}$ becomes proportional to the derivative of the (resonance) absorption curve with respect to the frequency [173]

$$U_{det} \propto \frac{\partial \Delta U}{\partial \nu} \Delta\nu, \tag{7.36}$$

see Fig. 62.

### 7.2.3 The measuring procedure and first results

The relevant physical quantities of the ac-susceptibility experiment are the temperature $T$, the dc-magnetic field $H$ and frequency $\nu$. During the measurements, two out of these three quantities were fixed while the third one was varied (swept) over the desired range. Typical measurements were performed sweeping the frequency, while keeping the temperature and

magnetic field at a constant value.
The implementation of a step motor allows us to perform an "in-situ" background subtraction. The sample is, thereby, first moved into one pick-up coil, then a complete measuring run is performed. Subsequently, the sample is moved out of the coil in order to measure the background, see Fig. 63. The consequent subtraction is then performed during the data-analysis [14]. The position of the pick-up coils in respect to the absolute coordinates of the step motor was previously determined by dragging the sample through the entire coil set-up. A characteristic "peak-valley" curve results, which is antisymmetric in respect to the center of the coil arrangement, see Fig. 64. The two extreme values of the curve define the position of the pick-up coils, respectively.
As a first test we used a commercially available quartz crystal ($\chi = -0.62 \cdot 10^{-8} m^3/kg$) with mass $m = 11.42 \times 10^{-3}$ g, volume $V = 9 \times 1.4 \times 0.25\ \mathrm{mm}^3$ and a known resonance-frequency $\nu_{res}$ ∼1 MHz, as a mechanical resonator, see Fig. 65. We measured the magnetic susceptibility of the quartz sample sweeping the carrier-frequency $\nu_c$ through the range in which a resonance phenomenon was expected. The modulation frequency was set to $\nu_m$= 131 Hz, a field amplitude $H^0_{ac} \approx 1.1$ Oe ≈ 89 A/m was reached and the filling factor was $V_f \approx 0.019$. During this measurement, the quartz crystal was floating inside one of the pick-up coils suspended on two cotton wires, which were carefully attached on two soldering joints, one on each side of the crystal.
Expressing the magnetic moment of the sample in terms of the instrumental and sample parameters used to perform this particular measurement, we get

$$m = \frac{U_{det} V_{sample}}{\mu_0 \omega N A V_f}, \tag{7.37}$$

which compared to our data demonstrates that we achieved in zero magnetic field a very high sensitivity of the order of $2 - 4 \times 10^{-13} \mathrm{Am}^2 \sim (= 2 - 4 \times 10^{-10}\ \mathrm{emu})$, almost an order of magnitude better than what is reached in a commercial SQUID magnetometer, see Fig. 65.
Applying higher magnetic fields up to $\mu_0 H = 9$ T, the detected quartz resonance signal vanishes within field-dependent parasitic resonances. It turned out to be not possible to achieve high precision simultaneously at low temperatures and in high magnetic fields. The most difficult aspect was the presence of a field-dependent parasitic background signal of unknown origin. As we see in Fig. 65 on the right side, the high-field data seriously suffer from a large, irreproducible background that makes the search for small resonance features virtually impossible. In this sense, we have to conclude that although we have reached a very high accuracy in zero-magnetic field, the measured high-field spectra are not accurate enough for the intended purpose. In spite of the great effort made to solve this problem we did not manage to locate the noise source within the time reserved for this thesis.

[14] It also possible to perform a measuring run using a "point-by-point subtraction" method, i.e., for every set frequency (or temperature / dc-magnetic field) value, the sample is moved first in and then out of the pick-up coil.

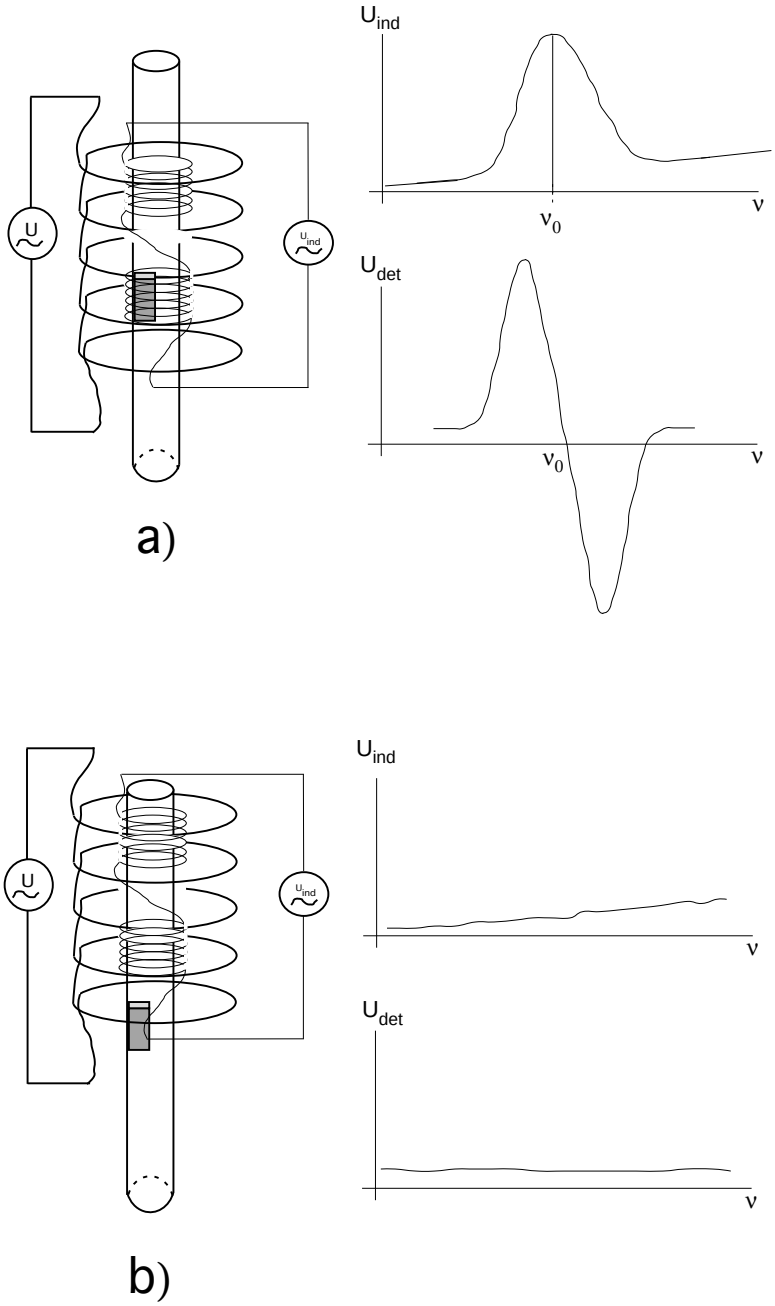


Figure 63: A schematic representation of the typical measuring procedure performed during RF-susceptibility measurements. a) As the sample is placed into one of the pick-up coils a measuring run is completed. b) A background measurement is performed after the sample has moved out of coil. It is also possible to accomplish an "in-situ" (point-by-point) background measurement. The frequency-modulation of the driving signal leads to a detected signal $U_{det}$ corresponding to the first derivative of the spectral feature with respect to the frequency.

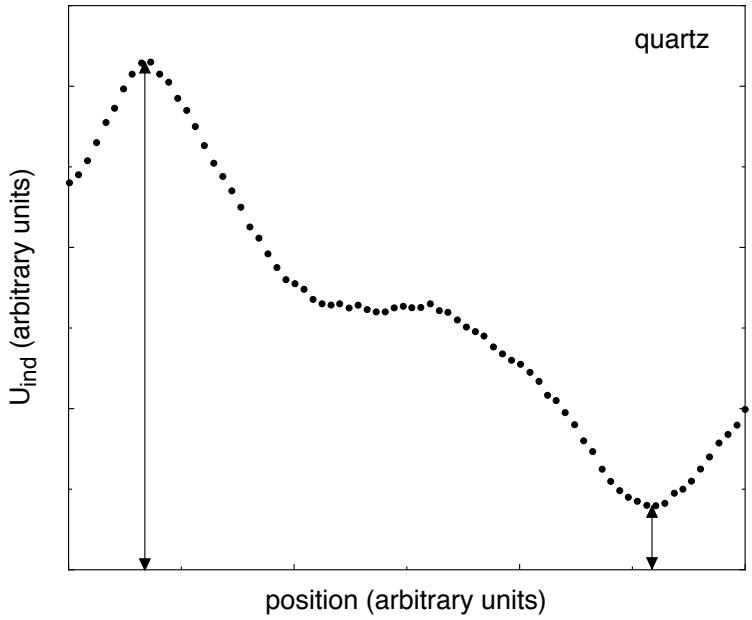


Figure 64: A position sweep of the quartz sample. Since the two pick-up coils are counterwound, the resulting curve is antisymmetric in respect to the center of the coil arrangement. The two extremes define the center of the pick-up coils, respectively.

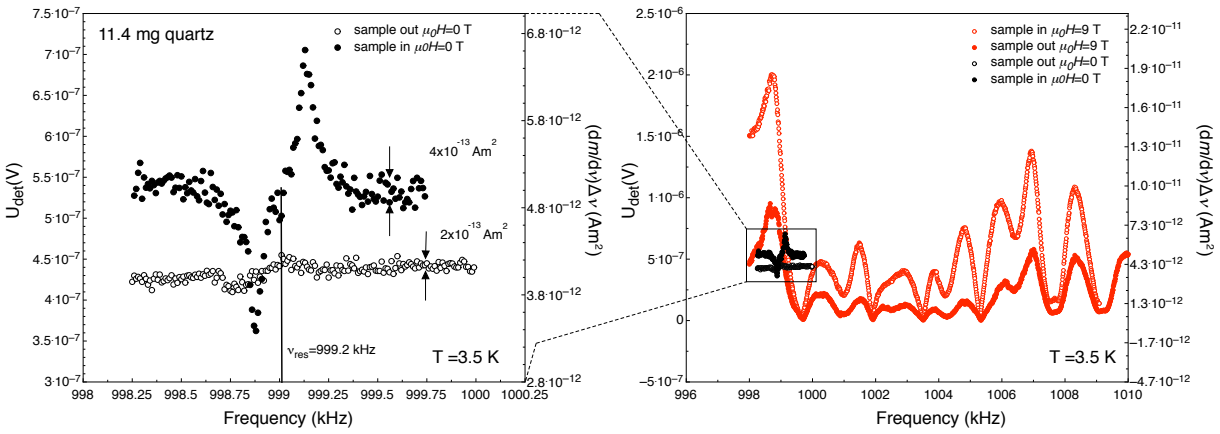


Figure 65: (left) The detected signal $U_{det}$ (left y-scale in Volt) and the corresponding total magnetic moment (right y-scale in A/m), respectively, of the ac-susceptibility measurement on the quartz crystal in zero dc magnetic field. In zero dc-magnetic field, a noise level of the order of $2-4 \times 10^{-13}\mathrm{Am}^2 \approx 2-4 \times 10^{-10}$ emu determines the resolution limit for this experiment. The detected resonance frequency is $\nu_{res}$ = 998.8 kHz. (right) Comparison of the zero-field raw data (black dots) and the data taken in $\mu_0 H$ = 9 T (red dots) demonstrates the huge field-dependent background noise. In zero magnetic field, the quartz resonance signal vanishes within parasitic noise resonances for corresponding high-field measurements.

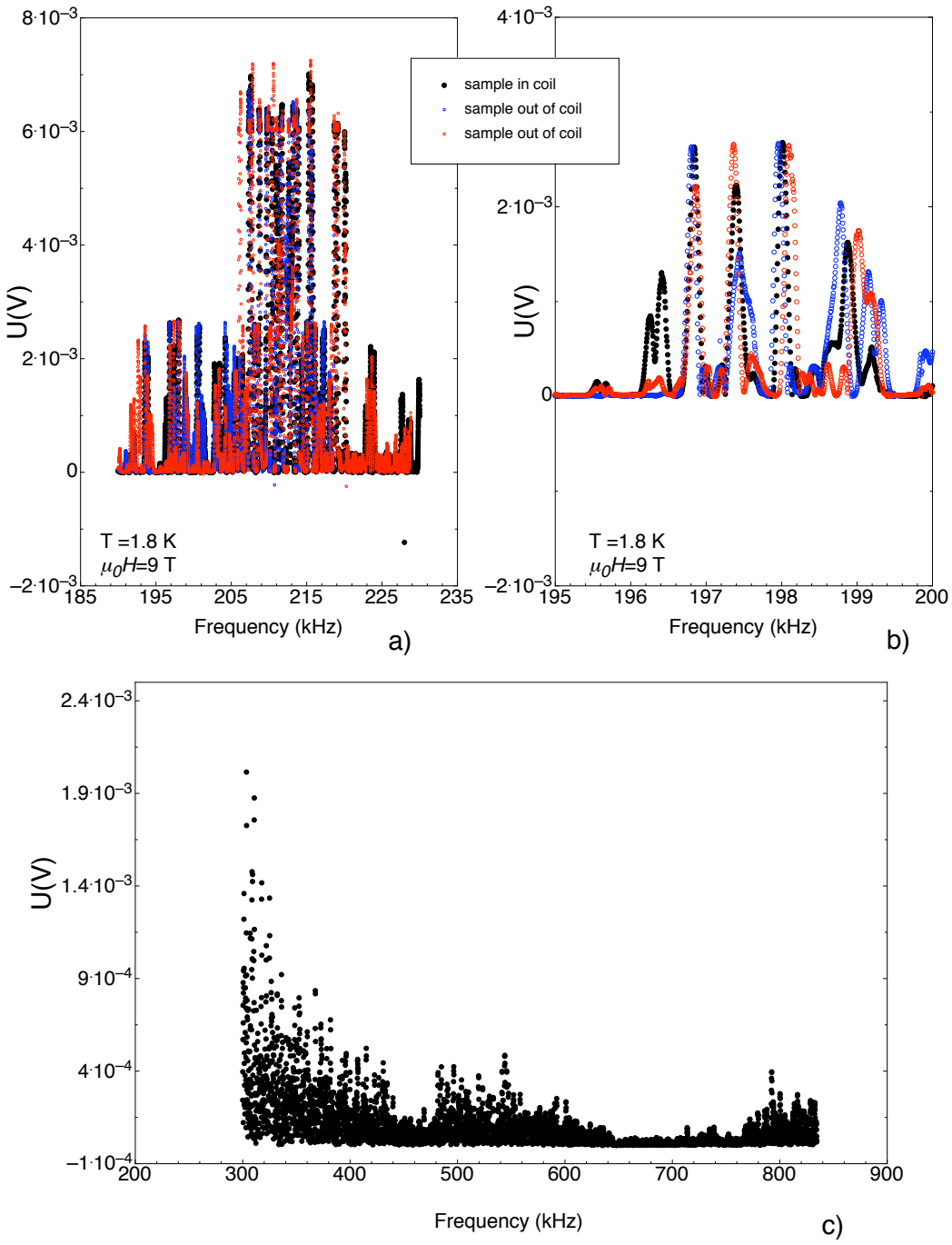


Figure 66: A measured spectrum for $TlCuCl_3$. (a)-(b) The same spectrum in a more restricted frequency range. The black dots correspond to the measured data while the sample was placed into one detection coil. The red and the blue dots are data taken as the sample was outside the detection coil. A quantitative satisfactory reproducibility is not achieved. c) A measured spectrum in a extended frequency range. The obtained resolution limit is not satisfactory.

Nonetheless, analogous measurements were performed on $\mathrm{TlCuCl_3}$ in order to detect second-sound modes. From dc-magnetization measurements we estimated the amplitude of a possible emerging peak-like feature due to (absorption) resonance-like phenomena to $\Delta M \cdot V_f \approx 0.7 \cdot 10^{-3}$ emu $\cdot 0.17 \approx 1.2 \cdot 10^{-4}$ emu $= 1.2 \cdot 10^{-7}$ Am$^2$ for $\mu_0 H$= 9 T, where $\Delta M$ is the magnetization contribution arising from the condensed particles, i.e., $\Delta M = M(T = 2\mathrm{K}) - M(T = T_c^{BE})$ and $V_f = \frac{V_{sample}}{V_{pick-up}}$ is the volume filling factor with respect to the used $\mathrm{TlCuCl_3}$-specimen. As expected, the non-reproducible background noise at higher magnetic fields and lower temperatures did not allow to draw of any reasonable conclusions, see Fig. 66. In this sense, there is no sign of "magnetic superfluidity" in $\mathrm{TlCuCl_3}$, yet.

A few more concluding thoughts on the "search for magnetic superfluidity" project are appropriate at this point.

The experimental proof for the existence of macroscopic coherence in a magnetic insulator (in our case in $\mathrm{TlCuCl_3}$) turned out to be a rather laborious undertaking. The reasons for that are manifold.

We were aware in the beginning that the design and development of a complete new measuring set-up is a time-consuming effort. However, a posteriori, we may assert that we have certainly underestimated the possible difficulties we might have been dealing with in realizing such a set-up. We only slowly succeeded in appraoching the desired functionality of the set-up, essentially by "trial and error". In this sense, we did not manage to entirely solve the remaining problems described above within the time reserved for this thesis. However, I want to note that the idea of detecting a "superfluid component" in magnetic condensates, in order to prove the presence of a macroscopic coherent state, was certainly a new and pioneering concept at the time we started this project. Only a year ago we became aware of a publication, see Ref. [166], which is explicitely mentioning out the possible existence of a spin-supercurrent in such materials. In this sense, we hope that our work and experience will be useful to eventually succeed in detecting "magnetic superfluidity" in magnetic Bose-Einstein condensates.

# 8 Conclusions and outlook

In the last years, the concept of Bose-Einstein condensation, i.e., the occupation of a single quantum state by a macroscopic number of bosons, has been extended from real bosonic particles to various types of quasiparticles with integer total spin. Experimental observations in a number of quantum spin systems can be explained within this theory, e.g., by a condensation of triplet states in dimerized spin-1/2 systems such as $\mathrm{TlCuCl_3}$. The bosonic character of the these magnetic quasiparticles allows the description of this spin-dimer system as a weakly interacting Bose gas.

Within the scope of this Ph.D thesis, we have presented an analysis of magnetization $M(T, H)$-data of $\mathrm{TlCuCl_3}$ and we calculated the density of condensed particles $\psi_0^\dagger \psi_0 = n_c(T = 0)$. The percentage of $n_c(0)$ with respect to the total density of triplons $n(0)$ is approximately 98% right above the critical field $H_c$ and slightly decreasing with increasing magnetic field. We demonstrated that this fraction is the same for both $\mathbf{H} \parallel b$ and $\mathbf{H} \parallel [201]$ if we assume the presence of a small number of intrinsic $S = 1$ magnetic moments that are not part of the Bose-Einstein condensate of triplons even at the lowest temperatures.

In addition, we have analyzed the spontaneous symmetry breaking in a Bose gas of triplet excitations in a low-dimensional spin system based on simple functional methods in the classical limit. Our results are in perfect agreement with former theoretical predictions based on HF approximated computations. Various experimental findings in $\mathrm{TlCuCl_3}$ such as the occurrence and the magnitude of an anisotropy gap in ESR data and a slight lattice distortion at the magnetic phase transition can be easily explained. We predict that the anisotropy gap can be suppressed by the application of a moderate uniaxial pressure perpendicular to the magnetic field direction. Furthermore, from our findings we can conclude that magnetic BEC systems might be intrinsically unstable towards a spontaneous anisotropic (lattice) distortion perpendicular to the external magnetic field, and that the evolving of an anisotropy gap for $H > H_{c1}$ observed in $\mathrm{TlCuCl_3}$ might be a consequence of the existence of such an anisotropy. Since ESR-measurements turned out to be a very reliable measuring method in order to detect possible existing quasiparticle gaps above the critical field $H_{c1}$, such measurements under pressure would certainly clarify if the anisotropic gap can be varied, i.e., enhanced, decreased or even closed by applying uniaxial pressure.

Nonetheless, one of the major aims of this Ph.D thesis was to set up an experiment in order to determine a superfluid component in magnetic Bose-Einstein condensates and especially in $\mathrm{TlCuCl_3}$ by means of the detection of coherent modes present in BE-condensates. Various designs were considered, constructed and tested. From our experience, the most promising set-up is presented in the last part of this work. We built an ac-susceptometer to perform high-frequency (0.2-2 MHz) magnetic-susceptibility measurements. The set-up has been continuously improved in the last two years to reach the desired sensitivity. It turned out to be

a difficult task to achieve high precision at low temperatures and high magnetic fields. The most difficult aspect, which we are still dealing with, was the avoidance of field dependent unreproducible background.

However, the presence of the anisotropy gap in $\mathrm{TlCuCl_3}$ for $H > H_{c1}$ has fatal consequences regarding the detection of a magnetic superfluid component in this particular frequency region. The resulting energy gap in the excitation spectrum of such coherent modes is of the order of $\sim$ 0.1-0.2 meV which corresponds to an excitation frequency of $\nu \approx 20 - 30$ GHz. Therefore, corresponding experiments at much higher frequencies than used here are required in order to detect such a superfluid component.

# 9 Acknowledgements

Firstly, I would like to express my deep gratitude to Prof. Dr. Andreas Schilling. It was always a pleasure discussing my ongoing work, including the problems and failures as well as successes (a few) with you. You were patient and encouraged me as things did not go that well. Thank you for that. You were interested, innovative and extremely devoted as exciting results were obtained. Thank you for your support. I really appreciated all of your suggestions and corrections (I realize there were quite a few!). I will definitely use this experience and all that I have learned from you with me in future.

Thank you to Prof. Dr. Hugo Keller and Dr. Jorge Gavilano for finding some time in their tight schedule and assist me in the last part of my thesis.
I would like to extend my appreciation to Dr. Josef Roos for his technical and overall support in the lab during some really frustrating times. You always found positive words for my job, even when little progress was made. I don't know if these were lies but they definitely kept my morale up!
A big thank you to Dr. Karl Krämer, as well. Without your crystals no measurements would have been possible.

Also a big thank you to my laboratory mates in and outside our research group. Mark, Andreas, Holger, Stefan, Simon and Stephen. Simon, many thanks for dragging me out of those four walls to our midday runs, especially when I was rather unmotivated. We were in quite good shape then!
Thanks to Claudio, Marco and Fabio, the Italian relations in the Institute. You showed me how to avoid taking this job too seriously (well, at least you, Marco!).

Many thanks, as well to the team of the mechanics workshop. You were always cooperative and understanding when something had to be accomplished quickly. Even more amazing, is how you managed to finish all the work pieces, in spite of my extremely accurate sketches! I definitely made some good friends (down) there.
Thanks to Peter Soland from the electronic workshop for his ideas and interest to the project, as well as his technical contributions.

My thanks to Andy Silver who went through all of these pages in search of weird language. It must have been fun to tackle a work by an Italian, born in Switzerland and writing in English. You can imagine the mess! Thanks Andy!

Thank you to all of my friends, quite a collection actually, who make it a funnier life! I

want to certainly thank to all the guys of the Racing Club ZH. Racing for ever! We are like a fine, rare Bordeaux- the older, the better!

A special thank you to my family for all of their support during these last years. I really appreciate! I hope to have much more time to spend all together now!
Anina, you have been in my life now for five years. Thanks for making it lovable and sweet, funny and sad, easy and difficult. I hope to be part of your life for many more years. Now it would naturally end with the ”L” word but this is a thesis so I’ll just say it at home when nobody else is listening or to be more accurate, reading!

# References

[1] M. Planck, *Ueber das Gesetz der Energieverteilung im Normalspectrum*, Adv. Phys. **309**, 553 (1901).

[2] H. Hertz, *Ueber einen Einfluss des ultravioletten Lichtes auf die electrische Entladung*, Adv. Phys. **267**, 983 (1887).

[3] W. Hallwachs, *Ueber den Einfluss des Lichtes auf electrostatisch geladene Körper*, Adv. Phys. **269**, 301 (1888).

[4] A. Einstein, *Ueber einen die Erzeugung und Verwandlung des Lichtes betreffenden heuristischen Gesichtspunkt*, Adv. Phys. **322**, 132 (1905).

[5] L. De Broglie, *Radiation-waves and quanta*, Comptes rendus **177**, 507 (1923).

[6] A. Einstein, *Quantentheorie des einatomigen idealen Gases*, Sitzungber. Preuss. Akad. Wiss. **1924**, 261 (1924).

[7] W. Ketterle, *When atoms behave as waves: Bose-Einstein condensation and the atom laser*, Rev. Mod. Phys. **74**, 1131 (2002).

[8] M.H. Anderson, J.R. Ensher, M.R. Matthews, C.E. Wieman and E.A. Cornell, *Observation of Bose-Einstein condensation in a dilute atomic vapor*, Science **269**, 198 (1995).

[9] K.B. Davis, M.-O. Mewes, M.R. Andrews, N.J. van Druten, D.S. Durfee, D.M. Kurn and W. Ketterle, *Bose-Einstein condensation in a gas of sodium atoms*, Phys. Rev. Lett. **75**, 3969 (1995).

[10] C.C. Bradley, C.A. Sackett, J.J. Tollett and R.G. Hulet, *Evidence of Bose-Einstein condensation in an atomic gas with attractive interactions*, Phys. Rev. Lett. **75**, 1687 (1995).

[11] C.C. Bradley, C.A. Sackett and R.G. Hulet, *Bose-Einstein condensation of lithium: Observation of limited condensate number*, Phys. Rev. Lett. **78**, 985 (1997).

[12] S. Chu, *The manipulation of neutral particles*, Rev. Mod. Phys. **70**, 685 (1998).

[13] C.N. Cohen-Tannoudji, *Manipulating atoms with photons*, Rev. Mod. Phys. **70**, 707 (1998).

[14] W.D. Phillips, *Laser cooling and trapping of neutral atoms*, Rev. Mod. Phys. **70**, 721 (1998).

[15] H.F. Hess, *Evaporative cooling of magnetically trapped and compressed spinpolarized hydrogen*, Phys. Rev. B **34**, 3476 (1986).

[16] F. London, *The lambda-phenomenon of liquid helium and the Bose-Einstein degeneracy*, Nature (London) **141**, 643 (1938).

[17] L. Tisza, *Transport phenomena in helium II*, Nature (London) **141**, 913 (1938).

[18] L.D. Landau, *The theory of superfluidity of helium II*, J. Phys. (Moscow) **5**, 71 (1941).

[19] N.N. Bogoliubov, *Theory of superfluidity*, J. Phys. (Moscow) **11**, 23 (1947).

[20] P. Sokol, *in Bose-Einstein Condensation, chapter 4, edited by A. Griffin, D. Snoke and S. Stringari*, Cambridge University Press, Cambridge , 51 (1995).

[21] D.M. Ceperley, *Path integrals in the theory of condensed helium*, Rev. Mod. Phys. **67**, 279 (1995).

[22] E.A. Burt, R.W. Ghrist, C.J. Myatt, M.J. Holland, E.A. Cornell and C.E. Wieman, *Coherence, correlations, and collisions: What one learns about Bose-Einstein condensates from their decay*, Phys. Rev. Lett. **79**, 337 (1997).

[23] E.W. Hagley, L. Deng, M. Kozuma, M. Trippenbach, Y.B. Band, M. Edwards, M.R. Doery, P.S. Julienne, K. Helmerson, S.L. Rolston and W.D. Phillips, *Measurement of the coherence of a Bose-Einstein condensate*, Phys. Rev. Lett. **83**, 3112 (1999).

[24] J. Denschlag, J.E. Simsarian, D.L. Feder, C.W. Clark, L.A. Collins, J. Cubizolles, L. Deng, E.W. Hagley, K. Helmerson, W.P. Reinhardt, S.L. Rolston, B.I. Schneider and W.D. Phillips, *Generating solitons by phase engineering of a Bose-Einstein condensate*, Science **287**, 97 (2000).

[25] M.R. Matthews, B.P. Anderson, P.C. Haljan, D.S. Hall, C.E. Wieman and E.A. Cornell, *Vortices in a Bose-Einstein condensate*, Phys. Rev. Lett. **83**, 2498 (1999).

[26] I. Affleck, *Bose condensation in quasi-one-dimensional antiferromagnets in strong magnetic fields*, Phys. Rev. B **43**, 3215 (1991).

[27] T. Nikuni, M. Oshikawa, A. Oosawa and H. Tanaka, *Bose-Einstein Condensation of Dilute Magnons in* $\mathrm{TlCuCl_3}$ , Phys. Rev. Lett. **84**, 5868 (2000).

[28] Ch. Rüegg, N. Cavadini, A. Furrer, H.-U.Gdel, K. KrŁmer, H. Mutka, A. Wildes, K. Habicht and P. Vorderwisch, *Bose-Einstein condensation of the triplet states in the magnetic insulator* $\mathrm{TlCuCl_3}$ , Nature (London) **423**, 62 (2003).

[29] J. Kasprzak, M. Richard, S. Kundermann, A. Baas, P. Jeambrun, J.M.J. Keeling, F. M. Marchetti, M.H. Szymanska, R. Andr, J.L. Staehli, V. Savona, P.B. Littlewood, B. Deveaud and L.S. Dang, *Bose-Einstein condensation of exciton polaritons*, Nature (London) **443**, 409 (2006).

[30] S.O. Demokritov, V.E. Demidov, O. Dzyapko, G.A. Melkov, A.A. Serga, B. Hillebrands and A.N. Slavin, *Bose-Einstein condensation of quasi-equilibrium magnons at room temperature under pumping*, Nature (London) **443**, 430 (2006).

[31] D. Snoke, *Coherent questions*, Nature (London) **443**, 403 (2006).

[32] V.N. Glazkov, A.I. Smirnov, H. Tanaka and A. Oosawa, *Spin-resonance modes of the spin-gap magnet* $\mathrm{TlCuCl_3}$ , Phys. Rev. B **69**, 184410 (2004).

[33] C.T. Lane, H.A. Fairbank and W.M. Fairbank, *Second Sound in Liquid Helium II*, Phys. Rev. **71**, 600 (1947).

[34] V.S. Zapf, D. Zocco, B.R. Hansen, M. Jaime, N. Harrison, C.D. Batista, M. Kenzelmann, C. Niedermayer, A. Lacerda and A. Paduan-Filho, *Bose-Einstein Condensation of S=1 Nickel Spin Degrees of Freedom in* $\mathrm{NiCl_2 - 4SC((NH)_2)_2}$, Phys. Rev. Lett. **96**, 077204 (2006).

[35] T. Radu, H. Wilhelm, V. Yushankhai, D. Kovrizhin, R. Coldea, Z. Tylczynski, T. Lühmann and F. Steglich, *Bose-Einstein Condensation of Magnons in* $\mathrm{Cs_2CuCl_4}$, Phys. Rev. Lett. **95**, 127202 (2005).

[36] S.N. Bose, *Plancks Gesetz und Lichtquantenhypothese*, Z. Phys. **26**, 178 (1924).

[37] N. Hugenholtz and D. Pines, *Ground-State Energy and Excitation Spectrum of a System of Interacting Bosons*, Phys. Rev. **116**, 489 (1959).

[38] J.F. Annett, *Superconductivity, Superfluids and Condensates*, Oxford University Press, 2004.

[39] A.J. Leggett, *Quantum liquids*, Oxford Oxford University Press, 2006.

[40] C. Cohen-Tannoudji, B. Diu and F. Lalo, *Quantenmechnik 1*, Berlin De Gruyter, 1997.

[41] F. Schwabl, *Quantenmechnik 2*, Springer Verlag, 2000.

[42] O. Penrose and L. Onsager, *Bose-Einstein Condensation and Liquid Helium*, Phys. Rev. **104**, 576 (1956).

[43] K. Huang, *in Bose-Einstein Condensation, chapter 3, edited by A. Griffin, D. Snoke and S. Stringari*, Cambridge University Press, Cambridge , 33 (1995).

[44] A.J. Leggett, *in Bose-Einstein Condensation, chapter 19, edited by A. Griffin, D. Snoke and S. Stringari*, Cambridge University Press, Cambridge , 454 (1995).

[45] J. Goldstone, A. Salam and S. Weinberg, *Broken Symmetries*, Phys. Rev. **127**, 965 (1962).

[46] M.J. Buckingham and W.M. Fairbank, *The Nature of the Lambda Transition*, Prog. Low Temp. Phys. **3**, 80 (1961).

[47] W.H. Keesom, *On the heat conductivity of liquid helium*, Physica **3**, 359 (1936).

[48] B.V. Rollin, *New measurements on the specific heat of liquid helium*, Physica **2**, 557 (1935).

[49] J.F. Allen, R. Peierls and Z. Uddin, *Heat conduction in liquid helium*, Nature (London) **140**, 62 (1937).

[50] J.F. Allen and A.D. Misener, *Flow of liquid He II*, Nature (London) **141**, 75 (1938).

[51] P. Kapitza, *Viscosity of liquid helium below the lambda point*, Nature (London) **141**, 74 (1938).

[52] P.E. Sokol, *in Bose-Einstein Condensation, chapter 4, edited by A. Griffin, D. Snoke and S. Stringari*, Cambridge University Press, Cambridge , 51 (1995).

[53] K. Huang, *in Bose-Einstein Condensation, chapter 4, edited by A. Griffin, D. Snoke and S. Stringari*, Cambridge University Press, Cambridge , 34 (1995).

[54] P.C. Hohenberg and P.C. Martin, *Microscopic theory of superfluid helium*, Ann. Phys. **94**, 291 (1965).

[55] J. Gavoret and P. Noziéres, *Structure of the perturbation expansion for the bose liquid at zero temperature*, Ann. Phys. **28**, 349 (1964).

[56] J.M. Kosterlitz and D.J. Thouless, *Ordering, metastability and phase transitions in two-dimensional systems*, J. Phys. C: Solid State Phys. **6**, 1181 (1973).

[57] D.J. Bishop and J.D. Reppy, *Study of the Superfluid Transition in Two-Dimensional $^4$He Films*, Phys. Rev. Lett. **40**, 1727 (1978).

[58] J.O. Wilhelm, A.D. Misener and A.R. Clark, *The Viscosity of Liquid Helium*, Proc. Roy. Soc A. **151**, 342 (1935).

[59] E. Andronikashvili, *Direct observation of two types of motion in helium II*, J. Exper. Theor. Phys. **18**, 429 (1948).

[60] G. Blatter, *Theorie der Wärme, Vorlesungsskript WS 97/ 98*.

[61] P. Noziéres and D. Pines, *The theory of Quantum Liquids*, (1990).

[62] C.J. Pethik and H. Smith, *Bose-Einstein Condensation in dilute gases*, (2002).

[63] R. Cowley and A. Woods, *Inelastic Scattering of Thermal Neutrons from Liquid Helium*, Can. J. Phys. **49**, 177 (1971).

[64] L.J. Campbell, *Relation between the condensate fraction and the surface tension of superfluid* $^4He$, Phys. Rev. B **27**, 1913 (1983).

[65] I.M. Khalatnikov, *An introduction to the theory of superfluidity*, (1989).

[66] A. Griffin and E. Zaremba, *First sound and second sound in a uniform Bose gas*, Phys. Rev. A **56**, 4839 (1997).

[67] P. Lemmens G. Güntherodt and C. Gros, *Magnetic Light Scattering in low-dimensional quantum spin systems*, Phys. Reports **375**, 1 (2003).

[68] S. Sachdev, *Quantum Magnetism and Criticality*, Nature Physics (London) **4**, 173 (2008).

[69] K. Schmidt and G. Uhrig, *Excitations in One-Dimensional* $S = \frac{1}{2}$ *Quantum Antiferromagnets*, Phys. Rev. Lett. **90**, 227204 (2003).

[70] S. Sachdev, *in Quantum Magnetism, chapter 9, edited by U. Schollwöck, J. Richter, D.J.J. Farnell and R.F. Bishop*, Springer-Verlag, Berlin Heidelberg , 381 (2004).

[71] T. Giamarchi and A. Tsvelik, *Coupled ladders in a magnetic field*, Phys. Rev. B **59**, 11398 (1998).

[72] S. Wessel and S. Haas, *Three dimensional ordering in weakly coupled antiferromagnetic ladders*, Phys. Rev. B **62**, 316 (2000).

[73] S. Wessel, M. Olshanii and S. Haas, *Field- Induced Magnetic Order in Quantum Spin Liquids*, Phys. Rev. Lett. **87**, 206407 (2001).

[74] T. Barnes, E. Dagotto, J.Riera and E.S Swanson, *Excitation spectrum of Heisenberg spin ladders*, Phys. Rev. B **47**, 3196 (1997).

[75] M. Troyer, H. Tsunetsugu and D. Würtz , *Thermodynamics and spin gap of the Heisenberg ladder calculated by the look-ahead Lannczos algorithm*, Phys. Rev. B **50**, 13515 (1994).

[76] T. Rice, *To Condense or Not to Condense*, Science **298**, 760 (2002).

[77] H.-J. Mikeska and A.K. Kolezhuk, *in Quantum Magnetism, chapter 1, edited by U. Schollwöck, J. Richter, D.J.J Farnell and R.F Bishop*, Springer-Verlag, Berlin Heidelberg , 58 (2004).

[78] M. Y. M. Oshikawa and I. Affleck, *Magnetization Plateaus in Spin Chains: "Haldane Gap" for Half-Integer Spins*, Phys. Rev. Lett. **78**, 1984 (1997).

[79] W. Shiramura, K. Takatsu, B. Kurniawan, H. Tanaka, H. Uekusa, Y. Ohashi, K. Takizawa, H. Mitamura and T. Goto, *Magnetization Plateaus in* $NH_4CuCl_3$, J. Phys. Soc. Japan **67**, 1548 (1998).

[80] M. Matsumoto, *Microscopic model for the magnetization plateaus in* $NH_4CuCl_3$, Phys. Rev. B **68**, 180403(R) (2003).

[81] G. cha, M.-H. Julien, Y. Fagot-Revurat, M.E. Hanson, L.P. Levy, C. Berthier, M. Horvatić and O. Piovesana, *Zero temperature phase transitions in spin-ladders: Phase diagram and dynamical studies of* $Cu_2(C_5H_{12}N_2)_2Cl_4$, Eur. Phys. J. B **6**, 167 (1998).

[82] S. Wessel and S. Haas, *Magnetic field induced Ordering in Quasi-One Dimensional Quantum Magnets*, Eur. Phys. J. B **16**, 393 (2000).

[83] Y. Chen, Z. Honda, A. Zheludev, C. Broholm, K. Katsumata and S. M. Shapiro, *Field-Induced Three- and Two-Dimensional Freezing in a Quantum Spin Liquid*, Phys. Rev. Lett. **86**, 1618 (2001).

[84] Z. Honda, K. Katsumata, Y. Nishiyama and I. Harada, *Field-induced long-range ordering in an* $S = 1$ *quasi-one-dimensional Heisenberg antiferromagnet*, Phys. Rev. B **63**, 064420 (2001).

[85] A. Zheludev, Z. Honda, C. L. Broholm, K. Katsumata, S. M. Shapiro, A. Kolezhuk, S. Park and Y. Qiu, *Massive triplet excitations in a magnetized anisotropic Haldane spin chain*, Phys. Rev. B **68**, 134438 (2003).

[86] H. Tsujii, Z. Honda, B. Andraka, K. Katsumata and Y. Takano, *High-field phase diagram of the Haldane-gap antiferromagnet* $\mathrm{Ni(C_5H_{14}N_2)_2N_3(PF_6)}$, Phys. Rev. B **71**, 014426 (2005).

[87] M. Hagiwara, H. Tsujii, C. R. Rotundu, B. Andraka, Y. Takano, N. Tateiwa, T. C. Kobayashi, T. Suzuki, and S. Suga, *Tomonaga-Luttinger Liquid in a quasi-one - dimensional $S = 1$ antiferromagnet observed by specific heat measurements*, Phys. Rev. Lett. **68**, 147203 (2006).

[88] F. Haldane, *Luttinger-Liquid theory of one dimensional quantum fluids: I. Properties of the Luttinger model and their extension to the general 1D interacting spinless Fermi gas*, J. Phys. C: Solid State Phys. **68**, 2585 (2001).

[89] T. Matsubara and H. Matsuda, *Lattice model of liquid helium*, Prog. Theor. Phys. **16**, 569 (1956).

[90] S. E. Sebastian, *Bose-Einstein condensation in spin-dimer compounds*, PhD thesis, Stanford University, 2006.

[91] M. Matsumoto, B. Normand, T. M. Rice and M. Sigrist, *Magnon dispersion in the field-induced magnetically ordered phase of $TlCuCl_3$*, Phys. Rev. Lett. **89**, 077203 (2002).

[92] A. Furrer and C. Rüegg, *Bose-Einstein condensation in magnetic materials*, Physica B **385-386**, 295 (2006).

[93] H. Tanaka, F. Yamada, T. Ono, T. Sakakibara, Y. Uwatoko, A. Oosawa, K. Kakurai and K. Goto, *Magnetic quantum phase transition from gapped spin liquid state in $TlCuCl_3$*, J. Magn. Magn. Mat. **310**, 1343 (2007).

[94] T. Giamarchi, C. Rüegg and O. Tchernyshyov, *Bose-Einstein Condensation in Magnetic Insulators*, Nature Physics (London) **4**, 198 (2008).

[95] J. Sirker, A. Weie and O.P. Sushkov, *The Field - Induced Magnetic Ordering transition in $TlCuCl_3$*, J. Phys. Soc. Japan **74**, 054423 (2005).

[96] W. Shiramura, K. Takatsu, H. Tanaka, K. Kamishima, M. Takahashi, H. Mitamura and T. Goto, *High-Field Magnetization Processes of Double Spin Chain Systems $KCuCl_3$ and $TlCuCl_3$*, J. Phys. Soc. Japan **66**, 1900 (1997).

[97] T. Nakamura and K. Okamoto, *Theoretical analysis of the experiments on the double-spin-chain compound $KCuCl_3$*, Phys. Rev. B **58**, 2411 (1998).

[98] G. Chaboussant, M.-H. Julien, Y. Fagot-Revurat, L. P. Lvy, C. Berthier, M. Horvatić and O. Piovesana, *Identification of Nuclear Relaxation Processes in a Gapped Quantum Magnet: $^1H$ NMR in the $S = \frac{1}{2}$ Heisenberg Ladder $Cu_2(C_5H_{12}N_2)_2Cl_4$*, Phys. Rev. Lett. **79**, 925 (1997).

[99] B.C. Watson, V.N. Kotov, M.W. Meisel, D.W. Hall, G.E. Granroth, W.T. Montfrooij, S.E. Nagler, D.A Jensen, R. Backov, M.A. Petruska, G.E. Fanucci and D.R. Talham, *Magnetic Spin Ladder $(C_5H_{12}N)_2CuBr_4$: High-Field Magnetization and Scaling near Quantum Criticality*, Phys. Rev. Lett. **86**, 5168 (2001).

[100] M. Jaime, V.F. Correa, N. Harrison, C.D. Batista, N. Kawashima, Y. Kazuma, G.A. Jorge, R. Stern, I. Heinmaa, S. A. Zvyagin, Y. Sasago, and K. Uchinokura, *Magnetic-field-induced condensation of triplons in Han purple pigment $BaCuSi_2O_6$*, Phys. Rev. Lett. **93**, 087203 (2004).

[101] A.K. Kolezhuk, *Continuum-field description of one-dimensional dimerized spin-1/2 Heisenberg antiferromagnets*, Phys. Rev. B **53**, 318 (1996).

[102] M. Crisan, I. Tifrea, D. Bodea, and I. Grosu , *Field-induced Bose-Einstein condensation of interacting dilute magnons in the three-dimensional spin systems: A renormalization-group study*, Phys. Rev. B **72**, 184414 (2005).

[103] G. Misguich and M. Oshikawa, *Bose-Einstein condensation of magnons in $TlCuCl_3$. Phase diagram and specfiic heat from a self-consistent Hartree-Fock caluculation with a realistic relation*, J. Phys. Soc. Japan **73**, 3429 (2004).

[104] M.T. Batchelor, X.-W. Guan, N. Oelkers and Z. Tsuboi, *Integrable Models and quantum spin ladders: comparison between theory and experiment for the strong coupling ladder compounds*, arXiv:cond-mat/ **0512489v3** (2007).

[105] M. Matsumoto, B. Normand, T. M. Rice and M. Sigrist , *Field and pressure-induced magnetic quantum phase transition in $TlCuCl_3$*, Phys. Rev. B **69**, 054423 (2004).

[106] N. Cavadini, G. Heigold, W. Henggeler, A. Furrer, H.-U. Güdel, K. Krämer and H. Mutka , *Magnetic excitations in the quantum spin system $TlCuCl_3$*, Phys. Rev. B **63**, 172414 (2001).

[107] J. Sirker, A. Weie and O.P. Sushkov, *Consequences of spin-orbit coupling for the Bose-Einstein condensation of magnons*, Europhys. Lett. **68**, 275 (2004).

[108] E. Ya. Sherman, P. Lemmens, B. Busse, A. Oosawa and H. Tanaka, *Sound Attenuation Study on the Bose-Einstein Condensation of Magnons in $TlCuCl_3$*, Phys. Rev. Lett. **91**, 057201 (2003).

[109] K.M. Diederix, H.W. J. Blöte, J.P. Groen, T.O. Klaassen, and N.J. Poulis, *Theoretical and experimental study of the magnetic properties of the singlet-ground-state system $Cu(NO_3)_2 \cdot 2.5H_2O$: An alternating linear Heisenberg antiferromagnet*, Phys. Rev. B **19**, 420 (1979).

[110] F.D.M. Haldane, Bull. Am. Phys. Soc. **27**, 181 (1982).

[111] F.D.M. Haldane, *Nonlinear Field Theory of Large-Spin Heisenberg Antiferromagnets: Semiclassically Quantized Solitons of the One-Dimensional Easy-Axis Néel State*, Phys. Rev. Lett. **50**, 1153 (1983).

[112] K. Katsumata, *Experimental studies on one-dimensional quantum spin systems*, J. Magn. Magn. Mat. **140**, 1595 (1995).

[113] I. Affleck, T. Barnes, E.H. Lieb and H. Tasaki, *Rigorous results on valence-bond ground states in antiferromagnets*, Phys. Rev. Lett. **59**, 799 (1987).

[114] J.C. Bonner, S.A. Friedberg, H. Kobayashi, D.L. Meier and H.W. Blöte , *Alternating linear-chain antiferromagnetism in copper nitrate* $Cu(NO_3)_2.2.5\ H_2O$, Phys. Rev. B **27**, 248 (1983).

[115] H. Tanaka, A. Oosawa, T. Kato, H. Uekusa, Y. Ohashi, K. Kakurai and A. Hoser, *Observation of Field-Induced Transverse Nel Ordering in the Spin Gap System* $TlCuCl_3$, J. Phys. Soc. Japan **70**, 939 (2001).

[116] A. Oosawa, T. Takamasu, K. Tatani, H. Abe, N. Tsujii, O. Suzuki, H. Tanaka, G. Kido and K. Kindo, *Specific heat study of the field-induced magnetic ordering in the spin-gap system* $TlCuCl_3$, Phys. Rev. B **63**, 134416 (2001).

[117] A. Oosawa, T. Takamasu, K. Tatani, H. Abe, N. Tsujii, O. Suzuki, H. Tanaka, G. Kido and K. Kindo, *Field-induced magnetic ordering in the quantum spin system* $KCuCl_3$, Phys. Rev. B **66**, 104405 (2002).

[118] N. Cavadini, Ch. Rüegg, A. Furrer, H.-U. Güdel, K. Krämer, H. Mutka and P. Vorderwisch, *Triplet excitations in low-*$H_c$ *spin-gap systems* $KCuCl_3$ *and* $TlCuCl_3$ *: An inelastic neutron scattering study*, Phys. Rev. B **65**, 132415 (2002).

[119] V.O. Garlea, A. Zheludev, T. Masuda, L.-P. Regnault, E. Ressouche, B. Grenier, H. Manaka, J.-H. Chung, Y. Qiu, K. Habicht, K. Kiefer and M. Boehm, *Excitations from a Bose-Einstein condensate of magnons in coupled spin ladders*, Phys. Rev. Lett. **98**, 167202 (2007).

[120] H. Manaka, I. Yamada, Z. Honda, H. A. Katori and K. Katsumata, *Field-Induced Magnetic Long-Range Order in the Ferromagnetic-Antiferromagnetic Alternating Heisenberg Chain System* $(CH_3)_2HNH_3CuCl_3$ *Observed by Specific Heat Measurements*, J. Phys. Soc. Japan **67**, 3913 (1998).

[121] A. Zheludev, V.O. Garlea, T. Masuda, L.-P. Regnault, E. Ressouche, B. Grenier, H. Manaka, J.-H. Chung, Y. Qiu, K. Habicht, K. Kiefer and M. Boehm, *Dynamics of quantum spin liquid and spin solid phases in IPA-CuCl3 under an applied magnetic field studied with neutron scattering*, Phys. Rev. B **76**, 054450 (2007).

[122] G. Chaboussant, Y. Fagot-Revurat, M.-H. Julien, M.E. Hanson, C. Berthier, M. Horvatić, L.P. Lévy, and O. Piovesana, *Nuclear Magnetic Resonance Study of the $S = 1/2$ Heisenberg Ladder $Cu_2(C_5H_{12}N_2)_2Cl_4$: Quantum Phase Transition and Critical Dynamics*, Phys. Rev. Lett. **80**, 2713 (1998).

[123] G. Chaboussant, P. A. Crowell, L. P. Lévy, O. Piovesana, A. Madouri and D. Mailly, *Experimental phase diagram of $Cu_2(C_5H_{12}N_2)_2Cl_4$ : A quasi-one-dimensional antiferromagnetic spin- $\frac{1}{2}$ Heisenberg ladder*, Phys. Rev. B **55**, 3046 (1997).

[124] H. Deguchi, S. Sumoto, S. Yamamoto, S. Takagi, H. Nojiri and M. Motokawa, *Magnetic properties of a Heisenberg spin-ladder $Cu_2(C_5H_12N_2)_2Br_4$*, Physica B **284**, 1599 (2000).

[125] S.E. Sebastian, N. Harrison, C.D. Batista, L. Balicas, M. Jaime, P.A. Sharma, N. Kawashima and I.R. Fisher, *Dimensional reduction at a quantum critical point*, Nature (London) **441**, 617 (2006).

[126] M. Fujisawa, H. Tanaka and T. Sakakibara, *Magnietc Field-induced Phase transition in the Quantum Spin System $Cu_2Cl_4 \cdot H_8C_4SO_2$*, Prog. Theor. Phys. Suppl. **159**, 212 (2005).

[127] T. Waki, M. Kato, Y. Itoh, M. Chishiro, Y. Kazuyoshi and T. Goto , *Triplon condensation of spin-gapped chain $Pb_2V_3O_9$*, J. Phys. Chem. Solids **66**, 1432 (2005).

[128] T.Waki, N. Tsujii, Y. Itoh, C. Michioka, K. Yoshimura, O. Suzuki, H. Kitazawa and G. Kido, *Magnetic susceptibility at high fields of $Pb_2V_3O_9$*, Physica B **398**, 148 (2007).

[129] M.B. Stone, C. Broholm, D.H. Reich, O. Tchernyshyov, P. Vorderwisch and N. Harrison, *Quantum Criticality in an Organic Magnet*, Phys. Rev. Lett. **96**, 257203 (2006).

[130] M.B. Stone, C. Broholm, D.H. Reich, P. Schiffer, O. Tchernyshyov, P. Vorderwisch and N. Harrison, *Field-driven phase transitions in a quasi-two-dimensional quantum antiferromagnet*, New Journal of Physics **9**, 31 (2007).

[131] S.E. Sebastian, V.S. Zapf, N. Harrison, C.D. Batista, P.A. Sharma, M. Jaime, I.R. Fisher, and A. Lacerda, *Comment on Bose-Einstein Condensation of Magnons in $Cs_2CuCl_4$*, Phys. Rev. Lett. **96**, 189703 (2006).

[132] B. Grenier, Y. Inagaki, L. P. Regnault, A. Wildes, T. Asano, Y. Ajiro, E. Lhotel, C. Paulsen, T. Ziman and J.P. Boucher, *Ordering and Excitations in the Field-Induced Magnetic Phase of* $Cs_3Cr_2Br_9$, Phys. Rev. Lett. **92**, 177202 (2004).

[133] B. Grenier, L.P. Regnault, Y. Inagaki, Y. Ajiro, T. Ziman and J.P. Boucher , *The field-induced magnetic phase of the spin-dimer system* $Cs_3Cr_2Br_9$*: Effect of field orientation*, Physica B **385**, 447 (2006).

[134] M. Toda, Y. Fujii, S. Kawano, T. Goto, M. Chiba, S. Ueda, K. Nakajima, K. Kakurai, J. Klenke, R. Feyerherm, M. Meschke, H. Graf, and M. Steiner, *Field-induced magnetic order in the singlet-ground-state magnet* $CsFeCl_3$, Phys. Rev. B **71**, 224426 (2005).

[135] V.S. Zapf, V.F. Correa, C.D. Batista, T.P. Murphy, E.D. Palm, M. Jaime, S. Tozer, A. Lacerda, and A. Paduan-Filho, *Magnetostriction in the Bose-Einstein Condensate quantum magnet in* $\mathrm{NiCl_2-4SC((NH)_2)_2}$, J. Appl. Phys. **101**, 09E106 (2007).

[136] K.M. Diederix, H.A. Algra, J.P. Groen, T.O. Klaassen, N.J. Poulis and R.L. Carlin, *The first experimental evidence of a field-induced magnetic phase transition in an* $S = 1$ *singlet ground state system*, Phys. Lett. A **60**, 247 (1977).

[137] H.A. Algra, L.J. de Jongh and R.L. Carlin, *Field-induced magnetic ordering in the* $S = 1$ *singlet ground-state system* $Ni(C_5H_5NO)_6(ClO_4)_2$ *studied by specific heat*, Physica B **93**, 35 (1978).

[138] N. Tsujii, O. Suzuki, H. Suzuki, H. Kitazawa and G. Kido, *Field-induced magnetic ordering in the Haldane system* $PbNi_2V_2O_8$, Phys. Rev. B **72**, 104402 (2005).

[139] G. Xu, C. Broholm, D.H. Reich and M.A. Adams, *Triplet Waves in a Quantum Spin Liquid*, Phys. Rev. Lett. **84**, 4465 (2000).

[140] L. Berger, S.A. Friedberg, and J.T. Schriempf, *Magnetic Susceptibility of* $Cu(NO_3)_2 \cdot 2.5\ H_2O$ *at low temperature*, Phys. Rev. **132**, 1057 (1963).

[141] J. Eckert, D.E. Cox, G. Shirane, S.A. Friedberg, and H. Kobayashi, *Magnetic ordering in* $Cu(NO_3)_2 \cdot 2.5\ D_2O$, Phys. Rev. B **20**, 4596 (1979).

[142] B. Grenier, J.-P. Boucher, J.-Y. Henry, L.-P. Regnault and T. Ziman, *Spin excitations throughout the field-induced magnetic phase of the spin 1/2 alternating chain compound* $Cu(NO_3)_2 \cdot 2.5\ D_2O$, J. Magn. Magn. Mat. **310**, 1269 (2007).

[143] A. Zheludev, V. O. Garlea, T. Masuda, H. Manaka, L.-P. Regnault, E. Ressouche, B. Grenier, J.-H. Chung, Y. Qiu, K. Habicht, K. Kiefer and M. Boehm, *Dynamics of quantum spin liquid and spin solid phases in* $\mathrm{IPA-CuCl_3}$ *under an applied magnetic field studied with neutron scattering*, Phys. Rev. B **76**, 054450 (2007).

[144] R. Willett, R. K. C. Dwiggins, Jr. Kruh, and R. Rundle, *Crystal Structures of $KCuCl_3$ and $NH_4CuCl_3$*, J. Chem. Phys. **38**, 2429 (1963).

[145] A. Oosawa, M. Ishii and H. Tanaka, *Field-induced three-dimensional magnetic ordering in the spin-gap system $TlCuCl_3$*, J. Phys.: Condens. Matter **11**, 265 (1999).

[146] N. Cavadini, G. Heigold, W. Henggeler, A. Furrer, H.-U. Güdel, K. Krämer and H. Mutka, *Quantum magnetic interactions in $S = \frac{1}{2}$ $KCuCl_3$*, J. Phys.: Condens. Matter **12**, 5463 (2000).

[147] A. Oosawa, T. Kato, H. Tanaka, K. Kakurai, M. Müller and H.-J. Mikeska, *Magnetic excitations in the spin-gap system $TlCuCl_3$*, Phys. Rev. B **65**, 094426 (2002).

[148] D.C. Johnston, M. Troyer, S. Miyahara, D. Lidsky, K. Ueda, M. Azuma, Z. Hiroi, M. Takano, M. Isobe, Y. Ueda, M.A. Korotin, V.I. Anisimov, A.V. Mahajan and L.L. Miller, *Magnetic Susceptibilities of Spin-1/2 Antiferromagnetic Heisenberg Ladders and Applications to Ladder Oxide Comounds*, arXiv:cond-mat/ **0001147v1** (2000).

[149] T. Lorenz, S. Stark, O. Heyer, N. Hollmann, A. Vasiliev, A. Oosawa and H. Tanaka, *Thermodynamics of the coupled spin-dimer system $TlCuCl_3$ close to a quantum phase transition*, J. Magn. Magn. Mat. **316**, 291 (2007).

[150] F. Yamada, T. Ono, H. Tanaka, G. Misguich, M. Oshikawa and T. Sakakibara, *Magnetic Field-induced Bose-Einstein Condensation of Magnons and critical behavior in the interacting spin dimer system $TlCuCl_3$*, J. Phys. Soc. Japan **77**, 013701 (2008).

[151] Omid Nohadani, Stefan Wessel, B. Normand and Stephan Haas, *Universal scaling at field-induced magnetic phase transitions*, Phys. Rev. B **69**, 220402 (2004).

[152] A.K. Kolezhuk, V. N. Glazkov, H. Tanaka, and A. Oosawa, *Dynamics of anisotropic spin dimer system in strong magnetic field*, Phys. Rev. B **70**, 020403 (2004).

[153] S.E. Sebastian, P. Tanedo, P. A. Goddard, S.-C. Lee, A. Wilson, S. Kim, S. Cox, R. D. McDonald, S. Hill, N. Harrison, C. D. Batista, and I. R. Fisher, *Role of anisotropy in the spin-dimer compound $BaCuSi_2O_6$*, Phys. Rev. B **74**, 180401 (2006).

[154] O. Vyaselev, M. Takigawa, A. Vasiliev, A. Oosawa and H. Tanaka, *Field-Induced Magnetic order and Simultaneous lattice deformation in $TlCuCl_3$*, Phys. Rev. Lett. **92**, 207202 (2004).

[155] The inclusion of a DM-like anisotropy term $i\gamma(\psi - \psi^\dagger)$ [95] would result in strictly imaginary $\psi$ because $u(\psi)$ has to be real-valued. Even a pseudo Goldstone mode can therefore not be easliy obtained within this formalism.

[156] J. O. Andersen, *Theory of the weakly interacting Bose Gas*, Rev. Mod. Phys. **76**, 599 (2004).

[157] T. Haugset, H. Haugerund and F. Ravndal, *Thermodynamics of a weakly interacting Bose-Einstein gas*, Ann. Phys. **266**, 27 (1998).

[158] R. Dell'Amore, A. Schilling and K. Krämer, *The fraction of Bose-Einstein condensed triplons in* $\mathrm{TlCuCl_3}$ *from magnetization* $M(T,H)$*-data*, arXiv:cond-mat/ **0806.2519v1** (2008).

[159] J. E. Lorenzo, K. Katsumata, Y. Narumi, S. Shimomura, Y. Tanaka, M. Hagiwara, H. Mayaffre, C. Berthier, O. Piovesana, T. Ishikawa and H. Kitamura, *Observation of a lattice instability at the field-induced phase transition of the spin-gapped compound* $\mathrm{Cu_2(C_5H_{12}N_2)_2Cl_4}$, Phys. Rev. B **69**, 220409 (2004).

[160] S. A. Zvyagin, J. Wosnitza, A. K. Kolezhuk, V. S. Zapf, M. Jaime, A. Paduan-Filho, V. N. Glazkov, S. S. Sosin and A. I. Smirnov, *Spin dynamics of NiCl2-4SC(NH2)2 in the field-induced ordered phase*, Phys. Rev. B **77**, 092413 (2008).

[161] J. E. Lorenzo et al., *Observation of a lattice instability at the field-induced phase transition of the spin-gapped compound* $\mathrm{Cu_2(C_5H_12N_2)_2Cl_4}$, Phys. Rev. B **69**, 220409(R) (2004).

[162] R. Calemczuk, J. Riera, D. Poilblanc, J.-P. Boucher, G. Chaboussant, L. Lévy and O. Piovesana, *Thermodynamic properties of the spin-1/2 antiferromagnetic ladder* $\mathrm{Cu_2(C_2H_{12}N_2)_2Cl_4}$ *under magnetic field*, Eur. Phys. J. B **7**, 171 (1999).

[163] H. Mayaffre, M. Horvatic, C. Berthier, M.-H. Julien, P. Ségransan, L. Lévy and O. Piovesana, *NMR Evidence for a "Generalized Spin-Peierls Transition" in the High-Magnetic-Field Phase of the Spin Ladder* $\mathrm{Cu_2(C_2H_{12}N_2)_2Cl_4}$, Phys. Rev. Lett. **85**, 4795 (2000).

[164] M. Matsumoto and M. Sigrist, *Ehrenfest Relations and Magnetoelastic E?ects in Field-induced Ordered Phases*, J. Phys. Soc. Japan **69**, 2310 (2005).

[165] A. S. Borovik-Romanov, Yu M. Bunkov, V. V. Dmitriev, Yu M. Mukharskiy and D. A. Sergatskov, *Investigation of spin supercurrents in* $B3$, Phys. Rev. Lett. **62**, 1631 (1989).

[166] H.Tanaka, F. Yamada, T. Ono, T. Sakakibara, Y. Uwatoko, A. Oosawa, K. Kakurai and K. Goto, *Magnetic quantum phase transitions from gapped spin liquid state in* $TlCuCl_3$, J. Magn. Magn. Mat. **310**, 1343 (2007).

[167] V.P. Peshkov, *Determination of the velocity of propagation of the second sound in helium II*, J. Phys. (Moscow) **10**, 389 (1946).

[168] P. Rosenbusch, V. Bretin and J. Dalibard, *Dynamics of a Single Vortex Line in a Bose-Einstein Condensate*, Phys. Rev. Lett. **89**, 200403 (2002).

[169] A. Oosawa, M. Fujisawa, T. Osakabe, K. Kakurai and H. Tanaka, *Neutron Diffraction Study of the Pressure-Induced Magnetic Ordering in the Spin Gap System* $TlCuCl_3$, J. Phys. Soc. Japan **72**, 1026 (2003).

[170] Ch. Rüegg, B. Normand, M. Matsumoto, A. Furrer, D. F. McMorrow, K. W. Krämer, H. -U. Güdel, S. N. Gvasaliya, H. Mutka and M. Boehm, *Quantum Magnets under Pressure: Controlling Elementary Excitations in* $TlCuCl3$, Phys. Rev. Lett. **100**, 205701 (2008).

[171] B. Normand, M. Matsumoto, O. Nohadani, S. Wessel, S. Haas, T. M. Rice and M. Sigrist, *Pressure- and field-induced magnetic quantum phase transitions in* $TlCuCl_3$, J. Phys.: Condens. Matter **16**, S867 (2004).

[172] M. Nikolo, *Superconductivity: A guide to alternating current susceptibility measuremets and alternating current susceptometer desing*, Am. J. Phys. **63**, 57 (1995).

[173] G.C. Bjorklund, *Frequency-modulation spectroscopy: a new method for measuring weak absorbtions and dispersions*, Optics Letters **5**, 15 (1979).

# Appendix

## A The coherent states

The coherent states are generally defined as the coherent superposition of stationary states, i.e. Eigenstates $\psi_n$ of the single-particle Hamiltonian. We can, therefore, define a **coherent state** by

$$|\varphi_\alpha\rangle = C\left(\psi_0(x) + \frac{\alpha}{\sqrt{1!}}\psi_1(x) + \frac{\alpha^2}{\sqrt{2!}}\psi_2(x) + \frac{\alpha^3}{\sqrt{3!}}\psi_3(x) + \dots\right), \tag{A.1}$$

where $\alpha$ is an arbitrary complex number and $C$ is the normalization constant. We therefore get

$$\begin{aligned} 1 = \langle\varphi_\alpha|\varphi_\alpha\rangle = C^2\sum_{n=0}^{\infty}\frac{|\alpha|^{2n}}{n!} = C^2 e^{|\alpha|^2} \\ C = e^{-\frac{|\alpha|^2}{2}}. \end{aligned} \tag{A.2}$$

The probability of observing a particle in the quantum state $\psi_n$ in a quantum measurement of state $|\varphi_\alpha\rangle$ is actually a Poisson distribution

$$P_n = |\langle\psi_n|\varphi_\alpha\rangle|^2 = \frac{|\alpha|^{2n}}{n!}e^{-|\alpha|^2}, \tag{A.3}$$

as can easily be checked using Eq. (A.1). In this distribution the standard deviation is defined as

$$\Delta n = \sqrt{\langle\hat{n}^2\rangle - \langle\hat{n}\rangle^2} = \sqrt{\langle\hat{n}\rangle}. \tag{A.4}$$

Since

$$\frac{\Delta n}{\langle\hat{n}\rangle} \backsimeq \frac{1}{\sqrt{\langle\hat{n}\rangle}} \to 0 \qquad \langle\hat{n}\rangle \quad \text{large}, \tag{A.5}$$

$\Delta n$ becomes negligible for coherent states with macroscopic numbers of particles.
It is very important to emphasize that a coherent state $|\varphi_\alpha\rangle$ has a definite **phase** $\theta$, although it does not have a definite quantum number $n$ (corresponding to the number of particles). Substituting $\alpha = |\alpha|e^{i\theta}$ into Eq. (A.1), we see that the term containing $\psi_n$ depends on $e^{in\theta}$. The phase $\theta$ and the quantum number $n$ are **conjugate operators**, which satisfy the uncertainty principle

$$\Delta n \Delta\theta \geq \frac{1}{2}. \tag{A.6}$$

For more details, please consult Ref.[38]

# B The two-fluid picture and the momentum carried by excitations

For a physical system which is invariant under Galilean transformations, the momentum density is equal to the mass current density satisfying the continuity equation for mass conservation.
In the ground state of a gas, the condensate is stationary and the total momentum is zero. The total momentum per unit volume carried by the excitations is expressed as

$$\mathbf{j}_{ex} = \int \frac{d\mathbf{p}}{(2\pi\hbar)^3}\mathbf{p}f_{\mathbf{p}}, \tag{B.1}$$

with

$$f_{\mathbf{p}} = \frac{1}{exp\left(\frac{\varepsilon_{\mathbf{p}}-\mu}{k_BT}\right)-1}. \tag{B.2}$$

Performing a Galilean transformation to a reference frame moving with velocity -$\mathbf{v}_s$, the condensate is therefore moving with $\mathbf{v}_s$. The total momentum changes by an amount $Nm\mathbf{v}_s$ and for the total momentum density we get

$$\mathbf{j} = \rho\mathbf{v}_s + \mathbf{j}_{ex}, \tag{B.3}$$

where $\rho = mn$ is the mass density.
Let us now consider a system in equilibrium at finite temperatures. We denote the velocity of the condensate by $\mathbf{v}_s$. The velocity of the gas of excitations is denoted as $\mathbf{v}_n$. The energy of an excitation measured in the original frame at rest is $\varepsilon(p) = \varepsilon_p + \mathbf{p}\cdot\mathbf{v}_s$, but the relevant distribution function is the one in equilibrium in the frame moving with velocity $\mathbf{v}_n$. The energy that enters the Bose distribution function is, therefore, the excitation energy in the original frame $\varepsilon(p)$, shifted by an amount $-\mathbf{p}\cdot\mathbf{v}_n$. It follows that the equilibrium distribution function is given by the following expression

$$f_{\mathbf{p}} = \frac{1}{exp\left(\frac{\varepsilon_p-\mathbf{p}\cdot(\mathbf{v}_n-\mathbf{v}_s)}{k_{\mathrm{B}}T}\right)-1}. \tag{B.4}$$

The total momentum per unit volume carried by the excitations is described in Eq. (B.1). By putting Eq. (B.4) into expression Eq. (B.1), we get

$$\mathbf{j}_{ex} = \rho_n(|\mathbf{v}_n - \mathbf{v}_s|)(\mathbf{v}_n - \mathbf{v}_s) \quad \text{and} \tag{B.5}$$

$$\rho_n(v) = \int \frac{d\mathbf{p}}{(2\pi\hbar)^3}\frac{\mathbf{p}\cdot\mathbf{v}}{v^2}\frac{1}{exp\left(\frac{(\varepsilon_p-\mathbf{p}\cdot\mathbf{v})}{k_{\mathrm{B}}T}\right)-1} \tag{B.6}$$

as the density of the normal fluid. For small velocities using the general derivative expression $\frac{\partial f}{\partial x} \cdot \Delta x = f(x + \Delta x) - f(x)$, where in our case $f = [exp(\varepsilon_p / k_{\mathrm{B}} T) - 1]^{-1} =: f_{\varepsilon_p}$, one finds

$$\rho_n(v) = \int \frac{d\mathbf{p}}{(2\pi\hbar)^3} (\mathbf{p} \cdot \hat{\mathbf{v}})^2 \left( \frac{\partial f_{\varepsilon_p}}{\partial \varepsilon_p} \right) = \int \frac{d\mathbf{p}}{(2\pi\hbar)^3} \frac{p^2}{3} \left( \frac{\partial f_{\varepsilon_p}}{\partial \varepsilon_p} \right), \tag{B.7}$$

where the $\frac{1}{3}$-factor on the right-hand side of Eq. (B.7) arises from averaging the three directions in momentum space. For a dilute gas, the spectrum of elementary excitations is defined by the Bogoliubov expression, see Eq. (4.15), which is linear $\varepsilon_p \simeq c_0 p$ at low temperatures ($T \ll T^* \approx \frac{nU_0}{k_{\mathrm{B}}}$). Performing the calculations with such a spectrum one finds from Eq. (B.7)

$$\rho_n \propto T^4. \tag{B.8}$$

At higher temperatures ($T \gg T^*$), the energy of an excitation is approximately that of a free particle $\varepsilon_p \simeq \frac{p^2}{2m}$. One finally get

$$\rho_n = m n_{ex}, \quad \text{with} \tag{B.9}$$

$$n_{ex} = n \left( \frac{T}{T_c^{BE}} \right)^{\frac{3}{2}}, \tag{B.10}$$

$n_{ex}$ is the density of excited particles (not part of the condensate) and $n$ the total particle density. Finally, by combining Eq. (B.1) and Eq. (B.5) we get

$$\mathbf{j} = \rho_n (\mathbf{v}_n - \mathbf{v}_s) + \rho \mathbf{v}_s. \tag{B.11}$$

Defining the superfluid density as the difference between the total density and the normal density

$$\rho_s = \rho - \rho_n, \tag{B.12}$$

one obtains the total momentum density defined in the two-fluid model

$$\mathbf{j} = \rho_s \mathbf{v}_s + \rho_n \mathbf{v}_n. \tag{B.13}$$

# C The two sound modes in a condensate

Starting from Eq. (4.21) and combining it with Eq. (4.20) and Eq. (4.22), we get

$$\rho_s \frac{\partial \mathbf{v}_s}{\partial t} = -\frac{\rho_s}{\rho} \nabla p + \frac{\rho_s}{\rho} \bar{s} \nabla T \tag{C.1}$$

$$\rho_s \frac{\partial \mathbf{v}_n}{\partial t} = -\frac{\rho_n}{\rho} \nabla p - \frac{\rho_s}{\rho} \bar{s} \nabla T, \tag{C.2}$$

where $\bar{s} = \frac{S}{\Omega}$ is the entropy per unit volume. It is immediately noticeable, that a pressure gradient acts in a manner that drives both fluid components in the same direction, whereas a

temperature gradient drives them in the opposite direction (opposite sign).
By taking the time derivative of Eq. (4.18) and then calculating the divergence of Eq. (4.22), one finds

$$\frac{\partial^2 \rho}{\partial t^2} = \nabla^2 \cdot p. \tag{C.3}$$

This equation relates the changes in density to those of pressure. Since in equilibrium the pressure depends solely on the density and on the temperature, Eq. (C.3) expresses the density changes due to temperature changes.
By combining Eq. (4.19) with Eq. (C.2) using Eq. (C.3) we get

$$\frac{\partial^2 \tilde{s}}{\partial t^2} = \tilde{s}^2 \frac{\rho_s}{\rho_n} \nabla^2 \cdot T. \tag{C.4}$$

The entropy per unit mass $\tilde{s}$ results to be a function of temperature and density. We therefore have derived the second relation between density $\rho$ and temperature $T$ in a superfluid. The Eq. (C.3) and Eq. (C.4) have now to be solved self-consistently.
The collective modes of the system are obtained by considering small oscillations of these variables. Let us fix the density $\rho$ and the entropy $\tilde{s}$ as the independent variables. We therefore can express the small changes in pressure $\delta p$ and temperature $\delta T$ in terms of infinitesimal changes in $\rho$ and $\tilde{s}$, respectively [15], obtaining

$$\begin{aligned} \delta p &= \left(\frac{\partial p}{\partial \rho}\right)_{\tilde{s}} \delta\rho + \left(\frac{\partial p}{\partial \tilde{s}}\right)_{\rho} \delta\tilde{s}, \\ \delta T &= \left(\frac{\partial T}{\partial \rho}\right)_{\tilde{s}} \delta\rho + \left(\frac{\partial T}{\partial \tilde{s}}\right)_{\rho} \delta\tilde{s}. \end{aligned} \tag{C.5}$$

Plugging these variations into Eq. (C.3) and Eq. (C.4) we finally find

$$\begin{aligned} \frac{\partial^2 \rho}{\partial t^2} &= \left(\frac{\partial p}{\partial \rho}\right)_{\tilde{s}} \nabla^2\rho + \left(\frac{\partial p}{\partial \tilde{s}}\right)_{\rho} \nabla^2\tilde{s}, \\ \frac{\partial^2 \tilde{s}}{\partial t^2} &= \tilde{s}^2 \frac{\rho_s}{\rho_n} \left[ \left(\frac{\partial T}{\partial \rho}\right)_{\tilde{s}} \nabla^2\rho + \left(\frac{\partial T}{\partial \tilde{s}}\right)_{\rho} \nabla^2\tilde{s} \right]. \end{aligned} \tag{C.6}$$

These are coupled partial differential equations which are solved with the following ansatz:

$$\begin{aligned} \rho &= \rho_0 + \delta\rho e^{[i(\mathbf{q}\cdot\mathbf{r}-\omega t)]} \\ \tilde{s} &= \tilde{s}_0 + \delta\tilde{s} e^{[i(\mathbf{q}\cdot\mathbf{r}-\omega t)]}, \end{aligned} \tag{C.7}$$

yielding a linear system of equations for $\delta\rho$ and $\delta\tilde{s}$

$$\left(\frac{\omega^2}{v_1^2 q^2} - 1\right) \delta\rho + \left(\frac{\partial p}{\partial \tilde{s}}\right)_{\rho} \left(\frac{\partial \rho}{\partial p}\right)_{\tilde{s}} \delta\tilde{s} \quad = 0 \tag{C.8}$$

$$\left(\frac{\partial T}{\partial \rho}\right)_{\tilde{s}} \left(\frac{\partial \tilde{s}}{\partial T}\right)_{\rho} \delta\rho + \left(\frac{\omega^2}{v_2^2 q^2} - 1\right) \delta\tilde{s} \quad = 0, \tag{C.9}$$

[15] we assume that a small pressure change does not lead to a temperature change and vice versa, that means $c_p = c_v$, which is true for low temperatures or when the thermal expansion is negligible small ($c_p - c_v = T * V \frac{\beta^2}{\kappa}$, where $\beta = \frac{1}{V}\frac{\partial V}{\partial T}$ is the volume expansion coefficient and $\kappa = -\frac{1}{V}\frac{\partial V}{\partial p}$ the isotherm compressibility).

where

$$v_1^2 = \left(\frac{\partial p}{\partial \rho}\right)_{\tilde{s}} \tag{C.10}$$

and

$$v_2^2 = \frac{\rho_s}{\rho_n}\tilde{s}^2 \left(\frac{\partial T}{\partial \tilde{s}}\right)_{\rho} = \frac{\rho_s}{\rho_n}\left(\frac{\tilde{s}^2 T}{C_v}\right). \tag{C.11}$$

To solve this equation system the determinant must vanish, which leads to the known result of Eq. (4.23).

# D The Hartree-Fock (Popov) approximation

So far, mathematical concepts were mainly explained for $T \to 0$, i.e. we assumed the system to be close to its ground state and single excitations were independent of each other. At higher temperatures interaction between excitations become important.
Here, we will discuss a few key points of the HF approximation which takes such interactions into account. Further explanations are found in Ref.[62].
The HF approximation applies to temperatures $T \gg \frac{nv_0}{k_\mathrm{B}}$, where $n$ is the particle density and $v_0$ is the interaction energy. In this temperature region, excitations correspond to the addition of one particle of momentum $\pm\mathbf{p}$ and simultaneous removal of one from the condensate. The wave function describing the Bose system is a product of single particle states symmetrized with respect to the interchange of particles to obey the Bose statistics

$$\Psi_{HF} = c_N \sum_{symm} \phi(\mathbf{r}_1)\phi(\mathbf{r}_2)\ldots\phi(\mathbf{r}_N), \tag{D.1}$$

where $c_N$ is the normalization factor.
In this approximation, a self-energy term $\Sigma_{HF} = 2v_0 n$ considers the effects of interactions. Thus a particle with momentum $\mathbf{p}$ has effectively the energy $\varepsilon_\mathbf{p} = \frac{\hbar^2 p^2}{2m} + 2v_0 n$, where the term arises from the mean-field of the other particles. Considering the above considerations, we obtain for the equilibrium distribution

$$f_p = \frac{1}{exp(\frac{\varepsilon_\mathbf{p} - \mu_{eff}}{k_\mathrm{B}T}) - 1}, \tag{D.2}$$

where now the excitation energy is $\varepsilon_\mathbf{p} = \frac{\hbar^2 p^2}{2m}$ and the chemical potential is given by

$$\mu_{eff} = \mu - 2v_0 n, \tag{D.3}$$

with $n$ being the total particle density.

# E The LabView software

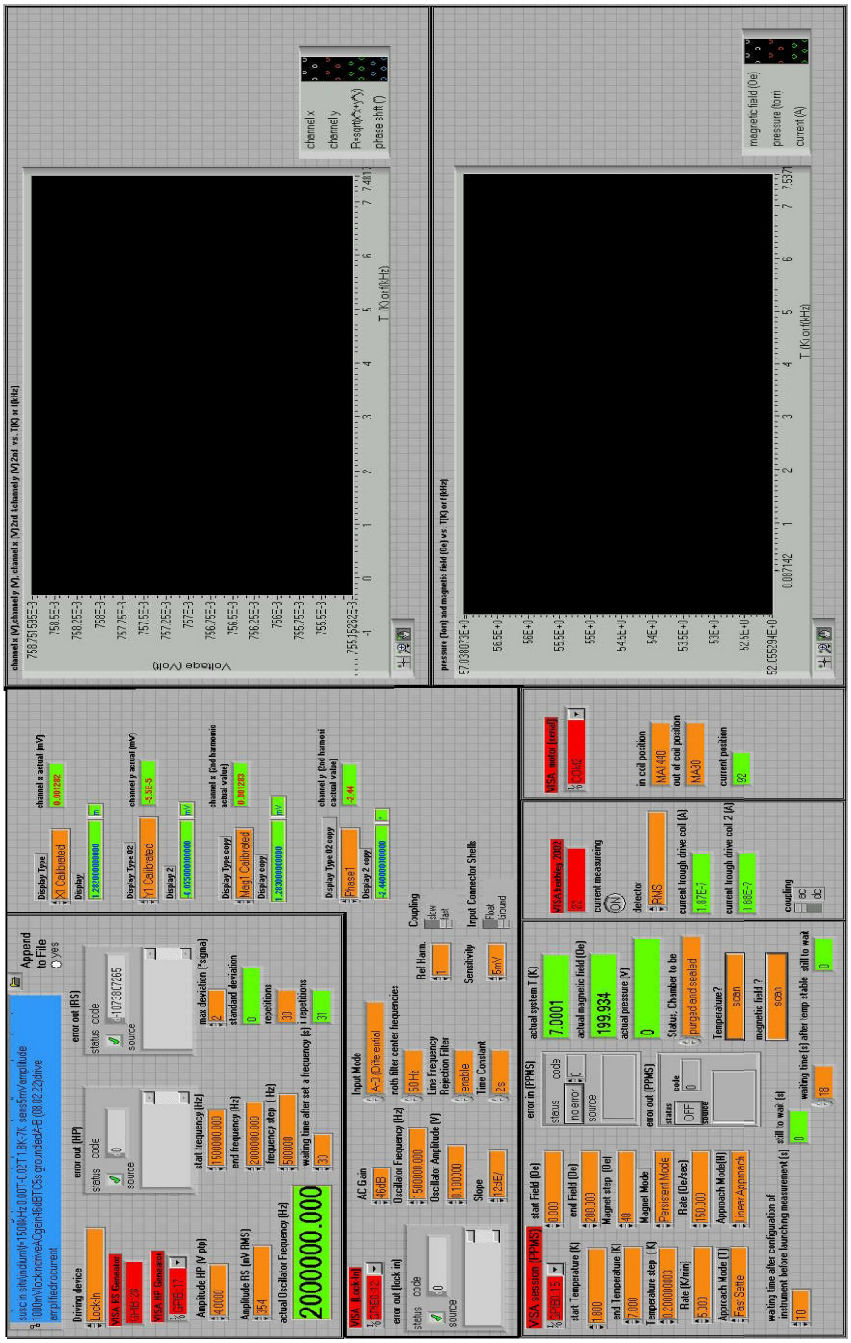

Figure 67: The GUI of the home-written LabView-software driving the experiment. The software can be find on the PPMS2-PC, C:Documents and Settings\dellamore\Experiments\VI's\prgms

# F The absolute values of the Bessel functions

| $x$ | Bessel-function order, n | | | | | | | | | | | | | | | | |
|---|---|---|---|---|---|---|---|---|---|---|---|---|---|---|---|---|---|
| $m_f$ | $J_0$ | $J_1$ | $J_2$ | $J_3$ | $J_4$ | $J_5$ | $J_6$ | $J_7$ | $J_8$ | $J_9$ | $J_{10}$ | $J_{11}$ | $J_{12}$ | $J_{13}$ | $J_{14}$ | $J_{15}$ | $J_{16}$ |
| 0.00 | 1.00 | — | — | — | — | — | — | — | — | — | — | — | — | — | — | — | — |
| 0.25 | 0.98 | 0.12 | — | — | — | — | — | — | — | — | — | — | — | — | — | — | — |
| 0.5 | 0.94 | 0.24 | 0.03 | — | — | — | — | — | — | — | — | — | — | — | — | — | — |
| 1.0 | 0.77 | 0.44 | 0.11 | 0.02 | — | — | — | — | — | — | — | — | — | — | — | — | — |
| 1.5 | 0.51 | 0.56 | 0.23 | 0.06 | 0.01 | — | — | — | — | — | — | — | — | — | — | — | — |
| 2.0 | 0.22 | 0.58 | 0.35 | 0.13 | 0.03 | — | — | — | — | — | — | — | — | — | — | — | — |
| 2.41 | 0 | 0.52 | 0.43 | 0.20 | 0.06 | 0.02 | — | — | — | — | — | — | — | — | — | — | — |
| 2.5 | –.05 | 0.50 | 0.45 | 0.22 | 0.07 | 0.02 | 0.01 | — | — | — | — | — | — | — | — | — | — |
| 3.0 | –.26 | 0.34 | 0.49 | 0.31 | 0.13 | 0.04 | 0.01 | — | — | — | — | — | — | — | — | — | — |
| 4.0 | –.40 | –.07 | 0.36 | 0.43 | 0.28 | 0.13 | 0.05 | 0.02 | — | — | — | — | — | — | — | — | — |
| 5.0 | –.18 | –.33 | 0.05 | 0.36 | 0.39 | 0.26 | 0.13 | 0.05 | 0.02 | — | — | — | — | — | — | — | — |
| 5.53 | 0 | –.34 | –.13 | 0.25 | 0.40 | 0.32 | 0.19 | 0.09 | 0.03 | 0.01 | — | — | — | — | — | — | — |
| 6.0 | 0.15 | –.28 | –.24 | 0.11 | 0.36 | 0.36 | 0.25 | 0.13 | 0.06 | 0.02 | — | — | — | — | — | — | — |
| 7.0 | 0.30 | 0.00 | –.30 | –.17 | 0.16 | 0.35 | 0.34 | 0.23 | 0.13 | 0.06 | 0.02 | — | — | — | — | — | — |
| 8.0 | 0.17 | 0.23 | –.11 | –.29 | –.10 | 0.19 | 0.34 | 0.32 | 0.22 | 0.13 | 0.06 | 0.03 | — | — | — | — | — |
| 8.65 | 0 | 0.27 | 0.06 | –.24 | –.23 | 0.03 | 0.26 | 0.34 | 0.28 | 0.18 | 0.10 | 0.05 | 0.02 | — | — | — | — |
| 9.0 | –.09 | 0.25 | 0.14 | –.18 | –.27 | –.06 | 0.20 | 0.33 | 0.31 | 0.21 | 0.12 | 0.06 | 0.03 | 0.01 | — | — | — |
| 10.0 | –.25 | 0.04 | 0.25 | 0.06 | –.22 | –.23 | –.01 | 0.22 | 0.32 | 0.29 | 0.21 | 0.12 | 0.06 | 0.03 | 0.01 | — | — |
| 12.0 | 0.05 | –.22 | –.08 | 0.20 | 0.18 | –.07 | –.24 | –.17 | 0.05 | 0.23 | 0.30 | 0.27 | 0.20 | 0.12 | 0.07 | 0.03 | 0.01 |

Figure 68: The absolute values of the Bessel functions

## Curriculum Vitae

| | |
|---|---|
| Name | Raffaele Dell'Amore |
| Birth | 08.04.1978 in Sarnen, Switzerland |
| Nationality | Italian |

### *Education*

| | |
|---|---|
| 1992-1998 | Kantosschule Obwalden, Sarnen, Switzerland |
| June 1998 | **Matura Typus B** |
| 1998-2002 | Undergraduate **Studies of Physics, ETH Zurich** |
| September 2002 - March 2003 | Diploma work at the ETH Zurich at the Department of Solid State Physics in the "Low -temperature physics and magnetism " group of Prof. Dr. H.-R. Ott<br>*Thesis Title*: "Energy transport in the low-dimensional spin system $Cu_2Te_2O_5Br_2$";<br>supervisors: Dr. A. Solokubenko (ETH Zurich) and Prof. Dr. H.-R. Ott (ETH Zurich) |
| April 2003 | Graduation dipl.phys ETH Zurich |
| since July 2003 | **PhD student** in the "*Phase Transitions and New Materials*" group of Prof. Dr. Andreas Schilling, **University of Zurich** |
| September 2008 | PhD Thesis; *Title*: "The Bose-Einstein condensation in $TlCuCl_3$: Any sign of superfluidity?"<br>supervisors: Prof. Dr. Andreas Schilling |

*Teaching and Working Experiences*

| | |
|---|---|
| August 2001- July 2002 | Teacher of Mathematics at the Kantonsschule Obwalden (33% work load) |
| since October 2003 | Teaching Assistant, University of Zurich<br>lab-courses for biology students and problem classes in elementary and advanced solid state physics.<br><br>Exam Assistent, University of Zurich<br>written and oral exams in elementary and advanced solid state physics |
| May 2005 | Supervisor of the bachelor thesis: "Messung der RichtungsabhŁngigkeit der spezifischen Waerme von $YBa_2Cu_3O_7$: Ein Indikator s- oder d-Wellen Supraleitung", passed by Stefan Menzi |
| March 2008 | Supervisor of the bachelor thesis: "AC-SusceptibilitŁt Messungen unterhalb 2K-Aufbau und Kalibrierung", passed by Dominik Boeni |

## Publications

1. A. Sologubenko, **R. Dell'Amore**, H.-R. Ott and P. Millet
   *"Thermal transport properties in* $Cu_2Te_2O_5Br_2$ *"*,
   Eur. Phys. Journal B **42 (4)**, 549 (2004)

2. **R. Dell'Amore**, A. Schilling and K. Krämer
   *"Fraction of Bose-Einstein condensed triplons in* $TlCuCl_3$ *from magnetization data"*,
   Physical Review B **78**, 224403 (2008), American Physical Society

3. **R. Dell'Amore**, A. Schilling and K. Krämer
   *"* $U(1)$*-symmetry breaking and violated axial symmetry in* $TlCuCl_3$ *"*,
   accepted for publication in Physical Review B, American Physical Society

4. A. Schilling, **R. Dell'Amore**, J. Karpinski, M. Medarde, K. Conder and K. Pomjakushina
   *"*$LaBaNiO_4$*: a Fermi glass"*,
   J. Phys.: Condens. Matter **21** 015701 (2009), IOP Publishing

# Fraction of Bose-Einstein condensed triplons in $TlCuCl_3$ from magnetization data

Raffaele Dell'Amore* and Andreas Schilling†
*Physik-Institut, University of Zurich, Winterthurerstrasse 190, 8057 Zurich, Switzerland*

Karl Krämer‡
*Department of Chemistry and Biochemistry, University of Bern, 3000 Bern 9, Switzerland*
(Received 3 June 2008; published 4 December 2008)

$TlCuCl_3$ is a quantum-spin-$\frac{1}{2}$ system which shows a gap between the singlet ground state of the $Cu^{2+}$ dimers and the first excited triplet $S^z=+1$ state for magnetic fields $\mu_0 H \lesssim \mu_0 H_c \approx 5.5$ T. At larger magnetic fields the gap is suppressed, and a Bose-Einstein condensation of triplets is supposed to occur, leading to a magnetic phase with antiferromagnetic long-range order of the transverse spin components. In this study we calculate the fraction of condensed magnetic quasiparticles of $TlCuCl_3$ from magnetization $M(T,H)$ data. At $T=0$ K and right above the critical field $H_c$, this fraction is $\approx 98\%$ of the total number of triplons, and is independent of the direction of the magnetic field if we assume the presence of a small intrinsic magnetic background with $S=1$ magnetic moments.

DOI: 10.1103/PhysRevB.78.224403 PACS number(s): 75.10.Jm, 75.30.Gw, 75.45.+j

## I. INTRODUCTION

Low-dimensional quantum-spin systems exhibit a variety of quantum phenomena that have gained much interest in the last decade.[1–5] $TlCuCl_3$, for example, is a material in which magnetic quasiparticles carrying spin $S=1$ (spin triplet states, here called triplons) are believed to form a Bose-Einstein condensate (BEC) above a critical field $\mu_0 H_c \approx 5.5$ T and at low temperatures.[4,5] Meanwhile several other materials have been found that exhibit various features which can be explained within the framework of a condensation of quasiparticles with integer spin.[6–9]

The magnetic properties of $TlCuCl_3$ are determined by the exchange interactions between the $Cu^{2+}$ ions which are arranged in dimer pairs within $Cu_2Cl_6$ clusters. The magnetic ground state of $TlCuCl_3$ is a nonmagnetic spin singlet that is separated from the first excited triplet state by an excitation gap $\Delta \approx 0.7$ meV in zero magnetic field. This gap has been measured, for example, by neutron-scattering and electron-spin-resonance (ESR) measurements[10,11] which revealed that this gap is due to the strong antiferromagnetic interaction $J=5.68$ meV in the planar dimer of $Cu_2Cl_6$. The neighboring dimers are coupled by strong interdimer interactions along the double chain and on the (1 0 −2) plane.[10,12]

As soon as the external magnetic field $H$ is larger than a critical field $H_c$ with $g\mu_B\mu_0 H_c(T=0)=\Delta$ (where $\mu_B$ is the Bohr magneton and $g$ is the Landé $g$ factor), the excitation gap closes due to the Zeeman splitting, and the triplet states $S^z=+1$ are populated, eventually forming the BEC. The three-dimensional (3D) interdimer interactions drive this quantum phase transition to finite temperatures, leading to a temperature-dependent critical field $H_c(T)$. The characteristic off-diagonal long-range order of the BEC manifests itself in the antiferromagnetic ordering of the spin system on the plane perpendicular to the applied magnetic field.[13]

The idea of BEC has already been used quite successfully to explain the transition of "normal" to "superfluid" $^4$He.[14,15] The strong interactions that exist in liquid $^4$He may alter the nature of the transition, however. For instance, while 90–95 % of the particles of an atomic ensemble are in the superfluid phase below the transition temperature of an atomic BEC, just a few percent (~9%) of the helium atoms are condensed in superfluid $^4$He.

In this paper we focus on the condensed phase of triplons in $TlCuCl_3$ at magnetic fields $\mu_0 H_c < \mu_0 H < 9$ T and at temperatures down to $T=1.8$ K. From magnetization $M(T,H)$ measurements, we extract the density of condensed triplons at $T=0$ K for $\mathbf{H}\|b$ and $\mathbf{H}\|[201]$. Taking various possible contributions to the total magnetization into account, we show that the density of triplons forming the condensate is in fact the same for both directions.[9] We also determine the magnetic-field dependence of the fraction of triplons forming the condensate. The quantitative results presented here confirm the scenario of the formation of a *weakly interacting Bose gas* of triplons right above $H_c$,[5,16] and we conclude that the interaction increases with increasing particle density, i.e., with increasing magnetic field $H$.

## II. MAGNETIC SUSCEPTIBILITY FOR $T>20$ K

Magnetic-susceptibility measurements were performed in a commercial physical property measurements system (PPMS; Quantum Design) on a $TlCuCl_3$ single crystal with mass $m=12.36$ mg, for 1.8 K $\leq T \leq$ 300 K at $\mu_0 H=1$ T for $\mathbf{H}\|b$ and $\mathbf{H}\|[201]$. The susceptibility $\chi(T)$ of $TlCuCl_3$ is typical for a low-dimensional spin gap system, showing a well-pronounced maximum at $T_{\chi_{\max}} \sim 36$ K and an exponential decrease at low temperatures indicating the existence of a gap $\Delta$ between the ground state and the first excited triplet state; see Fig. 1. For Heisenberg spin systems with identical spin subsystems that are weakly coupled to each other, a good fit to the data in the paramagnetic regime is provided by the molecular mean-field theory (MFT) and its extensions.[17] We therefore used this approach within the model of dimers coupled by an effective interdimer coupling $\tilde{J}$, representing the sum of all exchange coupling constants $J_{kl}$ for a given dimer $k$ interacting with neighboring dimers $l$.[17] An additional temperature-independent diamagnetic term

 

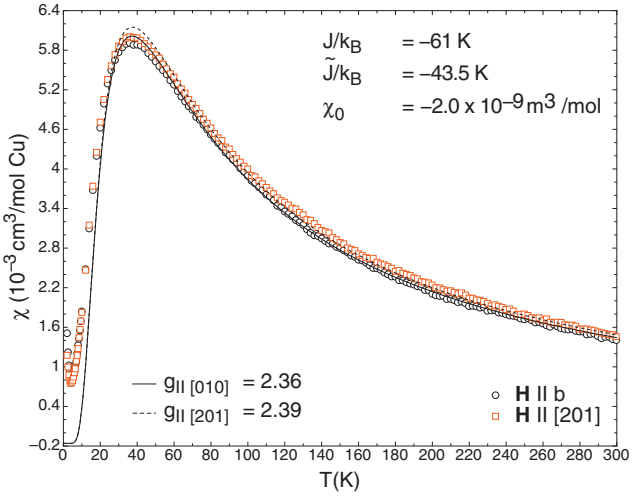


FIG. 1. (Color) The magnetic susceptibilities $\chi(T)$ of $TlCuCl_3$ with $\mu_0 H = 1$ T applied along the crystallographic $b$ axis and along [201]. The corresponding fits to the data are discussed in the text.

$\chi_0$ which contains the orbital diamagnetic core contribution $\chi^{\text{core}}$ (including the background contribution of the sample holder) and a paramagnetic Van Vleck contribution $\chi^{\text{VV}}$ are considered.

We therefore fitted the magnetic susceptibility $\chi(T)$ for temperatures $T > 20$ K according to

$$\chi(T) = \chi_0 + \chi_{\text{MF}}(T), \tag{1a}$$

with

$$\chi_0 = \chi^{\text{core}} + \chi^{\text{VV}} \tag{1b}$$

and

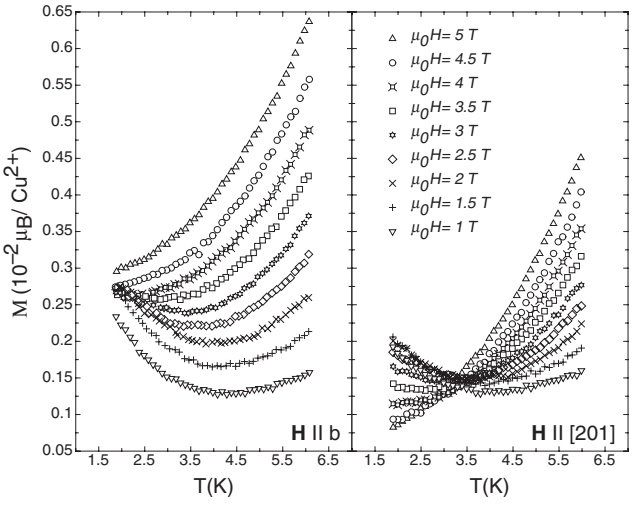


FIG. 2. The magnetizations $M(T)$ of $TlCuCl_3$ for $1\ \text{T} \leq \mu_0 H \leq 5$ T applied along the crystallographic $b$ axis (left) and along [201] (right).

TABLE I. The extracted fitting parameters from $\chi(T)$ data of $TlCuCl_3$ ($T \geq 20$ K). $\chi_0$, $J$, and $\tilde{J}$ were forced to be identical for the two field directions.

| | $H \| b$ | $H \| [201]$ | |
|---|---|---|---|
| $J/k_B$ (K) | −61 | | ±1 |
| $\tilde{J}/k_B$ (K) | −43.5 | | ±0.5 |
| $\chi_0$ ($m^3$/mol) | $-2.0 \times 10^{-9}$ | | $\pm 10^{-10}$ |
| $g$ | 2.36 | 2.39 | ±0.05 |

$$\chi_{\text{MF}}(T) = \frac{\chi^{\text{dimer}}(T)}{1 + \chi^{\text{dimer}}(T)\dfrac{\tilde{J}}{N_A g^2 \mu_B^2 \mu_0}}. \tag{1c}$$

Here,

$$\chi^{\text{dimer}}(T) = \frac{N_A g^2 \mu_B^2 \mu_0}{3 k_B T} \frac{2(S+1)\exp\left(-\dfrac{J}{k_B T}\right)}{1 + 2(S+1)\exp\left(-\dfrac{J}{k_B T}\right)} \tag{1d}$$

is the susceptibility of a noninteracting spin-dimer system with single spins $S = \frac{1}{2}$ and the intradimer coupling $J$. $\chi_{\text{MF}}$ accounts for the mean-field correction.[17]

For a given measured set of $\chi(T)$ data, we therefore used four fitting parameters: $\chi_0$, $g$, $J$, and $\tilde{J}$. We forced the values for $\chi_0$, $J$, and $\tilde{J}$ to be identical for both magnetic-field directions. This restriction is physically reasonable, since these three fitting parameters are independent of the magnetic-field orientation. A small anisotropy of the $g$ factor was considered, however, although it is not predicted by ESR measurements.[11] In fact, the obtained $g$ values for the two investigated crystallographic directions are the same within the error margin; see Table I. The best obtained fits are shown in Fig. 1. They yield a good description of the experimental data for $T \geq 20$ K. However, the distinct upturn in $\chi(T)$ at lower temperatures is not at all reproduced by the fits. We believe that this term is intrinsic for $TlCuCl_3$,[11,18] and we shall discuss it in more detail in Sec. III. Note that the inclusion of a Curie-type term for fitting the data at $T > 20$ K does not significantly change the results presented in Table I.

The value of the intradimer coupling $J$ is close to the result obtained by neutron-scattering measurements [$J/k_B \sim -64$ K (Ref. 10)]. For $TlCuCl_3$ the interdimer exchange interaction $\tilde{J}$ is a sum of three exchange constants $J_a$, $J_{a2c}$, and $J_{abc}$ which are defined in Ref. 10.

Unfortunately, the fit does not allow us to distinguish between these interaction constants, but the fact that $\tilde{J} \approx J$ clearly shows the strong 3D coupling between the dimers. From Eq. (1a) we find that the peak value $\chi_{\text{max}} = \chi(T \approx 36$ K) increases with increase in either the $g$ factor or the intradimer coupling constant $J$, or with decrease in the interdimer coupling constant $\tilde{J}$. Since our value of $J$ is consistent with published data from neutron-scattering measurements,[10]

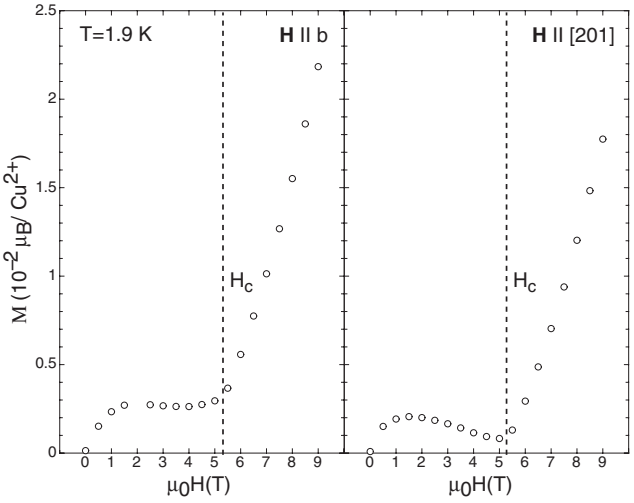


FIG. 3. The magnetizations $M(H)$ of $TlCuCl_3$ for $T=1.9$ K with $H$ applied along the crystallographic $b$ axis (left) and along [201] (right).

the slight overshoot of the fitting curve with respect to the measured data around $\chi_{\max}$ implicates an underestimate of $\tilde{J}$ and/or an overestimate of the Landé $g$ values. The latter scenario is supported by comparing our results to high-precision ESR measurements, which obtain a value of $g=2.06$ for both magnetic-field directions.

## III. LOW-TEMPERATURE MAGNETIZATION

In the theory of BEC of magnetic quasiparticles in insulating materials, the total magnetization (to be more precise, the total magnetic moment) $M=g\mu_B N$ is proportional to the total number of excited triplons, $N$, which depends on both the temperature $T$ and magnetic field $H$.[5] We therefore decided to analyze in detail the low-temperature region of the magnetization for both low magnetic fields ($1\ \mathrm{T} \leq \mu_0 H \lesssim \mu_0 H_c$) and high magnetic fields ($\mu_0 H_c \lesssim \mu_0 H \leq 9$ T) using a consistent approach including adequate contributions for the respective magnetic-field regions. We note here that all the magnetization data presented in this work are expressed as magnetic moment $M$ per single $Cu^{2+}$ ion. The later used quantity $m(T)=M(T)/N_d=g\mu_B n(T)$ [where $N_d$ is the number of dimers and $n(T)=N(T)/N_d$ is the total triplon density] differs from that by a factor of 2. All values extracted from fits and calculations are presented in the latter units.

### A. Magnetization $M(T)$ for $1\ \mathrm{T} \leq \mu_0 H \lesssim \mu_0 H_c$

Figure 2 shows the variation in $M$ of $TlCuCl_3$ at low temperatures along the crystallographic $b$ and the [201] directions for magnetic fields of up to $\mu_0 H=5$ T. The magnetization decreases exponentially to almost zero with decreasing temperature for both crystallographic directions, but shows an upturn at low temperatures for low magnetic fields. With increasing magnetic field the anisotropic behavior of the magnetization in the two different field orientations becomes apparent. Because in both field directions the upturn in $M$ at low temperatures is gradually suppressed with increasing $H$, the magnetization curves for $\mathbf{H}\|[201]$ cross at $T_{\mathrm{cross}} \sim 3.2$ K. For $\mathbf{H}\|b$, a similar crossing of $M(T)$ data cannot be seen in the analyzed temperature range; but by extrapolating the respective magnetization curves to lower temperatures, a $T_{\mathrm{cross}}$ below 2 K seems to be plausible.

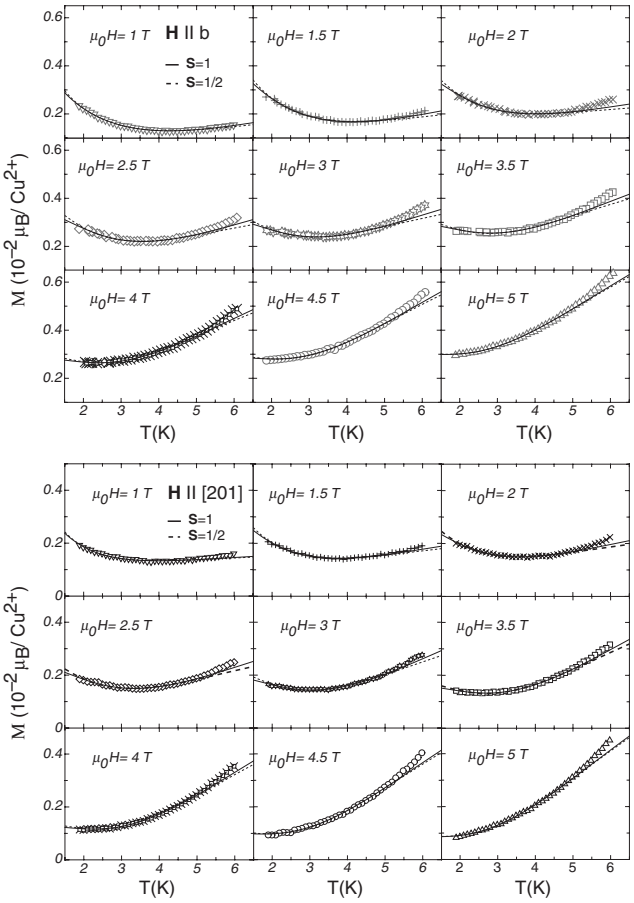


FIG. 4. The magnetizations $M(T)$ of $TlCuCl_3$ for $1\ \mathrm{T} \leq \mu_0 H \leq 5$ T applied along the crystallographic $b$ axis (upper frames) and along [201] (lower frames). The continuous and the dashed lines denote fits for $S=1$ and $S=\frac{1}{2}$, respectively (see text).

This crossing of $M(T)$ data is caused by the fact that the upturn in $M(T)$ at low temperatures does not grow linearly with $H$. Moreover, this upturn is quantitatively different in the two considered field directions. If this low-temperature contribution was due to an extrinsic paramagnetic impurity phase, it could be expected to be isotropic. We therefore consider this behavior to be intrinsic to $TlCuCl_3$. This upturn in $M(T)$ can be expressed as a temperature- and field-dependent Curie-Weiss-type term, assumed to be proportional to the Brillouin function $B_S(x)$ with $x=g\mu_B\mu_0 HS/k_B T$ and a constant $C_S$. Because we assume this term to be intrinsic to the here studied dimer system, it is reasonable to assign it to magnetic moments associated with the triplet states with $S=1$. A similar observation confirming this fact was reported in Refs. 11 and 18. The magnetic-field dependence of our low-temperature data showing an almost saturated behavior in $M(H)$ for $H<H_c$ (see Fig. 3) can indeed be qualitatively well reproduced by assuming a magne-

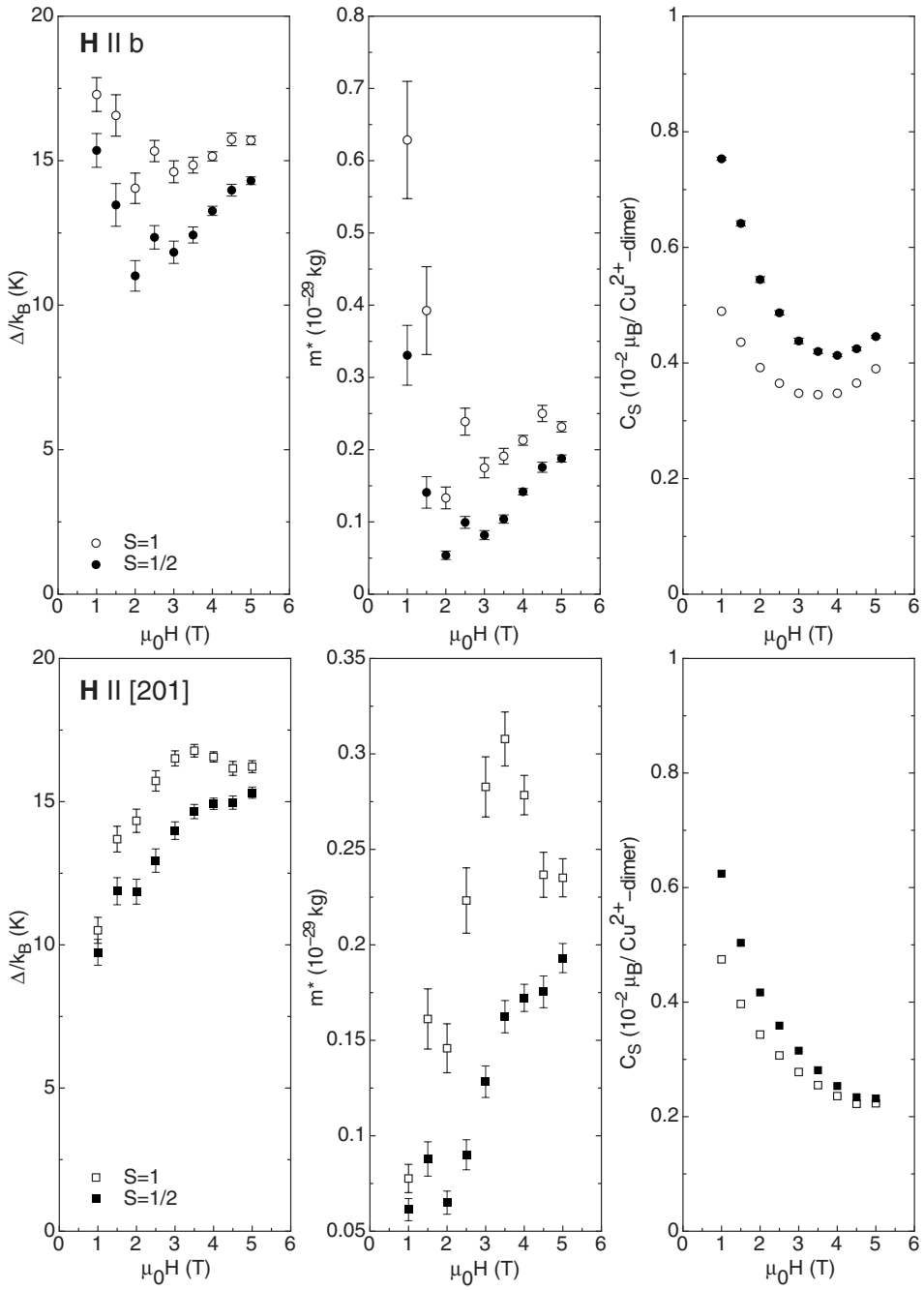


FIG. 5. The parameters $\Delta$, $m^\star$, and $C_S$ extracted from fits to the low-temperature magnetization data for $H\|b$ axis (upper frames) and for $H\|[201]$ (lower frames). Different scenarios for $m_{\mathrm{up}}$ are indicated with open marks ($S=1$) and filled marks ($S=\frac{1}{2}$). The error bars of $C_S$ are on the order of the dot size.

tization term that is proportional to a Brillouin function $B_S(x)$. The additional $H$ dependence for $H<H_c$ can be explained by taking again a diamagnetic term $m_{\mathrm{dia}}=\chi_0 H$ and an additional paramagnetic term $m_{\mathrm{HL}}(H)$ (to be discussed below) into account. However, the quality of corresponding fits to our low-temperature $M(H)$ data does not allow us to clearly distinguish between $S=1$ and $S=\frac{1}{2}$. Therefore, we will consider in the following both scenarios for the Curie-Weiss-type term $C_S B_S(x)$, and we will later argue that only the $S=1$ case fits to our data in a physically meaningful way.

From the expression for the free energy per unit length of a Heisenberg ladder,[19]

$$f=-\frac{k_B T}{2}\left[1+2\cosh\left(\frac{g\mu_B\mu_0 HS}{k_B T}\right)\right]z(T), \tag{2a}$$

with

$$z(T)=\frac{1}{2\pi}\int_{-\pi}^{\pi} e^{-\varepsilon_{\mathbf{k}}/k_B T}dk, \tag{2b}$$

we can estimate the magnetization per dimer by multiplying $f$ from Eq. (2a) with the mean dimer-dimer distance $\bar{a}=(abc\sin\beta)^{(1/3)}=0.79$ nm, where $a$, $b$, and $c$ and $\beta=96.32°$ are taken from crystallographic data of $TlCuCl_3$.[13] Using a simple quadratic approximation for the triplon dis-

persion relation, $\varepsilon_{\mathbf{k}} \propto \Delta + \hbar^2 k^2 / 2m^\star$ (where $m^\star$ corresponds to the effective mass of the triplons), one obtains[19]

$$z(T) \approx \frac{1}{2\sqrt{\pi}} \left( \frac{\hbar^2}{2m^\star k_B T} \right)^{-1/2} e^{-\Delta/k_B T}. \tag{3}$$

For the magnetization per dimer we therefore have

$$m_{\mathrm{HL}}(T) = -\bar{a} \frac{\partial f}{\partial H} = d\sqrt{T} e^{-\Delta/k_B T} \sinh\left( \frac{g\mu_B \mu_0 H}{k_B T} \right), \tag{4a}$$

with

$$d = g\mu_B \bar{a} \sqrt{\frac{k_B m^\star}{2\pi\hbar^2}}. \tag{4b}$$

In order to analyze the upturn in $M(T)$ at low $T$, we include the above-mentioned magnetization term,

$$m_{\mathrm{up}}(T) = g\mu_B S \cdot \beta \cdot C_S \cdot B_S\left( \frac{g\mu_B \mu_0 H}{k_B T} S \right) \begin{cases} \beta = 1 \ (S = 1) \\ \beta = 2 \ \left(S = \frac{1}{2}\right) \end{cases} \tag{5}$$

for a fixed magnetic field $H$. We distinguish between $S=\frac{1}{2}$ (nonintrinsic paramagnetic impurities $\beta=\frac{1}{2}$) and the scenario $S=1$ (intrinsic term related to triplet states $\beta=1$). The constant $\beta$ is introduced here in order to count the magnetic contribution $m_{\mathrm{up}}$ per dimer for both scenarios. We fitted the magnetization data at low enough temperatures ($T \leq 5$ K) and 1 T $\leq \mu_0 H \leq 5$ T for both field directions according to

$$\begin{aligned} m(T) &= \frac{M(T)}{N_d} = m_{\mathrm{HL}}(T) + m_{\mathrm{up}}(T) + m_{\mathrm{dia}} \\ &= g\mu_B \bar{a} \sqrt{\frac{k_B m^\star}{2\pi\hbar^2}} \cdot \sqrt{T} e^{-\Delta/k_B T} \sinh\left( \frac{g\mu_B \mu_0 H}{k_B T} \right) \\ &\quad + g\mu_B S \cdot \beta \cdot C_S \cdot B_S\left( \frac{g\mu_B \mu_0 H}{k_B T} S \right) + m_{\mathrm{dia}} \end{aligned} \tag{6}$$

with $g=2.06$.

Because we were using the $T$-independent diamagnetic contribution $m_{\mathrm{dia}}=\chi_0 H$ extracted from the high-temperature susceptibility fits presented above, only the gap $\Delta$, the constant $C_S$ (for $S=1$ or $\frac{1}{2}$), and the effective mass of a triplon, $m^\star$, were fitting parameters. The corresponding fits to the magnetization data are shown in Fig. 4, while the corresponding results for the fitting parameters are presented in Fig. 5. The values for the gap $\Delta$ slightly vary with magnetic field for both field directions around $\Delta/k_B \approx 13$ K, which is somewhat larger than $\Delta \approx 0.7$ meV $= 8.3$ K (Ref. 10) determined by neutron scattering. The triplon mass $m^\star \approx 0.2 \times 10^{-29}$ kg is an order of magnitude smaller compared to the results from calculations and a corresponding analysis of high-field magnetization data within the Hartree-Fock approximation.[20] This discrepancy might be explained by our choice of a simplified quadratic energy-dispersion relation for this temperature region. The range of validity of a quadratic approximation is indeed restricted to lower temperatures ($T<1$ K) (Refs. 16, 19, 21, and 22) that are not accessible in our experiment.

The Curie-type contribution $C_S$ decreases for both cases $S=1$ and $S=\frac{1}{2}$ with increasing magnetic field $H$. For both field directions $C_S(H)$ shows a similar trend, although the variation with $H$ is much less pronounced for $S=1$. Since $C_S$ is expected to be a constant for a given magnetic-field direction, this fact already here strongly supports an $S=1$ scenario for a correct description of the paramagnetic background. We may speculate that this Curie-type term with $S=1$ comes from a contribution of defects in the crystal or from dimers that are situated near the crystal boundaries.

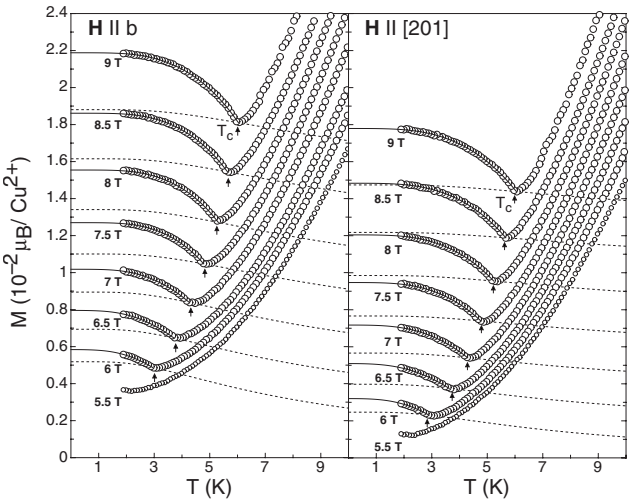


FIG. 6. The magnetizations $M(T)$ of $TlCuCl_3$ for 5.5 T $\leq \mu_0 H \leq 9$ T applied along the $b$ axis (left) and along [201] (right). The critical temperature $T_c^{\mathrm{BE}}$ is marked by arrows. The solid lines correspond to fits to the data according to Eq. (7) with $S=1$ for ($T < T_c$). The dashed lines represent calculated $M(T)$ curves using Eq. (7) and the same fitting parameters but with $n_0=0$.

### B. Magnetization $M(T)$ for 5.5 T $\leq \mu_0 H \leq 9$ T

The temperature dependence of the magnetization $M(T)$ along the applied magnetic field **H** shows a cusplike minimum at a critical temperature $T_c(H)$ for fixed magnetic field $H \geq H_c$; see Fig. 6. The increase in $M$ for $T<T_c$ is a consequence of the condensation of the magnetic quasiparticles and the increasing number of particles, $N_c$, in the ground state forming the condensate. Theoretical arguments suggest within a simplified model a $T$ dependence of $M \propto (1-\frac{T}{T_c})^{3/2}$ for $T<T_c$,[5] which is not observed in the experimental data, however.

At high magnetic fields we have therefore fitted the low-temperature magnetization per dimer, $m(T)$, according to a more general power law including the diamagnetic contribution that we extracted from high-temperature magnetic-susceptibility measurements, and again a net paramagnetic moment $m_{\mathrm{up}}(T,H)$ assumed to be proportional to the Brillouin function $B_S(x)$ for $S=1$ and $S=\frac{1}{2}$, respectively. For 6 T $\leq \mu_0 H \leq 9$ T we use

$$\begin{aligned} m(T) &= \frac{M(T)}{N_d} = g\mu_B \frac{N(T)}{N_d} + m_{\mathrm{up}}(T) + m_{\mathrm{dia}} \\ &= g\mu_B \left\{ n_{\mathrm{crit}} + n_0 \left[ 1 - \left( \frac{T}{T_c} \right)^\alpha \right] \right\} \\ &\quad + g\mu_B S \cdot \beta \cdot C_S(H) \cdot B_S\left( \frac{g\mu_B \mu_0 H}{k_B T} S \right) + m_{\mathrm{dia}}, \end{aligned} \tag{7}$$

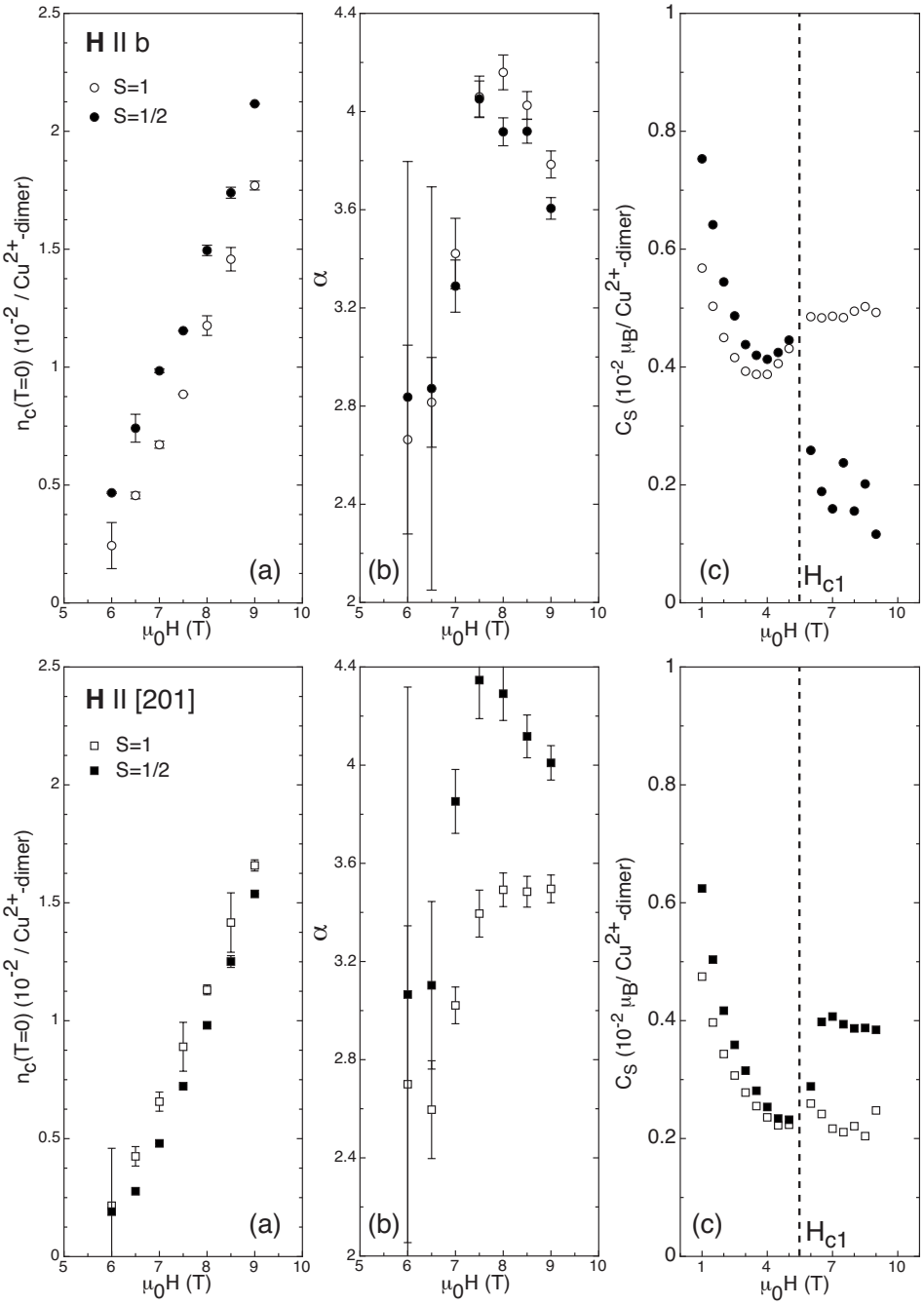


FIG. 7. (a) The condensate density $n_c(T=0)$, (b) the exponent $\alpha$, and (c) the Curie-type contribution $C_S$ for $H\|b$ (upper frames) and for $H\|[201]$ (lower frames). Different scenarios for $m_{\mathrm{up}}$ are indicated with open marks ($S=1$) and filled marks ($S=\frac{1}{2}$). The error bars of $C_S$ are on the order of the dot size.

where $n_{\mathrm{crit}}=N(T=T_c)/N_d$ is the critical density at which condensation occurs corresponding to the normalized magnetization $m(T=T_c)=g\mu_B n_{\mathrm{crit}}$. The physical meaning of the exponent $\alpha$ [see Fig. 7(b)] is not discussed here, although a possible interpretation is presented in the Appendix.

At zero temperature we have for fixed magnetic field $H$

$$m(T=0) = g\mu_B(n_{\mathrm{crit}} + n_0) + m_{\mathrm{up}}(T=0) + m_{\mathrm{dia}}$$
$$= g\mu_B n(0) + m_{\mathrm{up}}(T=0) + m_{\mathrm{dia}} \quad (8)$$

with the total triplon density at $T=0$ and $n(0)=n_{\mathrm{crit}}+n_0$.

For an ideal Bose gas $n(0)$ corresponds to the condensate density $n_c(0)$. As soon as interactions between the particles are considered, the depletion of the condensate has to be taken into account. The quantity

$$n(0) = n_c(0) + \tilde{n}(0) \quad (9)$$

is then a sum of the condensate density $n_c(0)$ and the density of noncondensed particles, $\tilde{n}(0)$. The latter term represents the number of triplons per $Cu^{2+}$ dimer scattered out of the ground state due to the interactions between the particles. It depends on the number of condensed particles and can be expressed as[5]

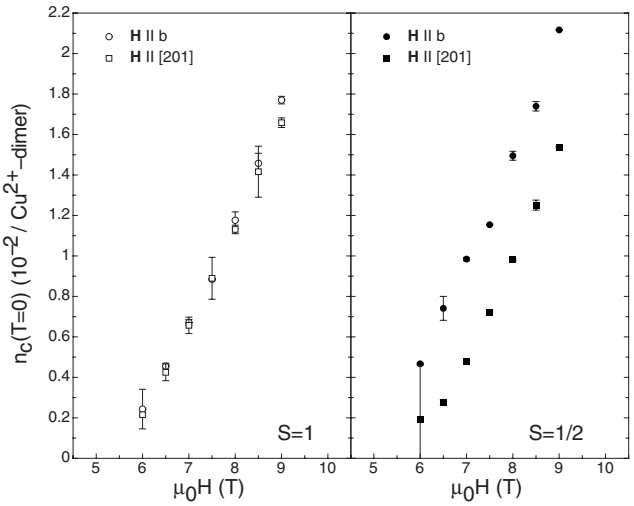


FIG. 8. The condensate density $n_c(T=0)$ with different scenarios for $m_{\mathrm{up}}$ (left: $S=1$; right: $S=\frac{1}{2}$).

$$\tilde{n}(0) = \frac{1}{3\pi^2}\left(\frac{mU_0 n_c(0)}{\hbar^2}\right)^{3/2}, \tag{10}$$

where $m^{\star} \approx 2.8 \times 10^{-29}$ kg is the mass of a triplon and $U_0/k_B \approx 315$ K (Ref. 20) is the two-particle interaction potential. Replacing $\tilde{n}(0)$ in Eq. (9) with the expression in Eq. (10), we obtain

$$n(0) = n_c(0) + \frac{1}{3\pi^2}\left(\frac{mU_0 n_c(0)}{\hbar^2}\right)^{3/2}. \tag{11}$$

From our fits according to Eq. (7) and with $n(0)=n_{\mathrm{crit}}+n_0$, we can now calculate the condensate density at zero temperature $n_c(0)$ for various magnetic fields using Eq. (11); see Fig. 7(a).

As one would expect from simple arguments,[5,20] $n_c(0)$ increases with increasing magnetic field. It is essential to note that the number of triplons $N_c(0)=n_c(0)N_d$ forming the condensate at $T=0$ is the same for both field directions only in the $S=1$ scenario for $m_{\mathrm{up}}(T)$ (see Fig. 8), and only in this scenario $n_c(0)$ extrapolates to zero at the correct critical field $\mu_0 H_c \approx 5.5$ T. These facts again strongly support our hypothesis that $m_{\mathrm{up}}(T)$ is intrinsic with $S=1$, and it confirms the interpretation of the magnetic field **H** acting as the chemical potential.[9] Right above the critical field $H_c$, the percentage of the condensed particles, $n_c(0)$, with respect to the total density of triplons, $n(0)$, is approximately 98% and slightly decreases with increasing magnetic field; see Fig. 9. This result is consistent with a similarly low noncondensed magnon density as calculated in Ref. 16, where $\tilde{n}(0)$ increases from zero for $H=H_c$ to approximately 7% of the total triplon density at $T=0$ in $\mu_0 H=7$ T. From the high percentage of condensed particles, we can confirm that the triplons in $TlCuCl_3$ form a *weakly interacting Bose gas*[16] right above $H_c$, and that the interaction increases with increasing particle density, i.e., with increasing magnetic field $H$.

Finally, we want to mention that the Curie-type contribution $C_S$ is small and essentially constant for $H>H_c$ in both the $S=\frac{1}{2}$ and the $S=1$ scenarios; see Fig. 7(c). However, the corresponding data for $S=1$ are more or less smooth continuations of the respective data for $H<H_c$, in very contrast to the $C_S$ data for $S=\frac{1}{2}$ that show a discontinuity around $H=H_c$; see Fig. 7(c). The comparably moderate variation in $C_S$ with $H$ over the whole considered range of magnetic fields for the $S=1$ scenario (covering both the normal phase and the BEC obeying an entirely different physics) may indicate that $C_S$ is indeed a constant for each magnetic-field direction, and that our interpretation of a $S=1$ paramagnetic background is correct.

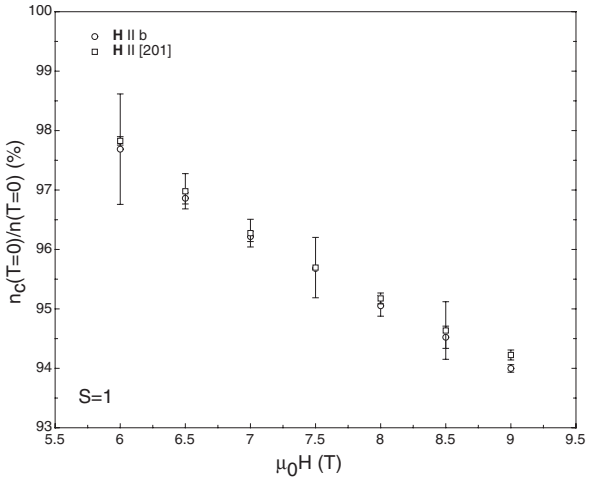


FIG. 9. The triplon fraction $n_c(0)/n(0)$ forming the condensate in the $S=1$ scenario for $m_{\mathrm{up}}$.

## IV. CONCLUSIONS

We have presented an analysis of magnetization $M(T,H)$ data of $TlCuCl_3$ and we calculated the density of condensed particles, $n_c(0)$ at $T=0$. The percentage of $n_c(0)$ with respect

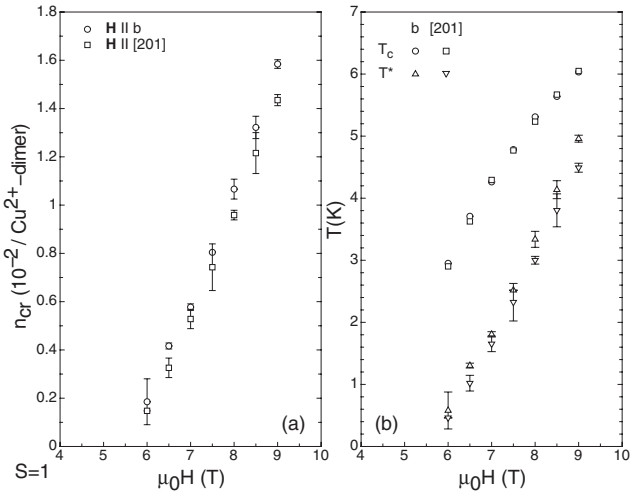


FIG. 10. (a) The critical triplon density $n_{\mathrm{cr}}$ and (b) the corresponding typical temperatures $T^{*} \approx n_{\mathrm{cr}}U_0/k_B < T_c$ in the $S=1$ scenario for $m_{\mathrm{up}}$ as functions of the applied magnetic field for $\mathbf{H} \| b$ (circles and upward triangles) and $\mathbf{H} \| [201]$ (squares and downward triangles).

to the total density of triplons, $n(0)$, is approximately 98% right above the critical field $H_c$ and slightly decreases with increasing magnetic field. We demonstrated that this fraction is the same for both $\mathbf{H}\|b$ and $\mathbf{H}\|[201]$ if we assume the presence of a small number of intrinsic $S=1$ magnetic moments that are not part of the Bose-Einstein condensate of triplons even at the lowest temperatures.

## ACKNOWLEDGMENTS

This work was supported by the Schweizerische Nationalfonds zur Förderung der wissenschaftlichen Forschung, under Grant No. 20-111653.

## APPENDIX

We want to emphasize that we do not interpret the exponent $\alpha$ in the power-law approach [Eq. (7)] used for fitting the low-temperature magnetization data at high magnetic fields as a universal critical exponent. In this sense its physical meaning is not clear. In general, the normal fluid density in a dilute Bose gas in the condensed phase is proportional to $T^4$ at low enough temperatures ($T \ll T^* \approx nU_0/k_B$), where $n$ is the total particle density and $U_0$ is the interaction energy.

In the case of $TlCuCl_3$ we can estimate $T^*$ by replacing $n \cong n_{cr}$ and $U_0/k_B \approx 313$ K (Ref. 22); see Fig. 10. The values for $\alpha$ extracted from the fits [see Fig. 7(b)] vary around $\alpha \sim 4$ with a decreasing tendency and increasing fitting error as $H \to H_c$. This can be explained by the fact that for high magnetic fields $T^*$ is fairly close to $T_c$, whereas for low magnetic fields the difference between the two characteristic temperatures increases, thereby restricting the validity of the $T^4$ power law to very low temperatures that are not accessible in our experiment. Nevertheless, it is clear that the increasing magnetization for $T \to 0$ is related to the increasing fraction of the condensed particles, $n_c(T)$. The evaluation of $n(0)$ from our phenomenological power law [see Eq. (7)] and the calculation of $n_c(0)$ using Eq. (11) give, in any case, a reliable estimate of the intercept of $n_c(T)$ at $T=0$, irrespective of the correct functional form of $n_c(T)$.

*dellamore@physik.uzh.ch
†schilling@physik.uzh.ch
‡karl.kraemer@iac.unibe.ch

[1] T. Matsubara and H. Matsuda, Prog. Theor. Phys. **16**, 569 (1956).
[2] I. Affleck, Phys. Rev. B **43**, 3215 (1991).
[3] B. C. Watson, V. N. Kotov, M. W. Meisel, D. W. Hall, G. E. Granroth, W. T. Montfrooij, S. E. Nagler, D. A. Jensen, R. Backov, M. A. Petruska, G. E. Fanucci, and D. R. Talham, Phys. Rev. Lett. **86**, 5168 (2001).
[4] Ch. Rüegg, N. Cavadini, A. Furrer, H.-U. Güdel, K. Krämer, H. Mutka, A. Wildes, K. Habicht, and P. Vorderwisch, Nature (London) **423**, 62 (2003).
[5] T. Nikuni, M. Oshikawa, A. Oosawa, and H. Tanaka, Phys. Rev. Lett. **84**, 5868 (2000).
[6] B. Grenier, Y. Inagaki, L. P. Regnault, A. Wildes, T. Asano, Y. Ajiro, E. Lhotel, C. Paulsen, T. Ziman, and J. P. Boucher, Phys. Rev. Lett. **92**, 177202 (2004).
[7] V. S. Zapf, D. Zocco, B. R. Hansen, M. Jaime, N. Harrison, C. D. Batista, M. Kenzelmann, C. Niedermayer, A. Lacerda, and A. Paduan-Filho, Phys. Rev. Lett. **96**, 077204 (2006).
[8] M. Jaime, V. F. Correa, N. Harrison, C. D. Batista, N. Kawashima, Y. Kazuma, G. A. Jorge, R. Stein, I. Heinmaa, S. A. Zvyagin, Y. Sasago, and K. Uchinokura, Phys. Rev. Lett. **93**, 087203 (2004).
[9] T. Giamarchi, Ch. Rüegg, and O. Tcherniyshyov, Nat. Phys. **4**, 198 (2008).
[10] N. Cavadini, G. Heigold, W. Henggeler, A. Furrer, H.-U. Güdel, K. Krämer, and H. Mutka, Phys. Rev. B **63**, 172414 (2001).
[11] A. Oosawa, M. Ishii, and H. Tanaka, J. Phys.: Condens. Matter **11**, 265 (1999).
[12] A. Oosawa, T. Kato, H. Tanaka, K. Kakurai, M. Muller, and H. J. Mikeska, Phys. Rev. B **65**, 094426 (2002).
[13] H. Tanaka, A. Oosawa, T. Kato, H. Uekusa, Y. Ohashi, K. Kakurai, and A. Hoser, J. Phys. Soc. Jpn. **70**, 939 (2001).
[14] F. London, Nature (London) **141**, 643 (1938).
[15] L. Tisza, Nature (London) **141**, 913 (1938).
[16] J. Sirker, A. Weisse, and O. P. Sushikov, J. Phys. Soc. Jpn. **74**, 129 (2005).
[17] D. C. Johnston, M. Troyer, S. Miyahara, D. Lidsky, K. Ueda, M. Azuma, Z. Hiroi, M. Takano, M. Isobe, Y. Ueda, M. A. Korotin, V. I. Anisimov, A. V. Mahajan, and L. L. Miller, arXiv:cond-mat/0001147 (unpublished).
[18] T. Lorenz, S. Stark, O. Heyer, N. Hollmann, A. Vasiliev, A. Oosawa, and H. Tanaka, J. Magn. Magn. Mater. **316**, 291 (2007).
[19] M. Troyer, H. Tsunetsugu, and D. Würtz, Phys. Rev. B **50**, 13515 (1994).
[20] F. Yamada, T. Ono, H. Tanaka, G. Misguich, M. Oshikawa, and T. Sakakibara, J. Phys. Soc. Jpn. **77**, 013701 (2007).
[21] E. Ya. Sherman, P. Lemmens, B. Busse, A. Oosawa, and H. Tanaka, Phys. Rev. Lett. **91**, 057201 (2003).
[22] G. Misguich and M. Oshikawa, J. Phys. Soc. Jpn. **73**, 3429 (2004).

PHYSICAL REVIEW B **79**, 1 (2009)

# $U(1)$ symmetry breaking and violated axial symmetry in $TlCuCl_3$ and other insulating spin systems

Raffaele Dell'Amore and Andreas Schilling
*Physik-Institut, University of Zurich, Winterthurerstrasse 190, 8057 Zurich, Switzerland*

Karl Krämer
*Department of Chemistry and Biochemistry, University of Bern, 3000 Bern 9, Switzerland*

(Received 19 November 2008)

We describe the Bose-Einstein condensate of magnetic bosonic quasiparticles in insulating spin systems using a phenomenological standard functional method for $T=0$. We show that results that are already known from advanced computational techniques immediately follow. The inclusion of a perturbative anisotropy term that violates the axial symmetry allows us to remarkably well explain a number of experimental features of the dimerized spin-1/2 system $TlCuCl_3$. Based on an energetic argument we predict a general intrinsic instability of an axially symmetric magnetic condensate toward a violation of this symmetry, which leads to the spontaneous formation of an anisotropy gap in the energy spectrum above the critical field. We, therefore, expect that a true Goldstone mode in insulating spin systems, i.e., a strictly linear energy-dispersion relation down to arbitrarily small excitations energies, cannot be observed in any real material.

DOI: XXXX PACS number(s): 64.70.Tg, 75.10.Hk, 75.30.Gw, 75.45.+j

## I. INTRODUCTION

The concept of the Bose-Einstein condensation (BEC), i.e., the occupation of a single-quantum state by a macroscopic number of bosons, has been extended from real bosonic particles to various types of quasiparticles with integer total spin.[1–11] Such discrete magnetic, electronic, or lattice excitations are then treated as a set of bosons forming a Bose gas.[9] These quasiparticles usually possess a small effective mass, which permits one to study BEC even at room temperature.[11] Both experiment[10,12] and theory[13,14] suggest that the occurrence of a BEC in a three-dimensional (3D) interacting Bose system has its origin in the spontaneous breaking of the $U(1)$ symmetry, thereby leading to a gapless and linear excitation spectrum in the long-wavelength limit, i.e., to a Goldstone mode.[15]

Experimental observations in a number of quantum spin systems can be explained within the theory of BEC, e.g., by a condensation of triplet states in dimerized spin-1/2 systems (hereafter called triplons) such as $TlCuCl_3$.[3,4,16] The bosonic character of these magnetic quasiparticles allows one to describe this spin-dimer system as a weakly interacting Bose gas. Inelastic neutron-scattering measurements in the condensate phase of $TlCuCl_3$ revealed, in accordance with theoretical investigations,[17] the presence of a seemingly gapless and linear excitation spectrum down to very low excitation energies of the order of 0.75 meV in $\mu_0 H = 14$ T.[4] This observation has been interpreted as a manifestation of the Goldstone mode.

In the last years various scenarios for the consequences of anisotropy on the properties of a magnetic BEC have been discussed in detail.[18–22] The presence of any kind of anisotropy will, in principle, explicitly break the rotational (i.e., axial) symmetry of the bosonic system.[21] The degree of spontaneous $U(1)$ symmetry breaking then depends on the order of magnitude of the anisotropic terms compared to the energy scale associated with the isotropic interactions of the Bose gas.[22] The relatively large triplon bandwidth in $TlCuCl_3$ (Ref. 23) exceeds the spin-nonconserving terms, such as an intradimer exchange (IE) anisotropy and a Dzyaloshinsky-Moriya (DM) anisotropy, by more than 2 orders of magnitude.[18,19,21] Nonetheless, the question to what extent the existing anisotropies in $TlCuCl_3$ do affect the magnetic phase diagram, the Goldstone mode, and other measurable quantities of $TlCuCl_3$ is still an issue under investigation.[18,19,21,24]

By taking a perturbative anisotropy term into account we will consider in the following the influence of an IE-like anisotropy that explicitly violates the axial symmetry, and we will study the consequences on the condensate phase of $TlCuCl_3$. The influence of a possible DM-type anisotropy[20,21] is not considered here.[25] Based on an energy consideration we will then argue that, as a consequence of an unavoidable magnetoelastic coupling, even an axially symmetric magnetic system is unstable toward a spontaneous violation of this symmetry as soon as the BEC state is formed.

## II. FUNCTIONAL METHOD

We describe the condensate at $T=0$ with a macroscopic wave function, a complex scalar field $\psi(\mathbf{r},\mathbf{t})$. Standard functional methods used to describe a dilute Bose gas in the classical limit at $T=0$ yield an extremal condition for the potential energy per dimer,[14] namely,

$$u(\psi) = -\mu\psi^\dagger\psi + \frac{v_0}{2}(\psi^\dagger\psi)\Big|^2_{\psi=\psi_0} = \min, \qquad (1)$$

where $\mu$ is the chemical potential, $v_0$ is a constant related to a repulsive short-range interaction,[13] and $\psi^\dagger$ is the complex conjugate of $\psi$. The minimum value $\psi_0$ then determines the condensate fraction $n_c(0)=\psi_0^\dagger\psi_0$, here defined as $n_c(0)=N_c/N_d$, with $N_c$ the number of condensed triplons and $N_d$ the number of dimers.

 

In a dimerized antiferromagnet, the chemical potential is $\mu = g\mu_B\mu_0(H - H_c)$, where $\mu_B$ is the Bohr magneton, $g$ is the Landé $g$ factor, and $H_c$ is the critical magnetic field beyond which a triplet $S=1$ state is energetically equally favorable as the singlet $S=0$ state. This can be expressed in terms of the energy gap $\Delta = g\mu_B\mu_0 H_c$ separating at zero field the $S=1$ and the $S=0$ states, respectively.

In the case of an explicitly violated axial symmetry we may include a perturbation term $|\tilde{\gamma}|(\psi\psi + \psi^\dagger\psi^\dagger)$ (Refs. 1 and 21) to the potential energy that can arise in a real magnetic system from various sources such as anisotropic intradimer and interdimer interaction constants, $J$ and $\tilde{J}$, respectively. For $TlCuCl_3$ we have, for example, $\mu_0 H_c \approx 5.6$ T,[26] $v_0/k_B = 315$ K,[27] and a $|\tilde{\gamma}|$ of the order of 0.01 meV,[18,21] depending on the orientation of the magnetic field $\mathbf{H}$ with respect to the crystal lattice.[18] Such an anisotropy term may arise from a pre-existing violated axial symmetry of the system or from a spontaneous distortion at the magnetic phase transition that we will discuss below. We, therefore, have to minimize

$$u(\psi) = -\mu\psi^\dagger\psi + |\tilde{\gamma}|(\psi\psi + \psi^\dagger\psi^\dagger) + \frac{v_0}{2}(\psi^\dagger\psi)^2, \qquad (2)$$

where we assume that $H_c$ itself is at first unchanged by the presence of the small perturbative anisotropy $|\tilde{\gamma}| \ll \Delta$.

We first want to compare the results of this simple formalism with corresponding predictions from advanced Hartree-Fock (HF) computations and with experimental data on $TlCuCl_3$. Despite the simple formalism used here, we can later make specific predictions that would otherwise be more difficult to obtain.

## III. RESULTS

### A. Comparison with results from the Hartree-Fock calculations

Without any explicit anisotropy (i.e., $|\tilde{\gamma}| = 0$) we obtain the well-known minimum value $\psi_0^\dagger\psi_0 = n_c(0) = \mu/v_0$.[3] The phase $\phi$ of $\psi_0 = |\psi_0|e^{i\phi}$ is not fixed in this case, leading to the $u(\psi)$ landscape sketched in Fig. 1 (left panel, "Mexican-hat potential"). However, any nonzero value for $|\tilde{\gamma}|$ locks the phase of $\psi_0$ to the imaginary axis (i.e., $\phi = \pm\pi/2$ and therefore $\psi_0 = \text{const}$) and leads to an optimum value $n_c(0) = (\mu + 2|\tilde{\gamma}|)/v_0$ in "Napoleon's hat potential" (see Fig. 1, right panel). The minimum potential energy becomes $u_{\min} = -(\mu + 2|\tilde{\gamma}|)^2/2v_0$ which is smaller than in the axially symmetric case. The saddle-point value for $u$ on the real axis for $\mu > 2|\tilde{\gamma}|$ is $-(\mu - 2|\tilde{\gamma}|)^2/2v_0$. Note that these energy densities are all expressed per dimer. The corresponding energies per triplon are $u/n_c(0)$.

A vanishing $n_c(0)$ is realized when $(\mu + 2|\tilde{\gamma}|) = 0$. As a consequence, the gap field $H_c$ that would be observed in an ideal system with axial symmetry is renormalized to a value $H_c^{\text{expt}} = H_c - \Delta H_c$ (with $\Delta H_c = 2|\tilde{\gamma}|/g\mu_0\mu_B$) above which condensation occurs. Taking a reasonable value for $|\tilde{\gamma}| \approx 0.01$ meV for $TlCuCl_3$ (Refs. 18 and 21) and $\mathbf{H} \| b$ with $g = 2.06$,[18] we obtain a renormalization of the critical field due to $|\tilde{\gamma}|$ alone by $\mu_0\Delta H_c \approx 0.2$ T for this particular magnetic-field direction.

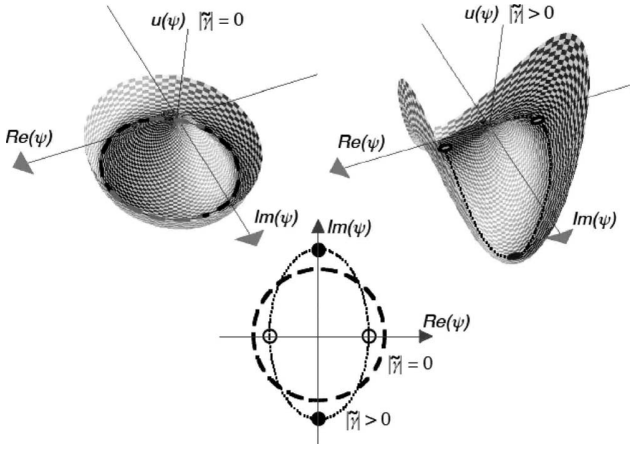


FIG. 1. Potential energy $u$ as a function of $\psi$ for axial symmetry (left panel, Mexican-hat potential) and violated axial symmetry (right panel, Napoleon's hat potential), respectively. In the symmetric case the minimum value $u_{\min} = -\mu^2/2v_0$ is realized along a circle (dashed line), while in the anisotropic case isolated minima $u_{\min} = -(\mu + 2|\tilde{\gamma}|)^2/2v_0$ are on the imaginary axis (filled circles).

The resulting condensate fraction, $n_c(0) = \mu^{\text{expt}}/v_0$, where $\mu^{\text{expt}} = g\mu_B\mu_0(H - H_c^{\text{expt}})$, is in full agreement with Hartree-Fock calculations for spin dimer systems.[3] In Fig. 2(a) we show the triplon condensate fraction $n_c(0)$ as deduced from our magnetization $M(T,H)$ data of $TlCuCl_3$,[28] see Fig. 2(b), that we have already corrected for a small fraction $\tilde{n}$ of noncondensed triplons.[3] These data have been obtained from the simple relation $M(0) = g\mu_B n(0) N_d$ [with $N_d$ as the number of dimers and $n(0)$ as the total triplon fraction at $T=0$],[3] without assuming any specific value for $v_0$. A linear fit to the data in the dilute limit $[\mu_0 H_c < \mu_0 H \lesssim 7.5$ T (Ref. 21)] yields $\mu_0 H_c^{\text{expt}} = 5.501 \pm 0.003$ T and $v_0/k_B = 311.4 \pm 0.5$ Km$^3$ which is in very good agreement with available literature values.[21,27,29] The deviation from the linear behavior at larger magnetic fields can be attributed to the contribution of higher triplet states.[5] Our simple formalism does not include the influence of such triplet states nor does it allow for a determination of $\tilde{n}$ itself; but this latter correction is of the order of a few percent at most in our data,[3,28] as it is typical for a weakly interacting Bose gas, see inset of Fig. 2(a).

Focusing further on the effects of an explicit violation of axial symmetry, the condensate fraction at $T=0$ is changed by $2|\tilde{\gamma}|/v_0$ in our calculation, see Figs. 2(c) and 2(d). If we use the fact that the total triplon fraction $n(0) \approx n_c(0)$ and take the result $n(T_c^{\text{BE}}) = n(0)/2$ from Ref. 3 assuming a quadratic triplon dispersion relation, we obtain a shift $|\tilde{\gamma}|/v_0$ in $n(T_c^{\text{BE}})$ that is again in full agreement with the corresponding HF calculations,[21] see again Figs. 2(c) and 2(d).

We may relate the minimum value $u_{\min}$ at $T=0$ to the transition temperature $T_c^{\text{BE}}$ if we assume that $|u_{\min}|/n_c(0)$, the energy gain per triplon upon condensation, is proportional to $k_B T_c^{\text{BE}}$ with a field-dependent proportionality factor of the order of unity. Any nonzero $|\tilde{\gamma}|$ leads to an increase in $T_c^{\text{BE}}$ as compared to the axially symmetric case, see Fig. 2(d). This trend can be clearly seen in the calculated $M(T,H)$ curves from Ref. 21, where the minimum in $M$ that is usually taken as a criterion to define $T_c^{\text{BE}}$ is shifted toward higher tempera-

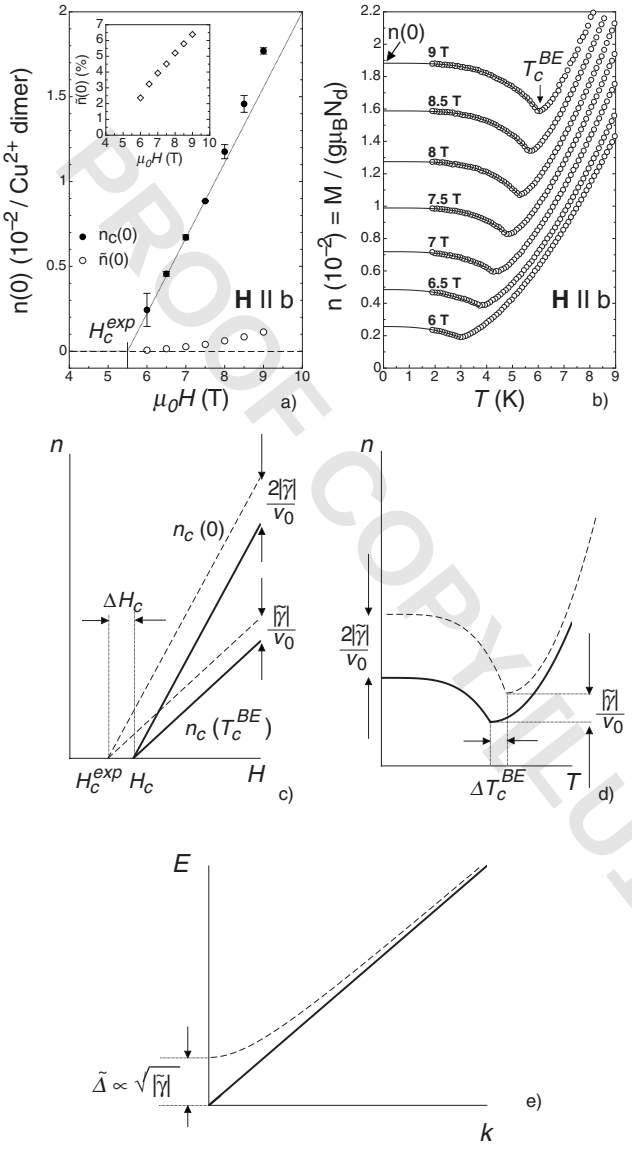


FIG. 2. (a) Condensate fraction $n_c(0)$, noncondensed triplon fraction $\tilde{n}(0)$, and the percentage of noncondensed triplons (inset) (Ref. 28). (b) Triplon-fraction $n(0)$ data obtained from magnetization $M(T)$ data for $\mathbf{H}\|b$ (see arrow for the $\mu_0 H=9$ T data and Ref. 28). (c) Schematic representations of the effects of violated axial symmetry on the triplon fraction at $T=0$ and at $T=T_c^{\mathrm{BE}}$, (d) on the triplon fraction at fixed magnetic field $H>H_c$ (Refs. 3, 20, and 21), and (e) on the excitation spectrum $E(k)$ (axes are not to scale). Solid and dashed lines represent an axially symmetric system and a system with violated axial symmetry, respectively.

tures as soon as $|\tilde{\gamma}|>0$. If we again take $|\tilde{\gamma}|=0.01$ meV we obtain a shift in $T_c^{\mathrm{BE}}$ of the order of $\Delta T_c^{\mathrm{BE}}\approx|\tilde{\gamma}|/k_B \approx +0.1$ K, which has to be compared to the result of the more precise HF calculations with $\Delta T_c^{\mathrm{BE}}\approx+0.5$ K.[21]

As a consequence of the anisotropy term $|\tilde{\gamma}|$ the original invariance of $u(\psi)$ with respect to a transformation $\psi \rightarrow \psi e^{i\phi}$ is lifted. The maximum variation in the potential energy per dimer $u$ along the ellipsoid contour with local minima in the radial $|\psi|$ direction, see Fig. 1, is $4\mu|\tilde{\gamma}|/v_0$ or $\tilde{\Delta}\approx 4|\tilde{\gamma}|$ per ground-state triplon. This determines the order of magnitude of an anisotropy gap that can be calculated to $\tilde{\Delta}=\sqrt{8|\tilde{\gamma}|g\mu_B\mu_0(H-H_c)}$.[21,30]

Excitations above the ground state $\psi_0$ with energies below $\tilde{\Delta}$ will clearly not show the typical gapless Goldstone-type behavior as expected for an axially symmetric system. For $TlCuCl_3$ we calculate, with $|\tilde{\gamma}|=0.01$ meV,[18,21] a gap $\tilde{\Delta}\approx 0.3$ meV for $\mu_0 H=14$ T along $b$, which is somewhat below what has been resolved in inelastic neutron-scattering measurements.[4] For excitation energies larger than $\tilde{\Delta}$ the presence of an anisotropy gap may remain unnoticed, see Fig. 2(e).

In $TlCuCl_3$ such a gap may arise from a pre-existing anisotropy that is already present in $H=0$.[19] In the following we argue, however, that even a perfectly axially symmetric magnetic system is unstable toward a spontaneous violation of this symmetry at $H_c$, which inevitably leads to the formation of a small anisotropy gap $\tilde{\Delta}$ above $H_c$ of real materials.

### B. Instability of the condensate toward violation of axial symmetry

A striking fact in our analysis is that the minimum potential energy per dimer is *smaller* with a nonzero $|\tilde{\gamma}|$ than in an analogous axially symmetric system with $|\tilde{\gamma}|=0$. This means that a distortion of the original crystal symmetry may spontaneously occur at $H_c$ together with an increase in $|\tilde{\gamma}|$, provided that the total energy, including both magnetic and crystal-lattice contributions, is lowered along with this distortion. This argument is so general that it should be applicable to all insulating spin systems that are supposed to show a Bose-Einstein condensation of magnetic bosonic quasiparticles. As we do not make any specific assumptions on the microscopic arrangement of the spin-carrying atoms, one cannot make any more precise universal statement about the details of the resulting lattice distortion.

The gain in potential energy per dimer upon condensation in combination with this simultaneous distortion is $2|\tilde{\gamma}|^2/v_0$, see Fig. 3(a). If the critical field is approached from below with $H$ increasing, the parameter $|\tilde{\gamma}|$ may therefore jump discontinuously from zero to its optimum value either at $H_c$ or at a transition field $H_c^\star$ with $H_c^{\mathrm{expt}}\leq H_c^\star\leq H_c$, while with $H$ decreasing the transition can take place at a different field in the same magnetic-field interval, see gray shaded area in Figs. 3(a) and 3(b). In an ideal situation with a perfect axial symmetry in $H=0$, the critical field $H_c$ corresponds to a "normal-state" value with $|\tilde{\gamma}|=0$ that is determined only by the gap energy, while in the condensate phase the effective critical field is $H_c^{\mathrm{expt}}=H_c-\Delta H_c<H_c$, lowered by $\Delta H_c=2|\tilde{\gamma}|/g\mu_B\mu_0$ with respect to $H_c$ due to the increase in $|\tilde{\gamma}|$. If the transition occurs at a transition field $H_c^\star$ that is strictly larger than $H_c^{\mathrm{expt}}$, one will observe at $T=0$ corresponding small discontinuities in $u$ [$\Delta u\leq 2|\tilde{\gamma}|^2/v_0$, see Fig. 3(a)], $n_c$ [$\Delta n_c\leq 2|\tilde{\gamma}|/v_0$, see Fig. 2(c)], and $M$ ($\Delta M=\Delta n_c g\mu_B N_d$), which would qualify the transition as of weakly first order with a maximum observable hysteresis width $\Delta H_c$. The occurrence of hysteretic effects in a real material may depend, however, on further conditions that are not considered here, such as material-quality issues or the relevance of possible

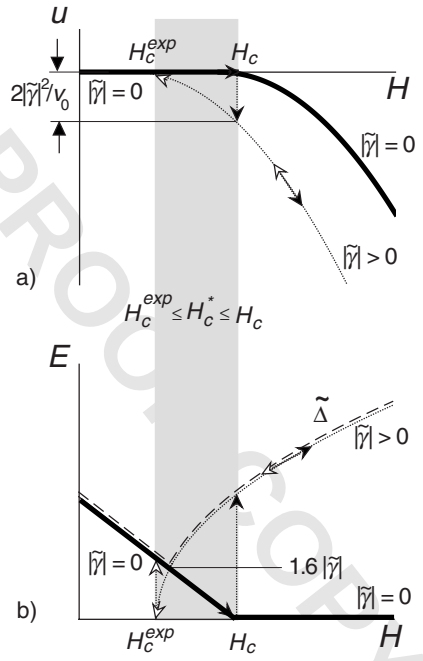


FIG. 3. (a) Potential energy per dimer and (b) energy-level scheme of the lowest triplon branch of an axially symmetric system ($|\tilde{\gamma}|=0$, thick solid lines) and of a system that shows a spontaneous axial distortion ($|\tilde{\gamma}|>0$) above $H_c^\star$ (thin lines and arrows, axes are not to scale), respectively. The gray shaded area indicates the maximum hysteresis width of a possible weakly first-order transition at $H_c^\star$ with $H_c^{expt} \le H_c^\star \le H_c$ (filled arrows: $H$ increasing; open arrows: $H$ decreasing). The dashed line in (b) reproduces the trend in the ESR data from Refs. 18 and 19 for $TlCuCl_3$ and $\mathbf{H} \| b$ (see text).

quantum fluctuations at $T=0$ to the order of the phase transition.

Even if a nonzero $|\tilde{\gamma}|$ evolves continuously above the critical field as a function of $H$ along with a continuous structural distortion with no detectable hysteresis, one should still be able to distinguish between the normal-state $H_c$ extracted from the experimental data taken below $H_c^{expt}$ and a $H_c^{expt} < H_c$ from corresponding data taken well above $H_c$, respectively, to obtain an estimate for $|\tilde{\gamma}|$ from the resulting difference $\Delta H_c$. In any case, if $H_c^{expt} < H_c^\star < H_c$, one expects a finite-energy difference $\le 1.6|\tilde{\gamma}|$ at the transition field $H_c^\star$ between the lowest-triplon state and the singlet states, respectively, see Fig. 3(b).

A possible pre-existing anisotropy that may already be present at $H=0$ (which is likely to be the case in $TlCuCl_3$) can be easily included in this formalism by identifying $H_c$ with a renormalized normal-state value that already contains this pre-existing anisotropy. Any additional $|\tilde{\gamma}|$ that may develop together with the lattice distortion around this critical field will somewhat change the value of the anisotropy gap $\tilde{\Delta}$. The difference $\Delta H_c$, however, and possible discontinuities in $u$, $n_c$, and $M$ are determined by the additional $|\tilde{\gamma}|$ alone.

It is remarkable that electron-spin resonance (ESR) data taken on $TlCuCl_3$ do indeed show a clearly gapped behavior at and above $\mathbf{H}=H_c^{expt} \| b$,[18,19] as we sketched in Fig. 3(b). Moreover, the ESR frequencies due to the lowest triplon gap in the normal phase for $\mathbf{H} \| b$ extrapolate to zero at a somewhat larger $H_c$ (by $\mu_0 H_c \approx 0.2$ T) than the square-root-like gap that we attribute to $\tilde{\Delta}(H)$ in the condensate phase and that can be fitted nicely with a $|\tilde{\gamma}| \approx 0.016$ meV, see energy-level scheme in Fig. 3(b). Our scenario may also be an explanation for the observed abrupt changes in the $^{35}Cl$ quadrupole shift[24] that has been interpreted as an indication of a weakly first-order lattice deformation, as well as for the pronounced hysteretic behavior (with a $\mu_0 \Delta H_c \approx 0.2-0.3$ T) of the observed peaks in the sound-attenuation data of $TlCuCl_3$ at $H_c(T)$.[31] These observations may indicate that $|\tilde{\gamma}|$ of $TlCuCl_3$ is indeed larger for $H > H_c$ than well below this value.

The present picture may also account for the first-order-like features that have been seen in the x-ray data of the spin-ladder compound $Cu_2(C_5H_{12}N_2)_2Cl_4$ (Ref. 32) and in the magnetocaloric effect of the axially symmetric $S=1$ system $NiCl_2$-4SC$(NH_2)_2$ (Ref. 33) at the respective magnetic phase transitions. It is also not unreasonable to assume that the observed gap feature in the ESR data of this latter compound at $\mu_0 H=8$ T (Ref. 34) is also related to a possible lattice distortion.

Such a spontaneous distortion arising from the interplay between the emerging magnetic Bose-Einstein condensate and its host crystal that lowers the total energy, with a tendency to increase or *even create* an anisotropy perpendicular to the external magnetic field above $H_c$ even in a perfectly axially symmetric system, is rather unique and is reminiscent of the spin-Peierls instability in one-dimensional magnetic chains. A spin-Peierls-type scenario has indeed been suggested to explain the NMR data on the spin-ladder compound $Cu_2(C_2H_{12}N_2)_2Cl_4$ around its critical magnetic field.[35,36] Such an instability should be a universal feature of magnetic BEC systems at their magnetic phase transition, and it is not expected to occur in axially symmetric Bose gases composed of real particles such as superfluid $^4He$ or atomic condensates, where the condensate cannot create an axial-symmetry-breaking term by itself.

In a microscopic picture, the tendency of a magnetic condensate to spontaneously violate the axial symmetry can be interpreted as a natural consequence of the transverse magnetic ordering that develops in the condensate phase and that locks to the crystal lattice due to unavoidable magnetoelastic coupling.[3,37,38] As soon as the transverse magnetic moments point to a specific energetically preferred crystal direction, the phase $\phi$ that is associated with the angle between these moments and the crystal axes[16] is indeed fixed [in $TlCuCl_3$ with an angle $\alpha \approx 39°$ to the $a$ axis (Ref. 37)], and the magnetic analog to a supercurrent velocity $\mathbf{v}_s = \hbar / m^\star \nabla \phi$ (where $m^\star$ is the effective mass of a triplon) is naturally zero for excitation energies below the anisotropy gap $\tilde{\Delta}$. This gap covers an excitation-frequency range that is crucial for experiments that rely on the existence of a long-lived phase-coherent condensate,[9] such as the detection of a long-lived spin supercurrent as in $^3He-B$,[39,40] of macroscopic second-sound-like oscillations as observed in superfluid $^4He$,[41] or of stable vortex-like structures as they have been observed in superfluid $^4He$ and in atomic condensates.[42] To achieve a lifetime of the order of seconds for a phase-coherent condensate, a corresponding anisotropy gap may not exceed a few femtoelectron volts.

In the absence of a Goldstone mode (for which all values of the phase $\phi$ have to be energetically equivalent), the quantity $\psi_0^\dagger\psi_0$ in the zero-frequency limit does no longer represent a condensate fraction, but it is rather related to the order parameter characterizing the antiferromagnetic state.[1]

## IV. CONCLUSIONS

We have analyzed the spontaneous symmetry breaking in a Bose gas of magnetic bosonic quasiparticles in insulating spin systems based on simple functional methods in the classical limit. Our results reproduce several results from earlier HF approximated computations,[3,20,21] and various experimental findings in $TlCuCl_3$ such as the occurrence and the magnitude of an anisotropy gap[18,19] and a weakly first-order-like behavior at the magnetic phase transition[24,31] can be explained. On the basis of an energetic argument we expect that all magnetic BEC systems in insulating spin systems are intrinsically unstable toward a spontaneous anisotropic distortion perpendicular to the external magnetic field, which leads to the formation of an anisotropy gap that is seriously limiting the lifetime of a phase-coherent condensate.

## ACKNOWLEDGMENTS

We thank O. Sushkov, A. K. Kolezhuk, and E. Ya. Sherman for stimulating discussions. This work was partly supported by the Schweizerische Nationalfonds zur Förderung der wissenschaftlichen Forschung under Grant No. 20-111653.

[1] I. Affleck, Phys. Rev. B **43**, 3215 (1991).
[2] T. Giamarchi and A. M. Tsvelik, Phys. Rev. B **59**, 11398 (1999).
[3] T. Nikuni, M. Oshikawa, A. Oosawa, and H. Tanaka, Phys. Rev. Lett. **84**, 5868 (2000).
[4] Ch. Rüegg, N. Cavadini, A. Furrer, H.-U. Gdel, K. Krmer, H. Mutka, A. Wildes, K. Habicht, and P. Vorderwisch, Nature (London) **423**, 62 (2003).
[5] P. Wachter, B. Bucher, and J. Malar, Phys. Rev. B **69**, 094502 (2004).
[6] M. Matsumoto, B. Normand, T. M. Rice, and M. Sigrist, Phys. Rev. B **69**, 054423 (2004).
[7] J. Kasprzak, M. Richard, S. Kundermann, A. Baas, P. Jeambrun, J. M. J. Keeling, F. M. Marchetti, M. H. Szymanska, R. Andr, J. L. Staehli, V. Savona, P. B. Littlewood, B. Deveaud, and L. S. Dang, Nature (London) **443**, 409 (2006).
[8] S. O. Demokritov, V. E. Demidov, O. Dzyapko, G. A. Melkov, A. A. Serga, B. Hillebrands, and A. N. Slavin, Nature (London) **443**, 430 (2006).
[9] D. Snoke, Nature (London) **443**, 403 (2006).
[10] R. Balili, V. Hartwell, D. Snoke, L. Pfeiffer, and K. West, Science **316**, 1007 (2006).
[11] V. E. Demidov, O. Dzyapko, S. O. Demokritov, G. A. Melkov, and A. N. Slavin, Phys. Rev. Lett. **100**, 047205 (2008).
[12] J. Harada, Phys. Lett. A **367**, 489 (2007).
[13] T. Haugset, H. Haugerund, and F. Ravndal, Ann. Phys. **266**, 27 (1998).
[14] J. O. Andersen, Rev. Mod. Phys. **76**, 599 (2004).
[15] J. Goldstone, A. Salam, and S. Weinberg, Phys. Rev. **127**, 965 (1962).
[16] T. Giamarchi, Ch. Rüegg, and O. Tcherniyshyov, Nat. Phys. **4**, 198 (2008).
[17] M. Matsumoto, B. Normand, T. M. Rice, and M. Sigrist, Phys. Rev. Lett. **89**, 077203 (2002).
[18] A. K. Kolezhuk, V. N. Glazkov, H. Tanaka, and A. Oosawa, Phys. Rev. B **70**, 020403(R) (2004).
[19] V. N. Glazkov, A. I. Smirnov, H. Tanaka, and A. Oosawa, Phys. Rev. B **69**, 184410 (2004).
[20] J. Sirker, A. Weisse, and O. P. Sushkov, Europhys. Lett. **68**, 275 (2004).
[21] J. Sirker, A. Weisse, and O. P. Sushkov, J. Phys. Soc. Jpn. **74**, 129 (2005).
[22] S. E. Sebastian, P. Tanedo, P. A. Goddard, S.-C. Lee, A. Wilson, S. Kim, S. Cox, R. D. McDonald, S. Hill, N. Harrison, C. D. Batista, and I. R. Fisher, Phys. Rev. B **74**, 180401(R) (2006).
[23] N. Cavadini, G. Heigold, W. Henggeler, A. Furrer, H.-U. Güdel, K. Krämer, and H. Mutka, Phys. Rev. B **63**, 172414 (2001).
[24] O. Vyaselev, M. Takigawa, A. Vasiliev, A. Oosawa, and H. Tanaka, Phys. Rev. Lett. **92**, 207202 (2004).
[25] The inclusion of a DM-like anisotropy term $i\gamma(\psi-\psi^\dagger)$ (Ref. 21) would result in strictly imaginary $\psi$ because $u(\psi)$ has to be real valued. A Goldstone-type mode can therefore not be obtained within this formalism.
[26] W. Shiramura, K. Takatsu, H. Tanaka, K. Kamishima, M. Takahashi, H. Mitamura, and T. Goto, J. Phys. Soc. Jpn. **66**, 1900 (1999).
[27] F. Yamada, T. Ono, H. Tanaka, G. Misguich, M. Oshikawa, and T. Sakakibara, J. Phys. Soc. Jpn. **77**, 013701 (2008).
[28] R. Dell'Amore, K. Krämer, and A. Schilling, Phys. Rev. B **78**, 224403 (2008).
[29] G. Misguich and M. Oshikawa, J. Phys. Soc. Jpn. **73**, 3429 (2004).
[30] This expression can also be qualitatively obtained within our formalism if we take $\Delta u=4\mu\tilde{\gamma}/v_0$, the maximum energy difference along the ellipsoid contour sketched in Fig. 1, to be approximately equal to $\tilde{\Delta}^2/v_0\cdot 1/v_0$ corresponds to the condensate fraction per energy $\partial n_c(0)/\partial\mu$ at the ground state $\psi_0$ and $\tilde{\Delta}$ represents a gap energy per condensed triplon that is needed to compensate for $\Delta u$.
[31] E. Ya. Sherman, P. Lemmens, B. Busse, A. Oosawa, and H. Tanaka, Phys. Rev. Lett. **91**, 057201 (2003).
[32] J. E. Lorenzo, K. Katsumata, Y. Narumi, S. Shimomura, Y. Tanaka, M. Hagiwara, H. Mayaffre, C. Berthier, O. Piovesana, T. Ishikawa, and H. Kitamura, Phys. Rev. B **69**, 220409(R) (2004).
[33] V. S. Zapf, D. Zocco, B. R. Hansen, M. Jaime, N. Harrison, C. D. Batista, M. Kenzelmann, C. Niedermayer, A. Lacerda, and A. Paduan-Filho, Phys. Rev. Lett. **96**, 077204 (2006).
[34] S. A. Zvyagin, J. Wosnitza, A. K. Kolezhuk, V. S. Zapf, M. Jaime, A. Paduan-Filho, V. N. Glazkov, S. S. Sosin, and A. I. Smirnov, Phys. Rev. B **77**, 092413 (2008).

[35] R. Calemczuk, J. Riera, D. Poilblanc, J.-P. Boucher, G. Chaboussant, L. Lévy, and O. Piovesana, Eur. Phys. J. B **7**, 171 (1999).
[36] H. Mayaffre, M. Horvatic, C. Berthier, M.-H. Julien, P. Ségransan, L. Lévy, and O. Piovesana, Phys. Rev. Lett. **85**, 4795 (2000).
[37] H. Tanaka, A. Oosawa, T. Kato, H. Uekusa, Y. Ohashi, K. Kakurai, and A. Hoser, J. Phys. Soc. Jpn. **70**, 939 (2001).
[38] M. Matsumoto and M. Sigrist, J. Phys. Soc. Jpn. **69**, 2310 (2005).
[39] A. S. Borovik-Romanov, M. Y. Bunkov, V. V. Dmitrieva, and Y. M. Mukharskiy, JETP Lett. **45**, 124 (1987).
[40] H. Tanaka, F. Yamada, T. Ono, T. Sakakibara, Y. Uwatoko, A. Oosawa, K. Kakurai, and K. Goto, J. Magn. Magn. Mater. **310**, 1343 (2007).
[41] V. P. Peshkov, J. Phys. (Moscow) **8**, 381 (1944).
[42] P. Rosenbusch, V. Bretin, and J. Dalibard, Phys. Rev. Lett. **89**, 200403 (2002).





PROOF COPY [LU11700B] 093845PRB

J. Phys.: Condens. Matter **21** (2009) 015701 (7pp) doi:10.1088/0953-8984/21/1/015701

# $LaBaNiO_4$: a Fermi glass

**A Schilling[1,5], R Dell'Amore[1], J Karpinski[2], Z Bukowski[2], M Medarde[3,4], E Pomjakushina[3,4] and K A Müller[1]**

[1] Physics Institute of the Universität of Zürich, Winterthurerstrasse 190, CH-8057 Zürich, Switzerland
[2] Laboratory for Solid-State Physics, ETH Zürich HPF F-7, CH-8093 Zürich, Switzerland
[3] Laboratory for Neutron Scattering, ETHZ and PSI, CH-5232 Villigen PSI, Switzerland
[4] Laboratory for Developments and Methods, ETHZ and PSI, CH-5232 Villigen PSI, Switzerland

E-mail: schilling@physik.uzh.ch

Received 13 September 2008, in final form 3 November 2008
Published 1 December 2008
Online at stacks.iop.org/JPhysCM/21/015701

**Abstract**
Polycrystalline samples of $LaSr_{1-x}Ba_xNiO_4$ show a crossover from a state with metallic transport properties for $x = 0$ to an insulating state as $x \to 1$. The end member $LaBaNiO_4$ with a nominal nickel Ni $3d^7$ configuration might therefore be regarded as a candidate for an antiferromagnetic insulator. However, we do not observe any magnetic ordering in $LaBaNiO_4$ down to 1.5 K, and despite its insulating transport properties several other physical properties of $LaBaNiO_4$ resemble those of metallic $LaSrNiO_4$. Based on an analysis of electrical and thermal-conductivity data as well as magnetic-susceptibility and low-temperature specific-heat measurements, we suggest that $LaBaNiO_4$ is a Fermi glass with a finite electron density of states at the Fermi level but these states are localized.

(Some figures in this article are in colour only in the electronic version)

## 1. Introduction

Certain transition-metal oxides show unique physical properties that are not only of academic interest but also make them technologically useful. The discoveries of high-temperature superconductivity [1] and colossal magnetoresistance [2] in such oxides have triggered tremendous activity in the research into these compounds with the aim of understanding their peculiar magnetic and transport properties.

The metallic state in the high-temperature superconductors, for example, is highly unusual because it evolves from originally electrically insulating oxides. Stoichiometric $La_2CuO_4$ is antiferromagnetic near room temperature, with copper in a Cu $3d^9$ (spin $S = 1/2$) configuration, and it is regarded as a Mott insulator. These features are generally believed to be important ingredients for the occurrence of superconductivity on subsequent doping of the compound with hole-type charge carriers, e.g. by the partial substitution of La by Ba or Sr [1]. In contrast, stoichiometric $LaSrNiO_4$, which shares the same $K_2NiF_4$ structure with $La_2CuO_4$, is metallic [3], although a $3d^7$ configuration of nickel in a low-spin $S = 1/2$ state might be expected that could also lead to an antiferromagnetic and insulating state. This fact has been explained with the partial occupation of the oxygen O 2p energy band of $LaSrNiO_4$ by hole states that hybridize with the nickel Ni $3d^8$ states, in contrast to $La_2CuO_4$ which shows a completely filled copper Cu $3d^9$ lower-Hubbard band [4]. The occupation of oxygen 2p hole states, leaving the nickel in an Ni $3d^8$ configuration, is very common in nominally trivalent-nickel oxides [5–7]. For this reason $LaSrNiO_4$ has not been considered as a serious candidate for a 'parent compound' of superconductors, and substitution experiments in $La_{2-y}Sr_yNiO_4$ over a wide range of doping (i.e. $0 \leqslant y \leqslant 1.5$) have not resulted in superconducting samples [3, 8].

In great contrast to the metallic character of $LaSrNiO_4$, the isostructural compound $LaBaNiO_4$ has been reported to be an insulator at zero temperature $T$, and to undergo a transition from a high-spin to a low-spin $S = 1/2$ state of Ni around $T \approx 120$ K with decreasing temperature [9]. It is therefore of particular interest to study the influence of a partial or a complete substitution of Sr by Ba in $LaSrNiO_4$ on the physical properties that are expected to be affected by a resulting stretching of the crystal lattice [9, 10]. We have found that there exists a solid solution of Ba in $LaSr_{1-x}Ba_xNiO_4$ for $0 \leqslant x \leqslant 1$, and we have measured the electrical and the thermal

[5] Author to whom any correspondence should be addressed.

 

conductivities, the magnetic susceptibilities and the low-temperature specific heats of polycrystalline $LaSr_{1-x}Ba_xNiO_4$ samples. Since possible magnetic-ordering phenomena as well as other physical properties may strongly depend on the exact oxygen stoichiometry, we have combined a thorough neutron-diffraction analysis of the end member $LaBaNiO_4$ with a chemical analysis and with additional heat-treatment experiments at an elevated oxygen pressure.

## 2. Experimental details

We have prepared polycrystalline samples of $LaSr_{1-x}Ba_xNiO_4$ for $x = 0$, 0.25, 0.3, 0.35, 0.4, 0.45, 0.5, 0.75 and 1.0 by a standard wet chemical procedure. Mixtures of corresponding metal nitrates were dissolved in nitric acid. The liquid was then slowly evaporated, and the remaining mixture of nitrate powders was pre-reacted at 900 °C for several hours in air. The remaining mixture of oxides was pressed into pellets and sintered at 1100 °C for 3 days in air. Samples of $LaSr_{0.5}Ba_{0.5}NiO_{4-\delta}$ ($x = 0.5$) and $LaBaNiO_{4-\delta}$ ($x = 1.0$) were post-annealed at temperatures between 400 and 600 °C and at an $O_2$ pressure of 500–880 bar (50–88 MPa). After testing the phase purity of all the samples with a Guinier camera using Cu K$\alpha_1$ radiation we have performed a thermogravimetric analysis on 100 mg of each as-prepared and high-pressure oxygen-annealed $LaBaNiO_{4-\delta}$, followed by neutron-diffraction experiments on 5 g powdered samples of the same batches at various temperatures between 1.5 and 550 K. These experiments were performed at the neutron source SINQ in Villigen, Switzerland, on the high resolution neutron powder diffractometer (HRPT) ($\lambda = 0.15$ and 0.18 nm) and the cold neutron powder diffractometer (DMC) ($\lambda = 0.245$ and 0.4 nm). The four-probe electrical conductivities and the AC magnetic susceptibilities were measured for all the samples in zero DC magnetic field. Specific-heat data were taken on three samples ($x = 0$ and high-pressure oxygen-annealed $x = 0.5$ and 1), while the thermal conductivities were measured only on the $x = 0$ and the high-pressure oxygen-annealed $x = 1$ samples. All the physical properties were collected using standard factory options in a commercial PPMS platform (Physical Property Measurement System, Quantum Design Inc., San Diego, USA).

## 3. Results

### *3.1. Chemical analysis and neutron-diffraction experiments*

A thermogravimetric analysis of the as-prepared $x = 1$ sample $LaBaNiO_{4-\delta}$ yielded an oxygen content 3.85(1) ($\delta \approx 0.15$) assuming a nominal cation ratio La:Ba:Ni = 1:1:1. Under the same assumption, a Rietveld refinement of the room-temperature neutron-diffraction pattern using the space group $I4/mmm$ proposed in previous work [9, 10] (see figure 1) also gave an oxygen content 3.85(1), with oxygen vacancies located both in the apical positions (≈33%) and in the basal planes (≈66%). A refinement with the restriction (La + Ba):Ni = 2:1 gave similar $R$-factors and suggested a composition $La_{1.27(2)}Ba_{0.73(2)}NiO_{3.97(2)}$ which would imply a considerable amount of unreacted BaO present as an impurity. However, we could not find any detectable amount of BaO and/or its carbonated subproducts, either in the diffraction patterns or by chemical methods. To clarify this issue we repeated the chemical analysis and the neutron-diffraction measurements on samples that were annealed at 400 °C under an oxygen pressure of 880 bar (88 MPa) for 50 h (annealing at 600 °C at elevated oxygen pressure resulted in a partial decomposition of the sample). According to the observed weight change we estimated an oxygen uptake of ≈0.16/f.u. during this procedure, which is consistent with the above value $\delta \approx 0.15$ for the as-prepared sample. The thermogravimetric analysis of the high-pressure oxygen-annealed sample resulted in an oxygen content 4.025(10), thereby confirming the nearly stoichiometric composition $LaBaNiO_4$ after the high-oxygen pressure treatment. The structural parameters of oxygen-annealed $LaBaNiO_4$ as obtained from DMC data refinements ($\lambda = 0.245$ nm) using the tetragonal space group $I4/mmm$ are listed in table 1 for three different temperatures $T = 1.5$ K, 295 K and 550 K, respectively.

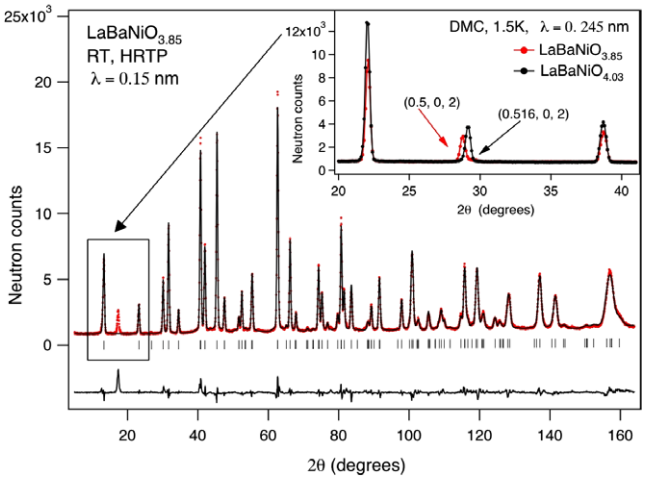


**Figure 1.** Neutron-powder-diffraction pattern of $LaBaNiO_{3.85}$ taken at room temperature, together with a Rietveld-refinement fit using the space group $I4/mmm$. The inset shows the displacement of the (1/2, 0, 2) Bragg reflection to the incommensurate position (0.516, 0, 2) upon increasing the oxygen content to 4.025.

**Table 1.** Lattice parameters and refined atomic coordinates of $LaBaNiO_4$ using the space group $I4/mmm$. (La, Ba): 4e (0 0 $z_1$); Ni: 2a (0 0 0); O1: 4e (0 0 $z_2$); O2: 4c (0.5 0 0).

| | $T = 1.5$ K | 295 K | 550 K |
|---|---|---|---|
| $a$ (nm) | 0.384 970(11) | 0.385 519(11) | 0.386 754(11) |
| $c$ (nm) | 1.273 670(56) | 1.278 893(57) | 1.286 938(58) |
| $z_1$ | 0.360 86(62) | 0.360 50(63) | 0.360 80(64) |
| $z_2$ | 0.164 97(57) | 0.165 09(59) | 0.165 68(58) |

As expected and also reported in [9, 10], the lattice parameters of $LaBaNiO_4$ are larger than those of $LaSrNiO_4$ ($a = 0.3826$ nm, $c = 12.45$ nm [11]), and vary smoothly from $x = 0$ to 1 according to our Guinier Cu K$\alpha_1$ diffraction patterns. In agreement with a report by Alonso *et al* [10] we detected a distinct extra reflection peak in the neutron-diffraction data of the as-prepared $LaBaNiO_{4-\delta}$ sample that

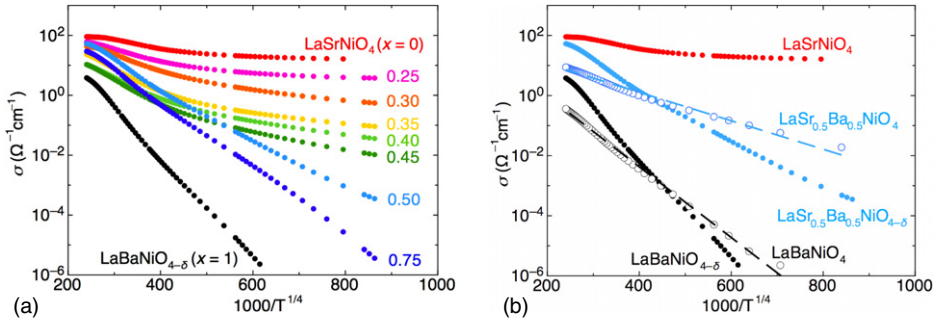


**Figure 2.** (a) Electrical conductivities $\sigma$ versus $T^{-1/4}$ of as-prepared samples (full circles) and (b) of high-pressure oxygen-annealed samples (open circles). The dashed lines are fits according to a variable-range hopping-type conductivity, see text.

can be indexed as (1/2, 0, 2), indicating a doubling of the unit cell in the $a$-direction and changing the crystal symmetry from tetragonal to orthorhombic. Upon high-pressure oxygen annealing, this peak slightly moved to an incommensurable position (0.516, 0, 2), see figure 1, and corresponding tiny higher-order peaks could also be indexed with a propagation vector $\boldsymbol{k} = (0.516, 0, 0)$. Since these peaks have not been observed in the x-ray diffraction patterns they could, in principle, be ascribed to the ordering of La/Ba [10] or they might even be of magnetic origin. This latter hypothesis can be safely excluded, however, since we did not observe any change in the respective peak intensities between 1.5 and 550 K. As the low-temperature oxygen treatment mainly affects the oxygen stoichiometry, the extra peak could also be ascribed to some kind of oxygen-vacancy and/or charge/stripe-ordering phenomenon, at least in the case of the oxygen-defective sample [12–14]. For stoichiometric $LaBaNiO_4$ with a nominally single-valent $Ni^{3+}$, this explanation does not seem to be very plausible, however. Another possibility that could explain the very similar intensities of the extra peak in both the as-prepared and the oxidized samples is the existence of a charge-density wave of the type $Ni^{3+\delta}/Ni^{3-\delta}$. Such a charge disproportionation, although difficult to observe with diffraction techniques, has been recently reported for other stoichiometric $Ni^{3+}$ compounds close to the boundary between localized and itinerant behaviour, such as $AgNiO_2$ [15] and $YNiO_3$ [16]. In the present $LaBaNiO_{3.85}$ and $LaBaNiO_4$ samples, however, we have not yet been able to establish a model for a charge and/or an oxygen-vacancy ordering that could sufficiently reproduce the observed intensity of the observed extra peak.

It is important to mention that apart from the displacements of the Bragg reflections due to thermal dilatation, the diffraction patterns for fully oxygenated $LaBaNiO_4$ at different temperatures look *exactly the same*. In particular there is no evidence for the appearance of additional reflections at low temperatures that would suggest any type of magnetic order in $LaBaNiO_4$.

### 3.2. Electrical conductivity

In figure 2(a) we show the electrical conductivities of the as-prepared samples, plotted as $\sigma$ versus $T^{-1/4}$ on a semi-logarithmic scale. The measured data for $LaSrNiO_4$, with a slight decrease of $\sigma$ with decreasing temperature, are perfectly in line with corresponding data from the literature [3, 8]. As a general trend, the low-temperature conductivity decreases with increasing Ba content, but more importantly, its temperature dependence changes from a relatively weak one for $LaSrNiO_4$ ($x = 0$) to a $\sigma(T)$ that varies over more than six decades from room temperature down to $T = 7$ K for $LaBaNiO_{4-\delta}$ ($x = 1$). In figure 2(b) we show the corresponding data of the samples that have been annealed at an elevated oxygen pressure. Although there is a change in the data of $LaSr_{0.5}Ba_{0.5}NiO_{4-\delta}$ and $LaBaNiO_{4-\delta}$ upon oxygen annealing, namely a decrease in the room-temperature conductivity and slight flattening of $\sigma(T)$, the strongly temperature dependent character of the electrical conductivity remains, confirming that stoichiometric $LaBaNiO_4$ is an insulator at $T = 0$. As was already noticed by Demazeau *et al* [9] the best physically reasonable fit to the $\sigma(T)$ data of $LaBaNiO_{4-\delta}$ is according to a strongly $T$-dependent 3D variable-range hopping-type (VRH) conductivity, $\sigma(T) = \sigma_0 \exp[-(T_0/T)^{1/4}]$ [17] (see dashed lines in figure 2(b)), which we will discuss later in section 4.

In the following we will restrict our discussion of the other measured physical properties to the samples $LaSrNiO_4$, the oxygen treated $LaSr_{0.5}Ba_{0.5}NiO_4$ (as a prototype of an intermediate composition) and $LaBaNiO_4$ to avoid unnecessary complications coming from an off-stoichiometric oxygen content.

### 3.3. Magnetic susceptibility

In figure 3 we present the magnetic-susceptibility $\chi(T)$ data of $LaSrNiO_4$ and oxygen treated $LaSr_{0.5}Ba_{0.5}NiO_4$ and $LaBaNiO_4$. Despite the large differences in the respective electrical conductivities, the three curves all look very similar, with an almost constant $\chi_0$ at high temperatures and a small Curie-like upturn in $\chi(T)$ at low temperatures, which is in agreement with the data for $LaSrNiO_4$ from the literature [3]. A corresponding fit to the data above $T = 40$ K assuming $\chi(T) = C/T + \chi_0$ gives an almost universal value $\chi_0 \approx 4 \times 10^{-4}$ emu mol$^{-1}$ and a Curie term $C$ of the order of 1–$2 \times 10^{-2}$ emu K mol$^{-1}$ (see table 2), which corresponds to only about 5% of the value for free low-spin $S = 1/2$ $Ni^{3+}$ ions. This indicates that the magnetic moments of Ni in electrically insulating $LaBaNiO_4$ are in a large majority *not localized*. A mathematically better fit to all the data, including

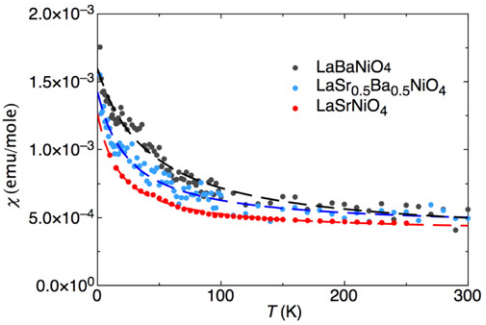


**Figure 3.** Magnetic susceptibilities $\chi(T)$ of $LaSrNiO_4$ (bottom), oxygen treated $LaSr_{0.5}Ba_{0.5}NiO_4$ (middle) and $LaBaNiO_4$ (upper curve). The dashed lines are fits to the data assuming $\chi(T) = C/(T + \Theta) + \chi_0$ (see text and table 2).

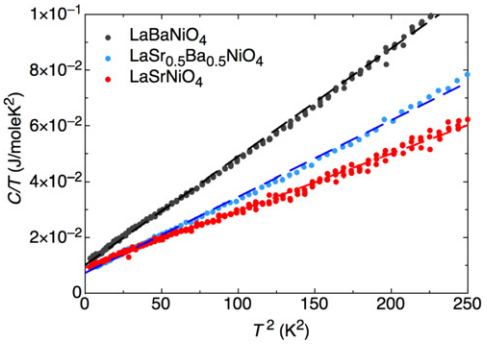


**Figure 4.** Reduced specific-heat $C/T$ versus $T^2$ data of $LaSrNiO_4$ (bottom), oxygen treated $LaSr_{0.5}Ba_{0.5}NiO_4$ (middle) and $LaBaNiO_4$ (upper curve). The dashed lines are fits to $C(T) = \beta T^3 + \gamma T$ (see text and table 3).

those at temperatures below 40 K, is obtained by allowing for a Néel-type expression $\chi(T) = C/(T + \Theta) + \chi_0$, see figure 3. However, the qualitative results, namely a $\chi_0$ of the order of 3–5 $\times$ $10^{-4}$ emu mol$^{-1}$ and a fairly small Curie term, remain the same. Note that the free-electron value for the Pauli-paramagnetic susceptibility of a metal is $\chi_0 \approx 4 \times 10^{-5}$ emu mol$^{-1}$ assuming one charge carrier per formula unit. The observed strong enhancement of the measured $\chi_0$ values over the free-electron value will be discussed below in section 4.

### 3.4. *Specific heat*

In figure 4 we have plotted the specific-heat data of $LaSrNiO_4$, $LaSr_{0.5}Ba_{0.5}NiO_4$ and $LaBaNiO_4$ as $C/T$ versus $T^2$ and for temperatures $T < 16$ K. A standard analysis accounting for a phonon contribution $\beta T^3$ and a linear term $\gamma T$ that is usually ascribed to a finite electron density of states at the Fermi level, gives the parameters presented in table 3. As expected from Debye theory, the Debye temperature $\Theta_D = (233.8nR/\beta)^{1/3}$ (with $n$ the number of atoms per unit cell and the gas constant $R = 8.314$ J mol$^{-1}$ K$^{-1}$) decreases for increasing molar mass, i.e. increasing Ba content. While the presence of a linear term in the specific heat of $LaSrNiO_4$ is not unexpected because of its metallic nature, corresponding linear terms of the same order of magnitude are also obtained

**Table 2.** Fitting results of the $\chi(T)$ data shown in figure 3. The first row for each compound corresponds to a fit according to $\chi(T) = C/T + \chi_0$, the second row to $\chi(T) = C/(T + \Theta) + \chi_0$.

| | $C$ (emu K mol$^{-1}$) | $\chi_0$ (emu mol$^{-1}$) | $\Theta$ (K) |
|---|---|---|---|
| $LaSrNiO_4$ | $1.10(2) \times 10^{-2}$ | $4.12(2) \times 10^{-4}$ | — |
| | $1.62(7) \times 10^{-2}$ | $3.90(5) \times 10^{-4}$ | $18.4 \pm 1.3$ |
| $LaSr_{0.5}Ba_{0.5}NiO_4$ | $1.60(11) \times 10^{-2}$ | $4.57(15) \times 10^{-4}$ | — |
| | $2.58(30) \times 10^{-2}$ | $4.23(21) \times 10^{-4}$ | $25.7 \pm 3.2$ |
| $LaBaNiO_4$ | $2.41(10) \times 10^{-2}$ | $4.49(13) \times 10^{-4}$ | — |
| | $5.40(60) \times 10^{-2}$ | $3.41(31) \times 10^{-4}$ | $43 \pm 5$ |

**Table 3.** Fitting results from the specific-heat data in figure 4 according to $C(T) = \beta T^3 + \gamma T$.

| | $LaSrNiO_4$ | $LaSr_{0.5}Ba_{0.5}NiO_4$ | $LaBaNiO_4$ |
|---|---|---|---|
| $\beta$ (mJ mol$^{-1}$ K$^{-4}$) | 0.204(1) | 0.273(1) | 0.388(1) |
| $\Theta_D$ (K) | 405 | 368 | 327 |
| $\gamma$ (mJ mol$^{-1}$ K$^{-2}$) | 9.15(11) | 7.27(16) | 10.1(1) |

for $LaSr_{0.5}Ba_{0.5}NiO_4$ and even for insulating $LaBaNiO_4$, which is rather surprising. The measured Sommerfeld coefficients $\gamma \approx 7$–$10$ mJ mol$^{-1}$ K$^{-2}$ are all of the same order of magnitude as in metallic $LaNiO_3$ ($\gamma \approx 13$ mJ mol$^{-1}$ K$^{-2}$ [18]) but they are large when compared to the free-electron value $\gamma \approx 2.0$ mJ mol$^{-1}$ K$^{-2}$ assuming one charge carrier per formula unit. In section 4 we will relate the measured Sommerfeld coefficients with the corresponding values for the Pauli-paramagnetic susceptibilities $\chi_0$ and the respective free-electron values.

### 3.5. *Thermal conductivity*

In section 3.2. we have shown that the electrical transport in $LaBaNiO_4$ is far from being metallic. However, from the magnetic-susceptibility and the specific-heat data alone one cannot distinguish between the physical properties of $LaSrNiO_4$ and those of $LaSr_{0.5}Ba_{0.5}NiO_4$ and $LaBaNiO_4$, all resembling those of a metal. We therefore carried out additional thermal-conductivity measurements on $LaSrNiO_4$ and $LaBaNiO_4$ to probe a further transport property. As can be seen in figure 5, the thermal conductivity of $LaSrNiO_4$ is somewhat larger than that of $LaBaNiO_4$. To be able to make a fair comparison we make use of the kinetic expression for the lattice contribution to the thermal conductivity, $\lambda_{latt} = C_{latt} v l/2$, where $C_{latt}$ is the lattice specific heat per unit volume, $v$ is the phonon group velocity and $l$ is the phonon mean free path. Since $v$ depends, to a first approximation, on the density $\rho$ of a material as $\rho^{-1/2}$, we have to compare the quantities $C_{latt}\rho^{-1/2}l$ to obtain an estimate for the respective lattice contributions. To calculate $C_{latt}$ over the entire temperature range we have used the standard expression for a Debye solid using the above values for $\Theta_D$, and used the x-ray densities $\rho = 6360$ kg m$^{-3}$ for $LaSrNiO_4$ and $\rho = 6980$ kg m$^{-3}$ for $LaBaNiO_4$, respectively.

Such a comparison is expected to work best in the high-temperature limit where we may assume that for a given temperature the phonon mean free path $l$ is approximately the same in both isostructural compounds, while $l$ is expected

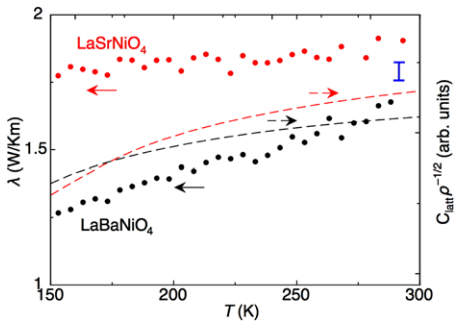


**Figure 5.** Thermal conductivities $\lambda(T)$ of $LaSrNiO_4$ and oxygen treated $LaBaNiO_4$ (left scale). The dashed lines correspond to $C_{\rm latt}\rho^{-1/2}$, which is related to the lattice contributions $\lambda_{\rm latt}$, see text. The solid bar at $T = 290$ K represents the electronic contribution $\lambda_{\rm el}$ for $LaSrNiO_4$ as estimated from the Wiedemann–Franz law near room temperature.

to be limited by extrinsic, sample dependent parameters at low temperatures. At the same time, the Wiedemann–Franz law that links the thermal conductivity to the electrical conductivity is expected to be valid at high temperatures as well. Therefore we focus on the quantity $C_{\rm latt}\rho^{-1/2}$, which should be proportional to $\lambda_{\rm latt}$ at a fixed temperature, e.g. at $T = 290$ K. In figure 5 we have plotted the thus obtained $C_{\rm latt}\rho^{-1/2}$ curves for both compounds in such a way that $C_{\rm latt}\rho^{-1/2}$ for $LaBaNiO_4$ approximately matches the measured thermal-conductivity data between 250 and 300 K. If we regard the thermal conductivity of this electrically insulating compound as a pure lattice thermal conductivity, the corresponding calculated $C_{\rm latt}\rho^{-1/2}$ curve for $LaSrNiO_4$ should then represent the lattice contribution of the latter compound as well. This calculated phonon contribution to the thermal conductivity is somewhat smaller than the measured data, however (see figure 5). As $LaSrNiO_4$ shows a metallic electrical conductivity, we may make use of the Wiedemann–Franz law to obtain the electronic contribution to its thermal conductivity, $\lambda_{\rm el} = L\sigma T$ with the Lorenz number $L = 2.44 \times 10^{-8}$ W$\Omega$ K$^{-2}$. Using the room-temperature electrical conductivity $\sigma \approx 90\ \Omega^{-1}$ cm$^{-1}$ we obtain $\lambda_{\rm el} \approx 6.6 \times 10^{-2}$ W K$^{-1}$ m$^{-1}$, which is of the correct order of magnitude to explain the difference between the measured thermal conductivity and the estimated lattice contribution of $LaSrNiO_4$ near room temperature (see figure 5).

## 4. Discussion

As a main result of the experimental sections we summarize that $LaSrNiO_4$ and $LaBaNiO_4$ represent two end members of the solid solution $LaSr_{1-x}Ba_xNiO_4$, in which the transport properties gradually change from metallic-like for $x = 0$ to insulating for $x = 1$. By contrast, the magnetic-susceptibility and the specific-heat data clearly resemble those of a metal, with no apparent difference between $LaSrNiO_4$ and $LaBaNiO_4$. We will first discuss the electrical conductivity alone and show that the variable-range hopping (VRH) scenario is certainly valid to explain the corresponding data for $LaSr_{0.5}Ba_{0.5}NiO_4$ and $LaBaNiO_4$. We then focus on the magnetic susceptibilities and the low-temperature specific heats and show that these two quantities are closely related to one another as they are in an ordinary correlated metallic system. We finally briefly discuss a plausible scenario that could explain these seemingly contradictory results.

**Table 4.** Characteristic parameters for the VRH type conductivity in $LaSr_{0.5}Ba_{0.5}NiO_4$ and $LaBaNiO_4$.

| | $LaSr_{0.5}Ba_{0.5}NiO_4$ | | $LaBaNiO_4$ | |
|---|---|---|---|---|
| | 2 K | 300 K | 2 K | 300 K |
| $T_0$ (K) | $1.4 \times 10^4$ | | $5.4 \times 10^5$ | |
| $\sigma_0$ ($\Omega^{-1}$ cm$^{-1}$) | 100 | | 210 | |
| $D(E_{\rm F})$ (J$^{-1}$ m$^{-3}$) | $2.1 \times 10^{47}$ | | $2.8 \times 10^{47}$ | |
| (states eV$^{-1}$/Ni) | 3.1 | | 4.3 | |
| $\xi$ (nm) | 0.76 | | 0.21 | |
| $R$ (nm) | 2.6 | 0.75 | 1.8 | 0.5 |
| $W$ (meV) | 0.40 | 17 | 1.0 | 42 |
| $\nu$ (Hz) | $2.7 \times 10^{11}$ | $3.4 \times 10^{12}$ | $9.6 \times 10^{11}$ | $1.2 \times 10^{13}$ |
| $\nu_{\rm D}$ (Hz) | $7.7 \times 10^{12}$ | | $6.8 \times 10^{12}$ | |

As we have seen in figure 2(b) the electrical conductivities of $LaSr_{0.5}Ba_{0.5}NiO_4$ and in particular that of $LaBaNiO_4$ are very well described by a 3D VRH-type temperature dependence $\sigma(T) = \sigma_0 \exp[-(T_0/T)^\alpha]$ with $\alpha = 1/4$ [17]. Other possible exponents such as $\alpha = 1/3$ (2D VRH [17]), $\alpha = 1/2$ (Coulomb-gap $T$-dependence [19]) or $\alpha = 1$ (activated finite-gap behaviour) result in a considerably worse agreement with the measured data. At first sight, $\sigma(T)$ of the series $LaSr_{1-x}Ba_xNiO_4$ shown in figure 2(a) strongly resembles the corresponding data measured on heavily doped semiconductors where the slope $|T_0^{1/4}|$ in a $\ln\sigma$ versus $T^{-1/4}$ representation progressively decreases as the system approaches the metal–insulator transition with increasing donor concentration (see, e.g. [20]). However, the physics of $LaSr_{1-x}Ba_xNiO_4$ is expected to be somewhat different from that of such systems where a number of localized states is supposed to be created within a sizeable band gap of an originally insulating or semiconducting system. Preliminary UV excited photoemission experiments that we have done on $LaBaNiO_4$ clearly exclude the presence of such a band gap that would also manifest itself in an activated (i.e. $\ln\sigma \sim -1/T$) temperature dependence of $\sigma(T)$ at high temperatures, which we do not observe. We can use the same argument to exclude a Mott transition upon stretching the crystal lattice by the substitution of Sr by the larger Ba that would also lead to a band gap. As the VRH conduction mechanism, in its original formulation [17], is not restricted to doped semiconductors but more generally assumes the hopping of electrons in a random potential with localized states, it may nevertheless be a valid description for the conduction mechanism in $LaSr_{1-x}Ba_xNiO_4$. In the present context we may mention the examples of Li-substituted and oxygen reduced $(La, Sr)_2CuO_4$, respectively [21, 22]. While in the former case $T_0 \approx 2 \times 10^6$ K is almost insensitive to the Li-concentration, this quantity increases from $\approx$2000 to $\approx 2 \times 10^5$ K as metallic $(La, Sr)_2CuO_4$ is progressively reduced. These values are comparable to what we obtain for $LaSr_{0.5}Ba_{0.5}NiO_4$ and $LaBaNiO_4$ (see table 4).

To check consistency, we can relate the parameters $\sigma_0$ and $T_0$ from the VRH expression for $\sigma(T)$ to the electron density of states at the Fermi level $D(E_F)$ as measured by the low-temperature specific heat, to the spatial extension $\xi$ of the quasilocalized wavefunction (localization length), to a mean hopping distance $R$, to the average hopping energy $W$ and to a hopping frequency $\nu$. The quantity $D(E_F)$ can be obtained from the measured Sommerfeld constant using $\gamma = \pi^2 k_B^2 D(E_F)/3$, while $\xi = [18/k_B T_0 D(E_F)]^{1/3}$. The $T$-dependent $R$ becomes $R = [9\xi/8\pi k_B T D(E_F)]^{1/4}$ and $W = 3/4\pi R^3 D(E_F)$. The hopping frequency $\nu = \sigma_0/e^2 R^2 D(E_F)$ should be, in principle, of the order of a typical phonon frequency, i.e. $\approx \nu_D = k_B \Theta_D/h$ (with $e$ the electron charge and $h$ the Planck constant) where we can use our specific-heat results for the Debye temperatures $\Theta_D$. In table 4 we present the corresponding values that we obtain for $LaSr_{0.5}Ba_{0.5}NiO_4$ and $LaBaNiO_4$.

The values for $\nu$ compare reasonably well with our rough estimate for the hopping frequencies, thereby confirming the validity of our approach. As the above relations are valid for an isotropic 3D system, we have to take the values for $\xi$ and $R$ with the reservation that $LaSr_{1-x}Ba_xNiO_4$ is certainly anisotropic. The related system $(La, Sr)_2CuO_4$ shows an anisotropy of the order of 10–20 of the electronically and magnetically relevant length scales in the metallic regime [23], depending on the crystal direction in which they are measured. The 'isotropic' values for $\xi$ may therefore be interpreted in the sense that the true localization lengths along the Ni–O planes are somewhat larger than our calculated $\xi$, i.e. of the order of a few times the lattice constant $a$, while the corresponding smaller localization length in the perpendicular direction is most likely only of the size of the extension of the hybridized Ni–O orbitals in the $c$-direction. The corresponding mean hopping distance is, according to the above estimate, of the same order of magnitude as $\xi$. The average hopping energies are consistent with the requirement $W \sim k_B T$ to make a hopping to distant sites possible.

From the measured Sommerfeld constants $\gamma$ given in table 3 we can calculate the density of states at the Fermi level $D(E_F)$ and compare them with the free-electron gas values $D_{f.e.}(E_F) = (3n/\pi)^{1/3} m_e/\pi\hbar^2$ (with the charge-carrier density $n$, electron mass $m_e$ and $\hbar = h/2\pi$) to obtain the electron effective-mass enhancement $m^*/m_e = D(E_F)/D_{f.e.}(E_F)$. Since we have a nominal $3d^7$ electronic configuration of Ni we may assume here one mobile charge carrier per formula unit to calculate $n = 2/a^2 c$. From $D(E_F)$ and the susceptibility data measured above $T = 40$ K (see table 2) we can also estimate the Stoner enhancement $1/(1-S)$ of the Pauli-paramagnetic susceptibilities using $\chi_0 = 2\mu_B^2 D(E_F)/(1-S)$. In table 5 we show the corresponding values for $LaSrNiO_4$, $LaSr_{0.5}Ba_{0.5}NiO_4$ and $LaBaNiO_4$.

These numbers are all comparable to those that have been measured for metallic $LaNiO_3$ ($\gamma \approx 13$ mJ mol$^{-1}$ K$^{-2}$, $S \approx 0.58$ [18]) and are usually interpreted as properties of a metal with rather strong electron correlations [4, 18]. Our value for $D(E_F) \approx 4$ states eV$^{-1}$ and the Ni atom for $LaSrNiO_4$ is also in fair agreement with the results from corresponding band-structure calculations for this compound with $D(E_F) \approx 6$ states eV$^{-1}$ [4].

**Table 5.** Electron density of states, effective-mass and Stoner enhancement from specific-heat and magnetic-susceptibility data.

| | $LaSrNiO_4$ | $LaSr_{0.5}Ba_{0.5}NiO_4$ | $LaBaNiO_4$ |
|---|---|---|---|
| $D(E_F)$ (J$^{-1}$ m$^{-3}$) | $2.66(3) \times 10^{47}$ | $2.07(5) \times 10^{47}$ | $2.81(3) \times 10^{47}$ |
| (states eV$^{-1}$/Ni) | 3.9 | 3.1 | 4.3 |
| $D_{f.e.}(E_F)$ (J$^{-1}$ m$^{-3}$) | $5.8 \times 10^{46}$ | $5.7 \times 10^{46}$ | $5.7 \times 10^{46}$ |
| $m^*/m_e$ | 4.62(6) | 3.62(8) | 4.96(5) |
| $1/(1-S)$ | 3.3(1) | 4.6(3) | 3.2(2) |
| $S$ | 0.70(2) | 0.78(5) | 0.69(4) |

The striking similarity of the low-temperature specific-heat and the magnetic-susceptibility data of $LaSrNiO_4$, $LaSr_{0.5}Ba_{0.5}NiO_4$ and $LaBaNiO_4$ as shown in the figures 3 and 4, with almost identical associated material parameters as summarized in table 5, suggests that the underlying physics that determines these parameters does not significantly change in $LaSr_{1-x}Ba_xNiO_4$ with varying $x$. This implies that $LaBaNiO_4$ has a finite density of states at the Fermi level, but these states obviously do not contribute to the transport properties, i.e. they must be localized. This situation, together with the observed VRH-type electrical conductivity [17], is very reminiscent of that in a Fermi glass [24–26]. In such a system, the Fermi energy $E_F$ lies below a mobility edge $E_c$ that separates localized electronic states from extended states. The free-electron density of states is then replaced by a quasiparticle density of states, but the expressions for the Sommerfeld constant and the Pauli-paramagnetic susceptibility of the system remain formally the same [25]. Very often $E_F$ can be tuned by changing the charge-carrier concentration to transform an insulating Fermi glass ($E_F < E_c$) to a metal ($E_F > E_c$). At this metal–insulator transition (Anderson transition at $E_F = E_c$), the conductivity at $T = 0$ is expected to be a constant $\sigma(0) = Ce^2/\hbar a$ with $C \approx 0.025$–$0.1$ [27], which corresponds to $\sigma(0) \approx 160 \cdots 640\ \Omega^{-1}$ cm$^{-1}$ in our case. By comparing this estimate with our results shown in figure 2 we conclude that $LaSrNiO_4$ with $\sigma(0) \approx 90\ \Omega^{-1}$ cm$^{-1}$ is indeed at the borderline of an Anderson-like metal-to-insulator transition. This interpretation is supported by measurements of the electrical conductivity on $La_{2-y}Sr_yNiO_4$ with varying Sr content $y$, where a finite $\sigma(0) \approx 100\ \Omega^{-1}$ cm$^{-1}$ is measured for polycrystalline samples with $y = 1$ [3] and on thin films at the corresponding metal–insulator transition around $y = 0.95$ [8]. With $y$ decreasing from $y \approx 1$, the resistivity $\rho(T) = \sigma(T)^{-1}$ diverges more and more rapidly as $T \to 0$ according to a VRH-type temperature dependence [8], while increasing $y$ above $y \approx 1$ results in a pronounced metallic behaviour in these measurements [3, 8]. In $LaSr_{1-x}Ba_xNiO_4$ we do not expect to significantly change the charge-carrier concentration, however, because we maintain a formal $Ni^{3+}$ oxidation state, and, as a consequence, our experimental values for $D(E_F)$ virtually do not depend on $x$. We therefore conclude that the progressive substitution of Sr by Ba increases $E_c$, rather than changing the charge-carrier concentration or even creating a Mott insulator with a band gap.

In the conventional Anderson metal-to-insulator-transition scenario the magnitude of the mobility edge $E_c$ is determined by the amount of atomic disorder. At first sight it may not be obvious why the isoelectronic substitution of Sr by Ba in $LaSr_{1-x}Ba_xNiO_4$ that is associated with an expansion of the crystal lattice should lead to a growth of such a disorder, with the stoichiometric $LaBaNiO_4$ as the composition with the largest $E_c$. In a plausible scenario we can relate the atomic disorder to the very large difference between the ionic radii of La and Ba, whereas the respective difference for La and Sr is comparably small. Therefore, atomic disorder is expected to grow with increasing Ba content. However, we want to mention the possibility that charge-localization phenomena that are known to occur in certain other stoichiometric Ni-oxides [15, 16] may also play a certain role in $LaSr_{1-x}Ba_xNiO_4$. In this spirit we can tentatively relate the observed superstructure peaks in our oxygen stoichiometric $LaBaNiO_4$ to such a charge-ordering phenomenon. Whether charge localization alone can lead to a Fermi-glass-type behaviour or not is not known to us. However, such a scenario could well explain that the charge-ordered $La_{2-y}Sr_yNiO_4$ samples for $y \leqslant 0.7$ (see, e.g. [28] and the cited references therein) show a VRH-type electrical conductivity [8, 29], but also a linear term in their low-temperature specific heats ($\gamma \approx 10$ mJ mol$^{-1}$ K$^{-2}$) and Pauli-like paramagnetic susceptibilities at high temperatures that are of the order of $\chi_0 \approx 6 \times 10^{-4}$ emu mol$^{-1}$ [29]. These observations, that are very similar to ours, may suggest that an Anderson-like transition is realized in $La_{2-y}Sr_yNiO_4$ around $y \approx 1$, mainly (but perhaps not exclusively) by tuning the Fermi energy with varying $y$, while in $LaSr_{1-x}Ba_xNiO_4$ it is most likely predominantly the mobility edge that is being tuned.

We conclude that we observe an Anderson-type metal-to-insulator transition in $LaSr_{1-x}Ba_xNiO_4$ around $x \approx 0$ that leads to a Fermi-glass behaviour of $LaBaNiO_4$, with insulating transport properties at $T = 0$ but at the same time with a finite density of states at the Fermi level. We suggest that this transition is caused by an increase of the mobility edge in conjunction with the progressive substitution of Sr by Ba and the increasing atomic disorder associated with it. The insulating state in $LaBaNiO_4$ neither shows antiferromagnetic order nor a finite band gap. We expect that a doping with charge carriers on the moderate level that is sufficient to induce metallic behaviour in the copper oxides (i.e. ≈0.15 holes per transition-metal atom [1]) will not lift the localization of the electronic states in the Fermi-glass state and will therefore not lead to metallic transport properties.

## Acknowledgments

We would like to thank to S Siegrist, B Bischof, L Keller, K Conder and V Pomjakushin for their technical assistance and to T Brugger for providing the photoemission data on $LaBaNiO_4$. This work was supported in part by the Swiss National Foundation through the NCCR MaNEP and grant no. 20-111653.

## References

[1] Bednorz J G and Müller K A 1986 *Z. Phys.* B **64** 189
[2] Jin S, Tiefel T H, McCormack M, Fastnacht R A, Ramesh R and Chen L H 1994 *Science* **264** 413
[3] Cava R J, Batlogg B, Palstra T T, Krajewski J J, Peck W F Jr, Ramirez A P and Rupp L W 1991 *Phys. Rev.* B **43** 1229
[4] Anisimov V I, Bukhvalov D and Rice T M 1999 *Phys. Rev.* B **59** 7901
[5] Kuiper P, Kruizinga G, Ghijsen J, Sawatzky G A and Verweij H 1989 *Phys. Rev. Lett.* **62** 221
[6] van Elp J, Eskes H, Kuiper P and Sawatzky G A 1992 *Phys. Rev.* B **45** 1612
[7] Eisaki H, Uchida S, Mizokawa T, Namatame H, Fujimori A, van Elp J, Kuiper P, Sawatzky G A, Hosoya S and Katayama-Yoshida H 1992 *Phys. Rev.* B **45** 12513
[8] Shinomori S, Okimoto Y, Kawasaki M and Tokura Y 2002 *J. Phys. Soc. Japan* **71** 705
[9] Demazeau G, Marty J L, Buffat B, Dance J M, Pouchard M, Dordor P and Chevalier B 1982 *Mater. Res. Bull.* **17** 37
[10] Alonso J A, Amador J, Gutiérrez-Puebla E, Monge M A, Rasines I, Ruiz-Valero C and Campa J A 1990 *Solid State Commun.* **12** 1327
[11] Demazeau G, Pouchard M and Hagenmüller P 1976 *J. Solid State Chem.* **18** 159
[12] Tranquada J M, Axe J D, Ichikawa N, Nakamura Y, Uchida S and Nachumi B 1996 *Phys. Rev.* B **54** 7489
[13] Chen C H, Cheong S W and Cooper A S 1993 *Phys. Rev. Lett.* **71** 2461
[14] Medarde M and Rodriguez-Carvajal J 1997 *Z. Phys.* B **102** 307
[15] Wawrzynska E, Coldea R, Wheeler E M, Mazin I I, Johannes M D, Sörgel T, Jansen M, Ibberson R M and Radaelli P G 2007 *Phys. Rev. Lett.* **99** 157204
[16] Alonso J A, García-Muñoz J L, Fernández-D íaz M T, Aranda M A G, Martínez-Lope M J and Casais M T 1999 *Phys. Rev. Lett.* **82** 3871
[17] Mott N F 1968 *J. Non-Cryst. Solids* **1** 1
Mott N F 1969 *Phil. Mag.* **19** 835
[18] Sreedhar K, Honig J M, Darwin M, McElfresh M, Shand P M, Xu J, Crooker B C and Spalek J 1992 *Phys. Rev.* B **46** 6382
[19] Shklovskii B I and Efros A L 1984 *Electronic Properties of Doped Semiconductors* (Berlin: Springer)
[20] Shafarman W N and Castner T G 1986 *Phys. Rev.* B **33** 3570
[21] Kastner M A, Birgeneau R J, Chen C Y, Chiang Y M, Gabbe D R, Jenssen H P, Junk T, Peters C J, Picone P J, Tineke T, Thurston T R and Tuller H L 1988 *Phys. Rev.* B **37** 111
[22] Osquiguil E J, Civale L, Decca R and de la Cruz F 1988 *Phys. Rev.* B **38** 2840
[23] Kohout S, Schneider T, Roos J, Keller H, Sasagawa T and Takagi H 2007 *Phys. Rev.* B **76** 064513
[24] Anderson P W 1970 *Comments Solid State Phys.* **2** 193
[25] Freedman R and Hertz J A 1977 *Phys. Rev.* B **15** 2384
[26] Müller K A, Penney T, Shafer M W and Fitzpatrick W J 1981 *Phys. Rev. Lett.* **47** 138
[27] Mott N F 1972 *Phil. Mag.* **26** 1015
[28] Ishizaka K, Arima T, Murakami Y, Kajimoto R, Yoshizawa H, Nagaosa N and Tokura Y 2004 *Phys. Rev. Lett.* **92** 196404
[29] Kato M, Maeno Y and Fujita T 1991 *J. Phys. Soc. Japan* **60** 1994